Rim instability in dewetting of thin polymer films

Dissertation
zur Erlangung des Grades
des Doktors der Naturwissenschaften
der Naturwissenschaftlich-Technischen Fakultät II
- Physik und Mechatronik -
der Universität des Saarlandes

von

Ludovic Marquant

Saarbrücken

2013

Tag des Kolloquiums: 17.04.2014

Dekan: Univ.-Prof. Dr. rer. nat. Ch. Wagner

Mitglieder des Prüfungsausschusses:

  Vorsitzender: Univ.-Prof. Dr. rer. nat. A. Ott
  Gutachter: Univ.-Prof. Dr. rer. nat. K. Jacobs
                             Univ.-Prof. Dr. rer. nat. M. Lücke
  Akademischer Mitarbeiter: Dr. J.-B. Fleury

à mes filleuls, neveux et nièces

Abstract

Understanding flow properties at the solid/liquid interface is important for numerous of technological applications in nanotechnology and microfluidic. The strong scientific interest in the field of thin liquid films led to new conclusions on the impact of hydrodynamic slippage on the dewetting dynamics and on the shape of the rim growing at the three phase contact line.

This work consists of verifying the validity of these findings at late stage of dewetting, *i.e.* while the rim instability develops, and of drawing new conclusions linking interactions at interfaces with the later instability. In a first part, a qualitative analysis demonstrates a rim instability decomposed into several regimes, while fingering solely develops with flows with strong interfacial slip length. A closer look of the instability at nanometric resolution evidences the onset of a second flow varying with slippage but also with viscosity. We finally propose a new method to determine to what extent hydrodynamic slippage interferes flow properties in the rim.

Kurzzusammenfassung

Das Verständnis der Fließeigenschaften an der Fest/flüssig-Grenzfläche ist wichtig für viele technische Anwendungen in der Nanotechnologie und Mikrofluidik. Das starke wissenschaftliche Interesse im Bereich der dünnen Filmen führte zu neuen Erkenntnissen, wie sich hydrodynamisches Rutschen auf die Form eines sich von der Drei-Phasenkontaktlinie eintwickeknden Randwulstes auswirkt.

Diese Arbeit verifiziert diese Ergebnisse in einen späten Stadium der Entnetzung, d.h. während sich die Randwulstinstabilität entwickelt. Sie zieht neue Schlussfolgerungen indem sie die Wechselwirkungen an der Grenzfläche mit denen der späteren Instabilität verknüpft. Zunächst demonstriert eine qualitative Analyse des Randwulstinstabilität, dass diese sich im verschiedene Regime einteilen lässt. Die Fingerstrukturen entwickeln sich im dabei ausschließlich unter Einfluss von starken Rutschen an der Grenzfläche. Ein genauer Blick auf die Instabilität zeigt, dass auf die nanometerskalar das Einsetzen eines zweiten Flussen nicht nur durch Rutschen sondern auch durch die Viscosität beeinflusst wird. Schließlich wird eine neue Methode zur Bestimmung inwiefern hydrodynamisches Rutschen auf den Fluss im Randwulst Einfluss nimmt, vorgeschlagen.

Contents

Contents

1 Introduction

"Caution wet floor!" Everyone reading this sign is alerted by the fact that an uncontrolled behavior might interfere one's controlled motion. Young children might just arrive at full speed and jump on the wet surface to see what distance they can reach, while a more cautious person might just reduce his/her initial speed to minima and walk through the surface leaning on a wall to avoid slipping.

Whether we deal with a water layer, a paint, a lubricant or a thin protective layer, situations in every day life or industry which necessitate a control of the stability of a wetting layer are multiple. The lacrimal film sandwiched between your eye and the contact lens should preferably be perfectly stable to provide you an optimal wearing, whereas the water layer on top of a road should rather quickly retract from your tire if an emergency break is needed. Similarly, a paint manufacturer would rather produce a paint which homogeneously spreads on any surface, whereas the company in charge of your windshield would prefer that rain drops immediately dewet the glass window.

Controlling flow properties of a fluid on solid substrates is not trivial, but has been part of today's essentials for scientists. Considerable knowledge was obtained on the behavior of flow properties under confinement in the last decades. Deviation from macroscopic flows assuming a no-slip boundary condition are observed. The presence of slippage changes the dewetting dynamics in thin polymer films, but also impacts on the rim shape. Methods used to quantify slippage, however, are still under debate and require the expertise and time of the person performing the experiments and doing the calculation. In the case the absolute value of the slip length is not mandatory, a rapid method would be useful to determine whether the substrate is subject to strong slippage at the solid interface. The final stage of dewetting illustrated Fig. 1.1 exhibits two different patterns produced by solely changing the substrate on which dewetting experiments take place. How are these patterns formed? What is the impact of slippage on the final picture?

While hydrodynamics of dewetting occur in-plane perpendicular to the three phase contact line forming a growing rim, a hydrodynamic instability takes place parallel to this contact line. In static situations, *i.e.* with a ridge of volume set at the onset of the instability, the ridge destabilizes into a series of droplets via the Rayleigh-Plateau instability with the amplitude

of the perturbation growing exponentially with time. In the dynamical case we present in this study, the flow along the ridge competes with the flow of the rim being fueled due the displacement of the three phase contact line.
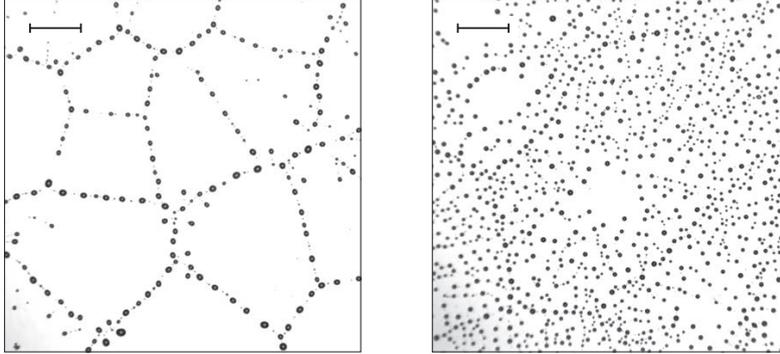
Figure 1.1: Late stage of thin film dewetting two different substrates at the same temperature (120 °C) The polymer film, identically prepared in both situations (PS10.3K of thickness 115(5)nm), covers a Si-wafer tailored with a DTS layer (left) or a AF 1600 teflon layer (right). Picture size $(700 \ \mu m)^2$. Scale bar 100 μm.

We propose with this work a detailed analysis and a complete understanding of the dewetting scenario combined with the rise of the perturbation which we propose as an alternative method to see the presence in a system of **slippage "by eye"**. In a first chapter we concentrate on the evolution of the in-plane instability. We study the impact of changes in morphology of the ridge and changes in the dewetting dynamics due to variations in the pattern formation, *i.e.* fingering. Then, we focus on the evolution of the rim profile, a cross section of the ridge in the dewetting direction. We concentrate on the evolution of monotonic rim profiles in presence of fingering. The dynamic version of the Rayleigh-Plateau instability, denoted **rim instability**, is then studied at early stage of dewetting. Atomic force microscopy enables to picture different evolution of the amplitude of the perturbation at early stage. Chapter 7 details the process of droplet detachment in the absence of the fingering regime. In the following chapter, we discuss the impact of film thickness on the rim instability observed in the strong slip case. Finally we discuss the impact of the geometry and introduce a novel set of experiments which helps to consider whether slippage also affects the static situation.

2 State of the art

2.1 Polymers at interfaces

2.1.1 Polymer physics

Polystyrene   Polystyrene (PS) is a macromolecule synthesized from the polymerization of styrene monomers, a vinyl benzene of mass $M = 104\,\text{kg.mol}^{-1}$. An atactic polystyrene is usually obtained when radical polymerization is used. This type of reaction ensures the production of an amorphous polymers with styrene groups placed randomly on either side of the polymer chain axis which avoids the creation of crystalline structures. This situation contrasts syndiotactic polymers and isotactic polymers where the phenyl group is placed alternatively on either side of the backbone chain, this mode is usually represented as ABAB, or the phenyl group is attached to the same side of the chain, mode denoted AAAA. The quality of the polymer preparation is usually verified with a polydispersity index which is the ratio of the weight average molecular weight to the number average molecular weight:

$$I = M_{\text{w}}/M_{\text{n}}, \qquad M_{\text{w}} = \frac{N_{\text{i}} M_{\text{i}}^2}{N_{\text{i}} M_{\text{i}}}, \qquad M_{\text{n}} = \frac{N_{\text{i}} M_{\text{i}}}{N_{\text{i}}}. \tag{2.1}$$

with N the number of moles of each species.

Glass transition temperature   Annealing the polymer involves a linear increase of the film thickness H, linear thermal expansion, as depicted in Fig. 2.1(a). The transition between the two slopes is known as the glass transition temperature T_{g}. A glassy stage of the polymer is known below T_{g} and a liquid state above. For PS, the bulk temperature shows a transition at $T_{\text{g}} = 100\,^{\circ}\text{C}$. Confinement observed due to the preparation of thin polymer films involves a reduction of the glass transition temperature with the film thickness, Fig. 2.1(b), as discusses in [64, 55, 37]. T_{g} also varies with the type of polymer used and its chain length M as

$$T_{\text{g}} = T_{\text{g}}^{\infty} - \zeta/M, \tag{2.2}$$

where T_{g}^{∞} is the glass transition for a polymer of infinite molar mass and ζ is a constant relative to the properties of the polymer. For this reason, a lower value of $T_{\text{g}}^{\text{bulk}}$ is observed on
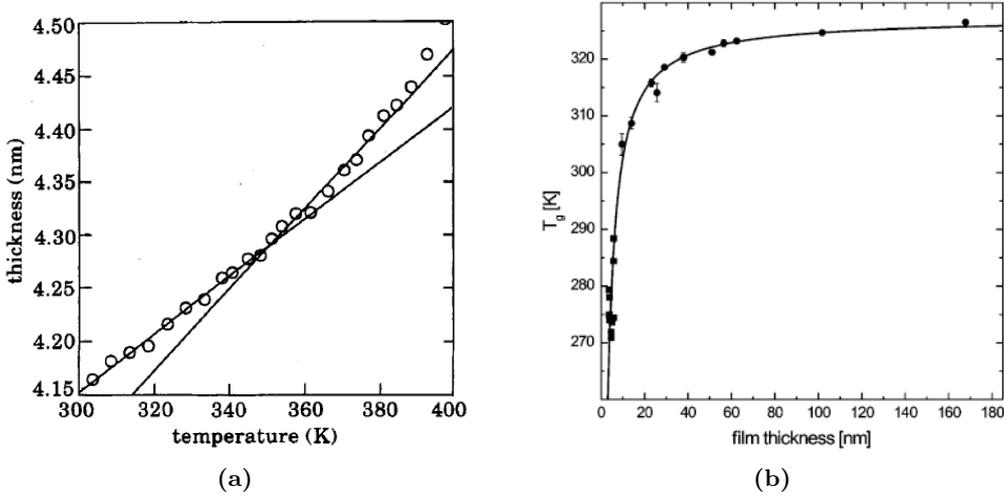
Figure 2.1: (a) Film thickness measurements at approximately 5 K increments in temperature. Lines of best fit through the data indicate a T_g of 350.8 K for this sample ($M_w = 501$ kg.mol^{-1}) that had been equilibrated at 413 K prior to the experiment. [64] (b) The glass transition of thin films of 2 kg.mol^{-1} polystyrene, as determined from thermal expansion (circles) and from the growth of spinodal waves (squares) with the model (solid curve). [55]

Fig. 2.1(b), the 2.2 kg.mol^{-1} PS chain consists of 21 styrene monomers and is considered as a polymer with small chain length.

Viscosity   Parallel to the linear increase of the film thickness, the increase of temperature also involves a decrease of the inner friction of the polymer chains, viscosity η. The function description this dependency is known as the WLF-equation (Williams, Landel, Ferry-equation)

$$\eta = \eta_g \exp \frac{B(T - T_g)}{f_g(T - T_\infty)}, \tag{2.3}$$

where η_g denotes the viscosity at T_g, B an empirical constant, f_g the free liquid volume fraction and T_∞ the Vogel temperature.

Viscosity also increases with the chain length of the molecule as $\eta \propto M^\nu$. Two growth behavior are found below and after a transition molar mass, where $\nu = 1$ below and $\nu = 3.4$ above. The steeper increase of entanglement length is explained by entanglement of polymer chains predominant above a critical chain length M_c. Above M_c a specific strand length is observed called the entanglement length M_e [107, 14]

Under Newtonian flow, the shear rate σ evolves linearly with viscosity with strain rate $\dot{\gamma}$, $\sigma = \eta\dot{\gamma}$. However, with long polymer chains, elastic properties of the polymer might change

the flow according to $\sigma - G\gamma$ with G the elastic modulus of the liquid. The two most used models combining the viscous and elastic properties of the flow, denoted viscoelastic properties, are the Maxwell model (equation 2.4) and the Kelvin-Voigt model (equation 2.5)

$$\dot{\gamma} = \frac{1}{G}\dot{\sigma} + \frac{1}{\eta}\sigma \qquad (2.4) \qquad\qquad\qquad \sigma = G\gamma + \eta\dot{\gamma} \qquad (2.5)$$

2.2 Stability of supported thin films

Understanding the stability of a thin liquid film deposited on top of a substrate is essential to predict the behavior of the system. Bäumchen and Jacobs reviewed recent advances in this field giving a clear connection between the stability conditions and the dynamics and the final pattern obtained [15].

The stability of a thin film is governed by the evolution of the effective interface potential as a function of the film thickness. Three cases are illustrated in Fig. 2.2(a), the stable, metastable and unstable. The function $\phi(h)$ is build from calculation of contribution between attractive and repulsive forces given in equation 2.6 for a system Si/SiO$_2$/layer/film. The index $_c$ represents a layer covering the substrate in case the Si-wafer is modified prior use.

$$\phi(h) = \frac{C_s}{h^8} - \frac{A_c}{12\pi h^2} + \frac{A_c - A_{\mathrm{SiO_2}}}{12\pi(h+d_c)^2} + \frac{A_{\mathrm{SiO_2}} - A_{\mathrm{Si}}}{12\pi(h+d_c+d_{\mathrm{SiO_2}})^2} \qquad (2.6)$$

Fig. 2.2(b) depicts the result for a metastable system. A film of thickness larger than $2.8\,\mathrm{nm}$ is metastable and becomes unstable as it thins. The transition occurs when the second derivative of the effective interface potential crosses becomes negative ($\phi''(h) < 0$. Below this thickness, the film thins without external forces to reach an equilibrium thickness h_{eq} represented by the minima in $\phi(h)$, which reveals the contribution of van der Waals forces and repulsive forces as detailed in [15]. This height is linked to the surface tension and Young contact angle, contact angle measured at the end of dewetting experiments.

$$\phi(d_{eq}) = \gamma_{lv}(cos\theta_Y - 1) \qquad (2.7)$$

2.3 Hydrodynamics in thin liquid films

This part draw main lines in the basic theoretical concepts for hydrodynamics in thin liquid films. More details are available in the topical review [15] and references therein.
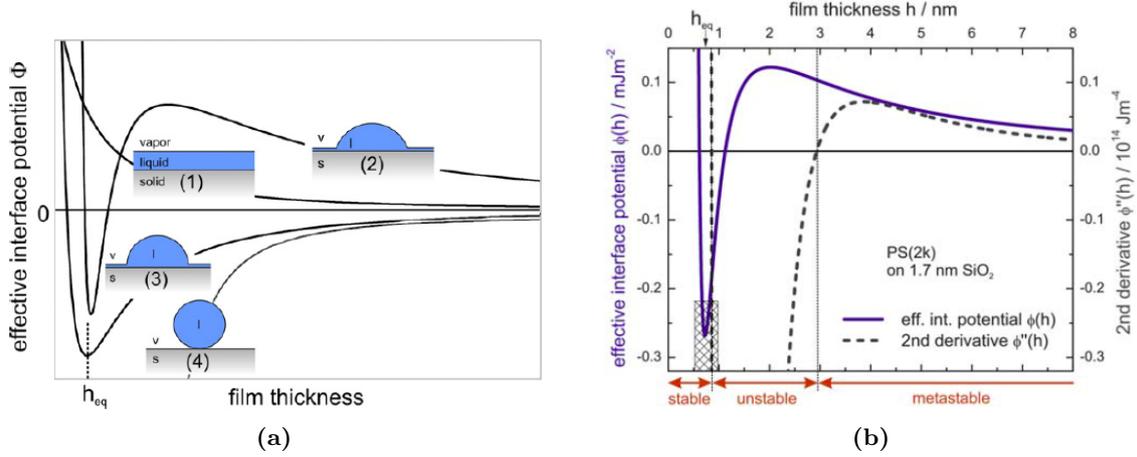
Figure 2.2: (a) Different shapes of the effective interface potential $\phi(h)$ associated with different wetting conditions. Curve (1) characterizes a stable liquid film. Curve (2) represents a metastable, curve (3) and (4) an unstable situation [14]. (b) Effective interface potential $\phi(h)$ (solid line) and its second derivative $\phi''(h)$ (dashed line) for a liquid polystyrene PS(2k) film prepared on a Si wafer with a 1.7 nm SiO$_2$ layer. The sign reversal of $\phi''(h)$ characterizes the stability of the film. The hatched rectangle indicates typical experimental errors of the contact angle measurement and the determination of the equilibrium film thickness h_{eq} [15].

2.3.1 Navier-Stokes equation

The Navier-Stokes equation (2.10) describes the dynamics of an incompressible fluid which suggests that inertia of a small amount of a fluid equals the sum of external forces. The latter equation starts with the equation of continuity which reads, according to the conservation of mass, as

$$\partial_t \rho + \nabla \cdot (\rho \mathbf{u}) = 0, \tag{2.8}$$

with $\mathbf{u}$ the velocity field of the fluid in the three dimensions. Working under conditions of an incompressible liquid of density ρ, partially and temporally constant, implies a simplified version of equation 2.8 : $\nabla \mathbf{u} = 0$. The conservation of momentum leads to the Navier-Stokes equation for incompressible fluids.

$$\rho \frac{\partial \mathbf{u}}{\partial t} + \rho(\mathbf{u} \cdot \nabla)\mathbf{u} = -\nabla p + \eta \nabla^2 \mathbf{u} + \rho \mathbf{f} \tag{2.9}$$

where the pressure gradient ∇p and the volume force $\mathbf{f}$ are contribute to forces driving the flow of the liquid. For thin polymer films inertia is small compared to viscosity ($Re << 1$), we can neglect the left-hand side term which leads to the Stokes equation

$$0 = -\nabla p + \eta \nabla^2 \mathbf{u} + \rho \mathbf{f} \tag{2.10}$$
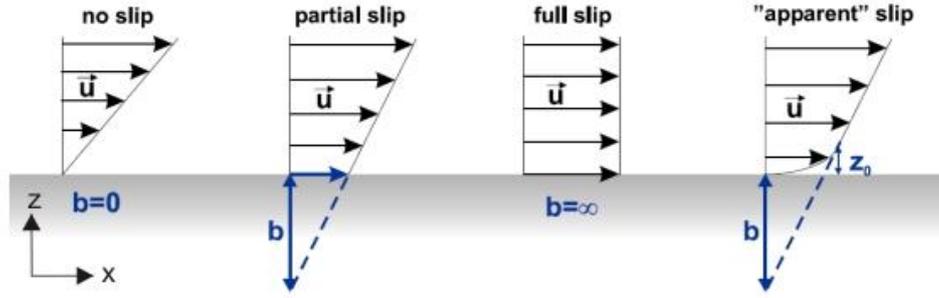
Figure 2.3: Different velocity profiles in the vicinity of the solid/liquid interface and illustration of the slip (extrapolation) length b. The situation of 'apparent' slip is illustrated on the right: according to a thin liquid layer of thickness z_0 that obtains a significantly reduced viscosity, the slip velocity $u_{x|z=0}$ is zero, but a substantial slip length is measured. [14]

2.3.2 Boundary conditions at interfaces

In case of thin liquid films, the tangential flow velocity $\mathbf{u}_\parallel$ differs from the bulk behavior assuming the no-slip boundary condition. As early as 1823, Navier states that $\mathbf{u}_\parallel$ evolves proportionally to the strain rate tensor with the slip-length b acting as constant of proportionality (equation 2.11, with $\mathbf{n}$ the normal component, perpendicular to the stress tensor) [88]. Focusing on an unidirectional flow, equation 2.12 demonstrates that the slip length in fact evolves as the inverse of the friction coefficient ξ.

$$\mathbf{u}_\parallel - b\mathbf{n} \cdot \dot{\gamma} \qquad (2.11) \qquad\qquad b = \frac{u_x}{\partial_z u_x}|_{z=0} = \frac{u_x \eta}{\sigma} = \frac{\eta}{\xi} \qquad (2.12)$$

Restricting the motion of the fluid to the xz–plane in turn enables an easy representation of flow profiles, as illustrated in Fig. 2.3, displaying both limiting cases, *i. e.* the no slip situation ($b = 0$) and plug flow ($b = \infty$). However, many experimental setup evidence an intermediate case, partial slip, where a non zero slip length can be defined with the method described in part 2.2. Apparent slip illustrates the case where slip length is non negligible, but a zero dewetting velocity at $z = 0$ is obtained as a result of a thin layer of reduced viscosity for the height z_0.

2.3.3 Thin film equation (Newtonian liquids)

The various flow profiles observed in the previous part result from fluid motion occurring under confinement far below the limit were bulk properties are observed. Gravitational forces are neglected for film thicknesses below the capillary length $l_c = \sqrt{\gamma_{lv}/\rho g}$, typically in the millimeter range. In turn, intermolecular forces become more important. Combined with the fact that the lateral length scale of the film thickness variations is much smaller than the film

thickness, we obtain a simpler version of Navier-Stokes equations. The thin film equation for Newtonian fluids reads [93]

$$0 = -\nabla(p + \phi'(h)) + \eta\nabla^2\mathbf{u}. \tag{2.13}$$

The disjoining pressure $\phi'(h)$ stands for the short range forces as the spatial derivative of the effective interface potential $\phi(h)$, described in part 2.2, which represents the competition between short range and long range forces.

2.3.4 Equations of motion

Applying the Navier slip boundary (equation 2.12) to the Navier-Stokes equations (equations 2.10) together with the assumption of the lubrication approximation, the equation of motion for thin films in the three dimensions then reads

$$\partial_t h = -\nabla[m(h)\nabla(\gamma_{\text{lv}}\nabla^2 h - \phi'(h))] \qquad \text{with} \qquad m(h) = \frac{1}{3\eta}(h^3 + 3bh^2). \tag{2.14}$$

The mobility coefficient $m(h)$ expresses motion at the solid/liquid interface according to the amount of slippage of the system. In the no-slip boundary condition the mobility of thin liquid film follows $m(h) = h^3/3\eta$ whereas $m(h) = bh^2/\eta$ if friction ξ at the solid/liquid interface is low.

2.3.5 Lubrication models including slippage

Strong slip models were developed by [86] and [62] in order to overcome the limitation of the low range of application of the slip length, a consequence of the lubrication approximation. In this case, the slip length is much larger than the initial film thickness. The monodimensional equation of motion and the kinematic equation then read:

$$u = \frac{2b}{\eta}\partial_{\text{x}}(2\eta h\partial_{\text{x}}u) + \frac{bh}{\eta}\partial_{\text{x}}(\gamma\partial_{\text{x}}^2 h - \phi'(h)), \qquad \partial_{\text{t}}h = -\partial_{\text{x}}(hu). \tag{2.15}$$

The range of application of these models was investigated using a linear stability analysis. A small perturbation δh is introduced to an initially flat film of thickness H.

$$h(x,t) = H + \delta h \exp(k\xi) \qquad \text{with} \qquad \xi = x - s(t) \tag{2.16}$$

where ξ is the comoving frame and $s(t)$ the position of the three phase contact line. A third order polynomial is then obtained for the lubrication model where k represent the solutions

(discussed in part 2.4.3).

$$(h_0 k)^3 + 4Ca(Hk)^2 - Ca\frac{h_0}{b} = 0 \tag{2.17}$$

Fig. 2.4 evidence that the range slip must be large to use the lubrication model. A generalized model is obtained using a third Taylor expansion [40].

$$\left(1 + \frac{h_0}{3b}\right)(h_0 k)^3 + 4Ca\left(1 + \frac{h_0}{2b}\right)(Hk)^2 - Ca\frac{h_0}{b} = 0 \tag{2.18}$$
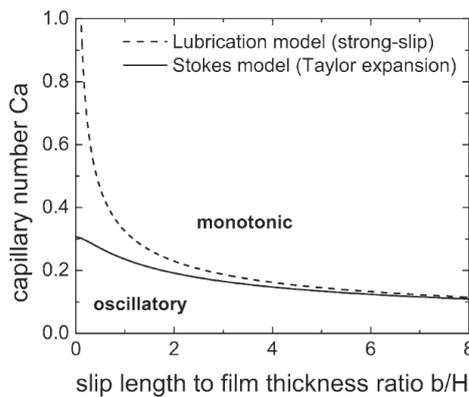
Figure 2.4: Comparison of the theoretically expected transition from oscillatory profiles to monotonic ones for the strong-slip lubrication model (dashed line) and the third order Taylor expanded Stokes model (solid line).[18]

2.4 Dewetting dynamics

Let consider the case of a supported liquid film partially wetting a smooth and passive substrate. The situation accounts for film thicknesses smaller than the capillary length $\kappa^{-1} = \sqrt{\gamma/\rho g}$ (typically in the millimeter range for water), but larger than few nanometers, which corresponds to the metastable case discussed in section 2.2. Dewetting takes place by heterogeneous nucleation of a hole, whose nuclei are defects such as dust particles, inhomogeneities on the surface. The distinctive feature of this rupture scenario is the random distribution of holes, a key point to distinguish this process from other scenario like spinodal dewetting[1] [60].

---

[1]Spinodal dewetting (dewetting that takes place by amplification of capillary waves) shows a periodic distribution of sites, following the capillary wavelength [111]. An accurate method to distinguish between dewetting by heterogeneous nucleation and spinodal dewetting uses the Minkowsky analysis, see details in [59]

2.4.1 Stages of dewetting

The system reaches equilibrium when a collection of droplets with a Young contact angle θ_Y lie on the substrate. The transition from the liquid film fully covering the substrate to the final equilibrated stage was divided in different stages reported by Brochard-Wyart et al. [9]. Each of which being limited by length scales taking into account the hole radius R and the slip length b.

Brochard-Wyart et al. made a theoretical description of the different dewetting regimes [10]. First, an exponential growth of the hole radius has been predicted right after the hole has formed: $R \propto \exp t/\tau$, where the characteristic time depends on the initial parameters, film thickness h_0, surface tension γ and viscosity η, $\tau = h_0 \eta / \gamma$. The growth law has been experimentally observed by Masson and Green under extreme conditions (dewetting under vacuum and with low contact angle) [79]. The absence of a hole characterizes this stage and last until the hole radius equals a critical radius R_c, with $R_c = \sqrt{bh_0}$. One should however note that the analysis considers viscoelastic polymers and is based on elastic dissipation for the stress release. The limit R_c might not be suitable for purely viscous films. Indeed, in the case of bursting of a soap bubble for newtonian liquids [30, 7], which is similar to dewetting of suspended films, a rim could be directly observed. The birth of the rim appears in a second stage where the temporal evolution of the hole radius is linear $R \approx \frac{|S|}{\eta}(\frac{b}{h_0})^{0.5}t$ and the rim becomes mature above another critical hole radius $R'_c = b$.

2.4.2 Mature rims

We concentrate in this section on the stage of dewetting where the rim is mature, rounded by the Laplace pressure. This stage is of peculiar interest to relate the change of friction at the solid/liquid interface to the diversity on dynamics observed in dewetting experiments.

Driving and dissipative forces

Driving force The three phase contact line resulting from the nucleation of a hole is in motion when the dynamic contact angle θ_d formed differs from the equilibrium contact angle θ_Y. The contact line moves into the film when the resulting capillary force per unit length F_c/l (eq. 2.19) is negative, *i.e.* when $\theta_d < \theta_Y$.

$$\frac{F_c}{l} = \gamma_{lv}(cos\theta_Y - cos\theta_d) = S + \gamma_{lv}(1 - cos\theta_d) \qquad (2.19)$$

On the back side of the rim (the 'wet' side)a positive capillary force with the dynamic component only ($\gamma_{lv}(1 - cos\theta_d)$) occurs so that the summation of forces at both sides of the ridge

gives the spreading coefficient eq. 2.20 [27] as resulting force for the system.

$$\frac{\mathbf{F_c}}{l} = S \tag{2.20}$$

We should note that no gravity plays a role as the initially prepared film thickness is much lower than the capillary length $h_0 << \kappa^{-1}$ (κ^{-1} is in the the millimeter range for water). The Laplace pressure influences the rounded shape of the rim, therefore influences indirectly the dewetting dynamics (as a contribution of the friction of the S/L interface via the rim width) in the evolution of the rim width.

The dewetting dynamics of velocity V of the system is balanced by the driving force $|S|$ and the sum of dissipations within the fluid and the corresponding velocities v_i, denoted by viscous friction F_v, and friction at the solid/liquid interface, denoted by F_s with s standing for slippage.

$$|S|V = F_v v_v + F_s v_s \tag{2.21}$$

No-slip boundary condition - Viscous dissipation In a system whose friction forces are purely viscous, the resulting dewetting velocity $V = v_v$ is constant (eq. 2.22) [9]. Redon et al. demonstrated that viscous fluids (silicon oils or alkanes of viscosity $\eta < 60\,Pa\,s$) in the range of $20 - 50\,\mu m$ dewet hydrophobic substrates with a dewetting velocity proportional to θ_Y^3 [101]. The constant of proportionality $C_v(\theta_v)$ reflects the dissipation at the three phase contact line.

$$V = C_v(\theta)\frac{|S|}{eta} \propto \frac{\gamma_{lv}}{\eta}\theta_Y^3 \tag{2.22}$$

The integration of the velocity $V = \dot{R}$ gives a linear growth of the hole radius as seen in eq. 2.23.

$$R \propto t \tag{2.23}$$

Plug flow - Full slippage at the solid/liquid interface Systems whose friction at the solid/liquid interface prevails show a decreasing dewetting velocity with time. In the plug flow situation (large slip length b), the velocity with a slip contribution varies with b/W with W being the rim width and b representing the friction at the solid/liquid interface: $b = \eta/\xi$, ξ is the friction coefficient.

$$V = \frac{1}{3}\frac{|S|}{\eta}\frac{b}{W} \qquad \text{with} \qquad W = C_s\sqrt{h_0}\sqrt{R} \tag{2.24}$$

Due to conservation of mass the rim with for a hole varies as $W \propto \sqrt{R}$, C_s is a constant of proportionality of representing the growth of W. The integration of the velocity $V = v_s$ gives a Radius growing as a power law with time, with an exponent $\alpha = 2/3$ (eq. 2.25).

$$R \propto t^{2/3} \tag{2.25}$$

Experimentally, Redon et al. observed that an increase of molecular weight together with a decrease of the initially prepared film thickness lead to dewetting dynamics following the plug flow situation [102]. We should note also that the geometry of the system doesn't affect the power law mentioned before as $W \propto \sqrt{R}$ in both cases according to [14].

General model – superimposition of both dissipation mechanisms

Both models derived for the limiting cases of either pure viscous dissipation or pure dissipation at the substrate/film interface have been completed by Jacobs et al. to cover a broader range of experiments [58]. The new model proposed a resulting dewetting velocity as a sum of both aforementioned velocity contributions: $V = v_v + v_s$, which was possible because the same driving force is applied for both dissipation mechanisms. Eq. 2.26, resulting from the separation of variable, is valid for both limiting cases: for $b \to 0$, $R \propto t$ and $b \to \infty$, $R \propto t^{2/3}$.

$$t - t_0 = \frac{K_v}{S}(R - 2\frac{K_v}{K_s}\sqrt{R} + 2(\frac{K_v}{K_s})^2 ln(1 + \frac{K_s\sqrt{R}}{K_v}))$$
$$\text{with} \quad K_v = \frac{\eta}{C_v(\theta)} \quad \text{and} \quad K_s = \frac{3\eta}{b}\frac{w}{\sqrt{R}} \tag{2.26}$$

2.4.3 Methods to determine slippage?

No clear explanation is given today to explain the mechanism of slippage of fluids at the solid interface. However, the numerous experimental methods which have been investigated the last decades [90, 72, 5] evidence the growing interest to understand or measure slippage. More recently, Jacobs et al. have concentrated on finding consistent methods characterize hydrodynamic slippage using the dynamics of dewetting, denoted hole growth analysis, and the profile of the rim obtained during dewetting experiments, rim profile analysis.

Hole growth analysis

The first clear evidence of the presence of slippage in the system was given by Fig 2.5(a) where the dewetting dynamics $R(t)$ of the system with the highest driving force, AF 1600 with green
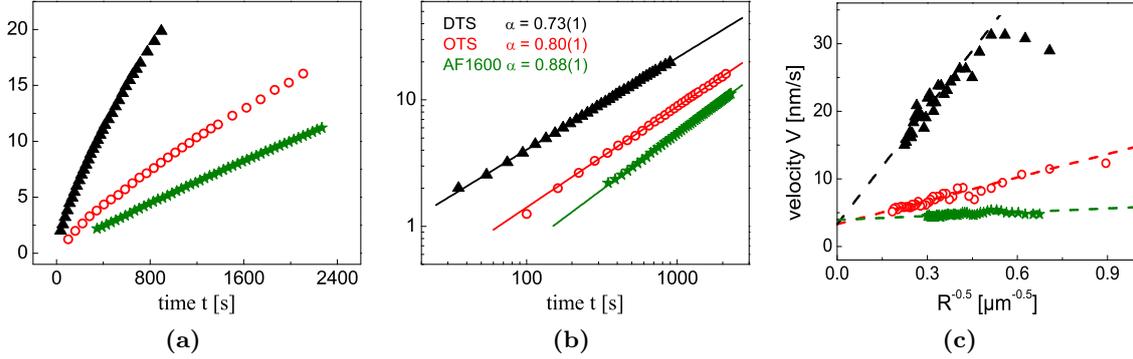
Figure 2.5: (a) Hole growth dynamics ($R(t)$) on DTS, OTS and AF 1600 and the corresponding double logarithmic representation (b) with the coefficient of the algebraic power law $R \propto t^{\alpha}$. (c) Dewetting velocity V as a function of $R^{-0.5}$ [16].

stars, are the slowest. A strong slip behavior is rapidly confirmed on Fig. 2.5(b) with the small coefficient α, close to 2/3 on DTS (black squares) compared to OTS and AF 1600. A quantitative value of b is calculated with a linear fit of the dewetting velocity V plotted as a function of $\sqrt{R}^{-1}$.

Based on the additive superimposition model previously described Fetzer and Jacobs proposed a method to extract the slip-length b from the dynamics of dewetting. The dewetting velocity $V = v_v + v_s$ can be written as follows:

$$ V = v_0 + \frac{K}{\sqrt{R}} \qquad \text{with} \quad K = \frac{1}{3} \frac{|S|}{\eta} \frac{b}{C_s \sqrt{h_0}} \tag{2.27} $$

Eq. 2.27 evidences that plotting the dewetting velocity V as a function of the inverse of the square root of the hole radius R, we can read directly the viscous velocity as the intercept of the linear extrapolation of $V(R^{-0.5})$ at zero and extract the slip length b from the slope K (see Fig. 2.5(c)). At large dewetting distances, *i.e.* $R^{-0.5} \to 0$, the height of the rim H is much larger than the slip-length. We are in the regime where viscous dissipation dominates as seen in section 2.4.1. This argument was verified by plotting the intercept $V(R^{-0.5} = 0) = v_v$ versus η^{-1}; a linear dependence has been shown for the measurement at different temperatures [39, 13].

Moreover it has been shown that v_0 is independent of the film thickness, which is another proof that $v_0 = v_v$ as viscous dissipation occurs mainly at the three phase contact line. Changes of film thicknesses, however, affect the slope K from which the slip length b can be extracted when the constant C_s is known. Investigating *in situ* experiments with AFM shows a self-similar growth of the rim whose measured rim width[2] W plotted versus $\sqrt{R}$ gives C_s.

---

[2]The rim width is defined as the distance between the three phase contact line and the rim in contact with the unperturbed film at 110 % of h_0

The slip length obtained from the hole growth dynamics is independent of film thickness. Comparing different systems, b is higher and temperature dependent on DTS and OTS substrate (samples hydrophobized by self assembly monolayer) $b >> h_0$, lower and temperature-independent on AF 1600 $b << h_0$.

Rim Profile analysis

We can also extract hydrodynamic slippage from the profile of the rim scanned with AFM. At a traveled distance of $R = 12 \ \mu m$ the sample is quenched to room temperature, *i.e.* the sample is rapidly cooled below the polymer glass transition temperature which leads to an instantaneous stop of the dewetting process and allows to scan the rim of the hole at the desired dewetted distance without modifying the shape of the ridge [3].

Besides the change in dynamics observed on different substrates, Fetzer et al. reported a change of the decay of the film at the 'wet' side of the rim, the side directly in contact with the unperturbed film. As shown in Fig. 2.6(a)-(c), the rim decays monotonically on DTS, whereas an oscillatory decay is observed on OTS.

The slip length b and the capillary number Ca are obtained by fitting the 'wet' side of the rim starting from the unperturbed film of thickness h_0 to a film height of at least 110 % of h_0 and insert the extracted parameters into the polynomial resulting from the Stokes model, equation 2.32.
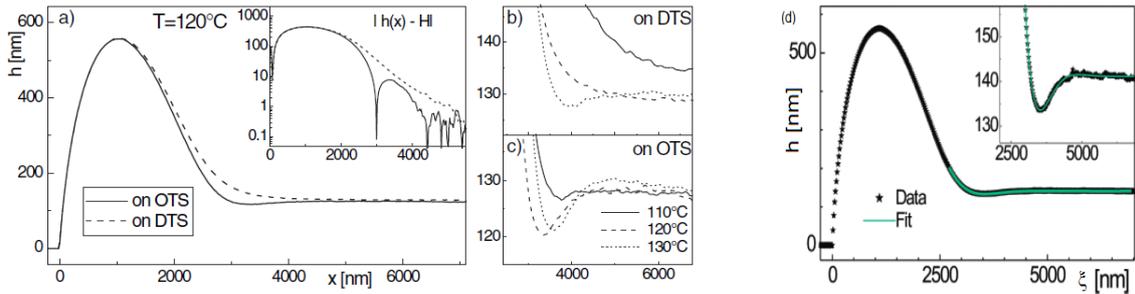
Figure 2.6: Rim profiles of 130 nm PS films on DTS and OTS covered Si wafers (a) at constant temperature (the inset depicts a semilog plot of $|h(x) - H|$), (b) and (c) at three different temperatures on DTS and OTS surfaces, respectively. Profiles are shown with the three-phase contact line shifted into the origin. [40] (d) Profile of rim shown in the region where it decays toward the undisturbed film (i.e., for small perturbations) is well fit by an exponentially decaying oscillation. [42]

---

[3] *In situ* measurements have shown the same result than *ex situ* measurements.

Fitting procedure   Fitting procedure starts with shifting the three phase contact line to $\xi = 0$ with the equation below where $s(t)$ is the position of the three phase contact line.

$$h(\xi) = h_0 - \delta h(\xi) \qquad \text{with} \quad \xi = x - s(t) \tag{2.28}$$

Fitting a damped oscillation, described by eq. 2.29, characterizes perfectly oscillatory profiles using δh_0, k_r, k_i and ϕ as fitting parameters, see Fig. 2.6(d).

$$\delta h_{osc} = \delta h_0 \exp(k_r \xi) cos(k_i \xi + \phi) \tag{2.29}$$

k_r and k_i are respectively the real and imaginary part used to determine the two solutions k_1 and k_2 of the polynomial.

$$k_{1,2} = k_r \pm i k_i \tag{2.30}$$

The monotonic profile observed for DTS is fitted by a superposition of two exponential decays given by equation 2.31, with fit parameters representing the amplitude δh_j and the decay length ξ_j of the jth exponential decay.

$$\delta h_{mon} = \delta h_1 \exp(k_1 \xi) + \delta h_2 \exp(k_2 \xi) \tag{2.31}$$

Extraction of b and Ca   Solving the resulting polynomial from the full Stokes model (eq. 2.18) allows to calculate the slip length and the capillary number using the constants previously extracted from the fitting procedure, k_1 and k_2 (eq. 2.32) [18].

$$
\begin{aligned}
b &= \frac{1}{4h_0} \frac{k_1^2 + k_1 k_2 + k_2^2}{k_1^2 k_2^2} - \frac{h_0}{2} \\
Ca &= -\frac{h_0}{4} \frac{k_1^2 + k_1 k_2 + k_2^2}{k_1 + k_2} + \frac{h_0^3}{6} \frac{k_1^2 k_2^2}{k_1 + k_2}
\end{aligned}
\tag{2.32}
$$

Results for OTS and DTS reported in Fig. 2.7 show a good agreement with theory. One should note that in the case of an oscillatory profile, b and Ca are calculated independently from each other. In the case of a monotonic profile , it is sometimes possible to fit only one exponential decay, which results in extracting one parameter k only. In this situation, we can calculate the capillary number as we know the dewetting velocity v right before quenching the sample to room temperature, the viscosity η and the surface tension γ: $Ca = \gamma v/\eta$; and finally obtain the slip length.
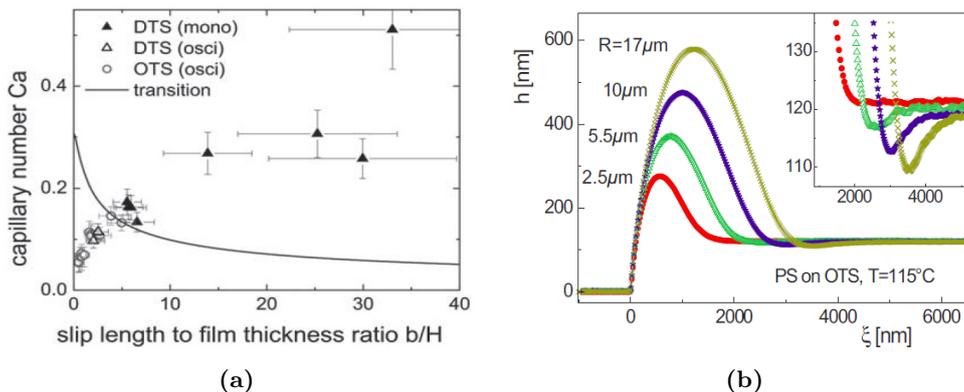
Figure 2.7: (a) Capillary number Ca versus the ratio of slip length b and film thickness H on OTS and DTS obtained from the third-order Taylor expanded Stokes model. [17] (b) Rim analysis at different dewetting stages. Cross-section of in situ SPM scans of the rim around a hole at radii 2.5 μm (filled circles), 5.5 μm (open triangles), 10 μm (stars), and 17 μm (crosses) (i.e., at different times) in a 130nm thick PS(13.7k) film on OTS at 115 °C. Between R = 2.5 μm and R = 5.5 μm we observe a transition from monotonic to oscillatory rim shape (see the enlarged view in the inset). [39]

2.4.4 Origin of slippage

Many efforts have been produced towards finding a common explanation to the origin of slippage. In the following, we cite some of the most with the greatest importance, further parameters influencing slippage are discussed in [14].

Molecular weight On AF 1600, increasing molecular weight of the PS film above $35\,\text{kg.mol}^{-1}$ provokes a drastic change of the boundary conditions, see Fig. 2.8(a) [17]. Slippage appears due to the reduction of entanglement at the solid/liquid interface [11]. The relation $b \propto N^3$ coincides between experiments[4] and theory of using the reptation model [26]. The freedom of chain appears then as a key factor in the role played by slippage.

Dimension of the rim Various growth dynamics of the three phase contact line were reported for the hole growth [8]. The exponent of the power law $R \propto t^{\alpha}$ varies from 1 to 2/3 depending on the aspect ratio between the rim width and the film thickness. In this case we might wonder whether changes in slip length at the solid/liquid interface occur or solely the predominance of viscous forces come into play.

---

[4]A correction should be given by due to reduction of entanglement length at the interfacial layer.

Conformational changes Gutfreund et al. revealed that surface order of a self assembled monolayers (SAM) affect the conformation of polymer chain segments adjacent to the solid boundary. Combining X-ray and neutron scattering, authors point out that chain segments of the SAM structure is replicated within the first polymer layer [52]. This results could be an explanation why a temperature dependence is observed on SAM whereas none is reported in AF 1600, see Fig. 2.8(b).

(a)   **(b)**
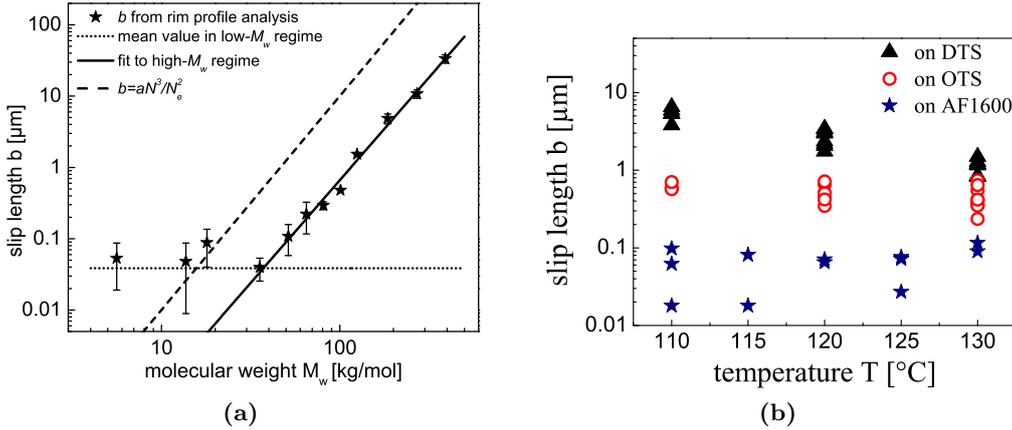
Figure 2.8: (a) Slip lengths of PS films on AF 1600. The solid line represents a fit to the experimental data from PS(35.6k) to PS(390k), the dashed line visualizes $b = aN^3/N_e^2$ using values for a and N_e given in the literature [107]. The dotted line represents the average of slip lengths for melts from PS(5.61k) to PS(18k) [17]. (b) Slip length b plotted versus temperature T on DTS, OTS, AF 1600 [16].

2.5 Hydrodynamic instabilities

In completion to the description of hydrodynamics phenomenon occurring at the solid/liquid interface described in the previous chapter, we focus in this part on phenomenon occurring at the liquid/air interface. Many types of hydrodynamic instability may rise at a solid/liquid interface [28, 24], but solely Rayleigh-Plateau type instabilities are found in the system studied. We first present this instability found in liquid jets, we focus on the impact of viscosity, the stage of droplet detachment and the use in technology. We then study this instability rising on supported liquid ribbons, the static case, before we investigate the dynamical case, the rim instability.

2.5.1 Liquid jets — Rayleigh-Plateau instability

The fluid instability observed commonly in everyday life for instance from the decay of a liquid thread into droplets at a faucet in the kitchen or at the shower head in the bathroom is well known as the Rayleigh-Plateau instability. The cylindrical jet geometry identified away from the nozzle of a liquid tap destabilizes as depicted in Fig. 2.9(a) and transforms into a series of droplets. The cylinder is rendered unstable by capillarity induced by a reduction of the surface energy $\Delta E = E_S - E_0$, calculated as the difference between the energy of the initial state (E_0) and the final stage (E_S) in equation 2.33 [28, 36].

$$\Delta E = \frac{A^2}{4R} E_0(q^2 R^2 - 1) \quad \text{with} \quad E_0 = \gamma . 2\pi\lambda \tag{2.33}$$

The perturbation of amplitude A and wavevector $q = 2\pi/\lambda$ develops when the energy of the liquid cylinder, of initial radius R, is reduced. This condition is verified when $q^2 R^2 < 1$, which is equivalent to write that each distance between droplets λ follows

$$\lambda > 2\pi R \tag{2.34}$$

Experimentally, first qualitative observations of the decay of a liquid jet took place as early as the beginning of the 19th century [108, 75]. In 1873, Plateau published a first experimental value of a distance between droplets after decay of $8.76R$. This value, greater than 2π, agrees with the precondition of lowering energy given by the previous equation, however, the strong deviation from the initial value was not explained. We need to wait until Rayleigh studies the dynamics of the instability to understand the significance of this number. Based on the linear stability analysis, Rayleigh obtained the dispersion relation whose simplified form is given in equation 2.35 for a perturbation $A = A_0 e^{-i\omega t}$, with A_0 constant and ω the **growth rate** of the perturbation.

$$\omega^2 = -\omega_0^2(kh_0)[1 - (kh_0)^2] \quad \text{with} \quad \omega_0 = \sqrt{\frac{\gamma}{\rho h_0^3}} \tag{2.35}$$

The complete form includes another term based on the Bessel function and its derivative [100, 36]. Its representation in Fig. 2.9b reveals a maximum dimensionless growth rate ω/ω_0 achieved for a **reduced wavenumber** $q_m/h_0 \approx 0.7$. At q_m, the time dependance of the amplitude of the perturbation is the fastest with a **time constant** of τ_m.

$$\tau_m \approx \frac{3}{\omega_0} \tag{2.36}$$

The theoretical value of the wavelength calculated for this mode reads $\lambda_m = 9R$, very close to the observation inferred by Plateau. The most unstable mode overcomes all other stable

and unstable modes. The cutoff frequency q_c observed at $x = 1$ defines a transition between modes which theoretically amplify and stable modes in good agreement with equation 2.33 and depicts the **onset of instability** since all frequencies higher than q_c are damped.
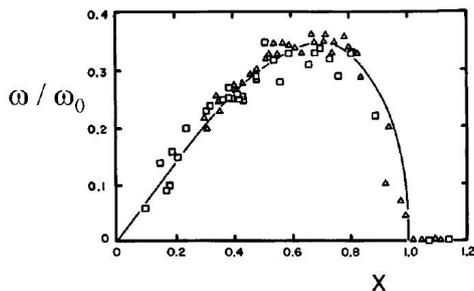
| (a) | (b) |

Figure 2.9: (a) Picture of a jet of water destabilizing from a water faucet. (b) Dimensionless growth rate of sinusoidal perturbations on a cylinder as a function of the dimensionless wave number kh_0. The solid line represents Rayleigh's theory for inviscid flow. [71].

Impact of viscosity

Another parameter to take into account when the motion of liquids is involved is viscosity η. Even if previous results show that preconditions for the rise of the instability is independent of η, the dynamics of the deformation are affected by changes in viscous forces in the fluid. The importance of the viscosity on the propagation of the wave is determined by the penetration length δ , which is a comparison of the kinematic viscosity with the growth rate, set by the Ohnesorge number Oh measuring the relative importance of viscosity $\eta = \nu \rho$ with ν the kinematic viscosity [36].

$$\delta = \sqrt{\frac{\eta}{\omega \rho}} \qquad Oh = \nu \sqrt{\frac{\rho}{h_0 \gamma}} \tag{2.37}$$

At large Oh number, the perturbation undergoes a **viscous slowing**. The growth rate of the instability decreases as the inverse of viscosity [99, 23].

$$\omega \approx \frac{\gamma}{2h_0 \eta} \tag{2.38}$$

Droplet detachment

Breakup between consecutive droplets sets the beginning of non linear dynamics of the stability analysis reviewed in [35]. At non negligible viscosity, the lowering of the timescale of the wave growing the fastest induces a thinning of the middle part into a flat region, a secondary thread. The pinching point sets close to the drop due to high Laplace pressure in this region at length l_ν and time scales t_ν whose dependence in viscosity is given via the kinematic viscosity ν in equation 2.39 [54]. As an example, a water jet would reach 10^{-6} cm in 10^{-10} s before breakup whereas the transition jet to drop would occur after 0.6 s for a length of 2.8 cm in the case of glycerol [122].

$$l_\nu = \nu^2 \frac{\rho}{\gamma} \qquad t_\nu = \frac{\nu^3 \rho^2}{\gamma^2} \tag{2.39}$$

Before contraction, the newly created thin liquid thread destabilizes with a secondary instability into droplets, much smaller than initial ones, commonly termed **satellite drops**. From the length scale introduced in the previous equation, it seems obvious that the latter stage is preferentially observed for viscous fluids as depicted in Fig. 2.10. The patterns reveals an inhomogeneity in the distribution of secondary droplets which is due to the contraction of the thin thread towards its center.

Figure 2.10: Top view of a supported liquid cylinder decaying into droplets vis the Rayleigh-Plateau instability.

RPI and technology

An industrial field where the Rayleigh-Plateau instability would rather be avoided is the technology of coating fibers. Among other parameters composing the capillary number, the velocity used to coat the fiber of radius r impacts on the final thickness h_0 of the coating. If we concentrate on the stationary stage where system is considered as the "static" situation (h_0 is fixed), waves at the liquid air interface when the wavelength λ verifies equation 2.34, and at maximal rate at λ_m with the time constant τ_m given in equation 2.40 [97].

$$\lambda_m = 2\pi\sqrt{2}r_f \quad \text{and} \quad \tau_m = 12\frac{\eta\, r^4}{\gamma h_0^3} \tag{2.40}$$

Equation 2.40 stresses the importance of two length, both the radius of the fiber r and the initial height of the coating h_0. The temporal evolution the perturbation increases with the thickness of the film at constant radius, but increases also drastically when the radius of the fiber shrinks. This phenomenon shows the importance of the support for the growth of the perturbation in the "static" case.

Ink-jet printing is a field where the Rayleigh-Plateau instability is desired, but should be highly controlled due to the new printing applications which are developed today [124] such as printable optical elements, printing integrated circuits.

2.5.2 Instabilities on supported surfaces

Liquid coatings on solid substrates may be subject to a wide variety of hydrodynamic instabilities which can be split into two groups differing from the interface where the instability is localized. On one hand, waves rise at the liquid air interface of flat films; the type of instability depends on the initial film thickness. For very thin film, corrugations of the surface develop spontaneously at a specific wavelength. This is the case for spinodal dewetting [111]. For thick films stagnating on top from the inside of a fridge, gravity destabilize the film into a range of well aligned droplets. On the other hand, the instability rises close to the solid liquid interface. This situation happening when some liquid agglomerate close to the three phase contact line (CL) can be divided into two subcategories depending on whether the amount of fluid in the rim is constant (static case) or the flow regenerates from other source (dynamic case). The latter situation involves a displacement of the CL which is induced by placing the fluid on an incline plane [119, 22], a temperature gradient [63] or other external forces such as magnetic field [34], electric field [91], centrifugal force [82]. All these instabilities are driven from a various types of flow with gravity forces, Marangoni forces, Coriolis forces. However, none of them is driven by a Rayleigh-Plateau instability. The surface tension instability, developing without external forces, occurs on both static and dynamic situations.

In the following, we first discuss theoretical advances and experimental results in the static situation. Both point of view from the theory and experiments are also discussed for the experimental situation. We shed light on the influence of the dynamics of the contact line, of the solid/liquid interface and compare results obtained from a wide range of experimental setup.

Instability in a liquid ribbon

The direct preparation of semi-cylinders deposited on a substrate is difficult to accomplish because the fluid destabilizes quickly. In order to avoid this critical issue, Park et al. used

a PDMS mold patterned with stripes to change a thin film into the rivulet structure at elevated temperature [94]. By means of spin-coating a polymer solution into a substrate pattern with wedge-shaped grooves, Khare et al. managed to investigate *in situ* measurements of the Rayleigh-Plateau instability [65]. With the same technique, McGraw et al. investigated the toroid structure on a flat substrate [81]. All authors unify in concluding that the number of drops obtained after breakup is proportional to the initial geometry of the ridge as depicted for the toroid shape in Fig. 2.11(a). Moreover, Khare et al. authenticate the exponential growth of the perturbation using atomic force microscopy. They also noted that the spacing N between droplets changes using a different substrate; the wavelength decrease was assigned by Khare et al. to the increase of contact angle formed at the contact line, see Fig. 2.11(b). The dependence of contact angle on the wavelength, quantified by Park et al. for a liquid thread prepared with a mold of width L and thickness h, follows

$$\lambda \sim \frac{8sin\theta}{\sqrt{\theta - sin\theta cos\theta}}\sqrt{Lh}. \tag{2.41}$$
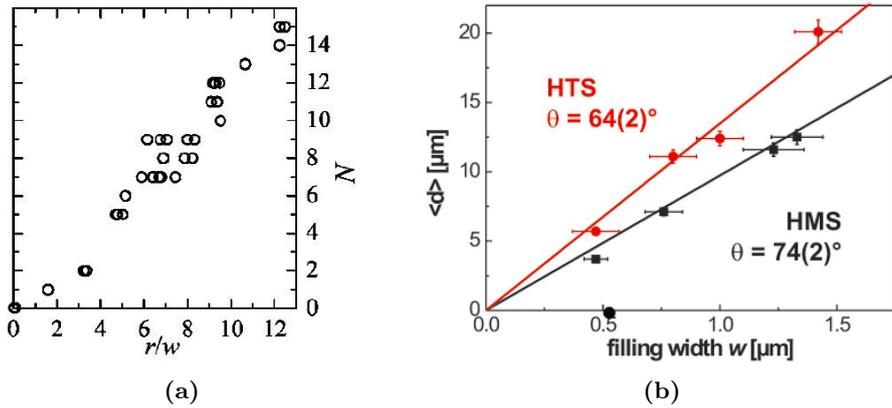
Figure 2.11: (a) Number of wavelengths around a torus as a function of the ratio of the overall radius to the section width, r/w at similar stages of development. N is linear in r/w as expected from the P-R instability. [81] (b) Normalized droplet distance d dh/w as a function of õ. The neutrally stable mode i*/w (—) and the fastest growing mode (imax) x2i*/w (-) are shown according to eq 3. (Inset) Preferred droplet distance d vs filling width w. The lines show the fastest growing mode imax according to eq 3 [65]

The theoretical analysis of thin liquid rivulets deposited on a flat substrate, pioneered by Davis, investigated with an energy-like integral of the Navier-Stokes equation a sufficient condition for stability in terms of the critical wavenumber, also termed marginal mode, as a function of contact angle [25]. Sekimoto et al. completed this work analyzing the stability of both geometries of a liquid toroid and a liquid ribbon [113]. Considering a ridge of width W,
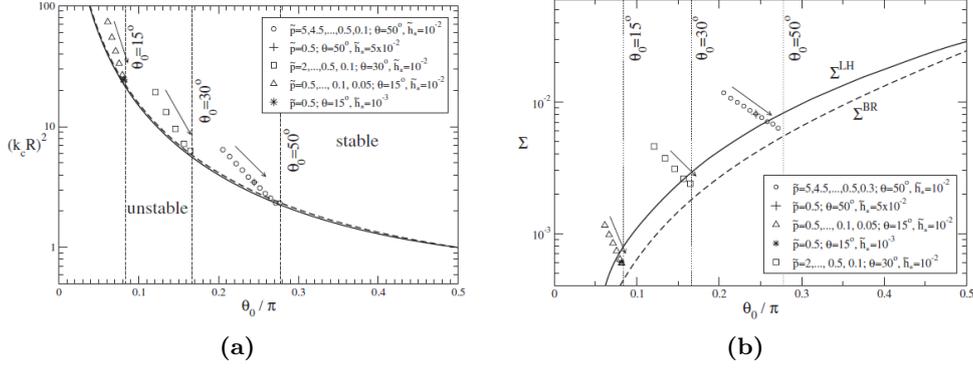
Figure 2.12: **(a)** Comparison of calculated critical wavenumber, k_c multiplied by the radius of the osculating circle, R note that $k_c R = kcR$, with the results from Ref. 12 (solid line) and Ref. 19 (dashed line). The arrows indicate decreasing values of p for the hollow symbols.**(b)** Comparison of calculated maximum growth rates, symbols, with Ref. 19 (solid line) and Ref. 7 (dashed line), given here by Eqs. (20) and (24), respectively. The arrows indicate decreasing values of p for the hollow symbols. [33]

Sekimoto et al. first discussed the energy dissipation for the deformation of two coupled contact lines for the **zigzag mode** and **varicose mode**, where the deformation of the contact line on both sides of the ridge is respectively in phase and out of phase. Denoting u_q the outward displacement of the contact line, the energy per unit length of a varicose mode follows

$$F_q = \gamma \theta_e^2 q u_q^2 \left[-\frac{2}{Wq} + tanh\frac{Lq}{2} \right] \tag{2.42}$$

with θ_e the Young contact angle. Diez et al. confirmed with a linear stability analysis a similar contribution of the contact angle on the evolition of the marginal mode with the wavenumber (Fig. 2.12(a)) and on the growth rate (Fig. 2.12(b)) of the perturbation [33].

Rim instability — Theory

The dynamic case of the instability developing in liquid rivulets involves the displacement of the three phase contact line. In order to differentiate from the static situation, we denote this system as **rim instability**. The displacement of the three phase contact line tends to complicate the theoretical work since we do not only deal with the the competition of several modes which result in the growth of the instability with the fastest rate q^*, but with a fastest mode which enters in competition with a bunch of other new modes initiated by the continuous uptake of polymer in the liquid ribbon. The direct experimental consequence of this remark is coarsening.

(a)   (b)
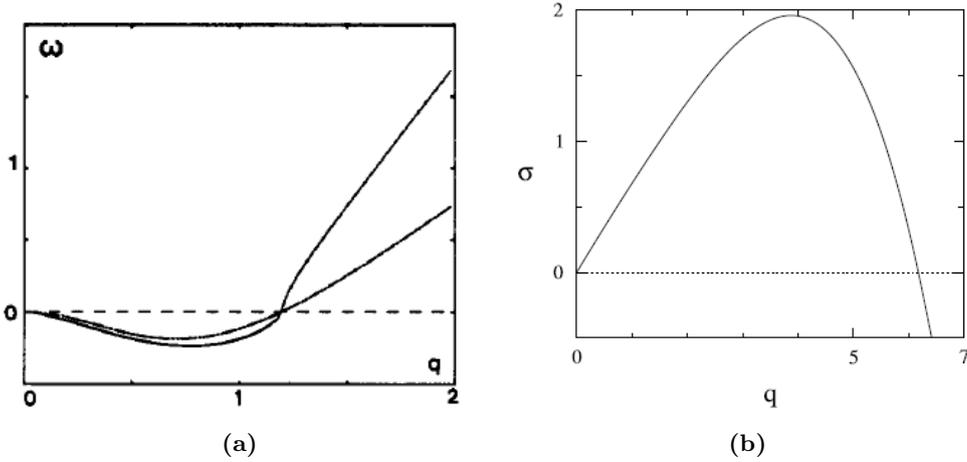
Figure 2.13: (a) Dispersion representation of $\omega = l/\tau$ versus L/q^2 in adimensional units: viscous regime (dashed curve) and viscoinertial regime (solid curve). The minimum value corresponds to the fastest mode and is equal to $q_{\mathrm{m}}L/2 = 3/4$. [8] (b) The dispersion relation showing the growth rate σ versus the wavenumber q for the intermediate-slip case. [85]

No slip situation   Brochard-Wyart and Redon investigated the rim instability considering the energy dissipation of two coupled contact lines. Based on [61], they first showed that the relaxation of a single contact line for very viscous fluids is purely viscous [8]. Then, they transferred the elastic energy of two coupled contact lines into viscous dissipation and combined it with equation 2.42). The outward displacement of two coupled contact lines following for the varicose mode and the no-slip boundary conditions, the rise time τ of the perturbation is estimated

$$\dot{u}_{\mathrm{q}} = -\frac{u_{\mathrm{q}}}{\tau_{\mathrm{q}}} \qquad \text{with} \quad \frac{1}{\tau_{\mathrm{q}}} = \frac{v * \theta^3}{3\ell} \frac{F(q)}{1 + \frac{4}{q^2 W^2}} \qquad \text{and} \quad F(q) = q \left[-\frac{2}{qW} + \tanh\left(\frac{qW}{2}\right) \right].$$
(2.43)

The dispersion relation of equation 2.43 depicted in Fig. 2.13a shows that the fastest unstable mode appears at $q_{\mathrm{m}}W/2 = 3/4$ which corresponds to a distance between droplets of $4W$.

Impact of slippage on the rim instability   Numerical simulations of the rim instability varying the boundary conditions at the solid/liquid interface were performed by Münch and Wagner based on the lubrication models introduced in section 2.3.5. They run simulations for both the intermediate slip model and the no-slip model introducing a perturbation of the form

$$h(x, y, t) = h_{\mathrm{b}}(x, t) + \delta h_{\mathrm{p}}(x, t) \exp(iqy),$$
(2.44)

where $h_{\mathrm{b}}(x,t)$ is a small perturbation of the base state, $\delta < 1$. An initial perturbation $h(t)$ the ridge at a time t_0 using an initial perturbation

$$h_{\mathrm{p}}(x,t_0) = \frac{\partial h_{\mathrm{b}}}{\partial x}(x,t_0), \qquad (2.45)$$

which corresponds to a zigzag perturbation, both sides of the ridge are perturbed in the same direction [67]. The corresponding dispersion relation given in Fig. 2.13(b) shows that various modes are unstable and grow at different rate for a time t above a critical wavenumber and one mode grows fastest.

Due to the continuous growth of the base state, the growth rate for a fixed wavenumber k is not constant and perturbations decay after reaching a maximum amplification as depicted in the insets of Fig. 2.14, which means that it is necessary to find the mode with the largest momentary amplification at any given time. Constraints of the numerical setup only allow to work with an asymptotic approach. Profiles for the perturbation h_{b} depicted for a fixed wavenumber in Fig. 2.14 behave differently at the 'back' side of the ridge for both lubrication models. At the maximal amplification, a pronounced 'bump' is found when simulations have run using the no-slip lubrication model, whereas no prominent bump is found at the back side of the rim for the intermediate-slip model.
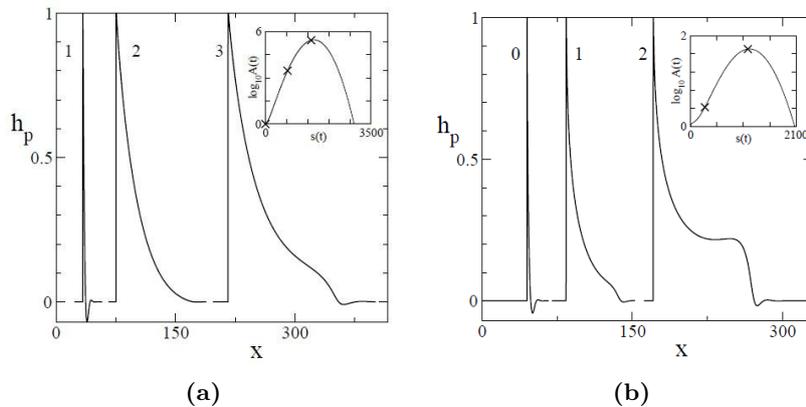
Figure 2.14: The perturbation profile for wavelength l = 264.7 for the intermediate-slip model (left) and the no-slip model(right), at different stages of its evolution, normalized and shifted along the x-axis for better comparison. The labels 1, 2, 3 correspond to the crosses in the inset, which indicate the position s(t) of the base state and the amplification A(t) achieved by hp(x, t). [85]

Münch and Wagner also run numerical simulations for the full nonlinear no-slip and intermediate-slip models. Small perturbations lead to a visible formation of bulges once the nonlinearities become important. In addition to the symmetric/asymmetric shapes predicted by linear stability analysis for the no slip/intermediate-slip case authors observe differences in the contour

(a)   (b)
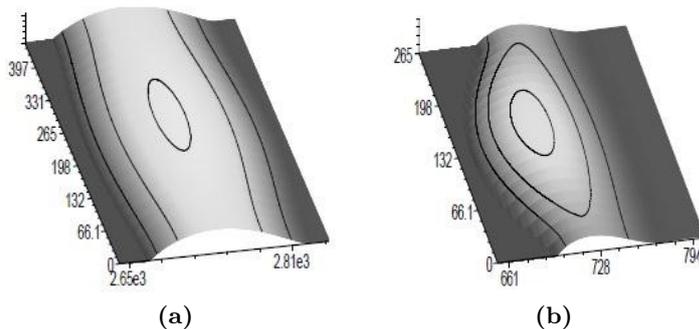
Figure 2.15: Top: Surface plot and contour lines for h(x, y, t) for the slip case at time $t = 93 \times 103$ (corresponding to $s(t) = 685$) and perturbation wavelength $l = 265$. M and S denote the location of the maxima and the saddle point, respectively. Bottom: Surface plot and contour lines for h(x, y, t) for the no-slip case at time $t = 104 \times 103$ (corresponding to $s(t) = 2.68 \times 103$) and perturbation wave length $l = 446$. M and S denote the location of the maxima and the saddle point, respectively.

line and surface plot (Fig. 2.15). For the intermediate slip model, the back side of the rim is fairly flat and a prominent bulge is formed at the dewetting front. The saddle point and maximum, respectively S and M, are shifted along the x-axis evidence an asymmetry of the bulge. In the no-slip case, the amplification reaches a similar stage much later. The surface plot and contour lines displayed for a longer wavelength evidence symmetric undulations, which is confirmed by the alignment of saddle point and maximum of contour lines in y-direction. The sequence of thicker and thinner parts develop similar to the varicose mode discussed earlier for the static case, although, the perturbation initially introduced to the base state corresponds to a zigzag perturbation where both 'front' and 'back' sides of the ridge are perturbed in the same direction.

Scaling eigenvalues with the speed, $\dot{s} \sim t^{-1/3}$, Münch and Wagner managed to obtain a time independent dispersion which gives a dominant wavelength λ^* and a critical wavelength λ_c for the system proportional to the rim width W [85]

$$\frac{\lambda^*}{W} \approx 2.4 \qquad \frac{\lambda_c}{W} \approx 2.03 \quad . \tag{2.46}$$

Rim instability - Experiments

The rim instability was investigated experimentally with a wide set of experiments using bare glass or Si-substrates with top layer being simply the native oxide layer or hydrophobized with alkyl-based grafted chains or spin-coated polymers. The film was formed of alkanes or polymers with molecular weight (M_w) starting from low up to values much higher than the entanglement length. Two methods were used to induce a flow: on one hand, nucleation of holes or retraction

of straight front was obtained from the thermal treatment of the system [8, 105, 103, 80, 44]; on the other hand, dewetting was initiated by placing the sample in a closed chamber with the vapor surrounding the polymer saturated with a good solvent [73, 125].
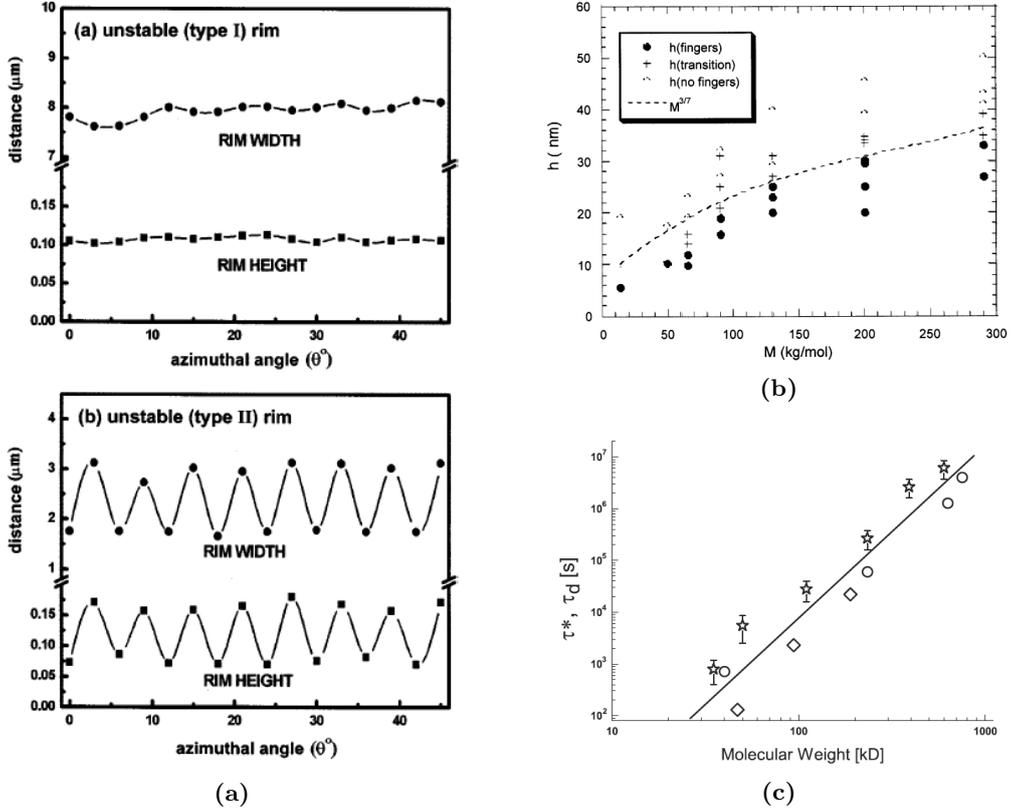
Figure 2.16: (a) Undulations in rim width and height given as a function of azimuthal angle as measured by atomic force microscopy (t534 s). Initial film thickness is 35 nm. (top) Undulations in rim width and height for type-I unstable rim with toluene as solvent. (bottom) Undulations in rim width and height for type-II unstable rim with acetone as solvent. [73] (b) A map of the fingering instability as a function of the initial film thickness, h, for samples of varying molecular weight, M. The line separating the regions of film thickness where fingers are present or absent corresponds to the theoretical prediction $h_c \propto M^{3/7}$. [80] (c) Onset times of rim instabilities, τ^*, together with disentanglement times, τ_d, versus molecular weights. τ_d was obtained by neutron reflectivity (circles) and viscosity measurements (lozenges). The full line in the logarithmic plot of τ^*, τ_d versus molecular weights corresponds to the relation: $\tau_d \sim M^{3.4}$. The error bars reflect the variance of the repeated measurements. [44]

Exp on Si-wafers   Dewetting experiments on Si wafers, were performed using thermal annealing [80] and solvent induced dewetting. The major advantage of the latter is to enable a wide range of experiments due to the large "palette" of choice of solvents available, which is very interesting from the polymer physics point of view since it gives access to other aspects of

viscous flow without being limited to temperature or the polymer chain. Lee et al. concentrated on the impact of polar interactions on the rim instability process using acetone and toluene. They showed that apolar solvents do not lead to fingering, the rim instability is not well developed as pictured in Fig. 2.16(a) [73], the ratio rim width to rim height differs completely from one system to the other. In contrast, Xu et al. did not mention the appearance of fingering more on one than the other system with the same solvent. With a chain length ranging from 3.6 to $44 \, \mathrm{kg.mol^{-1}}$, they showed that molecular weight do not impact on the occurrence of the rim instability, but does the film thickness [125]. The main drawback of solvent induced dewetting is the lack of control concerning the homogeneity of viscosity within the film and more importantly, of the presence of solvent regularly distributed at the solid/liquid interface, which is not the case for thermally induced dewetting, explained next.

Fig. 2.16(b) depicts results obtained by Masson et al. with large polymers chains, above $50 \, \mathrm{kg.mol^{-1}}$. According to their experiments, fingering appears only when the film thickness is below a certain threshold h_c proportional to molecular weight, $h_c \sim M^{3/7}$. Since this transition is related to the entanglement length [80], the phenomenon observed stresses the fact that films prepared below h_c are not at equilibrium which is possibly caused by a film thickness in the range or lower of the radius of gyration.

Exp on hydrophobic wafers   Experiments on hydrophobic substrates were solely performed with thermal dewetting. Reiter and Sharma showed that straight fronts of PDMS films turn into fingers if the coating retracts from a substrate rendered hydrophobic with PDMS grafted chains. The mean dewetting velocity is then constant for the whole dewetting process and decreasing with the inverse of M_w [105, 103]. — The molecular weight used for this setup, M_w, being above entanglement length necessarily involves the presence of slippage at the solid/liquid interface [29, 17]. Consequently, this systems shows fingering in the presence of slip. — Moving to PS films, Gabriele et al. justified the presence of fingers with viscoelastic properties of the film. At τ^*, the onset of fingering is a feature correlated to the disentanglement time of the polymer chain as depicted in Fig. 2.16c, τ^* corresponds to the transition from elastic to viscous regime $\tau_d \sim M_w^{3.4}$ [44].

The length of fingers L, which can be defined as the lateral distance from the initially straight front to the back side of the droplet short before it pinches off, also depends on M_w. With the use of short silane chains at the solid/liquid interface, Neto et al. observed empirically that L follows an algebraic law $L \propto M_w^4$ [89]. Finally, Haefner showed that the occurrence of fingering is not an intrinsic behavior of systems dewetting from substrate hydrophobized with grafted chains. High M_w PS films also show fingering on top of a spin-coated teflon® coating, the presence of which was explained by slippage [53].

Consequences of a moving contact line.

Displacement of the three phase contact line involves some of side effects which have to be considered in order to interpret the results in a proper manner. Deviation from the normal situation may come from pinning of the contact line, merging of successive droplets and the initial geometry of the dewetting rim, to cite the most important.

Coarsening A direct consequence of the proportionality between the number of droplets, related to the faster growing wavelength, with the width of supported liquid threads proved for the static situation [65, 81] is coarsening. As the rim thickens increases due to volume uptake in the dynamical situation, the conservation of volume in the ridge involves a transverse displacement of the material and merging of thicker parts of the ridge, the average wavelength increases, the number of droplet at breaking decreases. This phenomenon, obvious from experimental point of view was investigated theoretically for a liquid contact line flowing down an incline plane [123, 119, 32]. A retracting line which undergoes a Rayleigh-Plateau type instability was studied at late stage of dewetting by Kitavtsev and Wagner with numerical simulations, see details in [68]. With the lubrication models, they proved that the coarsening rate does not depends on the dewetting regime, but $N(t) \propto t^{-2/5}$. However, the pattern of collision changes for slip length above a critical value b_{crit}. Below b_{crit} it typically takes at least three droplets for a collision event, where the smaller droplet in the middle vanishes. Above b_{crit} collisions of just two droplets are typical owing to the fact that now the droplets move in the same direction as the flux.

Rim instability in dewetting holes The rim instability was discussed up to know independently of the geometry of the rim. Most polymer straight fronts retract instantaneously from hydrophobic substrates since the solid/liquid/vapor interface is formed immediately after the melting temperature of the polymer is reached, while nucleation of holes necessitates a time laps in order to form the three phase contact line and have the rim achieve a mature phase [102, 9, 39].

The equivalent of static holes, supported toroids, shed light on a feature of the circular geometry. The remnant of the ring in its initial state asserts a decrease of the liquid torus prior to the onset of instability [81]. Shrinkage of the ring indicates that a proper interpretation of the rim instability for the circular geometry involves a complex interplay between the width of the ring and the radii of the torus in order to determine the curvature of the system on which the Rayleigh-Plateau type instability is applied [81].

3 Materials and Methods

3.1 Substrate preparation and properties

3.1.1 Hydrophobic layer

Chemical and physical modification techniques were used to prepare hydrophobic wafers. The first technique consists of grafting silane molecules to the native oxide layer of the silicon substrate. The second is a simple spin-coating of a Teflon® layer.

Self assembly

Self assembled monolayers are produced from a spontaneous formation of a hierarchical structure by adsorption of a surfactant with a headgroup of specific affinity to a substrate. Today's most studied systems are thiols[1] on gold surfaces [109, 120] and silanes[1] on silicon surfaces. Used with trichlorosilanes, the latter systems produces highly ordered self assembled monolayers [49, 50, 78]. Best quality of surfaces is obtained with the following recipe, optimized from [12, 57, 121].

The substrate used is a disk of silicium oriented <100> or <111> of thickness $525 \pm 20 \, \mu$m, p-doped with boron, with a specific resistance of 10-20 Ω.cm. The Si wafer (Wacker Siltronic, Burghausen Germany) is covered with a 1.7 nm thick native oxide layer. The amorphous SiO_2 layer ends with silanol groups, the anchors point for silanes.

Several cleaning steps are necessary to favor a defect free monolayer. Majors organic contaminations are first removed from a succession of sonication for more than 5 minutes into three baths ethanol, acetone and toluene. The sample is quickly dried by blowing the sample with gaseous nitrogen of purity 5.0 at the end of each sonicating procedure. This allows to remove all superficial dust impinged in the solvent. Samples which are not used in their original size, but cut at desired dimensions with a diamond pen prior use, might encounter the presence of tiny particulates on the surface[2]. In this case, an additional cleaning step with CO_2 snow

---

[1] Thiols are organosulfurs R-SH where R represents an alkyl-derivated chain. Organochlorosilanes $RSiCl_nH_{3-n}$, with n$\leq$ 3, are commonly used. Functionalizing the body R broadens the possibilities to used the substrate.

[2] Such type of particulates are also found if the sample is not stored under proper conditions. The wafer containing Si wafers of pieces of Si wafers must be sealed in a laminar flow bench.

jet, a non destructive and non abrasive technique, is advised. The principle of CO_2 snow jet is to expand liquid carbon dioxide (CO_2, Praxair, Düsseldorf, Germany) through an orifice, which leads to the nucleation of small dry ice particles and a high velocity gas carrier system evidenced by a stream. In contact with the annealed surface, the stream removes micron and submicron particles and hydrocarbons via a transient solvent or freeze fracture [115]. Once the surface is free from external particles, a chemical oxidation is performed immersing the wafer during 30 minutes into piranha solution, a 1:1 volume ratio prepared from a mixture of concentrated sulfuric acid (Aldrich, München) with hydrogen peroxide prepared at 30 % H_2O_2 (Fluka, München). The violent reaction taking place as soon as the wafer comes in contact to the solution proves that the reactivity is sufficient if the freshly prepared piranha solution is used at room temperature. In order to avoid further contamination, it is highly recommended to clean all containers and tweezers in contact to the Si wafer and Teflon® are preferred to metal tweezers to avoid contamination such as chromium atoms. The wafer is then thoroughly rinsed for 15 minutes in hot of Milli-Q^{TM} water[3] baths, renewed twice. The cleaning is successful if total homogeneous wetting with water is observed.

Silanization is performed using wet chemistry with a solution prepared from mixing 50 mL bicyclohexane (Sigma-Aldrich, München) with 30 drops of tetrachloromethane (Sigma-Aldrich, München) and 13 drops of dodecyltrichlorosilane (DTS, Sigma-Aldrich, München) or octadecyltrichlorosilane (OTS, Sigma-Aldrich, München) depending on the type of substrate aimed. The *in situ* formation of polysiloxane, driving the mechanism of self-assembly [120], is decomposed into several steps: physisorption of the silane molecule with the reacting headgroup towards the oxide layer, hydrolysis of the chlorosilane group to silanol, formation of a siloxane from covalent binding between the silanetriol and intermolecular cross-linking of silanol groups to form a polysiloxane network [12], the latter step being more likely to happen at high temperature [3].

Physisorption is a critical step to form a robust layer [3, 21, 118]. A water layer adsorbed on top of the oxide layer of the substrate orients the molecules and favors a good silanization. This layer is obtained from placing the Si substrate upside down into a steam of a boiling bath of Milli-Q^{TM} water. A very quick rotating movement is performed and the wafer is plunged immediately into the beaker containing the freshly prepared silane solution for 15 minutes. The silanized wafer is then washed with chloroform to rince off non covalently bounded silane molecules from the substrate before plunging the sample into the solution for another 15 minutes and washed again to reach a fully covered surface.

The quality of the layer can be observed macroscopically since a mirror-like surface is obtained

---

[3]Milli-Q^{TM} water is an ultrapure water obtained from filtering devices produced by EMD Millipore Corporation, MA, USA. The purification processes involve successive steps of filtration and deionization to achieve a purity expediently characterised in terms of resistivity (typically 18.2 MΩ·cm at 25 °C).

for a perfect layer. Moreover, a drop of water travels through the substrate with a constant contact angle. Further characterization of the layer is provided in the next section.

Spin-coating of Teflon® layer

The other type of hydrophobic substrate, AF 1600, is prepared from spin-coating a fluoropolymer solution on a freshly cleaned silicon substrate. The degree of cleanliness mainly depends on the handling of the wafer prior use. The entire cleaning procedure used before silanizing wafers with DTS or OTS might be repeated, however, regular storing conditions in laminar flow bench and the non-chemical nature of the adhesion process for the amorphous layer usually do not necessitate a strong cleaning with piranha solution. The CO_2 snow-jet removal of micron and submicron particles is recommended to prepare samples of regular size, samples of $1\,cm^2$ are usually used for dewetting experiments.

AF 1600 is part of a family of amorphous perfluorinated polymers Teflon® AF from DuPont^{TM} prepared with various grades marking their glass transition temperature, 1600 stands for a T_g of $260\,°C$. Their strong mechanical properties favors their use as coating. A thin layer of AF 1600 is prepared by spin-coating approximately $60\,\mu L$ of a solution prepared dissolving $0.5\,wt\,\%$ poly[4,5-difluoro-2,2-bis(trifluoromethyl)-1,3-dioxole-co-tetrafluoroethylene] (Sigma-Aldrich, Germany) in perfluoro-compound FC-75^{TM} ($C_8F_{16}O$, Acros Organics), a fluorocarbon derivative of a tetrahydrofuran. The spin velocity chosen combined with the concentration of the solution leads to a 20 nm thick film.

Fluoropolymers are known to be chemical components which are difficult to dissolve. Optimal solubility of AF 1600 is obtained after shaking the solution for several days. Despite this precondition, tiny waves are observed after the preparation of the hydrophobic layer as depicted in Fig. 3.2(a). A cross-section of these waves demonstrates that the amplitude of the oscillation, in the nanometer range, is approximately four orders of magnitude smaller than the wavelength, which approaches $15\,\mu m$. This waves therefore causes visual artifacts on optical micrographs, however, do not impact on the rim instability in the course of dewetting as discussed in part 6.5.

3.1.2 Physical properties of the modified substrate

The quality of the silane layer and the AF 1600 coating were checked using various methods such as ellispometry, atomic force microscopy, contact angle measurement. Various methods are presented in the following and results are summarized in table 3.2.

Optical properties and thickness   Optical properties and film thickness of the material
are determined with ellipsometry, an optical method commonly used to characterize thin films.
This technique, thoroughly detailed in [4, 117], uses the interaction of polarized light with the
material to determine two quantities Δ and Ψ, usually denoted Del and Psi, modeled to extract
optical properties of the material such as the refractive index n and the extinction coefficient
k and the film thickness d of the layer.

Polarized light, obtained directly from the light source or passing the light source through
an optical element can be decomposed into a component of the electric field in the plane of
incidence, denoted parallel E_p, and another perpendicular to it, E_s mathematically determined
as a sinusoidal wave reading $A = A_0 \sin\left(-\frac{2\pi}{\lambda}(c - vt) + \phi\right)$ with a given maximum of the
amplitude A_0, wavelength λ, position on the axis x, velocity v, time t and phase ϕ. The
wave is elliptically polarized if the phase difference recorded at x between the perpendicular
and the parallel component differs from $n\pi$, with $n = \mathbb{Z}$ and various amplitude between the
perpendicular and parallel component.

The signal of an outcoming beam, reflected after passing through the material, differs from the
signal of the incoming beam. On one hand, part of the incident wave is refracted while it passes
through the material and deviates from its original angle ϕ_1, measured relative to the normal
of the interface as depicted in Fig. 3.1(a). The resulting angle ϕ_2 formed within the material
depends on the optical properties of the material $\tilde{N}$ according to Snell's law $\tilde{N}_1\phi_1 = \tilde{N}_2\phi_2$. The
complex index of refraction $\tilde{N}_i$ for the medium i is combined with a real part n_i, the refractive
index, and a complex part k_i, the extinction coefficient, $\tilde{N}_i = n_i - jk_i$. In case of materials
such as glass or polystyrene, the light is considered as fully transmitted ($k = 0$), equation 3.1
simplifies in a real form replacing $\tilde{N}$ by n.

On the other hand, the incident beam is reflected with the same original angle ϕ_1. This
difference is characterized by the Fresnel reflection coefficient r for each component of the
wave for a reflection at an interface between medium 1, air for example, and medium 2, the
tested material. Fresnel coefficients, given in equation 3.1 for both parallel and perpendicular
planes, are defined as the ratio of the amplitude of the reflected wave to the amplitude of the
incident wave for a single interface

$$r_{12}^p = \frac{\tilde{N}_2 \cos\phi_1 - \tilde{N}_1 \cos\phi_2}{\tilde{N}_2 \cos\phi_1 + \tilde{N}_2 \cos\phi_1} r_{12}^s = \frac{\tilde{N}_1 \cos\phi_1 - \tilde{N}_2 \cos\phi_2}{\tilde{N}_1 \cos\phi_1 + \tilde{N}_2 \cos\phi_2}, \tag{3.1}$$

where the superscript stands for the incident plane and the subscript stands for the medium.
For multiple layer systems, the reflectance is composed from the Fresnel coefficient for each
interface and a film phase thickness β reading for a three layer system of medium 1, 2 and 3

as [4]

$$R^{\mathrm{p}} = \frac{r_{12}^{\mathrm{p}} + r_{23}^{\mathrm{p}} e^{-j2\beta}}{1 + r_{12}^{\mathrm{p}} r_{23}^{\mathrm{p}} e^{-j2\beta}} \quad R^{\mathrm{s}} = \frac{r_{12}^{\mathrm{s}} + r_{23}^{\mathrm{s}} e^{-j2\beta}}{1 + r_{12}^{\mathrm{s}} r_{23}^{\mathrm{s}} e^{-j2\beta}} \mathrm{with} \beta = 2\pi \left(\frac{d}{\lambda} \right) \tilde{N}_2 \cos\phi_2 \qquad (3.2)$$

The parameter β varies with the ratio of the layer thickness d and the wavelength λ of the source.

The reflectance $\mathcal{R}$ is another measurable quantity which gives the total intensity of an incident plane wave that appears in the reflected wave for the p and s polarization, $\mathcal{R}_{\mathrm{p}} = |R_{\mathrm{p}}|^2$ and $\mathcal{R}_{\mathrm{s}} = |R_{\mathrm{s}}|^2$. $\mathcal{R}$ varies with the angle made by the incident beam with the normal of the interface ϕ. A minimum of the parallel component of the wave is found at the Brewster angle ϕ_{B}. The reflected wave in the plane of incidence disappears on the interface between two transparent media. This angle is a transitional case for the value of the parameters Ψ and Δ targeted.

The phase shift of the parallel component of the incoming wave differ upon reflection from a quantity δ_{rp}. The difference between this quantity and the same phase recorded from the perpendicular component δ_{rs} leads to the parameter Δ. Ψ evidences the ratio of the reflectance between parallel and perpendicular polarized light. In other words, Ψ and Δ determine the differential changes in amplitude and phase, respectively, experienced upon reflection by the component vibrations of the electric vector parallel and perpendicular to the plane of incidence.

$$\Delta = \delta_{\mathrm{rp}} - \delta_{rs} \quad \tan\Psi = \frac{|R^{\mathrm{p}}|}{|R^{\mathrm{s}}|} \qquad (3.3)$$

The fundamental equation of ellipsometry then reads

$$\rho = \frac{R^{\mathrm{p}}}{R^{\mathrm{s}}} = \tan\Psi e^{j\Delta} \qquad (3.4)$$

The instrument (EP³, Nanofilm Technologie GmbH, Göttingen, Germany) is setup from a series of elements aligned with an angle of incidence ϕ made with the normal of the surface. The typical setup depicted in Fig. 3.1(b) indicates thanks to the arrows the changing state of polarization light of passing through the polarizer P, compensator C and after reflection on the system S through the analyzer A. The light source of the so-called PCSA system[4] is in this case a monochromatic polarized light which becomes linearly polarized after passing through the polarizer and elliptically polarized after the compensator. The polarization state is indicated by the arrows on Fig. 3.1(b) evidence that the light returns linearly polarized after reflection on the sample. A null is reached as the light passes through the analyzer and is recorded the

---

[4]The PCSA system is termed from the order taken by each element light goes through. The polarizer P, element used to convert unpolarized light to polarized light, is placed before the compensator, also termed quarter wave plate which is emphasizes the phase difference between two axis perpendicular to each other (*p* and *s*). Upon reflection from the sample, the signal goes through the analyzer, a polarizer used to determine the state of polarized light by locating the null.

Table 3.1: 4 zones parameters, angle of compensator C$_i$, polarizer P$_i$ and analyzer A$_i$ of the zone i

zone	C$_i$ / °	Ellipsometric angles	
		Δ / °	Ψ / °
1	$-\frac{\pi}{4}$	$2P_1 + \frac{\pi}{2}$	A_1
2	$+\frac{\pi}{4}$	$-2P_2 - \frac{\pi}{2}$	A_2
3	$-\frac{\pi}{4}$	$2P_3 - \frac{\pi}{2}$	$-A_3$
4	$+\frac{\pi}{4}$	$-2P_4 + \frac{\pi}{2}$	$-A_4$

detector. Both the polarizer and analyzer rotate subsequently to observe the null region while the analyzer is kept fixed at $\pm\frac{\pi}{4}$.

Null ellipsometry is based on finding a set of azimuth angles for the polarizer and analyzer
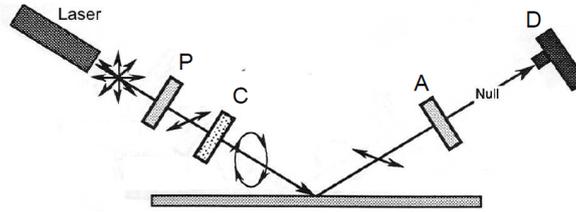
Figure 3.1: (a) Sketch of an ellipsometer with a light source (laser), polarizer P, Compensator C, Analyzer A and detector. Arrows drawn between each elements indicate the type of light in use. (b) Typical graph obtain with null ellipsometry if several parameters are unknown: Delta and Psi are plotted as a function of the angle of incidence

for a given angle of the analyzer such that the light flux falling on the photodetector is extinguished. Experimental ellipsometric parameters Δ and Ψ are calculated from the angle made by the polarizer P and the analyzer A given in table 3.1. Errors might become important if the light intensity is weak. In this case, we can make use of the symmetrical aspects of the ellipsometer. One set of measurements is provided in one zone only. Rotating the compensator of plus or minus $\frac{\pi}{4}$ provides symmetrical results in another zone. As a results it is possible to average results over four zones.

In addition to the average of ellipsometric parameters over several zones, it is often convenient to measure experimental values of Del and Psi for multiple angles of incidence (AOI). Varying the distance traveled by the light before reflection with changes of the angle of incidence ϕ provides a change in the penetration time and the phase difference of the reflected wave. Representing the evolution of the ellipsometric parameters for a series of ϕ recorded on a Si wafer covered with silane layers DTS and OTS, the biggest difference is observed on either side of the Brewster angle at which the parallel component of the reflectance is minimum.

By means of the Fresnel equation (equation 3.1) and the Drude equation (equation 3.2), the-

oretical trajectories of Del and Psi are known for a given refractive index and film thickness of the layer. Multiple AOI measurements helps to determine unknown values of the refractive index and the layer thickness, the latter being summarized in table 3.2 for both substrates.

Corrugations The last part explained the dependence of reflected waves on the optical properties of the material and the thickness of the layer. The optical micrograph of the Si wafer covered with a spin-coated layer of AF 1600 evidence undulations of the surface. The wavelength of the undulation is large compared to the height, consequently, the substrate is considered as smooth. We demonstrate in Fig. 6.11 that these corrugations do not impact on the system studied.

Stiffness Young Modulus of the Teflon$^{©}$ layer 0.6–0.9 GPa is considered as stiff. It doesn't move along with the dewetting of the thin polymer film. This system should not be confused with a system where dewetting experiments takes place on soft polymer layer used as a coating where deformations of the substrates. As an example, the latter was observed using PDMS of stiffness 0.3–0.8 MPa [70] , three order of magnitude lower than AF 1600.

Roughness The root mean square (abbreviated RMS or rms), also known as the quadratic mean, is a statistical measure of the magnitude of a varying quantity.

$$R_{\mathrm{q}} = \sqrt{\frac{1}{n} \int_0^n x^2 \mathrm{d}x} \qquad (3.5)$$

The roughness analysis provides information about the quality of the substrate at microscopic scale. Results measured with AFM (technique detailed in part 3.3.2) and summarized in table 3.2 assert that both substrates are atomically smooth: corrugation are 0.30 nm for AF 1600 and even lower for silane layers.

The large centrifugal force involved in the spin coating process together with the limited solubility of the perfluorinated polymers leads to the presence of corrugations illustrated above. The latter is characterized by, on average, a wave of 3–4 nm amplitude over a period of approximately 15 μm [13] do not impact on the $1 \times 1\,\mu$m^2 , neither on the experiments, see Fig. 6.11. A supplementary method is provided with in the following paragraph with contact angle measurements to ascertain the quality from a macroscopic scale.

Surface energy   The surface energy of the freshly hydrophobized layer is characterized with contact angle measurement. With this optical method, the contact angle of a droplet of a reference fluid deposited on top of the substrate is rapidly determined from a picture taken transversally as depicted in Fig. 3.2(c). The instrument, OCA 15 Plus conceived by Dataphysics Instruments GmbH (Filderstadt, Germany), consists of a series of devices mounted on a ramp aligned horizontally of height adjusted vertically with a micrometer screw and distance from the sample optimized sliding each device along the ramp. Pictures are acquired with a $1/2''$ monochrom CCD-videocamera (EHD kamPro02, resolution 752 x 582 Pixel, EHD Imaging GmbH, Damme) combined with an objective with a very large zoom (Optem Zoom 70XL, Thales Optem Inc., Fairport, NY, USA). The stage holding the sample is leveled to ensure a perfect flatness of the substrate which is necessary to obtain a homogeneous contact angle measured for the whole droplet at the three phase contact line. The droplet is deposited thanks to a cannula attached to a $200\,\mu$L reservoir used to control the volume of liquid we are working with.

The static contact angle θ_Y, also termed Young contact angle, of the droplet detached from the cannula is determined automatically using two methods which consist of, on one side, fitting the entire droplet with a semicircle or on the other side drawing the tangent of the droplet at the liquid air interface at the three phase contact line and calculating the angle formed with the base line. The good contrast required to properly define the contour of the droplet is not only obtained from a proper focus of the droplet, but also with an enhanced contrast provided with a light illuminating the background of the image. As a reason, the droplet depicted in Fig. 3.2(c) is dark.
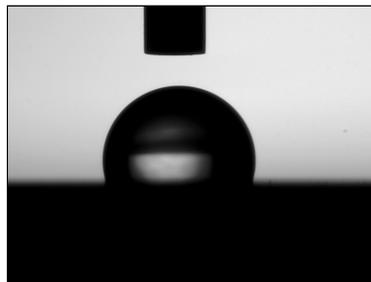
Figure 3.2: Image of drop deposited on a smooth hydrophobic substrate.

The surface energy γ_{sv} of the sample is determined combining experimental results obtained from the static contact angle of a droplet of water and another liquid with theoretical aspects developed by Good and Girifalco [47]. The surface tension γ_{sv} at the solid/vapor interface is

written as a function of the surface tension of the other interfaces [46, 48]

$$\gamma_{sl} = \gamma_{sv} + \gamma_{lv} - 2\sqrt{\gamma_{sv}\gamma_{lv}} \tag{3.6}$$

where indices s, l and v stand respectively for the solid, liquid and vapor phases. In combination with Young's equation

$$\theta_Y = \frac{\gamma_{sv} - \gamma_{sl}}{\gamma_{lv}}, \tag{3.7}$$

the surface energy of the substrate γ_{sv} is given as a function of the Young contact angle and the surface energy of the liquid

$$\gamma_{sv} = \frac{1}{4}\gamma_{lv}(1 + \cos\theta_Y). \tag{3.8}$$

This theory was verified for apolar liquids or other systems involving weakly hydrogen bounding liquids. As a comparison with results obtained previously, the newly prepared DTS sample was tested with 1-Bromonaphtalene (Sigma-Aldrich, München, Germany) and bicyclohexane (Sigma-Aldrich, München, Germany). The resulting static contact angle found with both liquids, $\theta_Y = 56(1)°$ and $36(1)°$ respectively, give a surface tension $\gamma_{sv} = 27.0(1)\,\text{mN.m}^{-1}$, very close to the value obtained with a former preparation [38]. The same method was used to determine the surface energy of other substrates summarized in table 3.2. AF 1600 evidences the lowest surface energy, $\gamma_{sv} = 15\,\text{mN.m}^{-1}$.

The high resolution video camera used for the setup allows measurements of the dynamic contact angle. In this case, it is necessary to keep the connection of the droplet with the canula. Starting with a droplet of width approximately equivalent to the diameter d of the cannula, liquid is added continuously until the volume of the drop reaches a diameter of approximately $5d$ while the advancing contact angle θ_{adv} is measured at both sides of the droplet with the tangent method. Averaged over the whole experimenting range, variations of this contact angle are low if the surface is cleaned. Before the droplet loses symmetry or inhomogeneities appear due to the large volume of the droplet, liquid is pumped back and the receding contact angle θ_{rec} is averaged in the same manner. The difference between advancing and receding contact angle, the contact angle hysteresis $\Delta\theta$, increases with the roughness and inhomogeneities of the sample. Consequently, $\Delta\theta$ is a rapid measure of the quality of the layer from a macroscopic point of view. The small $\Delta\theta < 10°$ reported in table 3.2 evidences a good quality of the substrates prepared.

Table 3.2: Properties of AF 1600, OTS, DTS substrates: layer thickness d, rms roughness, advancing water contact angle θ_{adv}, contact angle hysteresis $\Delta\theta$, surface energy γ_{SV}, Young contact angle θ_{Y}

layer	d / nm	rms / nm	θ_{adv} / °	$\Delta\theta$ / °	γ_{SV} / mN.m^{-1}	$\theta_{\mathrm{Y_{PS}}}$ / °
AF 1600	20(2)	0.30(1)	128(2)	10	15.0	88(2)
OTS	2.3(2)	0.09(1)	116(1)	6	23.9	68(2)
DTS	1.5(2)	0.13(2)	114(1)	5	27.0(1)	66(2)

3.2 Polymer film preparation

3.2.1 Spin-coating

The formation of a uniform thin film with the spin-coating process is divided into several steps starting with the deposition of a small amount of the polymer solution, approximately $60\,\mu$m, on top of a hydrophilic substrate. The droplet spreads slowly over the surface prior to the onset of gyration of the stage which engenders an immediate coverage of the whole substrate. The excess of polymer solution flings off the surface via centrifugal forces. The remaining layer thins with the evaporation of the solvent until an equilibrium thickness H has been reached. A rapid start of the rotating stage at the desired spin velocity ω with the maximal acceleration produces a homogeneous film within less than a minute. The film thickness varies with the spin velocity and the viscosity of the coating, set by the concentration of the polymer solution c and the molecular weight of the polymer M_{w} [57]. An empirical law shows that H evolves as $\sqrt{c^3/\omega}$ for a given M_{w} [13, 38].

The cleanliness of the substrate contributes to the formation of an uniform film free from defects. We use mica, an aluminosilicate with sheet like structures piled together up to a thicknesses reaching $0.7\,$mm. The robustness of the material allows to use vacuum to hold the substrate tight during the spinning process while avoiding any depletion formed due to the sucking process. Freshly cleaved mica sheets provide an optically flat material which is possible to replace by a silicon wafer or other hydrophilic substrates. Spin-coating the polymer solution of non-wettable substrates used for the dewetting experiments results in a vanishing droplet as soon as the sample holder rotates, usually between 2000 and 4000 rates per minute. The film preparation might require a preceding cleaning stage with CO_2 snow-jet technique if the substrate was stored under poor conditions. The latter technique consists of blowing the surface with ice CO_2 with a stream of CO_2 ice produced by a gun specifically designed to be attached to a gas bottle of carbon dioxide. In contact to the surface, the stream freezes solid particles whose bonding is weakened to the annealed substrate and blows the particle away. Working under these drastic conditions is necessary to avoid the presence of comets patterns which occurs when big articles impede the flow.

The polymer solution is another source of defects in the film. On one side, the presence of nanoparticles may also alter the usual flow conditions. On the other hand, the rapid change of surface tension of the newly formed layer might result in radially oriented lines, striations, caused by a Marangoni flow. Therefore, choosing a good solvent for the polymer in order to provide a uniform evaporation all over the substrate is crucial.

3.2.2 Transfer of the film onto the substrate

The floating procedure was used to transfer of the thin film onto the substrate since spin-coating of the film directly to the hydrophobic substrate is not possible. Placed tangential to the water surface, the polymer film detaches the mica sheet when the substrate plunges deeper into the water bath, a clean MilliQ$^{\text{TM}}$ water free from chemical and physical defects. The film is then picked with the hydrophobic substrate previously cleaned with successive baths of ethanol, acetone and toluene (Sigma-Aldrich, München, Germany). The whole process is performed under laminar flow bench class 100.

Under normal dewetting conditions of a metastable film, studied holes nucleate randomly. The straight front geometry is obtained when the film is slightly stabbed with a tip while film floating on top of the water surface. This action creates a front which is straight over several hundreds on micrometers. It is also possible to obtain a straight front with a nanoscratch with an AFM cantilever. The scratch attains the film thickness of the film, over one to two hundreds of microns.

3.2.3 Characterization

Film thickness

The film thickness is obtained using either ellipsometry, in which case the value of the film thickness is averaged from the area spotted by the laser beam, or atomic force microcopy, where the step height between the substrate and film is measured. The range of film thickness prepared in our experiments varies from 50 to 230 nm.

Contact angle

The contact angle of polystyrene on the substrate was measured with AFM as soon as the droplet reaches equilibrium, Young contact angle. Accurate results were found whether θ was calculated from fitting the entire droplet surface or drawing tangents on a close at the three phase contact line [69].

The higher contact angle on AF 1600 compared to DTS reported in table 3.2 is observed also on the minimum of the effective interface potential, Fig. 3.3.

Effective interface potential

The stability of the PS film on each substrate is determined with the effective interface potential. Recent advances on the understanding of the surface and interfacial forces of the last decades [56] applied to systems investigated for dewetting experiments allows a quantitative understanding of the stability of the film. Fig. 3.3 depicts the effective interface potential for a PS/DTS and the PS/AF 1600 substrate. The potential $\phi(h)$ was drawn based equation 3.9, where each parameter is provided in table 3.3. The Hamaker constant A_i was taken from [111] for Si, SiO_2 and DTS and [15] for AF 1600. The repulsion constant C_s was determined in [111] from the contact angle at equilibrium θ_Y for DTS, see section 2.2 for details. The same method was used for AF 1600. Each layer thickness d_i was determined with ellipsometry.

$$\phi(h) = \frac{C_s}{h^8} - \frac{A_c}{12\pi h^2} + \frac{A_c - A_{SiO_2}}{12\pi(h + d_c)^2} + \frac{A_{SiO_2} - A_{Si}}{12\pi(h + d_c + d_{SiO_2})^2} \tag{3.9}$$

The semi-logarithmic representation of the $\phi(h)$ depicted in the inset of Fig. 3.3 illustrates the positive part of the effective interface potential on DTS and AF 1600. Both systems are metastable. Dewetting by heterogeneous nucleation occurs after the three phase contact line is formed. In the case of straight fronts, dewetting is immediate since a solid/liquid/air interface already exists.

	Units	DTS	AF 1600
C_c	J/m^6	10^{-81}	7.10^{-81}
A_c	J	$1.9(3).10^{-20}$	$4.3(2).10^{-20}$
A_{SiO_2}	J	$2.2(4).10^{-20}$	$2.2(4).10{-20}$
A_{Si}	J	$-1.3(6).10^{-19}$	$-1.3(6).10^{-19}$
d_c	nm	1.5	20(2)
d_{SiO2}	nm	1.7	1.7
θ_Y	°	67(3)	88(2)
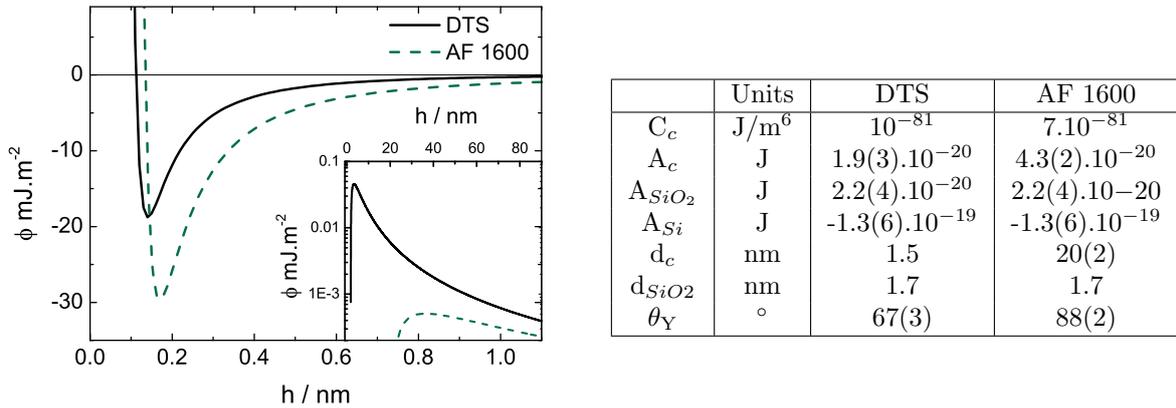
Figure 3.3 & Table 3.3: (a) Reconstruction of the effective interface potential based on equation 3.9 and parameters given in (b). (b) Experimental substrate parameters as a basis for the reconstruction of the effective interface potential, equation 3.9, Hamaker constants A_i for Si, SiO_2, DTS and AF1600 were taken from [111, 15]. The repulsion coefficients C_s for DTS and AF1600 were calculated to match the experimentally determined Young's contact angle θ_Y of PS on DTS or AF1600, respectively. The surface tension of PS is $31\,mJ.m^{-2}$ [6].

3.3 Experimental techniques

Two experimental techniques were used to study the rise of the rim instability during. AFM and optical microscopy are complementary, the high resolution of one technique involves a high acquisition time and lacks of a large area of interest for the measurement which are covered by the other technique.

3.3.1 Optical Microscopy

Studies of dewetting experiments are performed with an optical microscope (Leitz Laborlux, Leitz, Wetzlar, Germany) combined with a heating stage to perform *in situ* measurements. A magnification of 5–100 times is possible with the objectives mounted on the instrument, which is combined with a CCD-camera (Coolsnap Pro, resolution 1392 pdi $\times$ 1040 dpi $\times$ 12 bit). An objective placed before the camera allows another $10 \times$ magnification. The heating stage can reach temperatures approximating $180\,°C$ and move in the xy-direction. Image acquisition is easily automated using Image-Pro$^©$-Plus software (Media Cybernetics). A dark field microscopy mode is available to rapidly certify the cleanliness of the sample, free from dust particles. Dewetting experiments are run rising the temperature of the stage to the targeted temperature prior to place the sample on it. Despite the fact that optical microscopy is a convenient method to capture a bunch of images with *in situ* measurements experiments, information, especially the lateral resolution at early stage and the resolution in the z-direction for the whole dewetting process, acquired with the instrument is not sufficient to understand the mechanism of the rim instability on dewetting.

3.3.2 Atomic Force Microscopy

Atomic force microscopy is used to complete information lacking with the previous technique creating images with a higher resolution. If the art of work of optical microscopy is compared to the human eye, atomic force microscopy (AFM) would be the sense of touch of a blind person building his image with a stick [74]. The principle of AFM is to duplicate a three-dimensional (3D) surface by rastering a sharp tip across it. The topography of the surface is obtained with two main modes which are either using a bending tip in contact with the sample (contact mode AFM) or an oscillating tip sensing the substrate (Tapping mode^{TM} AFM). We describe the latter technique, which is the most relevant for the course of our study since this non contact mode avoids mechanical deformation of the soft material and minimizes the inelastic deformation of the sample [76]
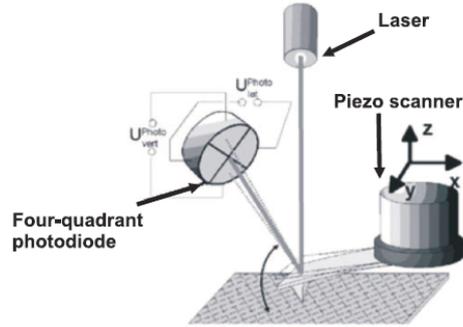
Figure 3.4: Typical AFM setup for the Tapping mode^{TM}. The deflection of a cantilever with a sharp tip is measured by reflecting a laser beam at the backside of the cantilever while it is scanning over the surface of the sample with a forced oscillation. The signal is detected on a four-quadrant photodiode.

Setup of Tapping-mode^{TM} AFM

Tapping-mode images are constructed by means of a series of three elements: a scan head, the sample holder and the detection unit sketched in Fig. 3.4.

The **scan head** holds a rectangular block of silicon or silicon nitride of millimeter size molded directly into a chip. One part of the block is fixed by the cantilever holder whereas the free side is extended with a thin strip approximately $100\,\mu$m long, $30\,\mu$m wide and $1\,\mu$m thick, termed cantilever. The size of the cantilever facing the sample is mounted with a sharp tip of pyramidal shape with aspect ratio, varying with the requirements of the measurement, approximating several microns height and a radius of the apex $4-30$ nm.

The sharp tip is directed towards the studied substrate fixed on a sample puck via a thin layer of double sided tape specially designed for AFM or other type of fixing method, such as a glue with specific heat resistance or conductivity adapted to the requirement of the method. The sample puck is then hold tight on the **sample holder** using either magnets or a vacuum. The sample is then moved in the x-, y- and z-directions by means of two different processes: mechanical or electrical. The area of interest of the sample is first located using endless screws. A very precise scanning is then obtained using motorsdriven with piezoelectricity: a quartz crystal is elongated or retracted using a current. The good control of the current input favors an exactness of the measurement.

Moves of the cantilever are controlled and monitored thanks to the **detector unit**, with a laser beam send on the back of the cantilever, usually coated with a thin gold layer to increase the reflection, and reflected into a photodetector build with four independent quadrants made of position sensitive photodiodes. The position of the laser beam sketched in Fig. 3.4 emphasize nanometric moves of the cantilever to a millimeter scale.

Imaging process   Tapping-mode[TM] AFM is a non contact mode or intermittent contact mode performed with a cantilever oscillating at its resonant frequency. The setup of the instrument allow to measure the low amplitude of the cantilever, whose regular oscillation is obtained thanks to piezoelectric element, at the photodetector unit. The strength of damping is altered with changes of the long range interactions between the substrate and the tip, reviewed in next paragraph. The topography of the sample surface is reproduced keeping the force of the oscillation constant, the strength being given by a setpoint value. The height of the sonde is regulated with a feedback loop mechanism responding to changes of the oscillation observed at the detector unit.

Interaction tip/surface   Interactions of the tip with the surface, detailed in [45, 114], are initiated by changes in topography and material properties of the sample. They are composed of long range van der Waals forces of strength calculated with the Hamaker constant, electrostatic forces, chemical forces, chemical forces and short range repulsive forces referred to a Pauli exclusion.

Resolutions and limits of the AFM   The vertical resolution of AFM measurements is mostly driven by thermal noise and varies with the inverse of $\sqrt{k}$ with k the spring constant [20]. Gan refers to a subnanometer resolution of $\Delta z \sim 0.01\,\text{nm}$ [45]. The lateral resolution, however, is mostly limited by the sharpness of the tip. Since the radius of the latter might vary in the range 4–30 nm, the AFM image is larger than the real image, the difference between both images being the radius of the tip varying with its sharpness. The convolution of the tip must therefore be considered to interpret AFM images.

Features characterized for the rim instability are rapidly larger than the lateral limit. The resolution is therefore not an issue for the dewetting experiments. The restrictive factors for experiments of the rim instability are rather the scan limits in-plane and vertically which depends on the stretching properties of the piezoelectric crystal. These properties are embedded to the type of instrument used. For example, the lateral scan limit on the Dimension Icon[®] approximates $100\,\mu\text{m}$ and the vertical limit several microns.

Another limitation of AFM measurements is the acquisition time of an image which can range from few seconds to hours depending on the resolution aimed due to the raster process which slow down image acquisition.

AFM and dewetting experiments

The time required to acquire an image being longer than the dynamics of dewetting necessitates to work with polymer film in glassy state, *i.e.* below the glass transition temperature. *In situ*

experiments are not possible, but *ex situ* experiments are investigated thanks to a heater/cooler placed on the stage. The same region is studied during the course of dewetting without shifting the position of the sample. We should note also that the time required to cool the stage from the experimenting temperature down to the scanning temperature ($90\,°C$), only few seconds, does not impact on the results obtained; our data are similar to data obtained with *in situ* measurements.

The advantage of the high resolution measurement permitted with AFM enable to quantify new features of the rim instability compared to optical microscopy measurements, such as the amplitude of the perturbation or the wavelength at early stage of dewetting. However, the maximal scan size of approximately $100\,\mu$m might be a limiting factor for a good approximation at late stage of dewetting on AF 1600 or with thicker films because it would be possible to measure less than three bulges in this range which is not sufficient to obtain good statistics. Limitation is also true for the vertical direction. On AF 1600, the whole volume of polymer is accumulated in the bulge which reaches a height of several microns at late stage. The length reaches the limits of the instrument.

3.4 Characterization of the rim instability

3.4.1 Methods used to determine the dewetted distance

The comparison of results obtained with optical microscopy (OM) and atomic force microscopy (AFM) is not trivial. Measurements of straight fronts done with optical microscopy necessitate a reference point from which local distances measured at thicker and thinner parts D_{peak} and D_{valley} are measured. The same procedure could be used for holes after we could estimate the center of the radius via, *e.g.* the nucleation point. However, the hole radius is more efficiently determined by automatically finding the minimum and the maximum radii of the hole, rendered possible using a specific function of the acquisition software. The automated method, however, can only be used in the absence of fingers. When bulges protrude from the substrate, we should either use the local measurement of R at thicker and thinner regions as introduced before or extract a mean dewetted distance R_{mean} from the dewetted area.

We don't have access to a reference point when straight fronts are measured with AFM since any starting point would be outranged after the onset of dewetting[5], but the preciseness of the measurement gives access to the exact volume of material accumulated in the ridge. Based on the fact that the dewetted film is accumulated at the three phase contact line and homogenously

---

[5]Even with accurate positioning of the stage, the error and time to find the position back are too large to be used.

(a) Sketch of a perturbed ridge represented in 3D. Black represents the substrate, blue stands for heights $0 < h(z) < H$ and green to red represents the accumulated volume, $h(z) > H$.

(b) Top view of an AFM picture of a hole. Horizontal scale of 10 μm, height scale of 780 nm.
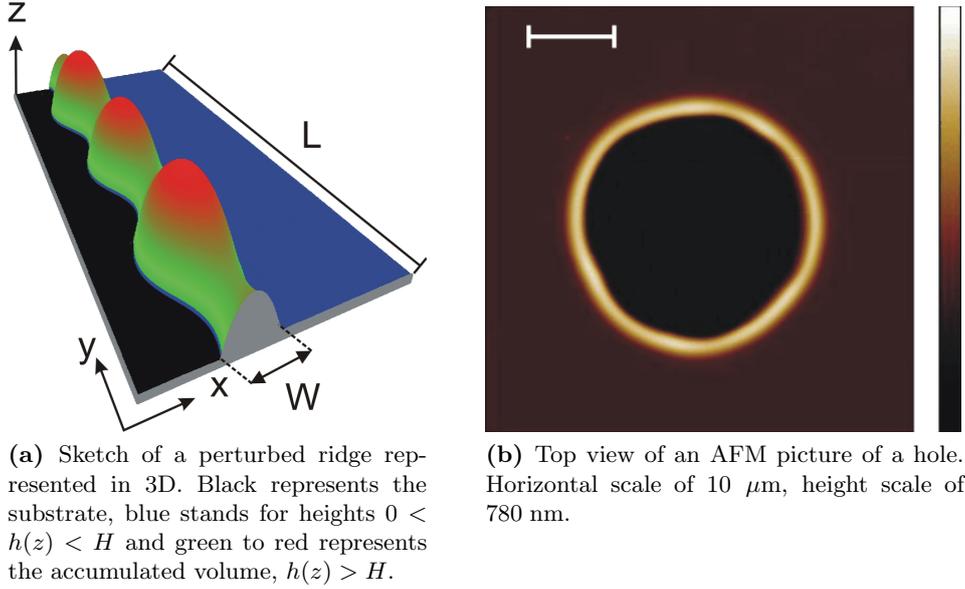
Figure 3.5: AFM images of a straight front (a) and a hole (b) used to calculate the dewetted distance from the volume in the rim.

distributed along the ridge, we can extract the dewetted distance from the volume accumulated on top of the ridge V_{acc}, the green to red area in Fig 3.5(a), above the initial film thickness. We obtain $D_{mean} = \frac{V_{acc}}{LH}$ with H the film thickness and L the length of the ridge measured. Usually V_{acc} can be directly measured with the AFM software using a function denoted "bearing tool". This tool was unfortunately not available on the newer version of the software we used and images obtained with the new software were not compatible with older versions of the software. Consequently we used the following method to calculate V_{acc}. ASCII files were exported from AFM data and transferred to Origin. The sample was shifted in height to set the substrate at $H = 0$ nm. We suppressed the remaining unperturbed film by setting the absolute difference in height lower than 10 nm to zero. We inserted a threshold to avoid changes at the tip of the ridge. Integrating the matrix obtained gives the total volume of the ridge V, from which we can extract the theoretical unperturbed rim height H_0 and width W_0[6], see part 5.3. We have then subtracted the film thickness H and obtained a new matrix whose integration gives the accumulated volume V_{acc}. A simple program was written in OriginLab to provide a reproducible routine, see appendix A.

Extracting the dewetted distance D_{mean} from the volume of the ridge gives reproducible results independently of the area scanned. We mostly worked at $L = 80$ μm, but reducing L to 50 μm doesn't affect the results as long as the instability remains homogeneously distributed.

---

[6]Note W_0 and H_0 are calculated from the total volume of the ridge $V = V_{acc} + V_{film}$ where V_{film} is the volume of the film sandwiched between the substrate and the substrate and V_{acc}.

Scanning a ridge at identical L, but at different positions on the film leads to an error lower than 5 % of the distance obtained.

As a consistency check, we have combined both methods of measurement. The hole depicted in Fig. 3.5(b) was scanned with AFM. We could compare the radius by measuring directly half the distance between two contact lines (R_{opt}) or extracting from the volume of the rim (R_{mean}). Both methods show a good agreement: $R_{\mathrm{opt}} = 12.3(5)$ μm and $R_{\mathrm{mean}} = 12.7(6)$ μm.

3.4.2 *In situ, ex situ* experiments

The cross-section of the ridge is captured for various times and the corresponding distance traveled by the straight front when the sample is quenched to $T_{\mathrm{s}} = 90\,^{\circ}$C. Imaging the ridge slightly below the glass transition temperature allows an instant capture of rim instability, in a 'frozen'-like stage. The sudden decrease of temperature to T_{s} provokes a minor decrease of the overall height which can be neglected because of the small expansion coefficient. The same characteristics of the film are found in this *ex situ* measurements compare to *in situ* measurements, the quenching and further rise of temperature of approximately $30\,^{\circ}$C takes place within seconds. In order to keep the measurement consistent, we have always measured rim profiles near the highest regions of the ridge, *i.e.* close to peaks. This implies that sometimes we had to shift the position of our measurement because peaks slightly move along the ridge. We should note that quenching doesn't affect the temporal evolution recorded as a decrease of $30\,^{\circ}C$ is done within few seconds.

Thanks to the heating stage available on the optical microscope and the short time to record an image, it is possible to record experiments *in situ* continuously which is not the case for dewetting experiments performed with AFM. However, the position scanned for a whole ridge with *ex situ* experiments are the same. AFM experiments can be considered as semi-continuous.

4 Rim instability — the origin of fingering

This chapter brings light on the impact of the solid/liquid boundary condition on the evolution of the rim instability during the course of dewetting. Fig. 4.1 evidences how the sole change of the hydrophobic layer covering the substrate strongly impacts, on one hand, on the shape of the growing ridge, on the other hand, on the dynamics of the retracting three phase contact line. We base our interpretation on previous studies, focusing on the early stage of dewetting, showing that changes in the dewetting dynamics result from different hydrodynamic slippage recorded at the solid/liquid interface for both systems [16, 39].

Although characteristics of the rim instability are observed in three dimensions, this chapter concentrates on the in-plane rim instability, *i.e.* the perturbation is studied in the xy-direction. The plane perpendicular to the substrate, also denoted as yz-plane or cross-section, is treated in chapter 6. After a phenomenological comparison of both systems studied under identical experimenting conditions (viscosity, temperature, M_w), we analyze in a second part the dewetting dynamics of the three phase contact line. Previous work of Jacobs et al. is studied for later stage of dewetting. An emphasis is then given on local variations of the dewetting dynamics at characteristic points of the ridge denoted **peak** and **valley**.

The following part strengthens the impact of slippage on the morphological growth of the ridge enabled thanks to the rectilinear geometry used. These morphological differences initiate slight changes in the dewetting dynamics, compared to the circular geometry, which are discussed in the following part to divide the whole dewetting process into a four stages varying whether slippage is important. Finally, the importance of the dewetting dynamics on the rim instability is verified with a new set of experiments changing the dewetting velocity of the system.

4.1 First observations

A thin polymer film is placed on top of a surface, a silicon substrate rendered hydrophobic by grafting a layer of densely packed silane molecules (DTS) or by spin-coating an amorphous layer of Teflon® (AF 1600). The 125(5) nm thick polystyrene film of molecular weight $M_w = 13.7$ kg/mol (PS13.7k) is annealed at 120 °C while optical micrographs are recorded *in situ*. The system is metastable under these conditions; the retraction of the liquid film occurs at
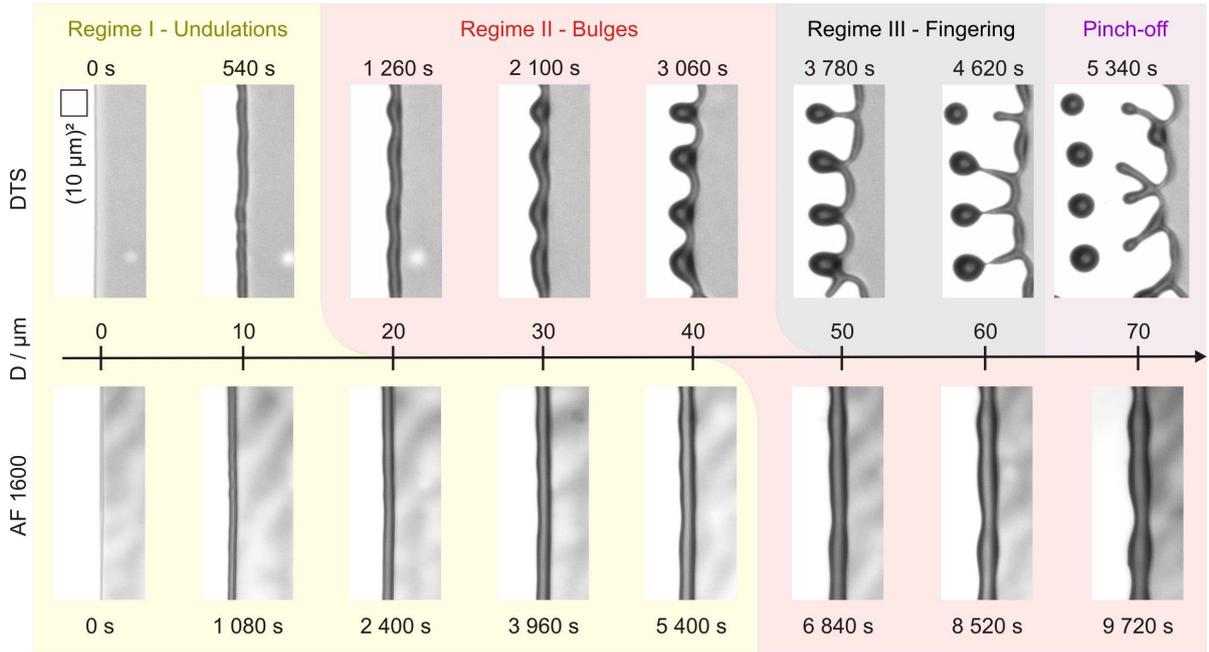
Figure 4.1: Dewetting of a thin polymer film on DTS (top) and AF 1600 (bottom) at 120 °C by retraction of an initially straight front (PS 13.7 kg.mol^{-1}, $H = 125(5)$ nm). A semi-cylindrical liquid rim is formed by the accumulation of polymer (dark grey). The advance of the front is characterized by the dewetted distance D(t) (see arrow). Optical images of straight fronts are 80 µm wide. Colors represent various regimes detailed in part 4.4

the three phase contact line. The activation energy required to initiate dewetting is lower for the rectilinear geometry than the circular geometry. The three phase contact line is formed before annealing for straight fronts, whereas nucleation of holes is required for the hole growth, treated in chapter 9. Dewetting is therefore immediate when the sample is placed at the desired annealing temperature.

Fig. 4.1 depicts the edge of a receding thin film moving from left to right with its position given by the dewetted distance $D(t)$ as indicated by the straight arrow. Pushed at the solid/liquid/air interface, the polymer agglomerates to form a rim rounded by the Laplace pressure, homogeneously distributed along the edge to form a **ridge**, the dark grey zone observed in optical micrographs. The semi-cylinder[1] shows significant undulations along its length as $D(t)$ increases, bulges develop on the ridge. The pattern develops differently depending on whether the retraction of the front takes place on DTS or on AF 1600[2]. In the case of DTS, top row, a

---

[1]We solely consider the ridge or semi-cylinder since we prove in chapter 5 that we can neglect the film thickness, small compared to the height of the ridge.

[2]In order to simplify readings, we abbreviate the system PS/SiO$_2$/Hydrophobic layer into the corresponding hydrophobic layer DTS or AF 1600.

strong asymmetry of the ridge is observed. At $D = 20\,\mu$m, the side in contact to the substrate, 'dry' side, is highly undulated, whereas the side plunging into the film, 'wet' side, remains straight. For D larger than $30\,\mu$m, bulges protrude from the ridge and form fingers before breaking into droplets at $D \approx 60\,\mu m$. In the other case (AF 1600, bottom row), undulations remain weakly developed at small dewetted distances. After $60\,\mu$m, the instability revealed with optical microscopy evidences a growth developing symmetrically to the axis of the cylinder, bulges remain in line of the ridge. The early developing of instability on DTS does not only take place at a smaller volume uptake, *i.e.* smaller distance traveled by the initially straight front, but also by the early time at which the undulation takes place.

4.2 Dewetting dynamics

In order to quantify the evolution of the retracting front on DTS and AF 1600, we need to record local variation of the moving contact line. We differentiate the dynamics of the ridge recorded at a thick region of the ridge, termed **peak**, to the thinnest region adjacent to the peak, termed **valley**. We present the local variation of the dynamics of the ridge and investigate the impact of friction at the solid/liquid interface on the influence of the dewetting rates.

4.2.1 Local and temporal evolution of $D(t)$

Local variations of the liquid front traveling on the DTS substrate are reported in Fig. 4.2a, with the definition of $D(t)$ measured at peak and valley displayed in the inset. A similar growth is observed up to $2200\,$s independently on which position along the ridge the measurement is performed. This time, denoted t_{b}, corresponds to a distance of $D_{\mathrm{b}} \sim 30\,\mu$m which marks the beginning of bulge protrusion as shown in Fig. 4.1. Beyond D_b, different growth rates are clearly observed: $D_{peak}(t)$ slows down, whereas $D_{valley}(t)$ grows almost linearly. The growing distance between $D_{peak}(t)$ and $D_{valley}(t)$ illustrates the increase of the finger length. The last point recorded at peak ($t = 4800\,$s) represents the maximal distance ($D_{max} \sim 39\,\mu$m) traveled by the finger before the pinch-off instability takes place. In contrast, running an identical experiment on AF 1600 shows a similar growth whether $D(t)$ is recorded at peak or valley as depicted in fig. 4.2b. No fingers are formed. The limit t_b is recorded after $10\,000\,$s, while the distance traveled by the polymer front is larger than $80\,\mu$m.

Focusing now on the evolution of $D(t)$ for thicker regions only, the faster dewetting dynamics recorded on DTS becomes obvious with the double logarithmic representation of $D_{\mathrm{peak}}(t)$ in Fig. 4.2c. At $t = 0\,$s motion at the three phase contact line starts and evolves as an algebraic power law $D \propto t^{\alpha}$. The fit, dashed line in Fig. 4.2, using this equation was first performed using

the method proposed in Fetzer et al. [42]. The fitting range initially used for the measurement (0 to 14 μm) was extended to higher distances until deviations of α from the initial value were observed. As a result, we see that the aforementioned algebraic law remains valid for large dewetted distances: 34 μm on DTS and 90 μm on AF 1600. In the case of DTS, the deviation appears earlier due to the thickening of the rim width forming fingers as discussed in part 4.4. Exponents α resulting from fits of Fig. 4.2c give $\alpha \approx 0.71$ for DTS and $\alpha \approx 0.87$ for AF 1600. The value obtained on both systems is within the limits of dewetting occurring when the plug flow ($\alpha = 2/3$) or the no-slip ($\alpha = 1$) situation are considered, as introduced in part 2.4.2 [3]. As a consequence, the retraction of the film takes place in a regime where friction at the solid/liquid interface differs in both systems, a strong slip situation is considered on DTS whereas a no-slip situation is more adequate on AF 1600. Results showing the exponent α being closer to 0.9 than the analytically predicted value for the no-slip system, $\alpha = 1$, are already reported from an experimental point of view [19] and for numerical situations [83].
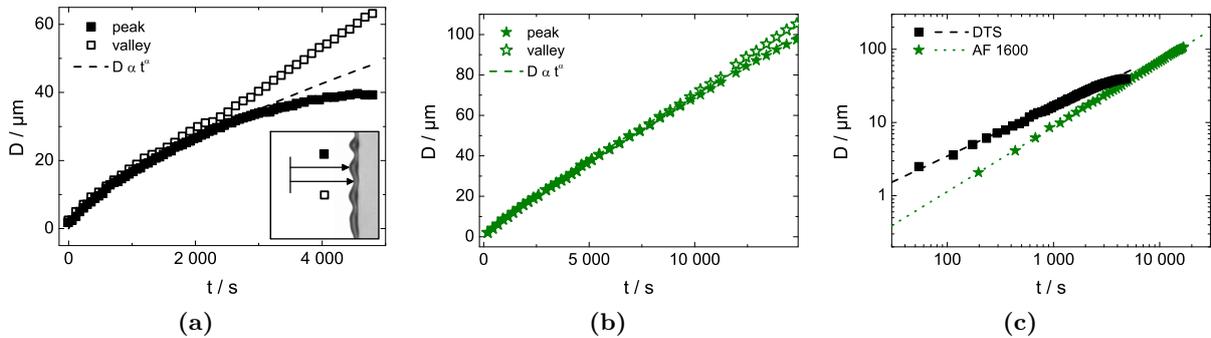
Figure 4.2: Retraction dynamics of the polymer initially straight fronts obtained from optical micrographs of Fig. 4.1. D(t) values, recorded at the three-phase contact line, depend on the position, peak or valley, along the rim as indicated in the insert of (a), which displays the dewetted distances D(t) of thicker and thinner rim regions, respectively closed and open symbols, for the PS film on DTS. (b) D(t) for the PS-film on AF 1600. (c) Slippage present in the system is confirmed by the growth laws D(t) with $\alpha_{\mathrm{DTS}} = 0.68(1)$ and $\alpha_{\mathrm{AF1600}} = 0.89(1)$, dashed curves depicted in (a)–(c). The system is a $125(5)\,\mathrm{nm}$ thick PS(13.7k). Dewetting experiments performed at $120\,°\mathrm{C}$.

4.2.2 Dissipation mechanisms at the solid/liquid interface

Fetzer et al. proved that two types of dissipation mechanism, the first being purely viscous and the second being friction at the solid/liquid interface, can be combined to explain why the dewetting velocity is fastest on DTS although the driving force is larger on AF 1600. An analysis of the dewetting dynamics with the resulting model, denoted as hole growth analysis in section 2.4.3, evidences that the contribution of friction at the solid/liquid interface dominates

---

[3]One should note that the 4th regime of full viscous dissipation is not observed in these experiments.

the dynamics of dewetting for DTS [40], with b a representative value of this contribution. b is calculated from the slope K of the velocity $v(D^{-0.5})$, given in equation 9.1, with S the spreading coefficient, η the viscosity, C_s a constant standing for the self-affine growth of the rim and H the initial film thickness.

$$K = \frac{|S| \, b}{3 \, \eta \, C_s \, \sqrt{H}} \tag{4.1}$$

The resulting b is in the order of microns ($b \approx 2 \, \mu$m), much larger than the initially prepared film thickness H. Based on the same analysis of the moving contact line Bäumchen et al. revealed a dominance of viscous friction on the dewetting dynamics for AF 1600 [16]. The slip-length b obtained in this case is much smaller than the film thickness ($b < 0.1 \, \mu$m).

We should note that the previously performed analysis gives a good approximation of the slip-length compared between both systems, however, Bäumchen addressed a systematic larger slip length using this method in comparison to the rim profile analysis, discussed in part 5; which is probably due to assumptions included in the energy dissipation model, *e.g.* the definition of the rim width does not reflect the lateral extent of slippage (in the x-direction).

4.3 Influence on the morphology of the ridge

We now concentrate on the evolution of the rim width for an entire bulge. Fig. 4.3 displays a selected part of a ridge scanned with AFM represented in two or three dimensions (respectively Fig. 4.3(a)-(b) and Fig. 4.3(c)-(d)). The bulge has been chosen to compare the situation of equivalent accumulated volume in the ridge for both AF 1600 and DTS systems ($D_{AF\ 1600} \approx 45 \, \mu$m and $D_{DTS} \approx 39 \, \mu$m).

A significant morphological difference appears when both systems are compared. For AF 1600, the perturbation at both sides of the ridge, *i.e.* the three phase contact line and the line directly in contact with the liquid film, develops out of phase along the ridge, similar to the varicose mode[4] observed in the static case of a supported semi-cylinder. A symmetrical pattern is produced. In the case of DTS the 'back' side of the rim, the side facing the thin film is straight, whereas the side in contact with the substrate is highly perturbed. A direct consequence of the asymmetrical pattern observed for DTS is a bulge protruding from the ridge. The isoheight lines representation of 200 nm interval ease to see that the sequence of peaks and valleys are not aligned with the ridge. In contrast, a rather good alignment is found for AF 1600.

---

[4]Considering the situation of a liquid ribbon deposited on a substrate, the term varicose mode (or peristaltic mode) is used when contact lines at both sides of the ribbon develop out of phase. The opposite situation where contact lines at both sides of the ridge develop in phase is named zigzag mode.
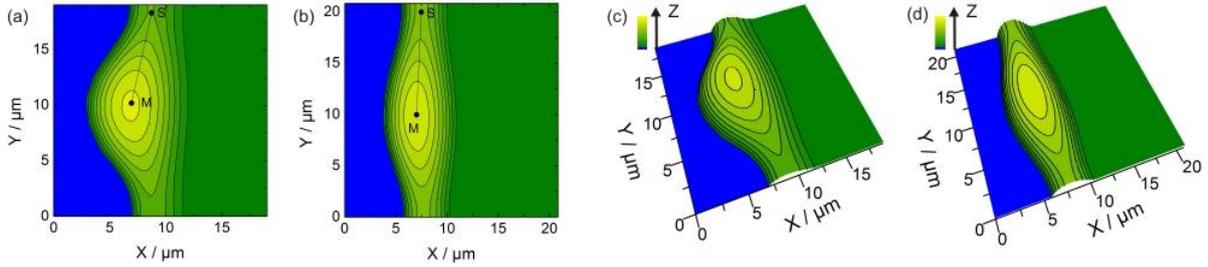
Figure 4.3: 25 $\mu m \times$ 25 μm AFM image of one bulge scanned on DTS (top) and on AF1600 (bottom). The situation represented in 2D (a)-(b) and 3D (c)-(d) compares bulges at equivalent accumulated volume (D_{DTS} = 53 μm (a), (c) and $D_{AF\ 1600}$ = 59 μm (b), (d)). Isoheight lines are set every 200 nm. Experiments take place at 120 °C for both DTS (125(5) nm thick PS(13.7k) film) and AF 1600 (115(5) nm thick PS(10.3k) film).

These observations are in complete agreement with results obtained with numerical simulations described in section 2.5.2. Introducing a 'zigzag' perturbation, *i.e.* both sides of the ridge are perturbed out of phase, to a lubrication model, Münch and Wagner showed that results of both the linear stability analysis and non linear dynamics lead to a universal conclusion: for the intermediate/strong slip regime, the side on the ridge in contact to the dewetted area remains highly undulated, whereas the other side of the ridge remains fairly flat. For the weak slip regime, the undulation of the ridge turns to be a varicose-like mode, both sides of the ridge are perturbed out of phase. The surface plot of Fig. 4.3(a-b) show that a bulge protrudes from the ridge for the intermediary slip situation whereas thinner and thicker regions are aligned in the weak slip model. The same feature is observed in the 3D projection of AFM images in Fig. 4.3(c-d); a bulge protrudes towards the dewetted area when scanned on DTS, undulations are symmetrical to the axis of the semi-cylinder on AF 1600.

In addition to the higher dewetting dynamics recorded on highly slippery systems, results obtained with numerical simulations and experiments support a common conclusion, being that slippage impacts on the morphology of the ridge; increasing slippage in the system emphasizes the asymmetry of the bulge. This change in morphology initiates local changes in the dewetting dynamics.

4.4 Regimes of the rim instability

Local changes in the dewetting dynamics observed in Fig. 4.2 are divided into four regimes defined in this part to provide a quantitative comparison between the DTS and the AF 1600 systems. The work initiated by Mainka [77] is pursued giving further insights and a more adequate definition of the existing stages.
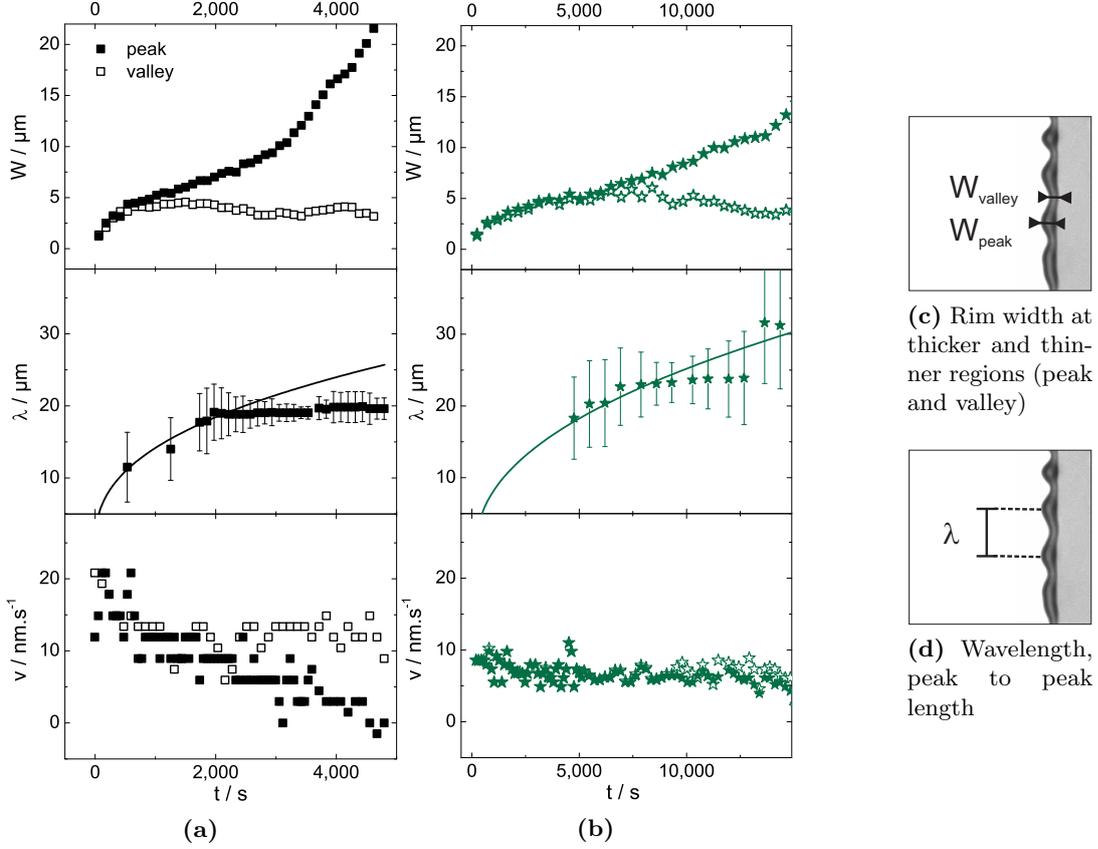
Figure 4.4: (a)-(b) Temporal evolution of the rim width $W(t)$ (top), wavelength $\lambda(t)$ (middle) and dewetting velocity $v(t)$ (bottom) obtained from optical micrographs of Fig. 4.1 on DTS (a) and AF 1600 (b). Values of $W(t)$ depend on thicker and thinner regions (close and open symbols) defined in (c). Each single scatter results from an average of values along several bulges. $W(t) = \frac{\sum W_{\mathrm{peak_i}}(t) + W_{\mathrm{valley_j}}(t)}{i+j}$. The wavelength is defined as the length between successive thicker regions with the part at early stage following the solid curve (guide to the eye), $\lambda(t) = \frac{\lambda_{\mathrm{i}}(t)}{i}$, $v(t)$ is the differentiate of $D(t)$ in Fig. 4.2.

We combine in this part conclusions drawn in the previous two sections are combined in this part to explain the various patterns observed in Fig. 4.1(a). Undulations of the moving front recorded on DTS develop quickly and change into fingers. Local variation of dynamics evidenced for DTS in Fig. 4.2 at thinner and thicker regions of the ridge are decomposed in four regimes: the onset of rim instability at $t^* \sim 1000$ s, the protruding of bulges at $t_b \sim 2200$ s followed by the formation of fingers at $t_f \sim 3600$ s and detachment of droplet at $t_{\max} \sim 4700$ s. The whole phenomenon is compared to the AF 1600 system, giving a comprehensible understanding of the impact of slippage on the rim instability developing in the xy-plane simply using optical microscopy as instrumental measurement.

59

Fig. 4.4 displays the temporal evolution of various parameters such as the rim width $W(t)$ [5], the wavelength λ defined as the peak to peak distance measured along the ridge (y-axis) between subsequent thicker regions and the local dewetting velocity $v(t) = \dot{D}(t)$ measured for the DTS/PS system (Fig. 4.4(a)) and the AF 1600/PS system (Fig. 4.4(b)).

4.4.1 Homogeneous spatial growth along the ridge

Rim widths measured at peak W_{peak} and valley W_{valley}, respectively filled and open symbols in top row of Fig. 4.4(a)-(b) represents the distance in x-direction between the three phase contact line and the wet side of the ridge as shown in Fig. 4.4(c). $W_{\mathrm{peak\ or\ valley}}(t)$ grow uniformly until a width of approximately 4-5 μm is reached whether dewetting takes place on DTS (squares) or on AF 1600 (stars). This rim width W^* appears at $t^* \approx 1000\,\mathrm{s}$ on DTS and $t^* \approx 5000\,\mathrm{s}$ on AF 1600. For $t > t^*$, the difference $W_{\mathrm{peak}}(t) - W_{\mathrm{valley}}(t)$ increases while $W(t)$ at thinner parts of the ridge slightly decreases. We explain the change by a flow along the ridge from valley to peak, which we define as **onset of the bulging regime**.

Parallel to the growth of the rim width, we observe prior to t^* a growth of the wavelength $\lambda(t)$, defined in Fig. 4.4(d) as the lateral distance between successive peaks λ_{i} averaged between i bulges over the largest possible length. The density of points being small in this region, due to the limited resolution of the optical microscope, the guide to the eye suggests the evolution of $\lambda(t)$ in the early stage. The theoretical and experimental explanations, discussed in chapter 6, evidence a coarsening of peaks.

The increase of the rim width strongly correlates with the decrease of the velocity recorded on DTS up to t^*. The superimposed model introduced in part 2.4.2 gives a clear explanation of this observation since the velocity $v(t)$ of the moving front evolves as $v(t) \approx W(t)^{-1/2}$ if the slip component of the dewetting velocity predominates. The latter contrasts with the second system. The dewetting velocity recorded on AF 1600 remains rather constant within scattering for the whole dewetting process.

4.4.2 Protrusion of bulges

At $t_b \approx 2200\,\mathrm{s}$, we observe parallel to the increase of $W_{\mathrm{peak}}(t)$ on DTS an abrupt slowing down of $\lambda(t)$ which reaches a plateau value of $\lambda_{\mathrm{max}} \approx 19\,\mu$m. In addition, a decoupling of the dewetting velocity recorded at peak and valley occurs when this stage is reached. **Bulges protrude** from the ridge.

---

[5]In this situation, the rim width has been measured as the distance between the three phase contact line and the back side of the ridge. Both limited to the optical resolution of the optical microscope and the contrast. A more precise measurement with AFM is presented in the following chapters.

The value of $\lambda_{\max}(t)$ being reached for $t > t_b$ implies a discontinuity of polymer flow along the ridge. The volume of polymer accumulated at the thinnest part of the ridge is only the volume collected from the advancing of the three phase contact line in the film reduced by the volume flowing tangential to the contact line towards thicker regions, denoted respectively as $v_{\rm acc}$ and $v_{\rm flow}$. No additional material comes laterally from the collapsing of nearby bulges. The constant velocity recorded at valleys for $t > t_b$ indicates that the uptake of material equilibrates with the flow of material towards peaks. The latter induces a thickening of the rim at peaks which causes a decrease of $v_{peak}(t)$, as observed in the Fig. 4.4(a), explained by the proportionality of velocity to the inverse of the rim width ($v(t) \propto W(t)^{-1}$, see part 2.4.2). The thickening of peak can also be observed in Fig. 4.2(a): tracking the temporal evolution of D_{peak} follow the algebraic power law $D_{peak}(t) \propto t^{0.68}$ until $t \approx t_b$.

The situation differs on AF 1600, as shown in Fig. 4.4b: only the slight decrease of $W_{\rm valley}(t)$ together with the increase of $W_{\rm peak}(t)$ of the points described above are observed; the wavelength grows continuously and $v_{\rm peak}(t) \approx v_{\rm valley}(t)$. We can conclude that the rim instability develops on AF 1600 by increasing the flow from thinner to thicker regions.

4.4.3 Fingering

A sudden increase of the growth dynamics of $W_{\rm peak}(t)$ can be appreciated on Fig. 4.4(a) at $t_{\rm f} \approx 3600\,$s. This increase is correlated to a decrease of $v_{\rm peak}(t)$, evidenced in the zoom-in depicted in Fig. 4.5(b). The new regime sets the **onset of fingering**.

The sequence of pictures recorded at small time interval in Fig. 4.5(a) illustrates the transition from bulge to finger. As the bulge further protrudes from the ridge, the three phase contact line on either side of the bulge becomes normal to the dewetting direction ($t < t_{\rm f}$). Beyond t_f, the cross section at the back of the bulge thins, a **neck** is formed. At this stage, the curvature at valley in the xy-plane is not uniformly described with a single wave, but additional components are necessary to fit the curvature of the whole contact line. The Laplace pressure in this region changes. Moreover, a force similar to the spreading coefficient is applied at the back side of the bulge which, coupled to the constant velocity recorded at valley $v_{\rm v} < v_{\rm p}$, initiates a **finger**. The finger whose shape is roughly similar to a supported semi-cylinder of secant d_f varying with the contact angle of the system grows until the droplet pinches-off at $t_{\max} \sim 4700\ s$.

The whole process starting from the onset of instability to droplet detachment takes place on DTS at distances traveled by the thicker regions below $40\,\mu$m. In contrast, a dewetting distance of $80\,\mu$m is reached on AF 1600 without any protrusion of the bulge. We introduce now a new procedure to quantify the protuberance of the bulge from the ridge. The **zigzag length** $x_{\rm pv}$, sketched in the inset of Fig. 4.5(c), represents the length recorded in the direction of dewetting
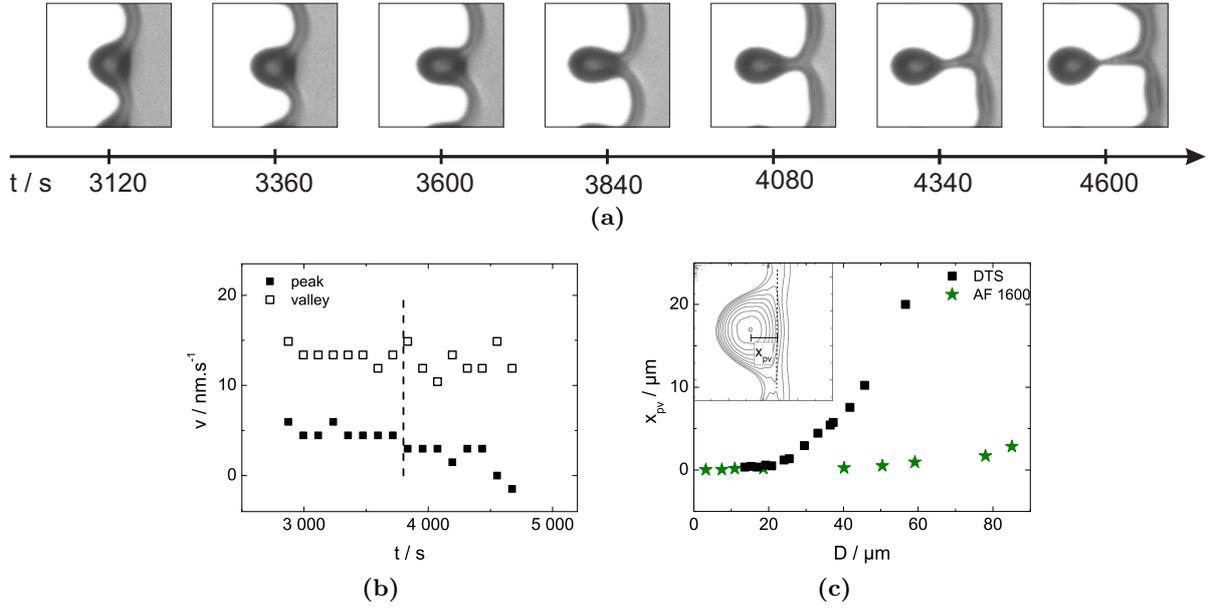
Figure 4.5: (a) Optical micrographs of one bulge obtained from DTS on Fig. 4.1 changing into a finger. The velocity v measured in this time range (b) is used to quantify the onset of fingering which happens as the bulge protrudes from the ridge at a distance x_{pv} larger than $5\,\mu$m. The zigzag length x_{pv}, used to quantify the protrusion of the bulge from valley to peak (inset), is measured on AFM images from a PS(10.3k) film of height 115(5) nm at 120 °C on DTS and AF 1600.

between the tip of the peak and valleys on either sides. The strong advantage of the method is to be independent of the wavelength $\lambda(t)$ of the system and consequently independent of the number of bulges used for the measurement which renders possible to introduce a new type of comparison based on the volume of polymer accumulated in the ridge represented by D, method described in part 3.4.1. The plot on Fig. 4.5(c) instantly confirms results previously obtained: $x_{pv}(D_{mean})$ grows rapidly on DTS, whereas remains steady on AF 1600. We should note that the distance of 60 μm reached on DTS, larger than the maximal value of $D_{peak}(t)$, is due to the fact that D takes into account the volume of the ridge at peak and valley (see part 3.4.1 for further details).

4.4.4 Droplet detachment

AF 1600: conical tip attached to a sharp front, DTS formation of a thread As the finger further protrudes from the ridge, the neck thins and the bulges turns into a spherical shape. The dewetting velocity recorded at the peak tends to zero. A slightly negative value of $v_{peak}(t)$ is observed in Fig. 4.5(b) at t_{max}. If we neglect the errors of the measurement due to the resolution of the instrument, the negative $v(t_{max})$ can be explained by a slight shift of the

contact light which moves in the opposite direction of dewetting immediately after the droplet pinches-off the ridge. At the release of the bulge from the finger, a force driven by the spreading parameter is applied to the newly formed contact line to round the droplet which creates a decrease of $D_{\text{peak}}(t_{\text{max}})$. The process of **droplet detachment** occurs when friction energy at the solid/liquid interface is higher than the kinetic energy and the cohesive energy which keeps the bulge connected to the ridge. Further discussion are given in chapter 7.

4.5 Influence of the dewetting velocity

In the previous sections, we demonstrated the impact of slippage on the dewetting dynamics, on the morphology of the ridge and consequently on the formation of fingers. This study, however, did not allow to determine which of the high dewetting velocity or of the high slip length determined in the systems has the strongest impact on fingering. In order to understand the weight of one on another, we designed a set of experiments where the dewetting velocity was varied from two orders of magnitude, whereas changes in the slip length remained low[6]. Thin PS films of thickness $H = 110 - 130\,\text{nm}$, the same range as used previously, deposited on top of AF 1600 or DTS and then annealed at temperatures ranging from 110 to 140 °C. The interval of temperature used involves a change of more than three orders of magnitude in viscosity. Since we are working under Newtonian flow conditions, changes in viscosity affect the dynamics of the whole process and slight changes of the slip length are known on DTS. However, the shape of the rim and the instability, both are driven by surface tension, remain unaffected. The slight change in molecular weight between the PS/DTS system (PS13.7k) and PS/AF 1600 (PS10.3k) can therefore be neglected in the following discussions.

Fig. 4.6 shows results of the dewetting dynamics obtained for all series. The pattern of each series is very similar to results depicted in Fig. 4.2 independently of temperature. The double logarithmic representation of closed symbols depicted in the inset $(D_{\text{peak}}(t))$ evidence that slippage at the solid/liquid interface is similar to the previous series. Values of the exponent α obtained from the fit of data with the algebraic law $D_{\text{peak}} \propto t^{\alpha}$ are $0.66 < \alpha < 0.68$ on DTS (top row) and $0.84 < \alpha < 0.91$ on AF 1600 (bottom row). We are in the situation of strong slippage for the PS/DTS system and weak slip for the PS/AF 1600 system. The increase of slip length on DTS with decrease of temperature is neglected in this part since the ratio slip length to film thickness remains high with the value reported in [42].

For each temperature, Fig. 4.6(a) mirrors the situation of PS on DTS presented in Fig. 4.2(a) with a shift in time resulting from the change in dynamics of the retracting front. The characteristic times and distances standing for the various regimes of the rim instability defined

---

[6]The effect of slip length on temperature is discussed in chapter 5.
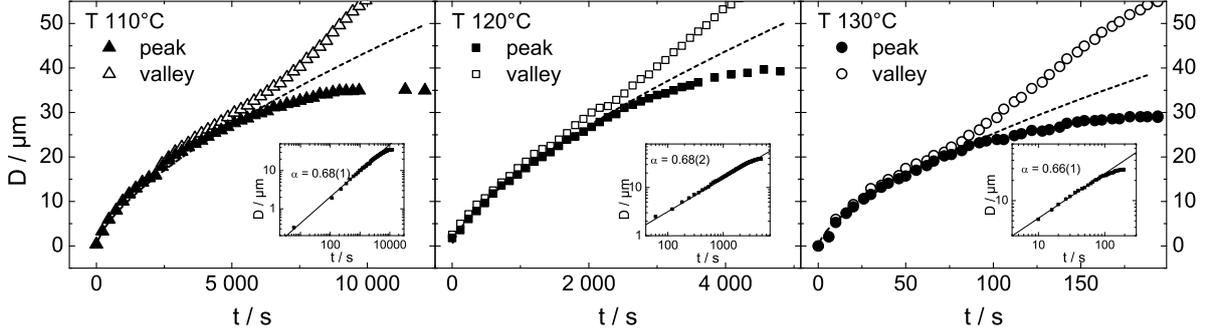
(a) Dynamics on DTS at 110, 120 and 130 °C of a PS(13.7K) film of thickness $H = 125(5)$ nm. The dashed line represents the algebraic power law $D \propto t^\alpha$ with the value α given in the inset representing a strong slip behavior.
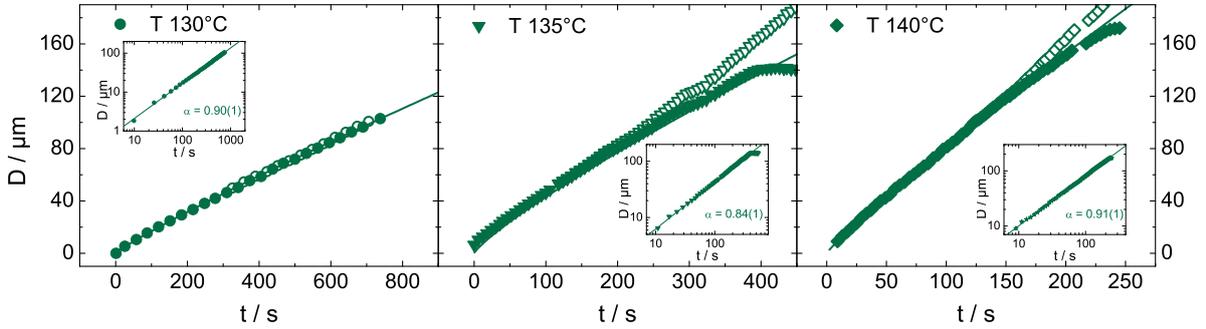
(b) Dynamics on AF 1600 at 130, 135 and 140 °C of a PS(10.3K) film of thickness $H = 115(5)$ nm. The solid line represents the algebraic power law $D \propto t^\alpha$ with the value α given in the inset representing a no-slip behavior.

Figure 4.6: Retraction dynamics of a polymer straight front recorded at peak (filled symbols) and valley (open symbols). The trend of each curve looks similar on DTS (a) and AF 1600 (b) despite the wide range of dewetting velocity, viscosity produced with the range of temperature T used. The trend of the dewetting dynamics varies with the substrate, especially the solid/liquid boundary condition, revealed with the inset as strong- and no-slip system on DTS and AF 1600.

previously are summarized in table 4.5. The onset of the bulging regime occurring at t^* and D^* are further discussed in chapter 6. We see that the higher dewetting velocity at thicker regions[7] $v_{\text{peak}}(t)$ gives the smaller the characteristic time when we concentrate on each system separately. In contrast, at equivalent $v_{\text{peak}}(t)$, all characteristic times taken on DTS appear earlier than on AF 1600. This observation remains valid even if v_{peak} is doubled. Consequently, we can state that the rim instability is driven by the dynamics of the moving front and accelerated when slippage is increased.

Concentrating now on characteristic distances, we see that transitions from one regime to another occur at approximately the same dewetted distance on DTS despite tremendous changes in the dewetting dynamics of the polymer front, whose velocity increases from almost two

---

[7]On DTS, the dewetting velocity v decreases with time. As a consequence, values given in table 4.5 high error bars and should be read as indicative data only.

orders of magnitudes from 110 to 130 °C. Distances are used to represent the situation at approximately equivalent volume in the ridge. We can therefore conclude that the rim instability is driven by the geometry of the ridge and, more precisely, the process of droplet detachment is driven by the area of liquid in contact with the ridge. Slippage at the solid/liquid interface takes precedence over the dewetting dynamics on the developing of the rim instability.

Bulges appear on AF 1600 at a distance D_b which is more than twice the distance measured on DTS on equivalent systems. This observation strengthens the idea of a geometry driven rim instability on AF 1600. Moveover, we should note that distances reported for the weak-slip situation vary with temperature, increasing with velocity and with the inverse of viscosity. The latter observation suggests a dependence of the rim instability on viscosity on AF 1600, viscous slowing reported for the Rayleigh-Plateau instability in [23, 99], competing with the dynamics of the three phase contact lime.

Table 4.1: Characteristic times and distances defined in part 4.4 as marking the transition to the onset of the bulging regime (t^*, D^*), the protrusion of bulges (t_b, D_b), fingering (t_f, D_f) and droplet detachment (t_{max}, D_{max}), the later further discussed in chapter 7. Transition times and distances are obtained from a series of experiments performed on DTS or AF 1600 with a PS film of initial thickness H, molecular weight M_w. Changes in the annealing temperature T involve changes in the velocity recorded at the three phase contact line of the thicker region v_{peak}.

substrate	T	H	M_w	t_b	t_f	t_{max}	D_b	D_f	D_{max}	v_{peak}
	°C	nm	kg.mol^{-1}	s	s	s	μm	μm	μm	nm.s^{-1}
DTS	110	115(5)	13.7	4730	8850	12250	26.0	34.5	35.0	3(3)
DTS	120	125(5)	13.7	2460	4440	4800	30.6	39.1	39.1	9(5)
DTS	120	115(5)	13.7	390	1050	1140	16.7	30.4	30.6	33(17)
DTS	130	115(5)	13.7	76	158	194	20.5	28.2	29.2	204(130)
AF 1600	120	125(5)	13.7	9560	–	> 16880	66.0	–	> 107.6	7(1)
AF 1600	120	115(5)	10.3	5900	–	> 7800	95.2	–	> 124.7	17(1)
AF 1600	130	115(5)	10.3	580	–	> 754	82.8	–	> 104.4	140(26)
AF 1600	135	115(5)	10.3	254	–	400	103.0	–	140.0	345(74)
AF 1600	140	115(5)	10.3	159	–	245	125.0	–	172.0	748(173)

At first sight, we might wonder why we are able to record on AF 1600 a distance D_b defined in part 4.4 as the distance where $v_{peak}(t)$ differs from $v_{valley}(t)$. This difference, appearing at large dewetted distance results from a strong shrinkage of the rim width at valley which initiates a more important flow towards peaks and a slight increase of $v_{valley}(t)$. This increase, however, remains small, such as the zigzag length, unlike on DTS. In the later case, we see that the finger length l measured right after the droplet pinches off, $l \sim D_{max_{valley}} - D_{max_{peak}}$, is also independent of the dewetting dynamics and viscosity. To conclude, we know that systems with

high friction at the solid/liquid interface are more subjected to fingering and the finger length on slippery systems is independent of viscosity and the dewetting dynamics.

4.6 Discussion

Method

The Rayleigh-Plateau type instability developing on a growing rim was studied with optical microscopy on two model systems, a newtonian liquid deposited on top of a hydrophized monolayer of alkylsilanes (DTS) and on top of a thin coating of a perfluorinated polymer (AF 1600). Both substrates were selected for their known opposite flow behavior at the solid/liquid interface mimicking two limiting cases in terms of slippage. On the one hand, the strong slip behavior characterized on DTS [42] with a slip length approximating the micron size, much larger than the initially prepared film thickness, approaches the plug-flow situation. On the other hand the weak slip behavior brought to light on AF 1600 [16] models the no-slip situation.

These two types of coating play a major role in the flow properties at the solid/liquid interface, however, changes in the chemistry and of the preparation process of both layers do not interfere with the interpretation of the results. Indeed, Bäumchen et al. discovered that AF 1600 shows similar flow properties than DTS, *i.e.* a strong slip behavior, for dewetting experiments performed with a polymer melt of high molecular weight [16]. Also, other types of silanes layers, *i.e.* OTS a silane with carbonyl length larger than DTS, evidence flow properties in the weak slip conditions, close to AF 1600 when annealed at 130 °C [16, 42]

The rectilinear geometry of the polystyrene film is used to simplify the analogy with the Rayleigh-Plateau instability in the moving film. The low contact angle hysteresis of several degrees only, as indicated in section 3.1.2, reflects the good quality of the system. However, pinning free surfaces are difficult to achieve despite the fact that the optimal preparation conditions limit defects at the three phase contact line. In the case of weak defects and a wiggly contact line no hysteresis is expected [61]. The sinusoidal deformation of the contact line is of low energy [31] which does not perturb the rim instability.

The minimal size of the defect inducing a deformation of the contact line which is strong enough to impact on the rim instability is hard to predict. Ondarcuhu and Veyssie reported that pinning happens for inhomogeneities larger than the radius of gyration of the polymer melt used [92]. This type of experiments should however consider the flow at the solid/liquid interface. Gutfreund et al. evidenced a depletion layer between the film and the DTS layer suggesting a conformational rearranging of polystyrene molecules in the vicinity of the substrate. For the

system PS/AF 1600, Bäumchen et al. reported a lowering of the entanglement density of high molecular weight PS approaching the substrate in the strong slip situation. Consequently, the minimal defect size should be a quantity dependent of the slip-length recorded on the substrate; slippery substrates are more sensitive to pinning.

Rim instability

At elevated temperature, the displacement of the moving front follows a growth law $D \propto t^{\alpha}$, with $\alpha = 1$ for the no-slip boundary condition and the $\alpha = 2/3$ for the plug-flow situation as detailed in section 2.4.1. α approximating 0.7 when the polymer front retracts from DTS and 0.9 from AF 1600 is rapid and reliable method used to determine whether we deal with the strong slip (DTS) or no or weak slip cases (AF 1600). However, the main drawback of this method is the lack of information on the actual value for the slip length. Bäumchen showed that $\alpha = 0.9$ is observed for a slip length, calculated from the hole growth analysis, ranging from approximately 10-100 nm; for $\alpha = 0.7$, values spread from the micron up to more than two orders of magnitude larger[13, 19]. Quantitative values of the slip length are therefore necessary and provided in chapter 5 using the rim profile analysis.

With dewetting experiments of nucleated holes, Fetzer and Jacobs assured that the power law is followed for hole radii up to $20\,\mu$m on DTS [39]. On AF 1600, hole radii reach without deviation of the law is $35\,\mu$m [13]. In our situation, despite the faster accumulation of polymer per unit length for the geometry of the straight fronts (see chapter 9 for further discussions), the distance achieved before experimental measurements of $D_{\mathrm{peak}}(t)$ and $D_{\mathrm{valley}}(t)$ deviates from the algebraic law at approximately $30\,\mu$m for DTS and 80-90 μm on AF 1600. The dissipation model remains valid as long as D reaches a threshold value which roughly corresponds to the length at which bulges are observed with optical microscopy D_{b}. Consequently, the flow in $xy-$direction observed at D^* with reduction of rim width does not impact on the dynamics of the moving front; the flow is homogeneously distributed along the ridge.

Inhomogeneities of the flow velocity along the contact line begins on DTS right after D_{b}. If slippage at the solid/liquid boundary is high, the contribution of the rim width on the dewetting velocity ($v(t) \propto W^{-1}(t)$) leads to a rapid increase of the gradient of velocity measured between thicker and thinner regions.

The transverse strong asymmetry of bulges observed on DTS, see for instance Fig. 4.3(a), is in total agreement with the theory introduced in section 2.5.2, whose non linear dynamics predict a strong perturbation of the 'dry' side of the rim whereas the 'wet' side remains flat [67, 85] in the strong slip situation. Running numerical simulations with a sinusoidal perturbation with a fixed wavenumber results in the protrusion of the bulge into finger. Experimentally, we also observe undulations of the contact line of the ridge combined with a flat back side of the ridge.

The continuous growth of the wavelength involves coarsening which hinders lateral expansion of the bulge caused by transversal flow of a bulge merging with other neighboring bulges. As a consequence, it is clear to note that the protrusion of bulges starts when the wavelength approaches λ_{max}. The distance between bulges becomes large enough to enable stretching of the bulge enabled thanks to the reduced coarsening rate[8]. In other words, the flow in the dewetting direction overcomes the lateral flow.

The elongation of the neck ends with a droplet pinching-off the finger, whose length is unaltered by the experimenting conditions. Neither the flow dynamics, nor the viscosity impacts on the final finger length and on the distance of droplet detachment D_{max}. All four stages of the rim instability in the strong slip situation are intrinsic to the boundary conditions at the solid/liquid interface, proportional to the area of the ridge in contact with the substrate. The flow modified by slippage in the vicinity of the substrate leads to extreme changes with the evolution of the rim instability.

As for DTS, the morphology of bulges obtained on AF 1600 is in complete agreement with numerical simulations: the rim instability develops symmetrically along the ridge, similarly to the varicose mode. Since the dissipation mechanism is almost purely viscous for this system, local changes in rim width for distances above D_{b} do not lead to substantial changes in dewetting velocity recorded at the contact line. Thicker regions remain aligned with thinner regions, no finger is formed.

The rim instability is observed $D_{\mathrm{b}} \approx 60\,\mu$m on AF 1600 (Fig. 4.1); much later than in the strong slip situation, where the whole process starts around $20\,\mu$m and ends below $60\,\mu$m. According to the fact that the rim instability is of Rayleigh-Plateau type, the growth of the perturbation is a feature intrinsic to the geometry of the ridge. Consequently, it is reasonable to assume that the growth of the rim instability at small distances is not captured with optical images due to the lack of resolution of this technique. Further investigations are required with a finer technique to understand the behavior of the ridge in this range. Results obtained with atomic force microscopy are presented in chapter 6.

Fig. 4.7 depicts the transition of bulges and the detachment of droplets, characteristic distances represented by D_{b} and D_{max} and with values listed in table 4.5, for viscosities of the melt varying from four orders of magnitude. As explained above, characteristic lengths measured on DTS are solely dependent of the area of polymer in contact with the substrate and independent of the experimenting conditions at fixed initial film thickness. A change of viscosity induced by the change in temperature do not impact on these lengths. In contrast, on AF 1600, we observe a dependence of viscosity on D_{b} which is explained in chapter 6.

---

[8]The spatial evolution of the wavelength, discussed in section 6.1, evolves at $\lambda \propto \sqrt{D}$. The spatial derivative $\lambda'(D)$ results in an evolution of the wavelength at high rate for small D and deceases with increasing D.

Due to the absence of finger for the PS/AF 1600 system, the droplet detachment occurs at a much larger distance D_{max} than on DTS. A different mechanism should therefore be considered for each system as discussed in chapter 7.
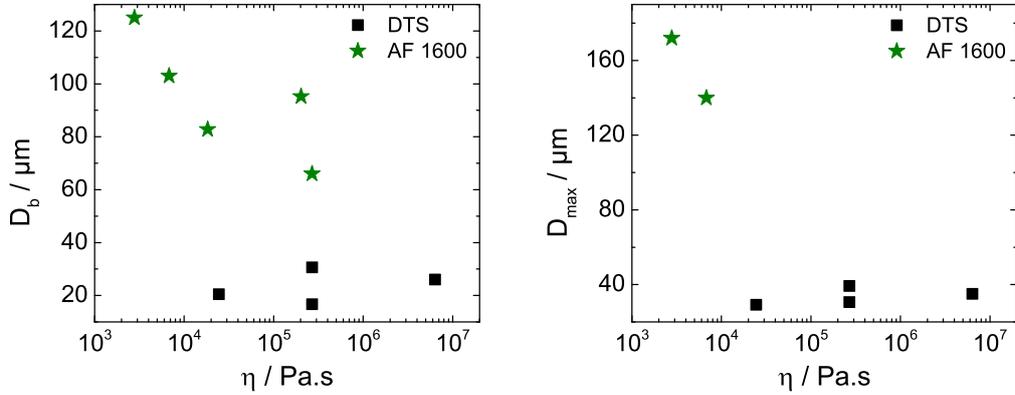
Figure 4.7: Characteristic distances plotted for the transition leading to the bulging regime (a) and to the droplet detachment (b) as a function of viscosity evidence two types of evolution with viscosity on DTS and AF 1600. Details of the system are given in table 4.5.

Litterature

The rim instability was analyzed in this chapter with dewetting experiments of a polymer melt flowing under newtonian conditions. The change of the substrate evidenced the impact of slippage on the formation of fingers which is possible to observe with a simple qualitative comparison performed with optical microscopy, as displayed in Fig. 4.1. The reasons of the genesis and the formation of fingers is still under debate in the litterature. The first theoretical and experimental approach published by Brochard-Wyart and Redon mentioned the difficulty to determine the onset of instability [8]. They observed perturbations in the rim without capturing the phenomenon of fingering with experiments performed in the no-slip conditions. This observation strengthens the fact that the rim instability develops on AF 1600 at early stage although the resolution of optical microscopy is to low to capture this effect.

Focusing on high molecular weight polymers, Gabriele et al. defined the onset of instability as the transition where fingering starts. The latter process initiated after disentanglment of polymer chains. This statement contradicts previous observations showing no finger, but the instability growing on the rim via the presence of successive wider and narrower regions of rim at the moving front. In our situation, the molecular weight of polymers we used are such as the viscoelastic effects are absent. Combining the last two remarks with results obtained with our experiments, we can first conclude that the rim instability develops before fingering starts, the definition of onset of instability given by Gabriele et al. [44] should be revised in onset

of bulges or onset of fingering as denoted in section 4.4. Second, our setup strongly indicates that the main factor inducing fingering is slippage. According to de Gennes' reptation model, slip length b scales with the size of the polymer as $b \propto N^3$, with N the number of monomers [29]. Using large molecules, it is impossible for Gabriele et al. to distinguish purely viscoelastic effects from effects induced by slippage with the setup used. In contrast, Bäumchen et al. managed with carefully selected experiments performed on AF 1600 to prove a growth of slip length with molecular weight above the entanglement length [17]. Flows at Weissenberg numbers lower than unity used for this setup allow to eliminate viscoelatic effects during the experiments. using the same setup, Haefner recently confirmed the presence of fingers for large molecular weight [53]. For a film prepared with polymer PS101k, the slip length being several times the film thickness in this case, Haefner pictured a situation similar to DTS on Fig. 4.1, which proves that slippage causes fingering.

The transition from bulge to finger appears at a stage where the balance between dissipative forces and driving forces varies locally. Friction at the solid/liquid interface of thinner parts of the ridge decreases with shrinkage of the rim. For strongly slippery systems, the contribution of the rim width W on the velocity discussed in part 2.4.2, $v_s(t) \propto W^{-1}(t)$, leads to a gradient of velocity along the ridge.

However, this decrease of rim width is counterbalanced by a transverse flow due the merging of bulges due to the increase of the wavelength in a given length. Coarsening acts on the slowing down of the growth of the ratio of rim width between thicker and thinner regions. The local gradient of dewetting velocities takes off after the spatial growth of the wavelength $\lambda(D)$ decreases as discussed in part 6.

The transition bulge to finger is determined by the protrusion of thicker part of the ridge opposite to the dewetting direction. Gabriele et al. characterized this start normalizing the length $L(t)$ of the contact line with the initial length of the front before dewetting [43]. This technique proposes a rapid way to set the transition, however, the value of the ratio recorded does not allow to compare series. Due to the temporal growth of the wavelength, we observe variations of the number of fingers per given length which are not taken into account in the calculations. In contrast, the zigzag length x_{pv} depicted in Fig. 4.5c has the advantage to be independent on the number of fingers and allows to average length over the length.

4.7 Summary

- As polymer accumulates in the rim at the three phase contact line, a Rayleigh-Plateau type instability develops at the liquid/air interface, the so-called rim instability.

- The rim instability rises as a varicose mode on AF 1600, *i.e.* thicker and thinner regions grow symmetrically along the y-axis. An asymmetrical growth of the instability, zigzag or peristaltic mode, is observed on DTS.

- From the early beginning of dewetting until the droplet pinches-off the ridge, the rim instability passes through four regimes on DTS whose transitions are marked as the onset of the bulging regime, the protrusion of bulges and fingering.

- No fingering is observed on AF 1600. DTS and AF 1600 are know from previous studies to behave as strong-slip and no-slip substrates for the system investigated for these experiments (M_{w} below the critical value of entanglement effects). The occurrence of fingering is intrinsically bound to slippage.

- A continuous growth of the wavelength, lateral distance between successive peaks, is observed on AF 1600. Thicker part of the ridge coalesce during the rise of the rim instability.

- Variations of temperature for the dewetting experiments impacts on the dewetting dynamics and the viscosity of the system. Characteristic times recorded at each transition from one regime to another vary with the dynamics, however, characteristic distances remain unchanged (within experimental errors) on DTS.

- Viscosity impacts on the characteristic distance on AF 1600.

5 Characteristics of the rim shape in presence of the rim instability

The interaction between the substrate and polymer melts plays not only a significant role on the dynamics of the flow or the morphology of the rim, as developed in the previous chapter, but also on the shape of the rim. The impact of slippage on the later was agreed from an experimental point of view [18, 40] and a theoretical point of view [86] to affect the back side of the rim. Monotonically and oscillatory profiles are observed for a limited distance traveled from the three phase contact line. The nature of experiments involving the study of the rim instability requires a knowledge of features of the ridge for very thick rims, *i.e.* at large distance traveled by the three phase contact line. In this chapter, we extend the range investigated for features found in the instability. We first describe the growth of the ridge observed macroscopically and the local evolution of the rim width and height. We then concentrate on the part of the rim plunging into the film, the tail, and extract the slip length using the rim profile analysis as described in [18]. Features of the rim decay are then investigated for both substrates. Finally a correlation is made between the local variations of the rim shape and the instability evolving along the ridge.

5.1 Macroscopic observation of cross-sections

Fig. 5.1(a) depicts a part of the dewetting straight front retracting from a distance D of $3\,\mu$m into the 110 nm thick polymer film. The temperature of the $10.3\,$kg.mol^{-1} PS layer was elevated to $120\,^{\circ}$C for a given time t before quenching to $90\,^{\circ}$C. The latter action enables to picture the ridge with atomic force microcopy (AFM) in the steady state. The temperature decrease only involves a slight decrease of the volume in the ridge due to the negative expansion coefficient which induces an error mainly in the measurement of the dewetted distance[1] D lower than $1\,\%$, which is overtaken by the experimental error of the system estimated around $5\,\%$.

---

[1] Dewetted distances are calculated from the volume of polymer accumulated in the ridge. The slight reduction of the volume induced by quenching will therefore play a role on D. The rim width is also slightly affected by the temperature lowering, however, measurements such as the amplitude and the wavelength of the perturbation, discussed in chapter 6, are not affected by quenching since freezing the system acts on the relative position of both thinner and thicker regions and does not involves displacement of the ridge.

(a) AFM image of a ridge on AF 1600 at $D \sim 14\,\mu$m, scan size $25 \times 8\,\mu$m^2.

(b) Rim profiles plotted in a 1/1 aspect ratio are selected to represent the early stage of the rim instability and the bulging regime.
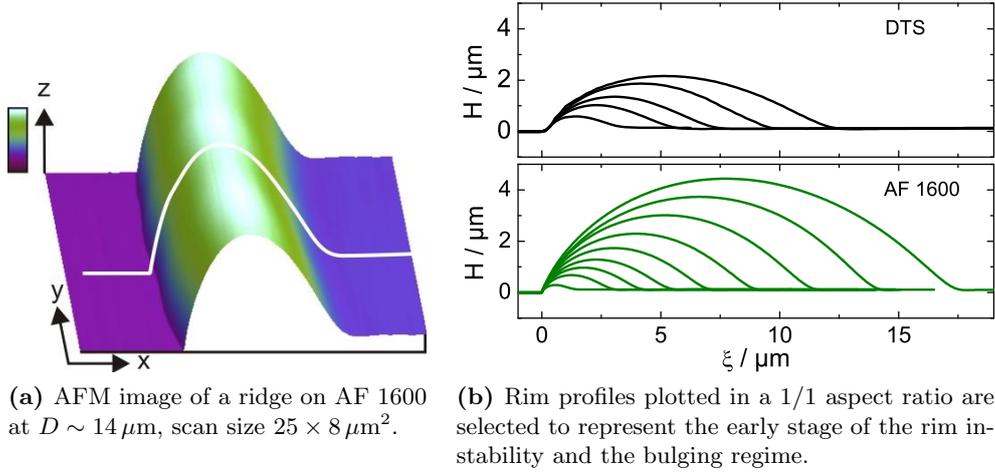
Figure 5.1: Material retracting from the three phase contact line $\xi = 0$ accumulates in a ridge rounded by the Laplace pressure. The 3D representation (a) evidences small undulations due to the rim instability. The while solid line represent a cross-section of the ridge, a rim profile, the corresponding bidimensional representation of the ridge in xz-direction. Growing rim profiles with $D(t)$ are superimposed (b) for the DTS (top) and AF 1600 systems (bottom). A semi-spherical is evidenced on both systems: PS(10.3k) film, $H = 115(5)$ nm at $120\,^\circ$C.

The use of Tapping-Mode$^{\text{TM}}$, a non-destructive technique, to scan the ridge allows to continuously follow the course of dewetting as if *in situ* experiments were performed. Characteristic features of the rim such as the rim profile, the self affine growth of the rim, discussed in the coming sections, are conserved either for DTS [38, 39] or for AF 1600 [13]. A great advantage of this technique is the high resolution for a height of few microns and lateral distances over $100\,\mu$m.

The solid line drawn in Fig. 5.1(a) represents the cross section of the ridge at the time and corresponding distance experiments were paused. A series of cross sections depicted in Fig. 5.1(b) are extracted from the image picture of same ridge at various experimenting time and distance chosen from the early beginning to the stage before the onset of fingering. The dewetting distance ranges from 12 to $42\,\mu$m for DTS (top) and from 1 to $101\,\mu$m for AF 1600 (bottom) as detailed in the footnote^2.

The occurring of dewetting clearly shows an accumulation of polymer into the rim. The 1 to 1 aspect ratio chosen for Fig. 5.1(b) evidences the small size of the film compared to the ridge. The film remains unperturbed until the ridge broadens and comes in contact to it. As a consequence, we can neglect the film and concentrate discussions on the evolution of the ridge; the system is considered as a semi-cylinder growing along the three phase contact line and moving

---

^{2}Each cross section is taken near the peak at 120 s (12 μm), 480 s (21 μm), 840 s (29 μm), 1080 s (37 μm) and 1320 s (42 μm) for DTS and 30 s (1 μm), 900 s (9 μm), 3210 s (19 μm), 8530 s (40 μm), 10630 s (50 μm), 14230 s (59 μm), 17830 s (78 μm), 21429 s (85 μm), 26250 s (101 μm) for AF 1600.

perpendicular to it into the film. This vision enables a direct comparison of the rim instability with the Rayleigh-Plateau instability.

Looking at the rim shape in the scaling provided in Fig. 5.1(b) stresses on the similarity of profiles at comparable rim height between both systems. However, a close loop at the side of the rim directly in contact with the unperturbed film, also named the tail or 'wet' side of the rim highlighted in the inset, evidences that the decay occurs on DTS either monotonically or with the presence of an oscillation dipping below the film thickness.

5.2 Long term evolution of the rim

5.2.1 Impact of slippage on the rim shape

The representation used in Fig. 5.2 emphasizes the presence of the oscillation in the back tail of the film using the absolute value of the difference between local film height $h(x,t)$ and the film thickness H. A trough appears clearly via the formation of dip for ξ larger than $5\,\mu$m. Setting the reference at the three phase contact line ($\xi = 0\,\mu$m), the comoving frame represented for the system PS on DTS at $110\,°$C, we clearly see that a transition from monotonic to oscillatory profile occurs when the front traveled a distance larger than $13\,\mu$m. This transition assures that the polymer melt slips on top of the DTS substrate.

Indeed, the slip contribution of the dewetting dynamics presented in part 2.4.2 leads to a dewetting velocity $v_{\rm s}$ which is inversely proportional to the rim width: $v_s = \frac{1}{3}\frac{|S|}{\eta}\frac{b}{w}$. Assuming that the slip length is constant for the range of D observed, the only variable in this equation, the rim width W, grows as a square root of the dewetted distance D as discussed in the previous part. As a direct consequence, the capillary number $Ca = \frac{\eta v}{\gamma}$, with v the dewetting velocity of the system, decreases. The rim passes from the monotonic profile to the oscillatory profile in the course of dewetting as predicted theoretically [40] and demonstrated experimentally [41].

A second dip appears at $D = 24\,\mu$m in Fig. 5.2(a) as material further collects into the rim. The dimensional view of the cross section of the rim at the given D, dashed curve superimposed with the red curve , shows that the origin of this second dip is the second part of the oscillation which crosses the unperturbed film thickness H, which eases the measure of the width of the trough. This dip does not stand for the second wave which is predicted in numerical simulations [40]. The latter oscillation takes place at a distance which is few orders of magnitude lower than the original one. Experimentally, this second oscillation is hardly possible to be observed. We reach the experimental limitations of the system: the roughness of the film becomes as high as the deepness of the trough and very difficult to observe.
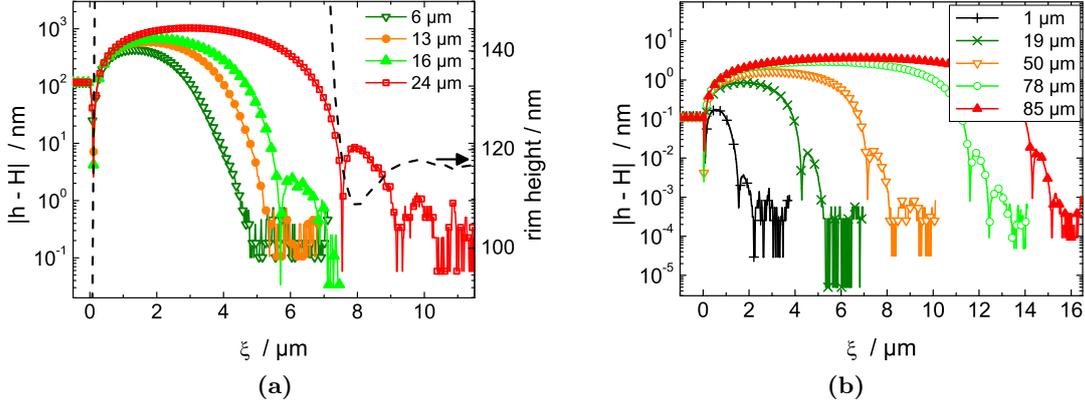
Figure 5.2: (a)-(b) Rim profiles of straight fronts of a $H = 115(5)\,\text{nm}$ thick PS(10.3K) film on DTS at $110\,°\text{C}$ (a) and AF 1600 at $120\,°\text{C}$ (b). A single bulge was scanned with atomic force microscopy upon various distances traveled by the front D displayed in the top right corner of each figure. The semi-logarithmic representation of $|h - H|$ shows the transition from a monotonely decaying tail to an oscillatory decay on DTS (a) where an oscillatory decay is observed for the whole dewetting process on AF 1600. The dashed curve (a) provides a direct comparison of the rim profile with the representation of $|h - H|$. The second oscillation observed in curves stands for a new value were $h = H$, no second oscillation observed in numerical simulations.

On AF 1600, we observe oscillations as early as for $D = 1\,\mu\text{m}$, the rim profile reaches the oscillatory regime at early stage of dewetting. This observation, in complete agreement with the theory based on the lubrication model detailed in section 2.4.3, results from the lower dewetting velocity recorded on the AF 1600 system compared to DTS together with the much lower slip length to film height ratio expected for this system, discussed in the next section. The damped oscillation is merged with the roughness of the film as soon as the height of the trough reaches back the film thickness for $D = 1\,\mu\text{m}$. At later stage, the second dip appears more clearer, the roughness of the film is shifted towards the film. We can ensure from this observation that the cross sectional flow is perturbed up to larger extend as dewetting proceeds. The depth of the trough and its width are probably proportional to the rim height as highlighted in [110].

5.2.2 Evolution of slip length, capillary number at late stage of dewetting

Thanks to the rim profile analysis introduced in section 2.4.3, we assert the slip length and the capillary number applying an appropriate fit function to the wet side of the rim, including the unperturbed film. From the damped oscillation δ_{osc} used for oscillatory profiles and the superposition of two exponential decays δ_{mon} for monotonic profiles, we obtain a value of the two parameters k_1 and k_2 directly from δ_{mon} and indirectly from δ_{osc}, see details in introduc-

tion, which are used to independently determine the slip length and the capillary number as follows:

$$b = \frac{1}{4H} \frac{k_1^2 + k_1 k_2 + k_2^2}{k_1^2 k_2^2} - \frac{H}{2} \qquad Ca = -\frac{H}{4} \frac{k_1^2 + k_1 k_2 + k_2^2}{k_1 k_2} + \frac{H^3}{6} \frac{k_1^2 k_2^2}{k_1 + k_2}$$

As a result, we see on Fig. 5.3(a) that slip lengths found on each series performed on AF 1600 are the lowest and much smaller than the initial film thickness H. Low capillary numbers are also recorded for these series. The region where points are located clearly shows that oscillatory profiles only are expected for this systems. As a proof that $k_{1,2}$ provides solutions which are physically possible, we calculate the viscosity from the capillary number $Ca = \frac{\eta v}{\gamma}$. The dewetting velocity v is averaged from the $D(t)$ curves obtained with atomic force microscopy[3]. Viscosity data calculated from the capillary number provided for various temperatures on AF 1600 in Fig. 5.3(b) are in complete agreement with bulk viscosity obtained from rheometry measurements. This ensures the excellent reliability of this method to extract the slip length and capillary number independently.

The same is true for experiments performed on DTS after the rim turns to be oscillatory. The quality of results is such that a good match is found between the bulk viscosity and viscosity resulting from the fit of rim profiles scanned on DTS. Values of slip lengths measured with the $k_{1,2}$ can therefore be considered as reliable.

The range of slip lengths recorded on DTS varies from 2 to 8 times the film thickness from one series to another. This range, which can be appraised on Fig. 5.3(a), is explained by two phenomenon. On one hand, the slip length difference visualized between experiments performed at 110 and 125 °C originates from a temperature dependence evidenced by Fetzer et al. [41]: b doubles if the temperature is reduced from 15 °C. This explanation, however do not stand for the series performed at 120 °C, showing a slip length approximately three time higher compared to the value found at 110 °C. We must look into details of the characterization of the DTS wafers given in chapter 3 which evidence that two types of systems are indeed used. Experiments run at 120 °C were performed on a substrate, termed DTS$_I$, hydrophobized anteriorly to experiments run at 110 and 125 °C whose substrate is denoted DTS$_{II}$. The consequence is that friction at the solid/liquid interface differs from one system to another and leads to a higher slip length for DTS_I. The mechanism explaining the variation of slip length with preparation is not completely clear and under investigation.

Looking at each series individually, values of the ratio b/H are much narrower. In contrast the capillary number, starting around 0.5 at early stage of dewetting for experiments performed at 110 and 120 °C, decreases drastically down to 0.1 passing through the monotonic to oscil-

---

[3]On part 3.4.1 we show that $D(t)$ curves are as reliable when D is evaluated from atomic force microscopy than for optical microscopy.

latory transition line, solid line in Fig. 5.3(a), representing solutions of the Taylor expanded Stokes model. Since experimenting conditions such as viscosity η and surface tension γ of the polymer are kept unchanged for the course of dewetting, the decrease of the capillary number $Ca = \eta v/\gamma$ is caused by the decrease of the dewetting velocity, the contribution of slippage the dewetting velocity, v_s introduced in part 2.4.2, is inversely proportional to the rim width. The growth of the latter contributes to the overall lowering of the dewetting dynamics at the three phase contact line.

The evolution of the ratio b/H depicted in Fig. 5.3(c) the fact that the slip length remains rather constant within scatter for the whole range of dewetting. The transition of the rim profile observed on DTS in Fig. 5.2(a) is solely related to the reduction of the capillary number via v and is an intrinsic feature of the dewetting dynamics. The flow at the solid/liquid interface follows a constant profile normal to the substrate over D. This latter point is clearly demonstrated in the region where oscillatory profiles are found since the capillary number and the slip length are calculated independently from each other. When profiles decay monotonically, two exponential decay are sometimes difficult to find. In the latter case the second parameter k_2 is calculated using the experimental capillary number based on the dewetting velocity calculated at D_i from the $D(t)$ curves and the viscosity evaluated from the WLF theory. The accuracy of this technique is sufficient to provide reliable values of slip length which we can compare with values obtained in the other region of oscillatory profiles, however, errors are broader for monotonic profiles due to the error of the dewetting velocity introduced in the technique. As a consequence, the value $b/H \approx 4$ observed at $Ca \approx 0.4$ on DTS at $120\,^{\circ}\text{C}$ does not compromises the integrity of the results, but should be treated with larger uncertainty.

We should note, however, that the difference of slip length recorded between both DTS substrates is not very large. Error bars, calculated from the law of propagation of error, are in the order of $20\,\%$ and undisplayed in Fig. 5.3(a) for clarity. With error bars, the difference between each DTS series is not as straightforward. Independently of the type of DTS used, the ratio b/H is always much larger compared to AF 1600, on which the ratio is much lower than unity. The variation between both DTS wafers won't affect the comparison between AF 1600 and DTS and will therefore be neglected for the study of the rim instability.

5.3 Growth of the ridge: dynamics at long term

We now discuss the impact of the rim instability on the evolution of the ridge. We first deal with the evolution of the growing rim before we investigate local variations of the rim width observed along the ridge. We compare the situation of the perturbed instability to the unperturbed one, an important point to verify the applicability of the theory of the Rayleigh-

(a) Capillary number Ca versus the slip length b to film thickness H ratio. The solid line represents the transition from monotonic rims (top) to oscillatory rims (bottom).

(b) Viscosity η calculated from the RPA as a function of temperature are compared to the WLF equation.

(c) Evolution of the slip length b as a function of distance D. Despite large fluctuations on DTS, we can consider the slip length constant during the course of dewetting.

Figure 5.3: Slip length calculated using the rim profile analysis (RPA) for all series studied with AFM. (a) A monotonic decay of the rim profile (open symbols) is first observed on DTS as predicted in theory. As Ca decreases for one series, *i.e.* the velocity, profiles turn oscillatory (see Fig. 5.1) crossing the third-order Taylor expanded Stokes limit. (b) Reliable slip-lengths obtained with the RPA are cross-proofed with the good agreement obtained between between the viscosity values extracted from the analysis and the WLF-equation. (c) Large distances traveled by the moving front do not affect the slip-length in either system studied, PS(10.3K), $H = 115(5)$ nm.

Plateau instability to moving cylinders. We finally concentrate on the dynamical aspects of the growth of the rim widths.

5.3.1 Self affine growth of the rim

Fig. 5.4(a) illustrates the growth of the rim width as a function of the rim height h^{max} measured at the apex of the ridge. The linearity of $W(h_{\mathrm{max}})$ with a slope of 3.7(3) obtained for the PS/AF 1600 system at various temperatures asserts from the self affine growth of the rim. This observation is in good agreement with the *in situ* experiments performed for a hole growing from a self-assembled [39] or spin-coated [13] hydrophobic layers. In the latter case, a slope of 3.75(6) was found for a rim width reaching up to 3 μm. A slope approximating 4 is found experimentally in DTS.

Despite local variations in the geometry of the rim happening along the ridge, the self-similar growth is valid during the whole course of dewetting and while the rim instability develops in regime I and II. The self-similar growth taking place at peaks or at valleys for a rim width as large as 20 μm is also a proof that the definition chosen for the rim width[4] is appropriate for further discussions.

---

[4]The rim width is defined as the length measured with the x-direction starting from the three phase contact line to the point where the 'wet' side of the rim reaches the 110 % of the initial film thickness.

(a) Rim width W versus rim height H of the ridge measured at peak and valley (filled and open symbols).

(b) Spatial growth of the rim width $W(D)$ comparing experimental with theoretical values at $120\,°C$ on AF 1600.

(c) Mean rim width W_0 quantified for all series on AF 1600. The solid line represent $W \propto \sqrt{D}$.
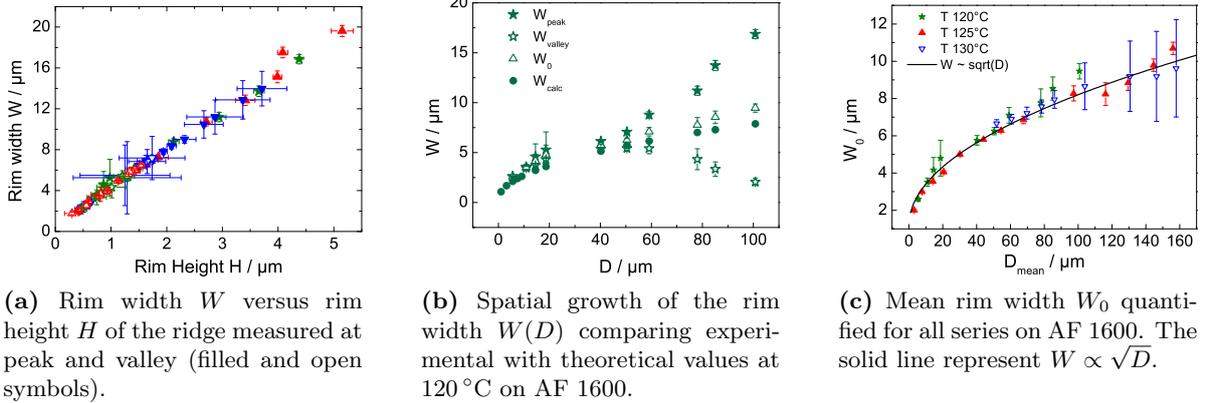
Figure 5.4: Quantifying the rim width W, (a) the linear behavior of $W(H)$ proves the self affine growth of the rim. The rim instability does not perturb the constant of proportionality. (b) Local discrepancies were observed on the evolution of $W(D)$ at peak compare to valley. The mean value $W_0(D)$, however, goes along W_{calc}, the theoretical width of an unperturbed ridge of volume V_i similar to the volume of the moving ridge at D_i. (c) W_0 is therefore a reliable value to determine the growth law of the rim width, proportional to $\sqrt{D}$. The system used is a PS(10.3K) film of 115(5) nm height at $120\text{-}130\,°C$.

5.3.2 Local evolution of the rim at different parts of the ridge

The sequence of thicker and thinner regions, peaks and valleys, rising along the ridge builds up in two stages as depicted in Fig. 5.4(b). In first instance, a broadening of the ridge is observed independently of the local position we look at. The difference between the rim width at peak and valley ΔW is small compared to the increasing averaged rim width $W(D)$. A second stage is characterized by the decrease of the rim width at valley happening at $W(D^*)$ [5] for a distance of approximately $50\,\mu m$ traveled by the dewetting front. Shrinkage of $W_v(D)$ generates a more significant flow due to the higher pressure found in the depleted zone. ΔW becomes rapidly larger than W_v.

Fig. 5.4(b) illustrates the evolution of the rim width of a PS front retracting from AF 1600, which implies that the rim instability develops as a varicose mode, *i.e.* symmetrical to the y-axis. We can consequently assume based on the conservation of volume, the self-affine growth of the ridge at any place of the ridge and on the fact that no fingering is observed on AF 1600, that the larger flow initiated above D^* is integrally retrieves transversally, from peak to valley. In the case of DTS, the second stage is followed by a drastic increase in the growth of the rim width at peak, described in section 4.4 as the onset of the fingering regime.

The presence of local transversal variations of the rim width renders the study of the rim instability in chapter 6 complicated to interpret. In order to provide a base state to discuss

---

[5]More details on $W(D^*)$ are given in section 6.3.2

the impact of slippage on the Rayleigh-Plateau instability rising along the ridge, we introduce the **mean rim width**, denoted W in Fig. 5.4(b), as the average between peak and valley $W(D) = (\overline{W_{\mathrm{p}}} + \overline{W_{\mathrm{v}}})/2$. W has no true physical meaning while the ridge is in motion, but aims to consider the ridge as if unperturbed by the rim instability.

In order to confirm that W is a reliable approximation for mean rim width, we compare $W(D)$ to W_0, the rim width of a supported unperturbed semi-cylinder. The volume of the semi-cylinder equals the volume accumulated in the ridge, $V_{\mathrm{acc}}(D)$, used to determine the distance D traveled by the liquid front, detailed in part 3.4.1, and the volume of polymer which did not traveled, *i.e.* planar area of the accumulated part times the film thickness. Using the contact angle of the polymer at equilibrium θ_{Y}. Knowing the contact angle θ_Y, we can extract the width W_0 and the height H_0^{max} of the cylinder. The good match found between open triangles and filled circles in Fig. 5.4(b) is a proof of the good agreement between W_0 and W_{mean}. The deviation observed for large D is explained by the fact that the ridge is not a perfect semi-cylinder, but the tail of the ridge plunges in the unperturbed film. Consequently, the mean rim width is a good approximation to compare the Rayleigh-Plateau instability of an unperturbed cylinder.

5.3.3 Dynamics of the rim

Fig. 5.4(c) depicts the spatial evolution of the mean rim width for a PS film retracting from AF 1600 at three different temperatures varying from 120 to 130 °C. The good agreement between all series proves that the growth $W(D)$ is solely governed by the displacement of the three phase contact line. Changes in dynamics of the retracting front and in viscosity induced by temperature do not intervene in the accumulation process of polymer into the ridge which is only governed by the displacement of the three-phase contact line. $W(D)$ follows the same law found by Fetzer and Jacobs for the radial geometry [39]

$$W(D) = C_{\mathrm{s}}\sqrt{hD}. \tag{5.1}$$

The constant C_{s} depends on geometrical aspects of the system depending on the contact angle of the PS front and on the dynamics of the uptake of material.

As a result of a linear fit applied to the squared equation 5.1, the solid line demonstrates a congruity with the previous equation: $W = 0.86(5)\sqrt{D}$. The resulting coefficient, averaged for various series in the range of temperature, gives for straight fronts $C_{\mathrm{s}} = 2.6(3)$ which is close to the value Fetzer and Bäumchen obtained investigating the radial geometry, $C_s = 2.1(1)$ for DTS [38] and for AF 1600 [13]. The first possible way to explain the deviation observed between both types of geometry is to suggest that the definition of the mean rim width, average of the

rim width over the whole ridge, leads to large error bars for large D caused by undulations present in the systems. The deviation can also come from the different geometry used. The linear geometry induces a faster volume uptake at comparable dewetted distance as discussed in chapter 9.

5.4 Characteristics of the rim under slip conditions

The flow profile observed at a finite distance of the tail of a rim was proved to change from a monotonic decay if a system with strong slip is used to an oscillatory decay if the extent of the slip length is lower than the film thickness see section 2.4.3. We showed for straight fronts in section 5.2 that the transition from monotonic to oscillatory profiles occurs on the DTS system when the distance D traveled by the liquid front increases, a phenomenon solely initiated for strong slip systems by the thickening of the rim width which provokes a decrease of the dynamics of dewetting v and consequently a decrease of the capillary number Ca.

The rim instability on the PS/DTS system is the ideal system to combine both conditions, strong slippage and local variations of the capillary number, to present the monotonic and the oscillatory profile in one frame. The fingering regime discussed in section 4.4 enables a local gradient of the rim width which enables a large difference of capillary numbers calculated between thicker and thinner parts resulting from local changes in the velocity of the moving front $v \propto W^{-1}$. As a result, a trough in the tail of the rim is observed for DTS at the thicker parts of the ridge, orange zone in Fig. 5.5(a), whereas a monotonic decay is expected anywhere else. Fig. 5.5(c) depicts three cross sections of the rim for various position represented by the three colored lines added to the three dimensional representation[6]. ξ representing the distance from the three phase contact line, the close loop at the tail of the ridge confirms the monotonic decay for the thin rim, black curve, plunging into the film at $\xi \approx 3\,\mu$m. Note that the value of ξ where the tail reaches the film thickness approximates the rim width. The cross-section was cut right after the section reaches the flat film for clarity purpose. When D approaches $28\,\mu$m, a small trough is identified for a rim width reaching $4\,\mu$m and becomes larger for $8\,\mu$m.

In contrast, the color scale used for this snapshot emphasizes the continuous presence of the trough along the ridge on AF 1600, darker zone at the back of the rim in Fig. 5.5(c). An oscillatory profile is found independently of the rim width. The three cross-sections depicted in Fig. 5.5(d) confirm that the trough is observed whether the tail of the rim reaches the film at 2 or $16\,\mu$m. We should finally note that the late stage of dewetting, selected on AF 1600 to compare rim width similar to the DTS situation, requires to tune scanning parameters to extreme conditions mainly due to the fact that the limit of the instrument are reached.

---

[6]Red was interchanged with purple to emphasize visibility with contrast enhancement
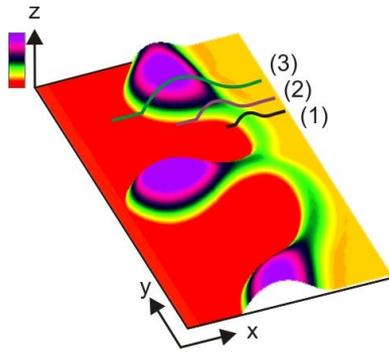
(a) Rim instability at late stage on DTS. AFM scan size $37 \times 20 \, \mu\mathrm{m}^2$.
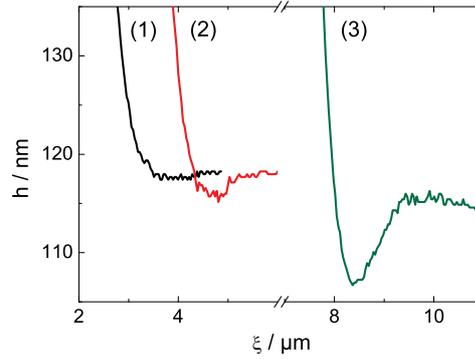
(b) Rim instability at late stage on AF 1600. AFM scan size $37 \times 23 \, \mu\mathrm{m}^2$.

(c) Zoom-in at tails of rim profiles (1)-(3) depicted from DTS (a).
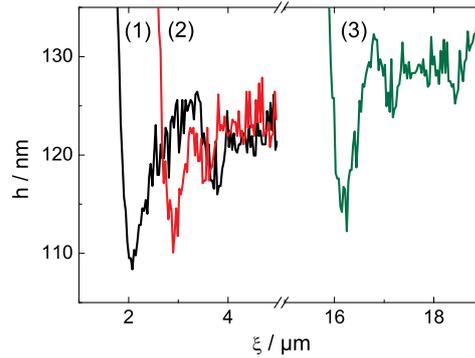
(d) Zoom-in at tails of rim profiles (1)-(3) depicted from AF 1600 (b).

Figure 5.5: AFM image of the ridge displayed at later stage of the rim instability. The mean distance traveled by the front is $D \sim 29 \, \mu\mathrm{m}$ on DTS (a) and $D \sim 100 \, \mu\mathrm{m}$ on AF 1600 (b). The darker zone at back side of the ridge illustrates the presence of a depletion area standing for an oscillatory profile. The three cross-sections depicted as the colored continuous lines from a smaller to a larger rim height (1)-(3) evidence the presence of monotonic and oscillatory rims on DTS (c) and solely oscillatory rims on AF 1600 (d). A 115(5) nm thick PS(10.3K) film was used on DTS at 110 °C and AF 1600 at 120 °C.

Consequently, the roughness recorded on unperturbed film are larger on Fig. 5.5(d) than on Fig. 5.5(c). Finally, the large distance $D \sim 100\,\mu$m selected to compare the rim width of similar size for both systems doesn't change the results; an oscillatory profile is observed for small D on AF 1600.

5.5 Discussion

A detailed understanding of the rim shape for dewetting holes was first investigated experimentally by Seemann et al. for the system PS/OTS [110]. An oscillatory shape was evidenced for the dewetting of a low molecular weight PS films (PS2.2k) with a depth of the trough growing proportionally to the height of the rim until a certain threshold value which stands for the upper limit where the whole tail can be fitted with a damped oscillation with a single wavelength. A constant depth is recorded above this threshold value. For larger molecular weight, a drastic change of the rim shape is observed. The monotonic profile observed of PS of molecular weight larger than $101\,$kg.mol^{-1} was suggested to result from viscoelastic properties of the film. Working at low Weissenberg numbers, Bäumchen et al. demonstrated with a PS/AF 1600 system that the monotonic shape was solely explained by the linear increase of the slip length with molecular weight above the entanglement length [17].

The latter statement is in accordance with earlier findings by Fetzer et al. who proved the presence of monotonic profiles at the edge of a hole for a PS film retracting from a DTS substrate. This situation was contrasted to the exact same experimenting condition performed on OTS where an oscillatory profile was observed [40]. Working with a polymer of molecular weight well below the entanglement length, the newtonian flow allowed to isolate viscoelastic effects from effects originating from hydrodynamic slip boundary conditions. Based on lubrication models [86] developed by Münch et al. for the strong slip situation and a third Taylor expanded Stokes model, the monotonic decaying rim was proved to initiate from the strong slippage recorded in the PS/DTS system compared to the PS/OTS system [42].

Despite the different flow evidenced at the tail of the rim, the monotonic profile shows features similar to the oscillatory profile in terms of 'macroscopic' observation: a self affine growth of the rim was observed [39, 38], *i.e.* the rim width increases linearly with the rim height, and the growth dynamics similar of the rim width $W(D)$ of the same order on DTS and AF 1600 [13, 39]. Consequently, shapes of rims discussed in this work have a very close aspect ratio whether rims decay monotonically or with a damped oscillation. Working with polymers of chain length below the critical entanglement length, the 1 to 1 aspect ratio of the cross section shows, as depicted in Fig. 5.1(b), that the both types of profiles are close[7] to the circular shape.

---

[7]See further discussions in chapter 7

The situation discussed in this work is far from monotonic profiles showed for high molecular weights where a tail in the millimeter range is predicted theoretically [27]. As a result, both monotonic and oscillatory profiles should not be treated as completely different regarding the curvature of the whole ridge. It is safe to neglect the difference between the two types of profiles previously discussed in terms of the curvature of the ridge in the following work.

In addition to the two types of profiles detected changing only the substrate [18, 40], we identified in section 5.2 that a monotonic decaying rims turn oscillatory on DTS as the ridge penetrates the film. This feature first discovered for holes [41] is a direct consequence of the closeness between both types of rim shapes. A slight decrease of the dewetting velocity results in a reduction of the capillary number which, due to a constant ratio slip length to film thickness, crosses the theoretical master curve, the solid line in Fig. 5.3(a) which represents the transition monotonic profile based on the third Taylor expansion of the Stokes model [42]. Monotonically decaying rims transit towards damped oscillated ones without the need to tune a parameter for the system.

From a theoretical point of view, oscillatory rim shapes account for the weak- or no-slip conditions, whereas the monotonically decaying rim for the stronger slip situation [42]. Münch and Wagner gave a physical explanation for the transition manifesting on DTS recalling first that the slip length b for the strong slip situation is much larger than the film thickness H. At the apex of the rim, the height reaches a magnitude exceeding thirty times the film thickness on DTS as depicted in Fig. 5.1(b). The dimension of the slip length relative to the rim height decreases. Non-dimensionalizing the slip-length with the initial film thickness in the mathematical model, it seems possible that we pass from one regime to another in the course of dewetting for long distances [85]. This point is further discussed in chapter 8.

The rim instability gives further insights on the evolution of the profile thanks to the presence of thicker and thinner regions along the ridge demonstrated in chapter 4. These local variations of the rim width initiate local variations of the dewetting velocity on DTS, the system displaying strong slippage, which in turns induces the presence of monotonic and oscillatory profiles on one ridge as illustrated in Fig. 5.5(a) when the difference of rim width between peak and valley becomes relevant. The latter point occurs despite the fact that a constant value of slip-length is recorded for the whole dewetting process. For the no-slip system, a large variation of rim width do not lead to any change in the rim profile. Monotonic and oscillatory profiles found in one image is therefore a **fingerprint** of the presence of slippage combined with the rim instability.

However, their is no direct link between the transition of the rim profile and the rise of the rim instability. On AF 1600, local variations of the rim width initiated by a perturbation growing along the ridge, detailed in the next chapter, occurs despite the fact that the flow profile and

the rim shape are unchanged. The argument provided by Gabriele et al. certifying that a transition of the rim profile resulting from a change from a flow with viscoelastic properties to a flow with viscous properties [44] is not valid. The rim instability is also observed for pure viscous flows. A more detailed explanation is given in chapter 8.

5.6 Summary

- Characterizing the growth of the rim with AFM experiments, we demonstrate a self affine growth of the rim for the whole course of dewetting. The rim instability does not perturb this growth.

- Rim profiles developing on AF 1600 substrates show an oscillatory decay at the tail of the ridge. A monotonic decay is solely found for DTS experiments. The latter eventually transits to an oscillatory decay.

- Values of the slip length obtained with the rim profile analysis confirm a much stronger slippage at the solid/liquid interface on DTS compared to AF 1600. These values are constant for the whole course of dewetting.

- The theoretical value of the rim width calculated for an unperturbed supported semi-cylinder follow the rim width averaged over thicker and thinner regions of the ridge. This comparison is essential for further discussions on the amplitude of the rim instability in chapter 6.

- Under certain conditions, visualizing both a monotonic and an oscillatory decay of the rim at the tail is rendered possible in the fingering regime if the capillary number measured at peak and valley passes through transition line of the Stokes model in the $Ca(b/H)$ figure. This stage is a fingerprint of the presence of strong slippage in the system.

6 Dynamics of the perturbation before fingering

The rim instability studied in the xy-plane with optical microscopy in chapter 4 is completed in this chapter with a focus on the evolution of the undulation normal to the ridge. The work benefits from the high resolution of the instrument used, atomic force microscopy, to give insight on the impact of slippage at the solid/liquid interface on the instability of the ridge, modeled as a semi-cylinder. The analogy is made with the theoretical case of the Rayleigh-Plateau instability focusing mainly on the stage prior to fingering to complete the work started with optical microscopy.

By means of *ex situ* measurements, we concentrate in a first part on the evolution of the wavelength λ of the perturbation in analogy to the Rayleigh-Plateau instability. In a second part we discuss the onset of the rim instability. We finally investigate the temporal and spatial evolution of the amplitude of the undulation recorded normal to the ridge $A_{\mathrm{z}}(t\,\mathrm{or}\,D)$, where slippage is first neglected before deviations are compared in the slip situation.

6.1 Evolution of the wavelength

As for the study performed with optical microscopy, a thin PS film of 10.3 kg.mol^{-1} (PS10.3k) is deposited on a hydrophobic surface, either DTS or AF 1600. The 115(5) nm thick film is annealed at the desired temperature to enable the newtonian flow of the liquid layer and then quenched after a time t to 90 °C, slightly below the glass transition temperature, to scan the ridge with atomic force microscopy under static conditions. The *ex situ* measurement was preferred to *in situ* measurements to enable access at the volume of polymer accumulated in the ridge, required to calculate the dewetted distance D_{mean} while the contact line is moving. However, as for *in situ* experiments, we continually record the same lateral portion of the ridge as t increases. The result of the comparison between both types of experiment performed by Fetzer and Jacobs, showed that the self affine growth of the ridge is conserved together with the characteristic of the rim shape observed in chapter 5 [39]. The only difference with *in situ* experiments is the decrease of volume due to the expansion of the film at elevated temperature, which takes place homogeneously all over the ridge.

(a) Rim instability for a dewetting polymer front at $125\,^\circ$C.

(b) Transverse sections of a ridge recorded at various times for dewetting at $120\,^\circ$C. The travelled distance varies in the range 3-$60\,\mu$m.
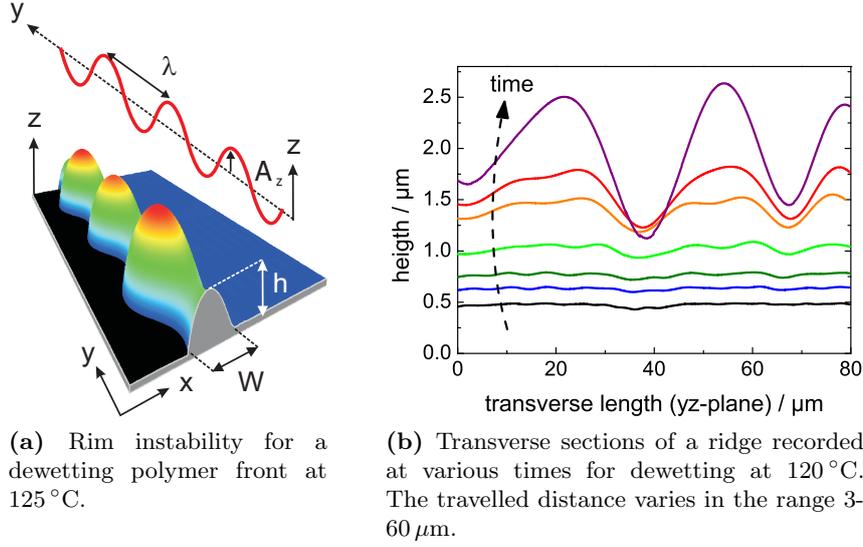
Figure 6.1: (a) Perspective of a ridge at advanced stage of dewetting. The rim instability evidences three successive bulges of mean amplitude A_z, wavelength λ, rim width W and height h. The transverse section recorded at the tip of the ridge (red line) is displayed in (b) for various time during the whole course of dewetting. This graph shows a continuous growth of the ridge and a coalescing of thicker regions.

6.1.1 Temporal evolution of the wavelength

The sketch depicted in Fig. 6.1(a) exemplifies a ridge scanned with AFM, including parameters defining the instability of the ridge normal to the substrate. The aspect ratio between the rim width $W(t)$ and the rim height $h(t)$ is sufficiently high to neglect the film and consider the ridge as a semi-cylinder: $\frac{W(D)}{H} > 20$ for $D > 5\,\mu$m on AF 1600 and $\frac{W(D)}{H} > 40$ for $D > 12\,\mu$m on DTS. Consequently, the geometry of the straight front is ideal to draw an analogy between the instability developing on the ridge and the Rayleigh-Plateau instability of a liquid thread deposited on a solid substrate; we study the situation preceding fingering.

Starting with an unperturbed cylinder of fixed initial rim width W_0, the Rayleigh-Plateau instability develops thanks to a reduction of the surface energy, as reported in part 2.5. A bunch of wavelengths compete until the optimal wavelength λ_m grows with the fastest growing rate. λ_m is proportional to the initial rim width with a constant of proportionality $C = \lambda_m/W_0$, denoted in the following as the **Rayleigh ratio** or reduced wavelength[1]. The theoretical investigations of Rayleigh showed a fastest growing mode at $C = 4.5$ [100], a value to similar to experimental results $C \simeq 3.1$ [95].

---

[1]This name was created in analogy to the term used for liquid jets: reduced wavenumber $q = \frac{2\pi}{\lambda}\frac{W_0}{2}$, with W_0 the width of the unperturbed cylinder [36].

In contrast to the previous situation, the growth of the ridge and the amplification of the undulation are synchronous concerning the rim instability. A succession of scans recorded with AFM at the tip of the ridge is depicted in Fig. 6.1(b) for various time intervals. The first section depicted of mean height H lower than $500\,\text{nm}$ (black curve) was taken at the early beginning of the dewetting process of PS on AF 1600 for a dewetting time $t = 30\,\text{s}$ at $120\,^\circ\text{C}$ and traveled distance by the front $D = 1\,\mu\text{m}$. The last section of mean height $H \approx 2\,\mu\text{m}$ (purple curve) was annealed for more than $7\,h$ while the ridge moved over $100\,\mu\text{m}$. From the begin to the end time, the number of bumps N, *i.e.* thicker regions or peaks, reduced from a factor 5 evidences the presence of **coarsening** in the system: the volume accumulated at the three phase contact line is conserved in the ridge. Two direct consequences of bulge collapsing are the growth of the wavelength λ, defined in our experiments as the distance between consecutive peaks averaged over at least three bulges, with time and the non negligible error resulting from the evaluation of λ caused by the non homogeneous distribution of bulges along the ridge.

Fig. 6.2(a) depicts the temporal growth of the wavelength of various series measured either with AFM or optical microscopy. In the latter case, we were able to record peaks at the three phase contact line when the deformation in the xy-plane was large enough or at the top of the ridge when the resolution of the micrograph enables to differentiate peaks from valleys. Consequently, results recorded with optical microscopy (open symbols) and AFM (filled symbols) are plotted together. The solid and dashed line are the guide to the eye, also depicted in Fig. 4.4(a)-(b) according to the function $\lambda \propto t^{\alpha/2}$. The choice of this function is explained in section 6.2.1. The good agreement of the temporal evolution of the wavelength proves that *ex situ* measurements are as reliable as *in situ* experiments.

The inset of Fig. 6.2(a) represents the dewetting dynamics for each series. The fact that $\lambda(t)$ follows $D(t)$ clearly demonstrates that the wavelength is driven by the motion of the three phase contact line.

6.1.2 Spatial evolution of the wavelength

The evolution of the wavelength compared at equivalent distance traveled from the contact line in Fig. 6.2(b) shows, in contrast to the previous situation, a similar growth law at low D ($D < 60\,\mu\text{m}$), independently of the experimental conditions. The wavelength clusters around the same law despite changes of the substrate (AF 1600 or DTS), the viscosity (PS10.3k or PS13.7k at $120\,^\circ\text{C}$), the dewetting dynamics or the technique used (AFM or OM). The spatial evolution of the wavelength $\lambda(D)$ depends on the volume of material accumulated in the ridge only. As a consequence, we can certify that the evolution of the wavelength is an intrinsic characteristic of the geometry of the semi-cylinder, $\lambda \propto \sqrt{D}$.
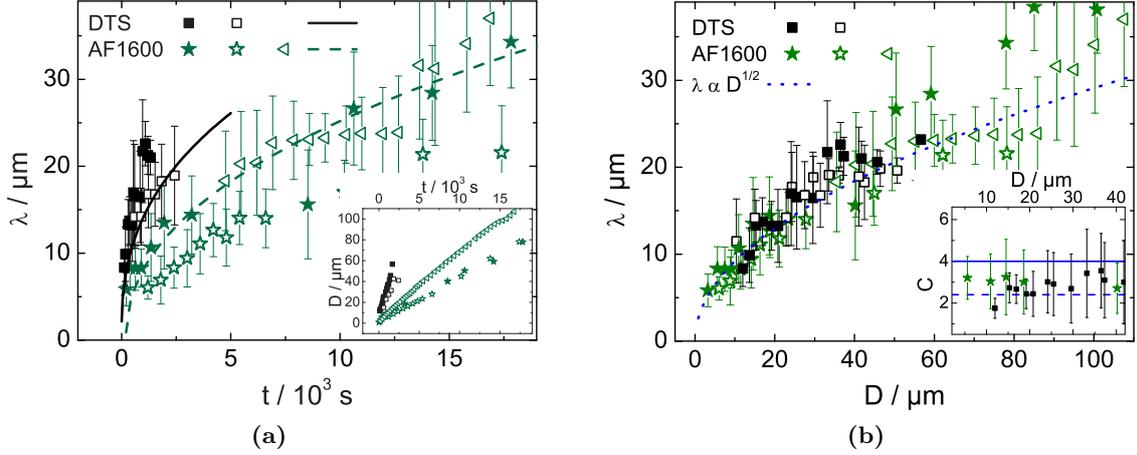
Figure 6.2: Temporal (a) and spatial (b) evolution of the wavelength λ measured for straight fronts recorded with AFM (filled symbols) and optical microscopy (open symbols) retracting from DTS (black) or AF 1600 (green). $\lambda(t)$ grows following a power law $\lambda \propto t^{\iota}$ represented for two series, dashed and solid line (AF 1600 and DTS). The coefficient ι is proportional to α, the coefficient of the dewetting dynamics curves $D \propto t^{\alpha}$ depicted in the inset of (a). Despite various dewetting dynamics for each series, a common growth is observed for the wavelength as a function of distance, $\lambda \propto \sqrt{D}$, blue dotted line in (b). This behavior is due to an increase of the rim width W with D since the Rayleigh ratio $C = \lambda/W$ is constant as indicated in the inset. Solid and dashed blue lines correspond to theoretical values. Error bars for the system are standard deviations of the wavelength measured over $N > 3$ bulges for the PS films of thickness 115–125 nm and M_{w} of 10.3–13.7 kg.mol^{-1}.

At $D \approx 60~\mu m$, we observe on DTS a maximal length separating thicker regions reached at $\lambda_{max} \approx 20~\mu m$. This value corresponds to the transition from bulges to fingers discussed in chapter 4.4. As the subsequent peaks and valleys remain aligned along the ridge for AF 1600, the wavelength continues to grow for dewetting distances larger than 60 μm. $\lambda(D)$ grows faster when recorded with atomic force microscopy (closed symbols) than optical microscopy (open symbols). λ is averaged on lengths of approximately 80 μm with AFM, whereas the average takes place over 150 μm with optical microscopy. The number of bulges ($N = 3$) imaged with AFM at $D \approx 60\,\mu m$ is less representative of the impact of coarsening than for the latter technique. Increasing the statistics with optical microscopy leads to a growth of $\lambda(D)$ which agrees better with theoretical expectations $\lambda \propto \sqrt{D}$ drawn in Fig. 6.2(b) (dotted line). Consequently, the deviation previously observed is the result of the different statistics allowed on each instrument.

We now restrict the analysis to the measurement performed with AFM up to $D < 40~\mu m$ in order to combine better statistics and the maximal accuracy for both the growth of $\lambda(D)$ and the evolution of $W(D)$ on DTS and AF 1600. Under these conditions, we can calculate the Rayleigh ratio of both systems. The constant value reported in the inset of Fig. 6.2(b)

shows that the wavelength scales with the width of the rim during the full dewetting process. This result proves that a preferred wavelength is chosen. Among all wavelengths, the most favorable is λ_{max}, the wavelength obtained at the maximum growth rate as it is the case in the Rayleigh-Plateau instability.

The value of C averaged over D obtained on AF 1600, $C = 3.5(7)$, is slightly higher than for DTS, $C = 2.8(2)$, but remains consistent with theoretical expectations calculated by Brochard-Wyart and Redon (C=4) [8] and Münch et al. ($C = 2.4$) [87] obtained with the fastest unstable mode, respectively dashed and solid lines in the inset of Fig. 6.2(b). No slip dependence is expected for the rise of the rim instability under the tested conditions. The driving force remains the surface tension similarly to the Rayleigh-Plateau instability.

At higher temperature, values measured on AF 1600 are in the same range than previous results: $C = 3.1(5)$ at 125 $^{\circ}C$ and $C = 3.4(7)$ respectively at 130 $^{\circ}C$. No impact of viscosity on the wavelength is expected, however, the dynamics of the rise of the instability, studied in the following part, might change.

6.2 Temporal evolution of the amplitude $A_{\rm z}$

Together with the merging of bulges depicted in Fig. 6.1(b), we observe a rise of the height difference between lowest and highest point of the ridge, which we report in the following as amplitude, denoted $A_{\rm z}$, sketched in Fig. 6.1(a). The amplitude of the perturbation recorded normal to the ridge is calculated as half of the height difference measured between consecutive peaks and valleys averaged along the ridge, whose length is typically $60 - 80\,\mu$m wide.

The high resolution brought by scanning the ridge with atomic force microscopy (AFM) enables an accurate measurement of the temporal evolution of the rim instability in the yz-plane, $A_{\rm z}(t)$, which will be first studied on AF 1600 with an attempt of a theoretical explanation. The low slip-length recorded for this system, makes it an ideal situation to compare to the Rayleigh-Plateau instability of a supported semi-cylinder. We then compare with results obtained under the influence of slippage for the DTS/PS system. Finally, we describe the spatial evolution of the instability $A_{\rm z}(D)$ for both the weak slip and strong slip cases, highlighting the onset of rim instability.

6.2.1 Case of AF 1600

Experimental observations

Fig. 6.3 depicts the temporal evolution of the amplitude of the instability $A_z(t)$ dewetting from AF 1600 at temperatures ranging from 120 to 130 $^{\circ}$C. As for the evolution of the wavelength

$\lambda(t)$ discussed in the previous section, large error bars illustrate the uneven distribution of peaks induced by coarsening from various bulges. The semi-logarithmic representation evidences a similar trend for the growth of $A_z(t)$ independently of changes in viscosity induced by temperature. We neglect in this part changes in surface tension which are small compare to variations in viscosity. The trend is observed whether the dewetting scenario takes place within $3\,000\,\mathrm{s}$ at $130\,^{\circ}\mathrm{C}$ or $30\,000\,\mathrm{s}$ at $120\,^{\circ}\mathrm{C}$, despite the various dewetting dynamics reported on AF 1600 in Fig. 6.5.

This observation is similar to results obtained for the instability developing in the xy-plane in section 4.5. The scenario of the rim instability is identical whether the $40\,\mu\mathrm{m}$ or the $80\,\mu\mathrm{m}$ distance recorded at thicker regions receding respectively from DTS or AF 1600 occurs in a small time interval ranging from $150\,\mathrm{s}$ to $15\,000\,\mathrm{s}$. The dewetting dynamics impacts on the position of the contact line at t, but features of the instability depend on the geometry of the ridge.
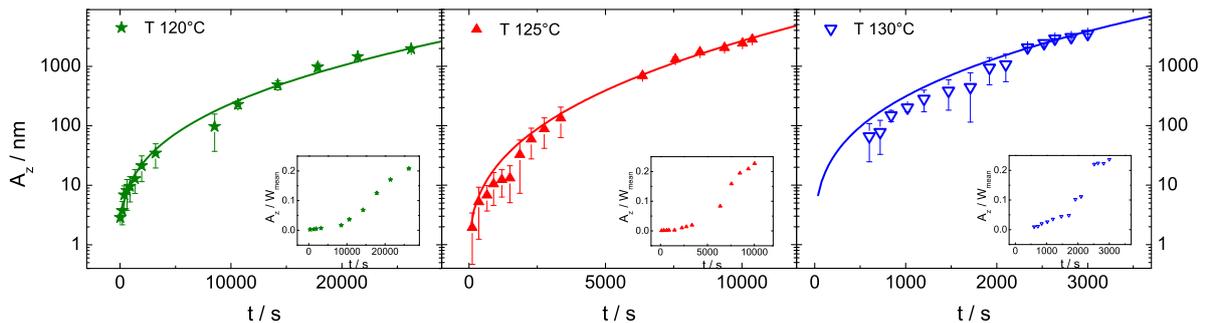
Figure 6.3: Semi-logarithmic representation of the growth of the amplitude of the perturbation A_z recorded on top of the ridge versus time t for a series of experiments performed on AF 1600 at various temperatures T. Solid lines correspond to the fit of experiments according to equation 6.5. The inset, $A_z/W(t) > 2\;\forall t$, shows that the perturbation remains small for the whole dewetting process; a Rayleigh-Plateau-type instability is valid over t. The system presented is a PS(10.3K) film of height $115(5)\,\mathrm{nm}$.

Since the developing of the instability is an intrinsic feature of the ridge, we apply the theory developed by Rayleigh on the instability of a cylinder introduced in section 2.5. The inset of Fig. 6.3 depicting a value of the ratio $A_z/W_{mean}(t)$ lower than 0.2 for the whole process proves that we are within the limit of small perturbations. The instability develops in a linear regime, suggesting an exponential growth of the amplitude $A_z(t)$. In contrast to expectations, the profile of $A_z(t)$ shows a more complex growth in our situation of a moving front. We give an attempt of explanation in the following section by coupling the theory of the instability with the dynamics of the moving front. The mathematical meaning of the application of both theories is discussed in section 6.5.

Theoretical explanation

Based on the fact that the wavelength clusters around the maximal growth rate λ_{m} for each distance D traveled by the dewetting front, we assume that the rim instability grows satisfying the development of the Rayleigh-Plateau-type instability at maximal growth rate ω_{m}. In the static situation, the perturbation of semi-cylinder deposited on a substrate writes

$$h(x,y,t) = H_0(x,t) + \delta h \exp(\omega_m t) \exp(iq_m y) \tag{6.1}$$

where H_0 is the height of the unperturbed ridge, the amplitude δh is small and $q_m = 2\pi/\lambda_m$ the wavenumber of the perturbation developing at maximal growth rate w_m. The temporal evolution of the amplitude $A(t)$ reads

$$A(t) = \delta h \exp(\omega_m t) \tag{6.2}$$

According to Brochard-Wyart and Redon, the growth rate of the instability, defined in-plane by $\dot{u}_{\mathrm{q}} = (1/\tau_{\mathrm{q}} u_{\mathrm{q}}$, follows equation 6.3, with $v^* = \gamma/\eta$ the wetting velocity, γ the surface tension, η the viscosity of the melt, θ the contact angle at equilibrium and ℓ a logarithmic factor reflecting the singularity of the flow near the contact line, treated as constant in the no-slip situation [8]. This study, based on the deformation of two coupled lines on each side of a semi-cylinder separated from W, concentrates on the instability rising in the xy-plane. The rim width chosen in our experiments is the distance in the direction of dewetting (following the x-axis) between the three phase contact line and the position where the rim height reaches $110\,\%$ of the film thickness in the back side of the ridge. This definition set by [39] is in good agreement with a width of a perfect semi cylinder as discussed in part 5.3.

$$\frac{1}{\tau_{\mathrm{q}}} = -\frac{v*\theta^3}{3\ell}\frac{F(q)}{1+\frac{4}{q^2W^2}} \qquad \text{where} \qquad F(q) = q\left[-\frac{2}{qW} + \tanh\left(\frac{qW}{2}\right)\right] \tag{6.3}$$

In Fig. 6.10, we proved that the amplitude of the perturbation of the rim recorded in the plane of dewetting A_{x} evolves linearly with undulations rising normal to the ridge, which is explained by the cylindrical geometry of the ridge. Consequently, we can apply the theory developed in the xy-plane to results in the yz-plane with a proportionality factor. Equation 6.2 originally standing for $A_{\mathrm{x}}(t)$ is also valid for $A_{\mathrm{z}}(t)$ due to the circular shape of the rim.

In order to take into account the fact that the rim grows constantly with time, we express the dynamical case of rim instability treating the situation as a series of static cases developing at maximal growth rate. We suppose that the transition from one stage to the next is quasi-spontaneous since the amplitude does not start from zero at each rim width W_{i} considered.

In other words, the competition of the mix of several wavelengths observed for the Rayleigh-Plateau instability to reach λ_m is neglected for the rim instability.

Under these circumstances, equation 6.3 simplifies to a function dependent on the wavenumber which is proportional to the rim width according equation 6.4. The next step consists of combining the growth of the ridge and the algebraic law of $D(t)$ also given in eq. 6.4.

$$q_m W = \frac{\lambda_m}{W} \equiv \text{cst.}, \quad W(D) = C_s \sqrt{H} \sqrt{D} \quad \text{and} \quad D(t) \propto t^\alpha. \tag{6.4}$$

As a result, the temporal evolution of the amplitude $A_z(t)$ (equation 6.2) simplifies into equation 6.5 with B a constant. If $\beta = 1$, the amplitude grows exponentially as in the static situation. However, β is a value depending on the exponent α of the power law driving the motion of the straight front. On AF 1600, the growth law with the coefficient $\alpha \sim 0.9$ remains valid for almost the entire dewetting process, the theoretical value of the exponent is $\beta = 0.55$.

$$A_z(t) = \delta h \exp(B\, t^\beta) \quad \text{with} \quad \beta = 1 - \frac{\alpha}{2} \tag{6.5}$$

Solid lines of Fig. 6.3 result from the fit of the linearized equation 6.5, $\log(\log A_z) = f(\log t)$. The good agreement between experiments and the shape of the fitting curve validates the fact that the instability develops at maximal growth rate for each distance D traveled by the moving front whose temporal growth is governed by the algebraic power law. Consequently, we can affirm that the rim instability developing under the weak-slip conditions grows based on the geometry of the ridge independently of the rate of volume uptake in the rim governed by the growth law governed by the balance of the driving force with mainly viscous dissipation.

Experimental values of β reported in table 6.1 are independent of the dewetting dynamics

Table 6.1: Resulting fitting parameters of equation 6.5 performed on AF 1600 for the system presented in Fig. 6.3.

T	β_{exp}	v	η
$°C$		nm.s^{-1}	Pa.s
120	0.34(2)	6(3)	$2.0\,10^5$
125	0.37(3)	19(3)	$5.7\,10^4$
130	0.33(3)	71(3)	$1.8\,10^4$

and viscosity. Similar to the growth dynamics $D(t)$ discussed in section 4.5, β_{exp} related from the weak slippery conditions at the solid/liquid interface. However, the absolute value is not in adequation with the theory, which cannot be smaller than 0.5 due to the maximal value $\alpha = 1$ reached in the no-slip condition. This deviation is probably due to approximations required to obtain the simplified form of $A_z(t)$ given in equation 6.5. For instance, the expression $q^2 W^2$

was considered in our case as a constant.

6.2.2 Case of DTS

In contrast to the previous situation, the temporal evolution of the amplitude displayed in semi-logarithmic representation of $A_z(t)$, Fig. 6.4, for the system PS/DTS evidences an exponential growth for the range of temperature investigated (110-125 °C). The experimental value of the exponent $\beta \sim 1$ cannot be explained using the previous theory which would occur only if $\alpha = 0$, a non-physical solution for the receding of the front $D(t)$. Consequently, discrepancies come either from a parameter of the growth rate changing with slip or being time dependent.

We first have to consider changes in the logarithmic factor ℓ of the growth rate (equation 6.3) which is the parameter where slip enters into the theory. This factor represents the viscous dissipation near the contact line via the ratio of the rim width W and a length ϵ: $\ell \equiv \ln W/\epsilon$. In the no-slip situation, Brochard-Wyart et al. noted that ϵ is given by a microscopic cutoff length a/θ_e and $\epsilon = b/\theta_d$ in the presence of slip [9]. Since $b > a$, the prefactor in the expression for the rise-time differs significantly between both cases. Moreover, the logarithmic factor considered as constant in the case of AF 1600, $\ell \sim 10$ [8], grows with the rim width when the system is affected by slip.
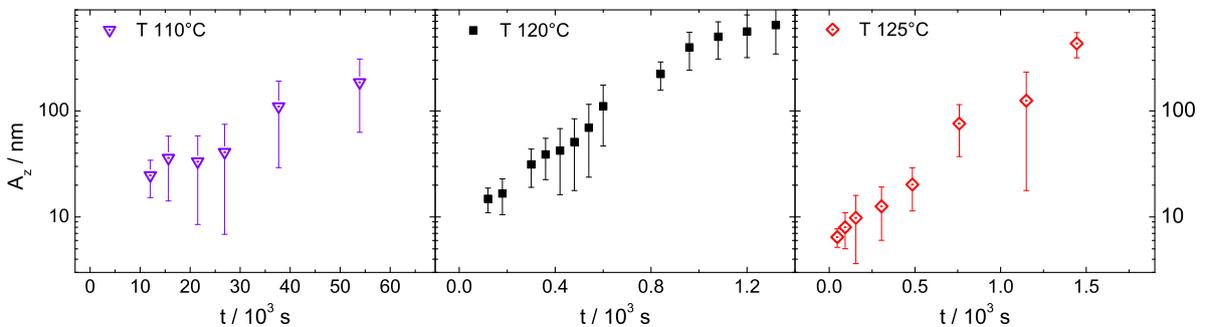
Figure 6.4: Semi-logarithmic representation of the growth of the amplitude of the perturbation A_z recorded on top of the ridge versus time t for a series of experiments performed on DTS at various temperatures T. In contrast to Fig. 6.3, an exponential growth $A_z \propto e^t$ is recorded before the fingering regime is reached. The system presented is a PS(10.3K) film of height 115(5) nm.

A second aspect to consider is the width and height of the ridge while the perturbation propagates. The flow near the solid/liquid interface differs on DTS compared to AF 1600 due to slippage. As polymer accumulates in the ridge with time, the hypothetical height of the unperturbed ridge h_0 increases. Consequently, the second flow induced by the instability developing

along the ridge is strongly influenced by slippage at early stage of dewetting and less sensitive at late stage which creates non-linearities in $A_z(t)$.

6.3 Spatial evolution of the amplitude A_z

Since the temperature and the substrate chosen for experiment impact on the temporal evolution of the amplitude via the dewetting velocity, we examine in this part the evolution of the amplitude at equivalent volume of polymer accumulated in the ridge represented by the distance D traveled by the three phase contact line. Treating the problem from this point of view allows to weight the influence of the dewetting dynamics, viscosity on the impact of slippage in the system.

After a brief description of the evolution of $A_z(D)$, we describe changes in the height of the ridge highlighted thanks to the technique used, atomic force microscopy. We show why this feature is a possible explanation of the onset of rim instability. We finally present the situation for dewetting taking place on AF 1600 and DTS.

6.3.1 Experimental observations

Differentiated from the $D(t)$ curves presented in Fig. 6.5(a), dewetting velocities $v(t)$ [2], averaged from the entire spectra, covers a large range of dewetting dynamics without changing the approximation of a small Reynolds number. In one hand, rising the temperature of experiments from 120 to 130 °C for the system PS/AF 1600 enables direct observations on the preponderance of v over the viscosity on the rim instability, since the slip length recorded on AF 1600 remains invariant with temperature [16]. The dewetting velocity ranges from 6 to 70 nm.s^{-1}. On the other hand, dewetting velocity ranging from 6 to 50 nm.s^{-1} for the system PS/DTS allow to cover changes dewetting dynamics given by changes of the substrate at a given temperature ($v_{\text{AF 1600}} \approx 6$ nm.s^{-1} and $v_{\text{DTS}} \approx 36$ nm.s^{-1} at 120 °C), but also see the impact of temperature and viscosity on the system. In the case of DTS, Fetzer et al. shows that the value of the slip length varies with temperature [41]. This change discussed in part 5.2.2 won't be considered in our situation since we deal with the strong slip situation where the slip length is high compared to film thickness.

Fig. 6.5(b) depicts the results of the amplitude $A_z(D)$ for all experiments performed on DTS and AF 1600. For $A_z(D)$ lower than approximately 150 nm, the rise $A_z(D)$ is slow on both substrates. Above this threshold value, the rim instability amplifies much faster and appears

---

[2]Note that velocities give an approximation of the dynamics present in the ridge along x for the whole process of dewetting. The value, however, does not represent that punctual value, given at a time t.
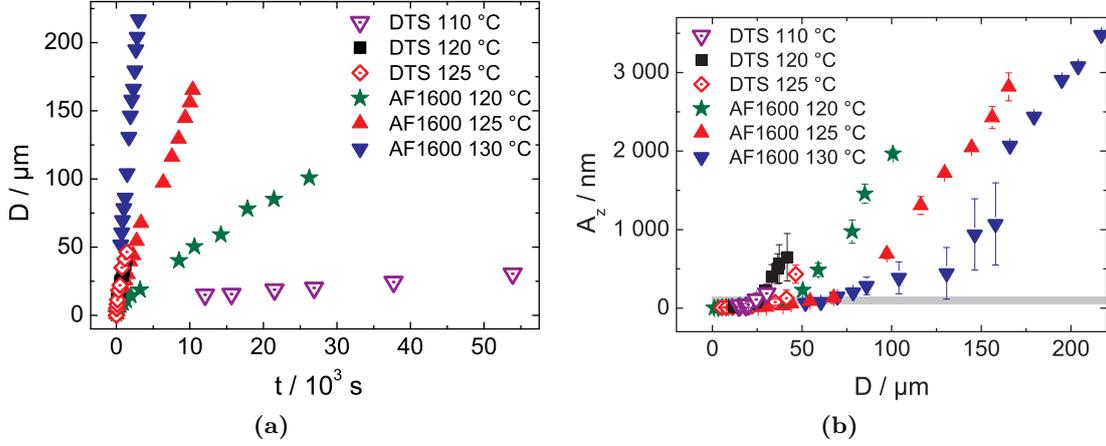
Figure 6.5: (a) Dewetting dynamics $D(t)$ of experiments studied with AFM where the distance D is calculated from the volume of polymer accumulated in the ridge. Spatial evolution of the amplitude $A_z(D)$ (b) for the corresponding series. Although dewetting velocities of experiments performed on both substrates are mixed, the amplitude always grows prematurely on DTS. The limit $A_z(D)$ before droplet detachment is much higher on AF 1600. Above the onset of rim instability, grey zone, the growth rate on AF 1600 is much higher at low temperature whereas the velocity is the lowest. Viscosity of the PS(10.3K) films of height 115(5) impacts on the rim instability.

unconstrained from the experimental conditions. Each series develops separately one from another, with systematic higher dynamics when dewetting takes place on DTS despite a faster dewetting velocity on AF 1600 in some cases.

The overall growth of $A_z(D)$ can therefore be divided in two regimes with the transition taking place at an amplitude of approximately 150 nm, grey zone in Fig. 6.5(b) discussed in part 6.3.4. The presence of both regimes is strengthened with the spatial derivative $A'(D)$ of Fig. 6.8(a). $A'_z(D)$ remains hardly distinguished from zero, $A'_z(D) \approx 10^{-3}$. Then $A'_z(D)$ follows a linear-like behavior with slopes at regime 2 in ascending order $0.95.10^{-4} \, \mu m^{-1}$ (AF 1600 120 °C), $0.29.10^{-4} \, \mu m^{-1}$ (AF 1600 125 °C), $0.17.10^{-4} \, \mu m^{-1}$ (AF 1600 130 °C) and $2.51.10^{-4} \, \mu m^{-1}$ (DTS 120 °C).

6.3.2 Close loop on the rim height

Let now consider the evolution of the ridge with regard to the substrate via the rim height $h(D)$. Fig. 6.6 displays heights averaged along the ridge at peaks ($h_p(D)$, left, filled symbols) and valleys ($h_v(D)$, right, open symbols). At low D, we observe a self-similar growth of $h(D)$ independently of the temperature and of the system chosen for the experiments. The rim height is a function of $\sqrt{D}$, dashed line in Fig. 6.6 with proportionality coefficient $k_p = 6.3(2) \, \mu m^{0.5}$ at peaks and $k_v = 5.9(2) \, \mu m^{0.5}$ at valleys. Coefficients k are averaged from experiments with the

largest density of points in this region, *i.e.* AF 1600 at 120 and 130 °C. Following discussions on the evolution $W(D)$ in section 5.3, $k = k_g C_s \sqrt{H}$, with k_g a coefficient depending on θ to link the rim width to the rim height. The small variation recorded between k_p and k_v indicates a shift between peaks and valleys.

At large D, $h(D)$ deviates from the dashed line. A growth of the height is observed at peaks, whereas a decrease is observed at valleys. Since we concentrate in this part on the regime before bulges protrude from the ridge, *i.e.* the volume of polymer is conserved in the ridge, we can conclude that a flow along the ridge from valley to peak is induced with the decrease of the amount of polymer at valleys. The distance at which the deviation of $h(D)$ looses proportionality with $\sqrt{D}$ is denoted D^* with * standing for the **onset of the bulging regime**, the transition where the rim instability is observed at microscopic level in part 4.4. The question now rises what happens at $D < D^*$.
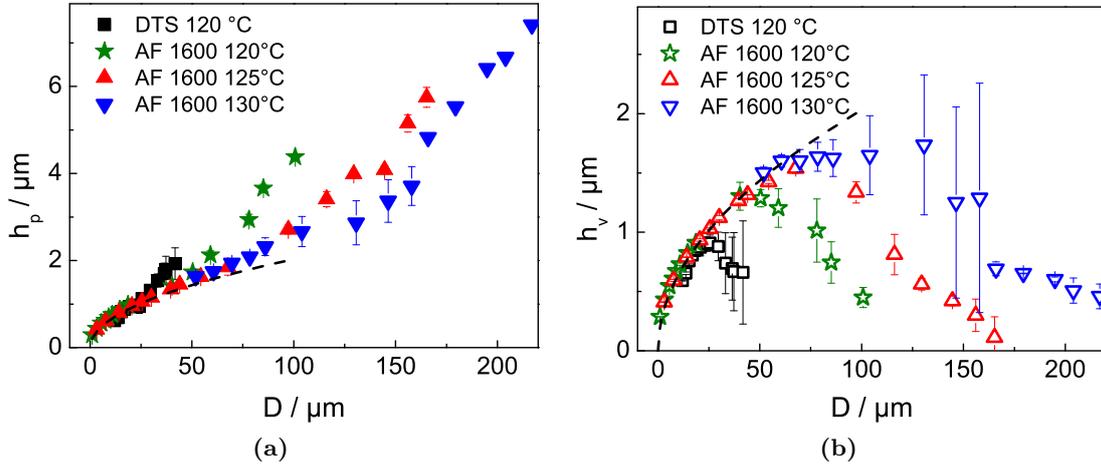
Figure 6.6: The rim height h versus distance D measured locally at peak (a) and valley (b) for the same series as in Fig. 6.5 evolves in two stages. In a first regime h_p and h_p grow proportionally to $\sqrt{D}$, dashed line. The second regime marks a decrease of $h_v(D)$ and an increase of $h_p(D)$ with faster rate. We set the transition between the two regimes as the onset of the bulging regime.

Onset of shrinkage at valleys

As for the Rayleigh-Plateau instability, the rim instability is driven by surface tension. Since variations of the latter parameter are neglected for the range of temperatures used, the onset of rim instability should take place at a distance D^* which is independent of the experiment selected on AF 1600. In contrast to predictions, deviations of experimental curves from $H \propto \sqrt{D}$ take place at distances increasing with temperature according to observations of Fig. 6.6. Table 6.2 summarizes times and lengthes measured on the ridge at h^*. An increase of onset

value for D and H is observed when series are ranged in the order given in the table: DTS at $120\,^{\circ}$C, then AF 1600 from 120 to $130\,^{\circ}$C. The fact that t^* follows a different order than the previous quantities evidenced that onset of rim instability is not solely driven by the dynamics of dewetting. The geometry of the ridge, however, is not the only parameter impacting on the onset of shrinkage at rim widths since variations of H^* are identified on AF 1600 for various temperatures. We can expect a contribution of viscosity.

The self-affine growth of the rim discussed in section 5.3 involves a growth of $W(D)$ propor-

Table 6.2: Summary of the time t^*, distance D^*, rim height h^*, rim width W^* and amplitude A_z^* obtained for various series (same as in Fig. 6.5) at the onset of rim instability.

substrate	DTS	AF 1600	AF 1600	AF 1600
Temperature / $^{\circ}C$	120	120	125	130
t^* / s	540(60)	9500(1500)	3800(500)	1100(130)
D^* / μm	23(3)	45(7)	70(5)	82(5)
H^* / μm	1.0(1)	1.30(5)	1.55(5)	1.65(5)
W^* / μm	5.7(9)	6.0(4)	6.4(5)	6.6(5)
A_z^* / nm	80(30)	160(90)	200(100)	240(60)

tional to $h(D)$. Consequently changes observed in the rim height lead to changes of the rim width; the rim width shrinks when the rim height decreases at $D > D^*$. The evolution of A_z^* is discussed in the following section.

6.3.3 Hypotheses on the occurrence of D^*

The spatial growth rate $A_z'(D)$ of the rim instability evidences a change of growth rate of the ampltide before D^* (discussed in details in part 6.3.4) and after the onset of rim instability. We now try to dress several hypotheses to explain the phenomenon we observe.

Laplace pressure at valley

By means of comparing the Laplace pressure at valley before and after the transition appears and the evolution of the growth rate of the rim instability, we attempt to explain why the rim instability takes place at a rim width approximating $6-7\,\mu$m on AF 1600. Fig. 6.7(a) depicts a three dimensional surface plot of a bulge centered at a thinner region. The one to one aspect ratio of the AFM scan illustrates the curvature at valley directly after the onset of shrinkage. More precisely, the cross-section and the transverse section provided in Fig. 6.7(b) centered at the valley of the same part of the ridge before and after the onset evidences a reduction of the Laplace pressure at the through. A rough approximation gives a difference of pressure varying

from $\Delta p_{t_1} \approx 18000$ to $\Delta_{t_2} \approx 7000$. This decrease is large but the difference is not significant enough to explain a sudden diminution of rim height at valley.

Laplace pressure is sufficient to explain the presence of the perturbation at early stage, nevertheless, the small difference of figures at valley cannot initiate the presence of the second regime. It is therefore necessary to consider another explanation, looking at the flow itself.

(a) $125\,°C$, $D = 97\,\mu m$ **(b)**
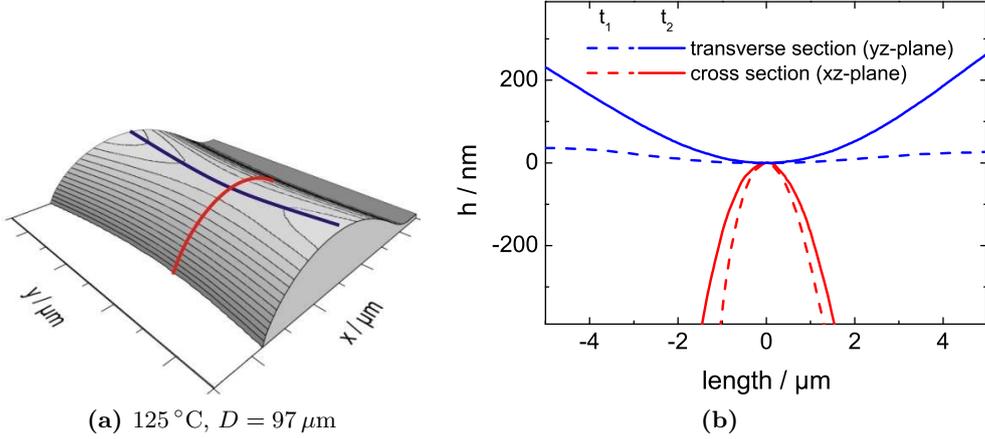
Figure 6.7: Red and blue semi-circles depicted on the AFM image exemplify curvature at valley in the dewetting direction and transverse to the ridge (a). Both curvatures are compared in a 2D graph for a dewetting time $t_1 = 900\,s$ ($D = 9\,\mu m$) and $t_2 = 10600\,s$ ($D = 50\,\mu m$). Isoheight lines in (a) are displayed each $200\,nm$.

Growth rate of the instability

If we now consider the growth rate of the rim instability given in equation 6.3 and suppose the undulation developing at the fastest mode q_{m_i}, the growth rate ω_{m_i} reaches a constant value at a given rim width W_i, depicted in Fig. 6.8(b) for a collection of W_i in the range $0 - 20\,\mu m$. Amplification of the undulation following $\dot{u}_q = -\omega_q u_q$ slows down when a width of the rim reaches approximately $6\,\mu m$ which, together with the decrease of the Laplace pressure at valley, enables other types of flow to develop.

Flow at the rim tail

We might wonder if the various flows observed on DTS leading to either a monotonic or an oscillatory decay of the rim tail into the film impact the rim instability. Fig. 5.2(a) evidence that the transition from the first profile to the second occurs while the straight front retracts the substrate from $13\,\mu m$ to $16\,\mu m$ with experiments performed on DTS at $110\,°C$. The onset
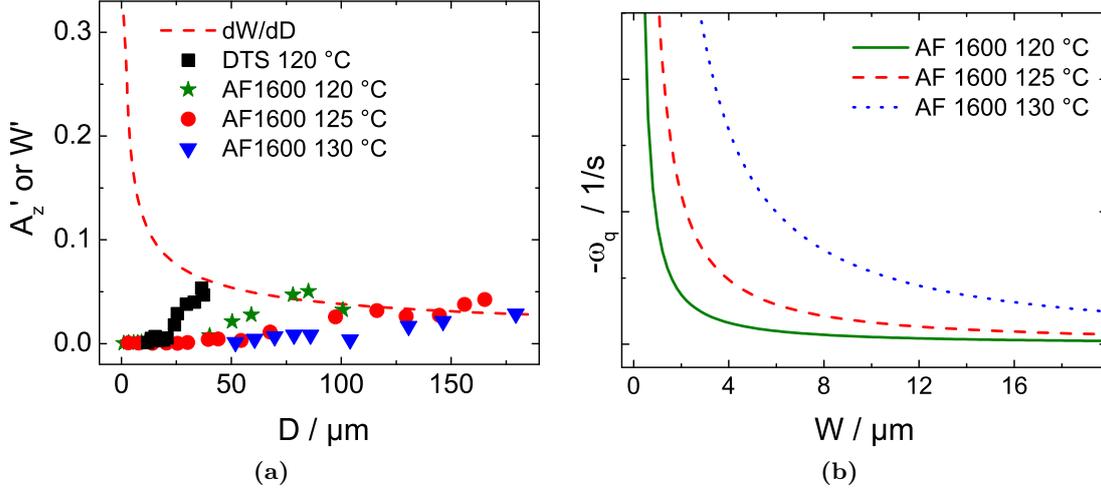
Figure 6.8: (a) The derivative of the spatial growth of the amplitude $A'_z = \partial A_z/\partial D$ plotted versus D evidence two different growth rate before and after D^*. In parallel, a rapid decrease of the growth rate of the rim width $W'(D)$ is observed. (b) Evolution of the growth rate of the rim instability based on equation 6.3 as a function of the rim width calculated for an unperturbed rim.

of the bulging regime, however, takes place at $D^* > 20\,\mu$m while the rim is already in the oscillatory regime. The same is observed for the other dewetting experiments performed on DTS. On AF 1600, the transition between two regimes at D^* is observed although the whole course of dewetting occurs with an oscillatory rim profile. Changes in flow at the rim tail has therefore no impact on the onset of rim instability. We could however wonder whether D^* could be observed with monotonic profiles.

Flow $xz-$ vs. $yz-$direction

One characteristic feature of the rim instability in dewetting straight fonts is the presence of two flows of polymer normal to each other. Along the ridge the flow induced by the Rayleigh-Plateau instability competes with the flow generated by dewetting experiments. If the three phase contact line was easy to pinch and fix, the ridge would certainly transform into droplet beads (neglecting the film behind). The motion of the straight front involves a growth of the rim width as $W \propto \sqrt{D}$ [42]. The spatial derivation of the previous, dashed line in Fig. 6.8(a), evidence a rapid widening of the rim for the first tens of microns traveled by the moving front, then the growth rate lowers. As a consequence, the flow in the dewetting direction possibly dominates the process of the rim instability at early stage, which is not the case when $W'(D)$ lowers.

6.3.4 Dynamics of $A_z(D)$

This part consists of explaining the various dynamics of $A_z(D)$ introduced in section 6.3.1. By means of a semilogarithmic representation of $A_z(D)$ in Fig. 6.9, we evidence a growth of $A_z(D)$ of exponential-type below the threshold value, whose region is indicated for all series by the grey area, and of power-law type after this value is passed. We first concentrate on dewetting experiments taking place on AF 1600, where we can neglect effects of slippage, then the case of DTS is explained.

Case of AF 1600

Comparing the rim instability of straight fronts for the system PS/AF 1600 is the best analogy to the Rayleigh-Plateau instability, the "static" case of the rim instability with a friction at the solid/liquid interface which we neglect. Since the instability is surface tension driven, we can expect a universal growth of $A_z(D)$ when plotted as a function of $D(t)$ independently of the temperature and the dewetting velocity selected.

Experimentally, Fig. 6.9(a) exhibits a trend different from expectations: the amplitude rising on AF 1600 slows down at higher temperature. As for the instability rising in the $xy-$plane discussed in section 4.5, we first neglect influence of the velocity. For a dewetted distance of $100~\mu$m, we obtain $A_z \sim 2000$, 700 and 350 nm varying temperature from 120 to 130 °C. We clearly see an influence of viscosity η.

The interest of comparing the shape of the undulation at a given distance, *i.e.* a given rim width, is to draw a parallel with the "static" situation treated in section 6.2.1. We know that the growth rate of the rim instability developing at fastest mode varies as $\omega_{q_m} \propto -\eta^{-1}$ according to equation 6.3. Consequently, the temporal rise of the undulation is faster at higher viscosity or lower temperature for a given D_i or W_i and varies from Δt_i.

In order to extend results to the whole range of distances investigated, we assume that the situation previously described for D_i is repeated at D_{i+1}. Moreover, the time necessary to reach the amplitude $A_{z_{i+1}}$ is small since we do not start from an unperturbed ridge but a ridge with the amplitude of the instability of A_{z_i}. Δt_i cumulate and the difference becomes larger as D increases. This qualitative analysis explains not only why slopes $A'(D)$ linear fits of Fig. 6.5(c) strongly increase above A^* when η decreases, but also explains the shift of D^* observed in table 6.2 as temperature increases.

$A_z(D)$ developing on DTS at 120 °C gives a proof that the disregard of the dewetting velocity in the analysis is a fair assumption. Indeed, the dewetting velocity v calculated on DTS at 120 °C and AF 1600 at 130 °C are of the same order. However, the dynamics of $A_z(D)$ are

much larger on DTS. we can therefore speculate a strong effect of slippage at the solid/liquid interface on $A_z(D)$.

Case of DTS

Focusing on the region $D \sim 50\,\mu$m depicted in Fig. 6.9(b), it seems obvious that show that the amplitude of the perturbation is largest on DTS at $120\,°$C despite the fact that the velocity is smaller than the system AF 1600 at $130\,°$C. We can explain this behavior by slip contribution along the ridge. The distance considered reflects the regime characterized by a decrease of the rim height, but no protrusion of the bulge. The large value of $A_z(D)$ on DTS results from a larger flow gradient from valley to peak. It is known that slippage increases the dewetting velocity in the direction of dewetting v_{xz}. Consequently, slippage may also affect the velocity measured along the ridge v_{yz}. We can therefore assume that slippage is **isotropic**.

6.4 Optical microscopy vs. AFM measurements

Both techniques used to characterize the rim instability, *i.e.* optical microscopy and atomic force microscopy, known as AFM, shed complementarily light on various aspects on the rim instability due to the antagonism between the resolution permitted by the instrument and the time required to capture a picture. The first technique captures the evolution of the in-plane instability instantly which allows to setup *in situ* experiments. In contrast, the high resolution
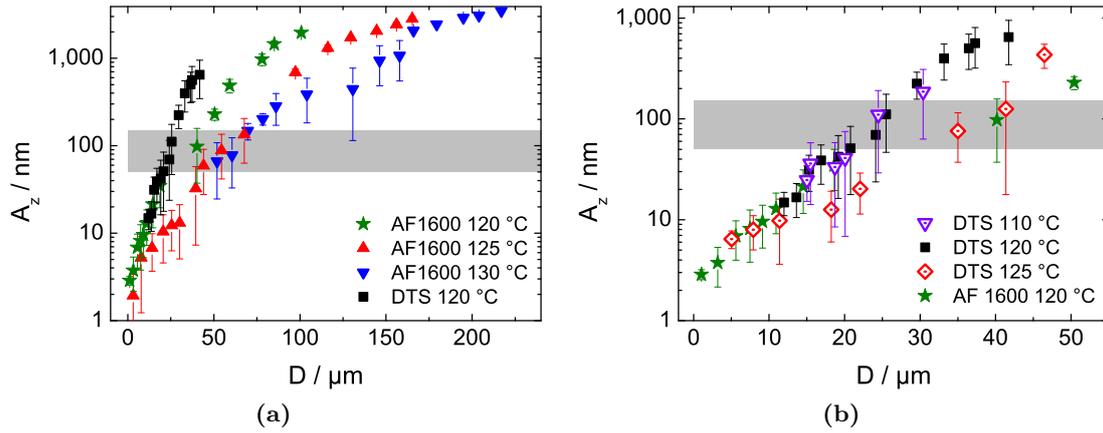
Figure 6.9: The semi-logarithmic representation of the spatial growth of the amplitude $A_z(D)$ gives clear evidence of the growth of the perturbation before the onset of rim instability (grey zone) on AF 1600 (a) and on DTS (b). The series are identical to Fig. 6.5, plots at $120\,°$C serve as a reference point.

obtained with AFM increases the laps time to record an image and consequently favors to work with stationary polymer fronts. An *ex situ* scan of the ridge, quenched according to the method detailed in chapter 3, enables an accurate measurement of diverse quantities like the amplitude of the perturbation and the volume of the ridge used to determine the dewetted distance. The exactness of both techniques to determine the dewetted distance was cross-proofed in part 3.4.1. The dynamics of the rim instability leads to the same results if both techniques are used.

Looking at the Rayleigh-Plateau instability, it seems obvious from the cylindrical shape of liquid jets that the perturbation develops homogeneously in every direction taken along the ridge. Thicker parts expand and thinner parts shrink equally independently of the side chosen to look at. The theory of Rayleigh with liquid jets or de Gennes et al. with liquids surrounding a fiber benefits from this symmetrical shape treating the situation simplified to one dimension [100, 28]. The same homogeneity is supposed to happen for thin fluids lying steady on a flat substrate.

Brochard-Wyart and Redon also treated the system similar to the static situation. They considered a wave developing on both side of the ridge via the varicose mode, an out-of-phase rise of the perturbation. This case differs from the previous by a flow tangent to the unperturbed ridge induced by the displacement of two contact lines [8]. Experimentally, the displacement is mainly driven by the spreading force applied at the three phase contact line. Therefore, it is reasonable to wonder if the scenario observed with optical microscopy is equivalent to one analyzed on top of the ridge.

Fig. 6.10 depicts the result of the comparison of the perturbation measured in-plane (A_x) compared to the perturbation rising on top of the ridge. This system, PS/AF 1600, illustrates the case where the force applied on the retracting front via the spreading coefficient S is the strongest $|S| = 18.8\,\mathrm{mN.m^{-1}}$. According to values of the amplitude $A_\mathrm{z}(D)$ obtained in Fig. 6.5, linearity between A_x and A_z covers almost the entire dewetting process. Complementarity of the instability characterized from the side or the top view occurs for dewetting distances reaching $100\,\mu\mathrm{m}$, which enables the comparison since AFM studies are used to characterize mostly the early stage of the rim instability.

6.5 Discussion

The rim instability was investigated in this part with atomic force microscopy to gain insight in the evolution of the perturbation at early stage of dewetting. The theoretical description of the static case (fixed rim width) shows that a mix of stable and unstable waves compete until the most unstable wavelength λ_m, *i.e.* the perturbation growing with the fastest rise-time, is
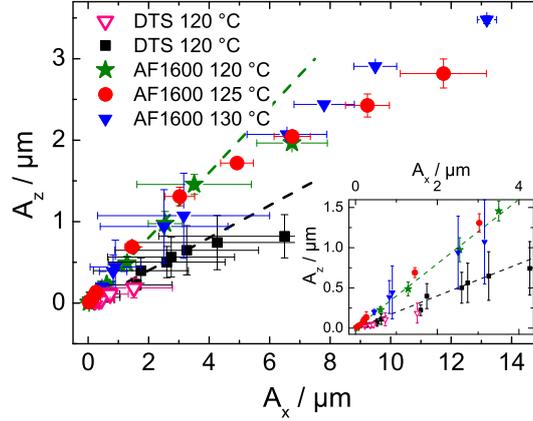
Figure 6.10: Comparison of the rise of the perturbation measured at the tip of the ridge A_z with the in-plane rise of the rim instability A_x, measured at the three phase contact line for identical series as in Fig. 6.5. A linear growth is observed for $A_z < 2\,\mu$m, illustrated in the zoom-in of this region in the inset. The guides to the eyes (dashed lines) confirm the linear behavior and also show a different slope for each substrate for which the contact angle is responsible. Deviations from the dashed lines occur as the rim instability enters the bulging regime.

selected. The transition from stable to unstable mode is evidenced with the dispersion relation by a change of sign in the growth rate $\omega(q)$. This marginal mode, appearing at a critical wavelength λ_c, defines the onset of instability and turns the undulations from exponential decay into exponential growth.

Calculating the dispersion relation for the varicose mode of a liquid ridge [8], Brochard-Wyart and Redon proved that modes are unstable above a critical wavelength $\lambda_c = 2.61W$ and the fastest rise-time appears for a proportionality between the wavelength and the rim width of $\lambda_m \approx 4W$. The main dissipative mechanism in the ridge considered in this study is viscous dissipation, *i.e.* the no-slip boundary conditions. Based on lubrication models, Münch et al. found that the maximum growth rate under the weak slip conditions occurs at $\lambda_m \approx 2.4$. In Brochard-Wyart's theory, it is possible to include a dependence of the slip length via the prefactor of equation 6.3 which has the consequence that slip impacts on the rise-time of the perturbation only. The wavelength selected is independent of the boundary conditions at the solid/liquid interface.

We can therefore wonder where the difference in λ_m for both theories comes from. Brochard-Wyart and Redon treats the energy dissipation of the displacement of lines at each side of the ridge. The interaction polymer/substrate is limited to the three phase contact line. In contrast, the theory of Münch et al. considers friction at the interface and the effective interface potential via the lubrication model. The interaction polymer/substrate is therefore analyzed over the whole width of the ridge in contact with the substrate. The second theory is surely more

accurate for slippery systems. If we now compare figures of characteristic wavelengths between both theories, we realize that the maximal growth rate of Münch et al.'s theory approximates the cutoff wavelength of predictions from Brochard-Wyart and Redon. It is clear that the onset of instability developing on a supported rim occurs at a wavelength $\lambda < 2.4W$.

Experimental observations in the literature confirm previous interpretation on the domain of validity of each theory for a certain boundary condition. In the no-slip situation, Brochard-Wyart and Redon ascertained a distance between thicker parts of roughly $4W$ [8], whereas Gabriele et al. reported a much lower experimental value of $\lambda = 2.1(2)W$ [44] for dewetting experiments performed on PDMS, a system with slip length of $10\,\mu$m according to [105]. Our results go in the same line. For a slip-length smaller than the film thickness, the system PS/AF 1600 shows a ratio wavelength to rim width around 3.3. This ratio lowers to approximately 2.8 on DTS, where the slip length is higher than the film thickness. The difference recorded on both substrates is however small and the large error bars, mainly caused by coarsening, makes it difficult to draw clear conclusions on the impact of slippage on the selected mode. One can be certain, though, that the Rayleigh ratio is rather constant for the whole dewetting scenario.

The fact that the constant of proportionality measured experimentally is achieved for values much lower than or close to the critical wavelength λ_c predicted by Brochard-Wyart and Redon suggests that this theory is not the most suitable for slippery systems. The cutoff wavelength should appear at $\lambda < 2.1W$. Consequently, it is safe to assume that upon dewetting on DTS and AF 1600 the ridge builds up and shows undulations of a mix of unstable frequencies. The average of all these wavelengths clusters around a value which is theoretically predicted with the Rayleigh ratio.

The amplitude of the perturbation represented in Fig. 6.5(b) for each volume of polymer accumulated as the dewetting front travels, $A_z(D)$, evidences a growth of the instability in two steps with a transition taking place at D^*. The difference between the first regime and the second is the evolution of the height of the ridge at valley. The flow of the ridge is first composed by two components, an in-plane flow initiated by the uptakes of polymer at the three phase contact line and a transverse flow coming from the Rayleigh-Plateau type instability. A rough approximation of both entities demonstrates that the spatial evolution of in-plane flow, $\partial H(D)/\partial D$, predominates over the transverse flow, $\partial A_z(D)/\partial D$. A difference of one order of magnitude is quantified during the first regime, a figure which lowers down close to unity at late stage of dewetting. The analogy between results obtained with the rim height and width is rendered possible by the circular shape of the rim; consequently, the transition also stands for the onset of decrease of the rim width at the thinner part, which is explained by an abrupt drop of $\partial W(D)/\partial D$ if we consider that the rim width grows as $W(D) \propto \sqrt{D}$. The second

(a)   **(b)**
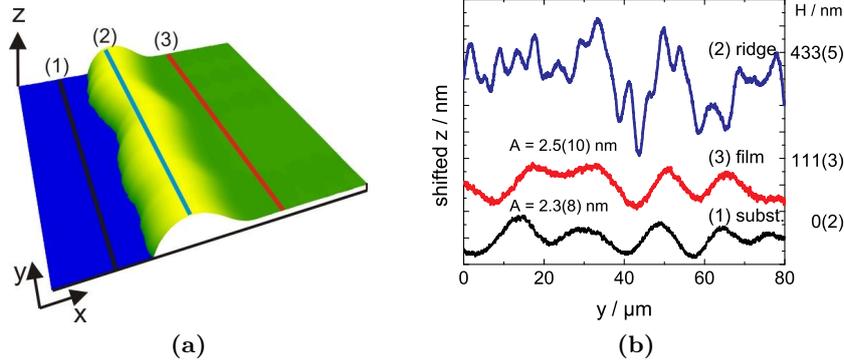
Figure 6.11: (a) AFM image of a PS(10.3K) film on AF 1600 pictures at early stage ($D = 3\,\mu$m). A cross section in the y-direction of the substrate (blue part of the image, section denoted (1)) is compared to a section at the tip of the ridge (yellow, (2)) and the film (green, (3)). The result depicted in (b) show fluctuation of the substrate (1) are found identical on the film (3), but differs from the ridge (2). Fluctuations on the ridge are due to the rim instability, independently of the substrate. The measurement of A_z is not affected by fluctuations coming from the preparation of AF 1600 thanks to the measurement method implying a to take half of the difference between rim heights measured successively at peak and valley average over the width length. Scan size of he image $80 \times 8\,\mu$m^2.

regime takes advantage of this flow dynamics, $\partial A_z(D)/\partial D$ increases above D^*.

At first sight, undulations of the ridge might be interpreted for this regime as noise or coming from the substrate for the weak-slip situation. Small waves of 2-3 nm amplitude and 10-15 μm peak to peak distance detected with optical microscopy (Fig. 6.11) are inevitable when the AF 1600 coating is spin-coated. The undulation of the substrate, replicated identically on the smooth unperturbed thin films if the peak to peak distance is larger than the healing length [2], is compared to the perturbation of the rim in Fig. 6.11 via transverse sections scanned with AFM. Thanks to a shift in height of each section depicted at the same scale, we clearly see that small waves of the substrate do not perturb at all the evolution of the instability. The slight depression observed on the ridge in the middle of the scan is because the polymer film is not completely straight at the nanoscopic scale. This section depicts a section of the ridge close but different from the top. As a consequence, it is safe to neglect long scale inhomogeneities of the substrate on measurement of the amplitude of the rim instability. The last remark is strengthen by the method used to measure the amplitude, detailed in part 3, which consists of calculating the amplitude with reference to the substrate for each peak or valley measured.

Another argument disfavoring the analogy of the signal recorded with noise is made comparing the static situation for other supported systems introduced in section 2.5.2. Khare et al. filled wedges with polystyrene. Each initial width ranging from few hundreds of nanometers to micrometers of the thread formed decomposes in a series of droplet separated from λ which is proportional to the filling width [65]. Similarly, McGraw et al. observed on flat surfaces

that torus of a polystyrene melt destabilize in N droplets, the number of droplets increasing with the ratio radius to width of the toroid [81]. These experiments support the fact that thin threads turn into droplets via the Rayleigh-Plateau type instability starting from several hundreds of nanometers. The latter argument is valid for both systems.

For $D > D^*$, the change in dynamics of the transverse flow is caused by a decrease in height of the ridge at valleys. The difference in height and most importantly width of the rim between peak and valley becomes large enough to distinguish thicker from thinner regions with the resolution of an optical microscope. This difference also induces a lateral gradient of velocity of dewetting due to the proportionality of the slip component of the velocity v_s to the inverse of the rim width which initiates fingering on DTS.

Now the question rises whether the first regime shall be considered as mature phase of the Rayleigh-Plateau type instability process. For each static situation of a supported cylinder or liquid jet, thicker regions broaden and thinner ones shrink immediately after the onset of instability, *i.e.* after an unstable mode is selected. Consequently, if we come back to the dynamic case, the rise of the rim width observed at valleys in dewetting experiments during the first regime gives matter to reflect concerning the notion of onset of instability in our case. The spatial evolution of wavelength shows that fluctuations recorded with AFM are continuous independently of the regime focused on. In the case where D^* would corresponds to the onset of instability, a shift of the Rayleigh ratio would be observed at this transition. The consistency of the Rayleigh ratio measured despite the large scatter confirms the proportionality of the wavelength with the rim width. Unstable modes amplify from the early stage of dewetting. Fluctuations measured on top of the ridge respond the definition of a rising instability from a mathematical point of view for the whole dewetting scenario.

Reiter and Khanna claimed the opposite of our observations. With optical microscopy, they found no rim instability in the no slip situation [104] and at early stage. The onset of instability is initiated by viscoelastic effects [44]. The conclusion of this publication arises despite the fact that they recorded a wavelength for a rim width in the range 2-25 μm. The confusion between the onset of instability and the first undulations observed comes probably from the instrument with which they restrict their measurement. The lack of resolution of optical microscopy do not allow accurate measurements for small deviations.

Linearity of the in-plane instability A_x with the instability measured normal to the substrate A_z reported in part 6.2 links observations performed with optical microscopy and atomic force microscopy. The transition from one regime to another occurring at a small value, $A_z^* \sim 100$ nm, compared to the point where non-linearities start, happening at $A_z > 1.5\,\mu$m, demonstrates that linearity prevails on the regimes. We can therefore extrapolate results obtained normal to the substrate to the instability rising in-plane. No onset of instability is

awaited for optical microscopy measurement; instead, the low resolution of the latter technique restricts information extracted from the data to the instability rising during the second regime which creates a confusion between the onset of instability and shrinkage of rim width at valley. On DTS, non linearities of A_z with A_x lead to an immediate outgrowth of the thicker parts which form fingers quantified by the zigzag ratio in Fig. 4.5.

Solid/liquid boundary conditions The earlier growth of the zigzag ratio on DTS evidences the macroscopic impact of slippage on the protrusion of bulges and fingering. It is necessary to look at the amplitude $A_z^*(D^*)$ of the transition to get insight into the microscopic effect of slip on the instability. The transition happens at a distance in the range 20–40 μm when the film retracts from DTS and 40–75 μm from AF 1600. If we neglect the dynamics of the contact line, which is at first a proper approximation since each series covers a wide range of dewetting velocities with common limits, we can conclude that slippage is an indissociable element from the growth rate of the perturbation for the transverse flow. The onset of shrinkage at valleys appearing fastest on DTS quantifies the fact that slippage acts not only towards dewetting direction but is a multidirectional component and justifies the introduction of slippage in equation 6.3. However, one should note limitations of Brochard-Wyart and Redon's model which considers the flow at the three phase contact line only. In order to reasonably quantify the impact of slip on the entire ridge, it is necessary to extend the previous model with considerations of the full effective interface potential, including van der Waals forces, Born repulsions and an average of the rim width.

From previous results on the rim profile of the hole growth analysis, we know that slip lengths quantified with either technique reveal a dependence of values of b with temperature when dewetting takes place on substrates coated with silane layers, such as DTS [41]. More precisely, the slip length grows linearly with the inverse of viscosity independently of the method used to characterize the value [18]. The reason for the viscosity dependent behavior is still unclear, but Gutfreund et al. gave a hint for the explanation identifying a depletion layer formed at the PS/DTS interface combining x-ray and neutron scattering [51]. They claimed that surface order of a DTS coating affects the conformation of polymer chain segments adjacent to the solid boundary. Chain segments lie completely flat which we can be pictured as a layer with higher mobility than bulk polymer. The exact slip length to film thickness ratio b/H discussed in chapter 5 varies for the PS/DTS system at various temperatures from 2 to 8 at maximum. This value is significant compared to the unperturbed film thickness and allows a reliable comparison of the experiments with results obtained with simulations for the intermediate slip model. However, values of slip length remain small compare to the height recorded at the tip of the ridge h_{tip}; for instance, the rim height is larger than twenty times the film thickness for the system PS/DTS at 120 °C. The variation of slip length with temperature

can be neglected for the rim instability experiments.

Entanglement in the polymer melt On AF 1600, no temperature dependence of the slip-length is observed. In order to adjust the boundary conditions on this substrate, it is necessary to use high molecular weight polymers. Increasing the chain length of the PS molecule above the critical value M_c of entanglement effects, $M_c = 35 \, \text{kg.mol}^{-1}$ for PS [107], provokes a drastic change of the flow at the solid/liquid interface via the reduction entanglement by a factor 4 hypothesized by Brown and Russell [11] and evidenced by Bäumchen et al. [17]. The slip length follows the algebraic law $b \propto N^3$ predicted by de Gennes [26], where N denotes the number of monomers. Together with the increase of slip length with molecular weight, Bäumchen et al. noted a strong asymmetry of the rim for dewetting experiments performed with large molecules. Non-newtonian effect such as viscoelasticity were disregarded thanks to a careful selection of experiments which allow to work at Weissenberg numbers smaller than unity. This result corroborates with the conclusion of chapter 5 pointing that the transition oscillatory to monotonic profiles is solely caused by slippage.

With a similar setup, Haefner identified fingering for high molecular weight polymers with straight fronts on AF 1600 [53]. For instance, fingers of 12–13 μm length develop around 60 μm on a PS101k film; slip length for this system approximates five times the film thickness, similarly to our results of a PS10.3k film on DTS. This result is of importance to prove that fingering does not come from the influence of the hydrophobic coating produced by the silane molecules, but slippage at the solid/liquid interface. Moreover, since viscoelastic effects are neglected for these experiments, we can certify that neither molecular relaxation of entangled polymer chains nor the transition from monotonic to oscillatory profile, both arguments claimed in [44], are the reason for fingering. Bulge detaching from the ridge and leaving behind a long finger is an intrinsic characteristic to strongly slipping polymer melt.

Results obtained by Haefner, based on optical microscopy measurements, exhibit the rim instability developing during the second regime [53], *i.e.* after D^*. Working with polymer of higher M_w immediately induces a higher viscosity, a stronger force required to move the liquid. Bäumchen reported approximately three orders of magnitude difference comparing the viscosity of PS films of molecular weight varying from 1 order magnitude [13]. Since surface tension keeps rather constant in this range of measurement, we might wonder if the first regime is observed with high M_w polymer melts. Indeed, combining high viscosity with a fast growth rate of the rim width $W'(D)$ might produce large forces able to counterbalance or simply hide the growth of the rim instability during the first regime. Also, the transition from monotonic to oscillatory profile reported [17] makes this system ideal to test whether the onset of rim instability solely sets in on oscillatory decaying rims or also on monotonic decaying rims.

Fingering beginning around 60 μm if experiments are setup with a PS film of 101 kg.mol^{-1}

(PS101k) on AF 1600 such as done in [53] or with a film PS10-14k on DTS in our experiments, both systems on which the evaluated slip length is equivalent, is a proof that whether the coating results from densely packed grafted silane molecules or a spin-coated layer with a perfluorinated polymer has no impact on outcome of the dewetting process. The same remark is true for the different polymer chain lengths as long as we restrict to a flow within small Reynolds numbers and Weissenberg numbers smaller than unity. In order to come to this conclusion, it was essential to consider the spatial evolution of the system instead of the temporal dynamics, since no time characteristic such as relaxation time, as specified in [44], is awaited with our setup.

Temporal rise of the amplitude   Two regimes are also distinguished for temporal evolution of the perturbation $A_z(t)$; however, the broad range of dewetting dynamics used for all series involves to see the impact of the dewetting velocity on the rise of the amplitude. The semilogarithmic representation of $A_z(t)$, Fig. 6.3 demonstrates that the instability amplifies as a continuous process. From the non linearity of this representation, we can ensure that this process is not solely driven by the Rayleigh-Plateau instability which would involve an exponential growth of $A_z(t)$, but must include the volume uptake. Including the theory of the dynamics of the contact line in the theory of the Rayleigh-Plateau instability helps to weight the dewetting velocity on the perturbation. The good agreement between $A_z = \exp t^\beta$, equation 6.3, and data points on AF 1600 during the whole dewetting process indicates that the volume accumulation assigned by the dewetting velocity drives the process whether the whole scenario occurs within less than $1\,000$ or more than $60\,000\,\mathrm{s}$. The displacement of the three phase contact line being much larger than the rise of the ridge explains the reason why no regime is evidenced for the temporal representation of the rim instability.

From a mathematical point of view, combining both the dynamics of dewetting with the dynamics of the Rayleigh-Plateau instability is based on a naive approximations which lacks of rigor and is strongly questionable. This action was motivated by the fact that the characteristic lengths obtained for each series of a system were found within the same range despite huge variations in dewetting dynamics. Thus, the system can be perceived as a sequence of rises of the instability in static situations happening one after another. For each distance D_i, the wave grows at fastest growth rate ω_i, which would lead to a decay into droplet beads for each instant t_i if the volume of the ridge was kept constant (see chapter 10). Combined to the motion of the front, the volume of polymer in the ridge at t_{i+1} undergoes the Rayleigh-Plateau instability with a growth following $\tau_{m_{i+1}}$. In other words, the growth should be represented as an increase step by step rather than a continuous increase.

Parameters impacting the undulations   The spatial evolution of A_z enables a better understanding on the impact of temperature or dewetting velocity on the rim instability. While slippage explains the presence of fingering and an earlier rise of the perturbation compared to non-slippery systems, the increase with temperature of the distance D^* at which the transition between both regimes occurs is not defined yet. Since both the variation of temperature and the dewetting velocity are imbricated, we first deal with the impact of changes of temperature on viscosity. For liquid jets, Stone and Brenner showed that the dispersion relation evolves as $\omega \propto \eta^{-1}$ which characterizes a viscous slowing of the dynamics of the process with temperature [116]. Identically, from the theory developed by Brochard-Wyart and Redon, ω evolves as the inverse of viscosity [8]. Based on theoretical predictions, the increase of D^* observed experimentally for all series, the value A_z for a given D with temperature are counterintuitive. Viscosity cannot explain results obtained.

Variations of temperature have a direct impact on the viscosity, but also an indirect impact on the dewetting velocity via the lowering the viscous friction with the increase of temperature, which provokes a drastic change of the dynamics of the receding front. For instance, heating the systems of $10\,^\circ$C higher lead to reduce the timescale down to one order of magnitude on AF 1600. The timescale necessary to accumulate a volume equivalent to a traveled distance $D = 130\,\mu$m at $130\,^\circ$C is very small compared to the timescale of the perturbation. We can expect a possible delay of the rise of the instability since a change of temperature affects the growth rate to lower extent as depicted in Fig. 6.8. To conclude, a possible explanation of the increase of D^* comes from the dewetting velocity. The difference in dynamics is observed in the spatial evolution of A_z, but not in the Rayleigh ratio. The prefactor of equation 6.3 should be revised to include a stronger impact of the dewetting velocity v or a ratio v/v^*, with the characteristic velocity $v^* = \gamma/\eta$, which might enable to weight one velocity on another since Brochard-Wyart and Redon's theory does not explain experimental results.

As introduced in section 2.5.2, Diez et al. pointed out that contact angle impacts on the growth rate and the critical wavenumber of the instability in the static situation [33]. For $\theta > 50\,^\circ$, the increase of the growth rate with contact angle expected from numerical simulations contradicts our experimental observations since the contact angle on AF 1600 is much larger than DTS. We can therefore conclude that the flow on the boundary conditions, *i.e.* slippage, prevails over the contact angle in the dynamic case of the rivulet instability. An opposite behavior is also observed from results of the reduced critical wavenumber, which corresponds to our Rayleigh ratio. The decrease of the latter with the increase of θ is expected with the linear stability analysis while we notice with our experiments a slightly higher value on AF 1600.

Numerical simulations   The different assumptions made to give an attempt to explain the complex results we obtained in this part are hard to prove experimentally since a change of

one parameter immediately results in a change of other parameters. It is therefore required to investigate the system with simulations in order to shift one parameter only and observe the result on the perturbation. Any type of simulations on this system are, however, very difficult to investigate due to the dynamics coming from dewetting, the instability and the continuous growth of the rim. The most accurate numerical simulation defined in King et al. studies a system in between the static and the dynamic situation using a continuously growth of the base state, but introducing the wave perturbed at a wavenumber which remain constant as D increases. First steps towards the growth of the wavelength with D were investigated in [68], where Kitavtsev and Wagner followed droplet migration separated by a fixed wavelength with lubrication models in order to study how slip affects coarsening. This first step needs now to be broadened to include coarsening in the simulations, which would enable to compare the impact of the temporal evolution of the instability with the dewetting dynamics. Based on time, the system is experimentally always subject to strong variations; an easier comparison with experiments would require to present results presented as a function of distance.

Since we proved that the rim instability develops at a constant Rayleigh ratio, simulations could also be considered by adjusting the number of droplets N being always proportional to the rim width as a first step. In clear, this would mean to let the straight front traveling as $D(t)$ with $N(t) \propto D(t)$. The next step would be to investigate both out of equilibrium solutions where coarsening dominates dewetting and the opposite case. Numerical simulations of this type of system is a key to understand the increase of D^* with temperature.

6.6 Summary

- The wavelength of the rim instability grows with time following $\lambda(t) \propto t^\iota$, where ι is proportional to α, the power law of the dewetting dynamics $D(t) \propto t^\alpha$. The wavelength depends on the flow properties at the solid/liquid interface via the dynamics of dewetting.

- A common growth of the wavelength is observed when plotted as a function of dewetted distance $\lambda(D) \propto \sqrt{D}$. The Rayleigh ratio $C = \lambda/W$ is constant over D. Hence, the theory of the rim instability and of dewetting are complementary.

- Experimental values of the Rayleigh ratio agree well with values obtained for numerical simulations.

- The complex temporal evolution of the amplitude of the perturbation is explained with a simple model combining theory of the rim instability with theory of the dynamics of dewetting (equation 6.3) on AF 1600.

- The exponential growth of the perturbation $A_z(t)$ does not follow the same growth than the static situation (Rayleigh-Plateau instability), but a non linear contribution of the growth rate is expected for the perturbation certainly issued from a non constant impact of the slip length as the rim height increases.

- The two regimes observed in the growth of $A_z(D)$ are explained by a change in flow dynamics before and after the onset of the bulging regime. Above D^* the existing flow of the rim instability is combined to a transverse flow from valley to peak coming from the decrease of the rim height at valley.

- A large variation of D^* is observed for the set of experiments investigated. This difference is understood if we combine various events being the decrease of $W' = \frac{\partial W}{\partial D}$ and of the growth rate of the perturbation $\omega_q(W)$.

- Although a viscous slowing is expected as in the Rayleigh-Plateau instability, increase of temperature on AF 1600 initiate a decrease of the growth rate $A_z(D)$. The rim instability is a complex system involving the competition between the dynamics of the instability and dynamics of dewetting.

- Observation made for the rim instability rising normal to the substrate are identical to instability observed in-plane. A_z grows linearly with A_x until the bulging regime is achieved.

7 Rim instability at late stages

Unless prepared under stable conditions, each thin liquid film wetting a substrate turns into a series of liquid droplets forming different patterns, illustrated in Fig. 1.1, wether the drop detaches directly from the moving ridge or decays from a perturbed semi-cylinder initiated from two merged neighbored rims. The typical pattern known for the latter decomposition leads to a series of polygons whose size and number of segments depend on the density of holes nucleated, as discussed in [96], if solely holes are considered.

The earlier type of droplet detachment is much more intricate since the mechanism varies with the boundary conditions. A first process was presented in part 4.4 for the PS/DTS system as resulting from the formation of fingers. At equivalent volume of polymer accumulated in the ridge, illustrated in Fig. 7.1, the perturbation of the rim instability is much less amplified for AF 1600. Doubling the volume of polymer in the ridge is necessary to observe pinch-off. As a consequence, a completely different mechanism is expected from DTS.

In a first part we investigate the mechanism of droplet detachment on DTS and AF 1600 via studying the evolution of the temporal cross section of the ridge. Then we consider the stage right before the droplet detaches for both substrates and discuss the occurrence of finger length. The pattern on DTS right after breakup is finally compared to AF 1600.

7.1 Droplet detachment

Fig. 7.1 contrasts the final pattern of a dewetting front obtained on the PS/DTS system with the same system obtained on AF 1600. A clear fingering structure is developed when the thinner part of the ridge reaches $60\,\mu$m on DTS. On AF 1600, thicker parts remains fairly aligned to thinner parts of the undulated front which further retracts into the film above $60\,\mu$m, bulges coalesce and become larger. Pinch-off takes place well above 100μm with a mechanism different from DTS.

7.1.1 Mechanism on DTS

Mechanism of formation of a finger depicted in Fig. 4.5 evidences a long neck arising after the bulging regime from the dependence of the dewetting velocity with the inverse of the rim
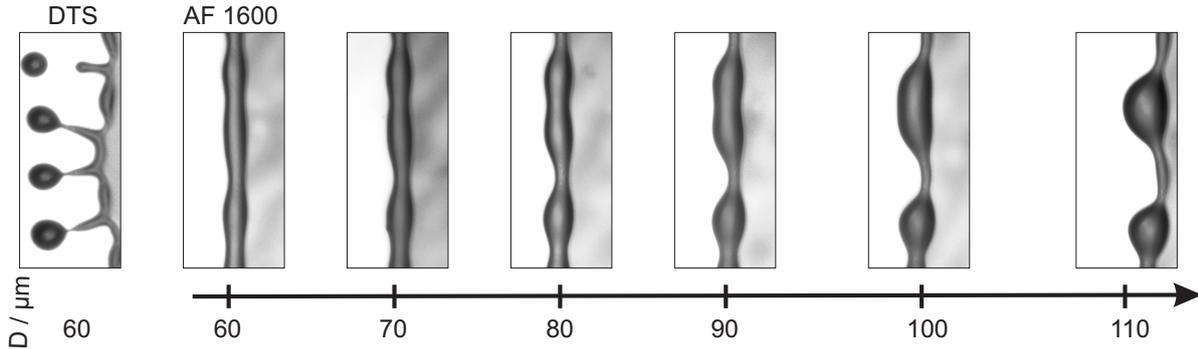
Figure 7.1: Dewetting of a thin polymer film on DTS (top) and AF 1600 (bottom) at 120 °C by retraction of an initially straight front (PS 13.7 kg.mol^{-1}, $H = 125(5)$ nm). The process stopped at $D = 70\,\mu$m on Fig. 4.1 further continues evidencing large bulges which remain attached to the ridge. Optical images of straight fronts are 80 μm wide.

width. The bridge linking the protruded bulge to the dewetting front, well known for viscous fluids in the field of liquid jets [35, 36], breaks up following a length scale ℓ_ν and time scale t_ν which read as follows [54]:

$$\ell_\nu \sim \nu^2 \frac{\rho}{\gamma}, \qquad t_\nu = \frac{\nu^3 \rho^2}{\gamma^2} \tag{7.1}$$

with ν the kinematic viscosity $\nu = \frac{\eta}{\rho}$. The time scale of droplet breakup in the rim instability is strongly embedded to the dynamics of displacement of the moving front and will therefore not be considered in the following. The length ℓ_ν evolves with the square of viscosity, the predominant parameter in equation 7.1.

We noted in section 4.5 that the pinch-off regime is reached at $D_\mathrm{m} = 34(5)\,\mu$m for dewetting temperatures ranging from 110 to 130 °C which reveals the predominance of slippage and especially the contact area of the solid/liquid interface in the breakup process. The length ℓ_ν therefore impacts on the length of the thread, discussed in the following section.

A closer look at the evolution of the rim profile was investigated with atomic force microscopy. The cross-section of the ridge is captured for various times and the corresponding distance traveled by the straight front when the sample is quenched to $T_\mathrm{s} = 90$ °C. Imaging the ridge slightly below the glass transition temperature allows an instant capture of rim instability, in a 'frozen'-like stage. The sudden decrease of temperature to T_s provokes a minor decrease of the overall height which can be neglected because of the small expansion coefficient. The same characteristics of the film are found in this *ex situ* measurements compare to *in situ* measurements, the quenching and further rise of temperature of approximately 30 °C takes place within seconds. In order to keep the measurement consistent, we have always measured rim profiles near the highest regions of the ridge, *i.e.* close to peaks. This implies that

sometimes we had to shift the position of our measurement because peaks slightly move along the ridge. We should note that quenching doesn't affect the temporal evolution recorded as a decrease of $30\,^{\circ}C$ is done within few seconds.

The comoving frame of each cross-section is weighed with the maximal coordinates of the tip of the rim (ξ_c, H_c) in Fig. 7.2(a). The representation enables a direct comparison of the curvature for each profile. The superimposed curves observed for the part of the rim starting from the three phase contact line, $\xi = 0$, to the tip of the ridge, $\xi = \xi_c$ confirms the self similar growth of the rim. The tail of the rim asymptotically reaches $\xi > 4.5\xi_c$ down to 0 at early stage of dewetting and decreases to $\xi \approx 2.5\xi_c$ right before pinch-off. The rim rounds due to Laplace pressure until a neck builds up at the tail of the rim, which provokes an increase of the ratio ξ/ξ_c. The later cross-section is undisplayed in Fig. 7.2a for clarity.

(a) DTS at $110\,^{\circ}C$

(b) AF 1600 at $120\,^{\circ}C$
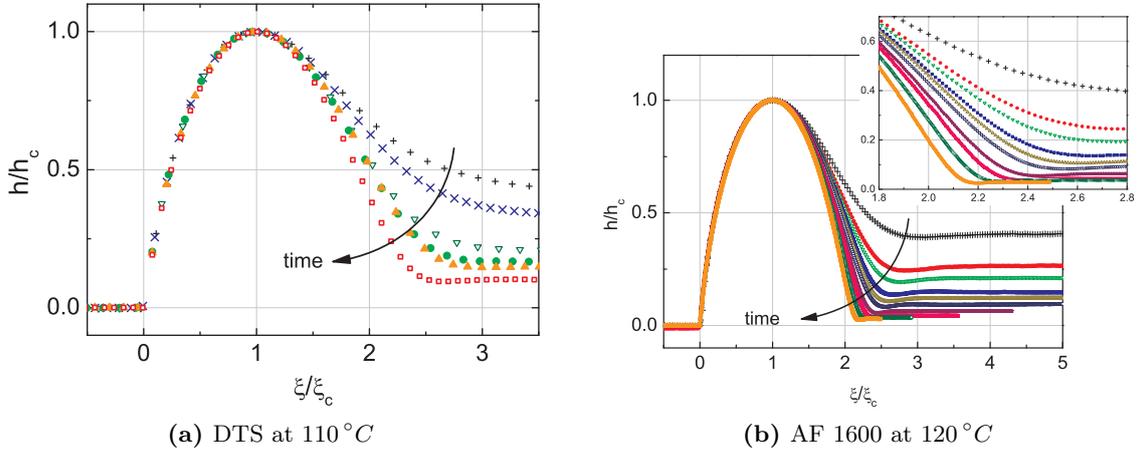
Figure 7.2: Rim profiles of straight fronts of a 115(5) nm thick PS(10.3k) film. Normalized h, ξ with the coordinates at maximum h_c, ξ_c illustrates the approach of a universal shape. The tail of the asymmetric rim plunges into the film around $\xi/\xi_c = 3$ at early stage to finally reach a value around 2.5 on DTS before the fingering regime is reached (a). In contrast, the asymptotic growth is approached on AF 1600, $\xi/\xi_c = 2.1$ at late stage. The density of point of profiles of the PS(10.3K) film 115(5) nm thick was reduced for each curve for clarity.

7.1.2 Mechanism on AF 1600

The same representation of rim profiles weighted with the maximum coordinates is provided on AF 1600 in Fig. 7.2(b). As before the self-affine growth of the rim for the whole dewetting process is evidenced with the superimposed curves depicted from the part $\xi = 0$ to $\xi = \xi_c$. The back side of the rim also starts with an elevated value of the asymptotical extrapolation of the tail, $\xi \approx 3$ at the beginning of the dewetting experiments, which decreases over time. In

contrast to DTS, the rim on AF 1600 tends to the perfect symmetrical shape with a value of the tail of $\xi \approx 2.1\xi_c$, the semi-cylinder being reached for $\xi = 2\xi_c$. The shape of the bulge is close to a sphere before the droplet detaches the ridge. As a consequence, the droplet pinches-off naturally as it reaches an equilibrated state. Forces at both sides of the ridge equilibrate, the force rising from the Laplace pressure becomes larger than the viscous force linking the bulge to the moving front.

7.2 Before pinch-off

The stage before the droplet detaches the moving front shows significant differences if the rim instability developing at late stage on DTS is compared to AF 1600. On the one hand, the size of the bulge is much larger for the system PS/AF 1600 due to the larger distance traveled by the front before D_m is reached. On the other hand, the bulge remains fairly aligned to the rest of the moving front on the same system whereas a strong deviation is obtained on DTS system due to the finger build between the bulge and the moving front.

7.2.1 Impact of viscosity on the finger length

The fingering regime, shown with optical micrographs of Fig. 7.3(a)-(c) right before the system enters the pinch-off regime, evidences an increase of the finger length L_f as the temperature of dewetting is reduced on DTS. The rise of the finger length, in plane length measured perpendicular to the dewetting front from the back side of the droplet to the apex of the finger before it merges into the ridge and decays into the film, with viscosity follows the internal length ℓ_ν introduced in the previous section. The power law, however, should be verified with further experiments.

7.2.2 Finger or thread?

The scenario of the late stage of the bulging regime and the pinch-off regime illustrated in Fig. 7.4 indicates that the breakup process is rapid takes place within approximately 30 s on AF 1600 at the given temperature. This short time is probably due to the low viscosity and the large velocity of approximately $400\,\mathrm{nm.s^{-1}}$ that the straight front moves. At equivalent viscosity provided in Fig. 7.1, the morphology of the breakup process on AF 1600 is the same as depicted in Fig. 7.4, but the time scale rises up to 1200 s for a velocity v of the moving front of $15\,\mathrm{nm.s^{-1}}$. With approximately twice the dewetting velocity, the breakup process takes place within 1000 s on DTS, see figures 4.5; the timescale necessary for droplet detachment on

(a) optical micrographs of experiments performed at (1) 110 °C, $t = 13320\,\mathrm{s}$, $D_\mathrm{p} \sim 35\,\mu\mathrm{m}$, $D_\mathrm{v} \sim 68\,\mu\mathrm{m}$, (2) 120 °C, $t = 4680\,\mathrm{s}$, $D_\mathrm{p} \sim 39\,\mu\mathrm{m}$, $D_\mathrm{v} \sim 62\,\mu\mathrm{m}$ (3) 130 °C, $t = 168\,\mathrm{s}$, $D_\mathrm{p} \sim 29\,\mu\mathrm{m}$, $D_\mathrm{v} \sim 49\,\mu\mathrm{m}$.

(b) Finger length as a function of annealing temperature for experiments performed on DTS.
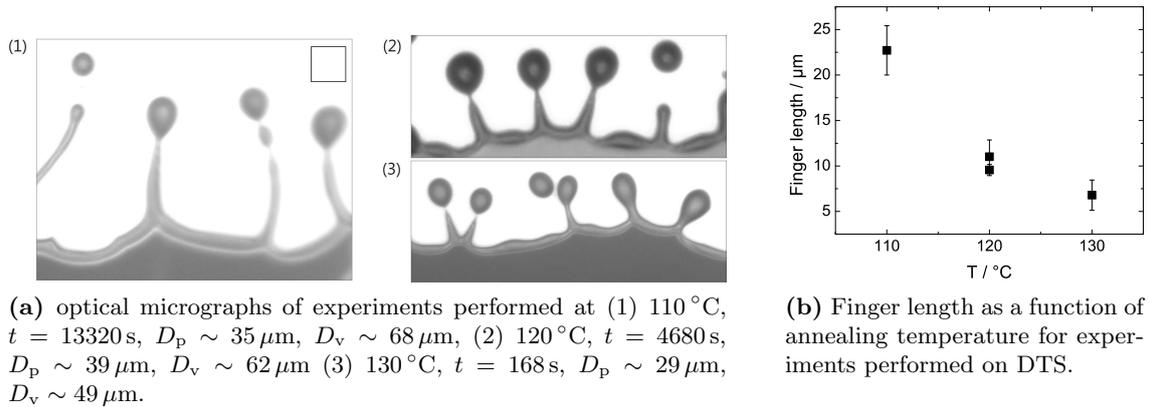
Figure 7.3: Rim instability for dewetting experiments performed on DTS shortly before the pinch-off regime is entered. (a) Optical micrographs are depicted with the same scaling with the square in (a1) of $10\,\mu\mathrm{m}^2$. The finger length varies with temperature (b). Experiments performed for a 125(5) nm film of PS(13.7K).

DTS is therefore increased compare to AF 1600 at equivalent viscosity.

Besides times and distances, it seems important to compare the ratio between the diameter of the droplet and the width of the neck. On AF 1600 the value averaged over several series at various temperatures gives a figure, 7.3(7), approximately three times larger than the same ratio on DTS.

In any case a thin thread of polymer links the detaching droplet to the moving front. This thread, well known in the field of decaying liquid jets with polymeric fluids, is always present at the pinch-off regime. On AF 1600, the neck changes into a tip of polymer which detaches immediately the drop formed. In contrast, a finger of length increasing with viscosity builds up on DTS from the local gradient of the dewetting velocity, varying with the inverse of the rim width.

Comparing optical micrographs right after the velocity measured at peaks reduces to zero, similarities might be found between both systems. However, the transverse flow from valley to peak differs between both systems. If friction at the solid liquid interface is high, the flow is only driven by the Laplace pressure. On the other system, fingering requires material uptake which originates from a transverse flow larger on DTS despite the same viscosity and same range of dewetting velocity used than on AF 1600. This observation therefore suggests a hydrodynamic slip behavior present in any direction of the flow, slippage is isotropic.
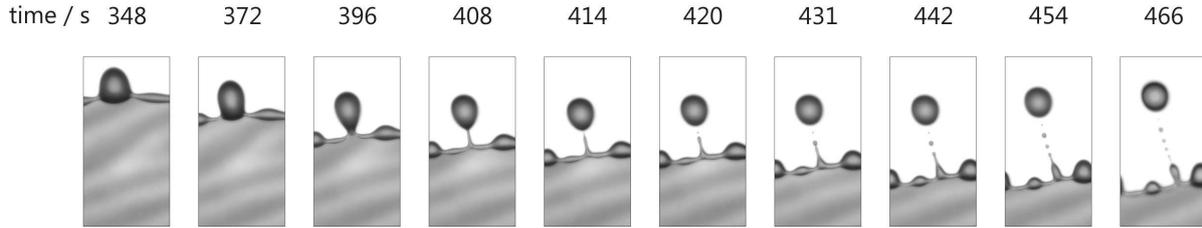
Figure 7.4: The transition from bulging regime to droplet detachment on AF 1600 is depicted with a series of snapshots of one bulge at dewetting times varying from 348 s to 466 s. Distances traveled by the 115(5) thick PS(10.3K) film at 135 °C range at thicker part from 126 to 141 μm and thinner parts from 140 to 200 μm. The $45 \times 90\,\mu$m^2 optical micrographs evidence a secondary droplet of diameter much smaller than the initial drop.

7.3 After breakup

The presence of a finger or a simple neck at pinch-off initiates two different patterns via the formation of the primary droplet and secondary droplet. The latter must not be mixed up with a satellite drop which is observed under certain conditions. We compare in this part the three types of droplet obtained for both systems with the knowledge obtained in the field of physics of liquid jet [35] in order to explain the final patterns illustrated on Fig. 7.5.

7.3.1 Primary droplets

Majors differences of the primary droplets found between DTS and AF 1600, respectively Fig. 7.5(a) and (b), are the droplet diameter and the lateral distance between each drop, both of which are largest on AF 1600. This observation corroborates previous results on the value of D_{m}, the maximal distance traveled by thicker parts before breakup, discussed in chapter 4. D_{m} represents the volume of material accumulated in the course of dewetting[1]. The value of D_{m} being three time larger on AF 1600 than on DTS necessarily involves a larger size of the rim and *a fortiori* of the droplet at breakup due to conservation of volume.

The distance between droplets is also interconnected to D_{m}. We showed in section 6.1 that the fastest growing wavelength selected for the growth of the perturbation is proportional to the width of the ridge $W(D)$ and follows the square root of the distance traveled by the moving front, $\lambda \propto \sqrt{D}$. The result of the smallest value of D_{m} obtained on DTS implies a shorter distance on DTS as depicted in Fig. 7.5.

We should also note that the alignment of the primary droplets asserts from the good quality of the dewetting experiments. Side effects such as pinning or other inhomogeneities which lead

---

[1]$D_{\mathrm{m}}(t) = V(t)/(L.H)$ where the size of the image L and the initial film thickness H are constant, but the volume of polymer accumulated $V(t)$ varies with time.

to irregularities in the rise of the undulated ridge involve a premature pinch-off. Under these circumstances primary droplets are recorded at a wide range of D_m.

7.3.2 Secondary droplets

The size of the secondary droplet observed on optical micrographs of Fig. 7.5 is much larger on DTS with a ratio between the primary to secondary drop close to unity. On AF 1600 the diameter of the first drop is seven times larger than the second one. We have to use the knowledge achieved in the hydrodynamics of liquid jets to understand the origin of this secondary droplet [35, 36]. The thread of polymer is strongly stretched. The pinched region, termed tip, of length ℓ_tip has no solution using the usual hydrodynamics description after breakup. The tip recedes into the detached thread at a velocity proportional to $|t|^{-1/2}$. The high retracting velocity initiates a rim in the vicinity of the newly created contact line. This velocity competes with the dewetting velocity of the retracting front. The newly elongated thread formed with a smaller droplet rapidly detaches from the moving tip or finger as previously described.

Right after pinch-off, the dewetting velocity at the tip v_tip is much slower than the velocity at valley in case a finger is formed (slippery system). The finger further grows and v_tip slows down until the droplet rapidly detaches. The width of the neck on AF 1600 is much smaller than the finger and no accumulation of liquid in the tip is expected since the ratio v_tip to v_v approximates unity in the no-slip case. Consequently, slippage affects the final pattern via the presence of fingers in the timescale of dewetting considered.

(a) Optical micrographs of a PS film on DTS at 120 °C

(b) Optical micrographs of a PS film on AF 1600 at 135 °C
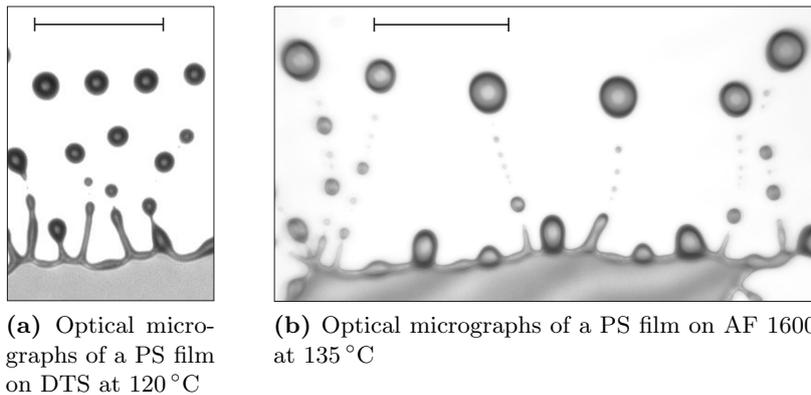
Figure 7.5: Comparison of the final pattern of the rim instability for a system passing through the fingering regime (a) before droplet detach and a system where pinch-off occurs directly after the bulging regime (b). The scale bar of 50 μm places in both optical micrographs show a difference in the wavelength, the size of the primary and secondary drops and their aspect ratio. Both films for each system are 125(5) nm thick and prepared with PS(13.7K).

7.3.3 Satellite drop

Despite the large radius of the primary drop relative to the secondary drop obtained on AF 1600, the latter shall not be confused with a satellite droplet which is created after either side of the thread is pinched-off close to thicker parts and collapse into one drop or more if the newly formed microthread is prone to further destabilizing. A symmetrical and an asymmetrical situation are found in dewetting thin films depending of the method of formation of the thread.

The most common case where satellite drops are found happens when neighboring holes coalesce. The thread formed illustrated is in a steady state from the point of view of the hydrodynamics of dewetting, *i.e.* the axis of the thread is fixed. Slight displacements of the three phase contact line arise from dynamics of the rim instability. The selected wavelength grows exponentially proportionally to the width of the ridge. The newly formed thread thins faster than breakup, symmetrical pinch-off is localized near the drop. The timescale the drop retracts is small due to the small amount of material involved. A secondary satellite drop is produced if the thread is very thin and long. The maximal amount of material accumulates in the middle of the thread. The secondary satellite droplet stands between the main drop and the satellite drop.

A satellite drop is also observed at the neck of the bulge during the pinch-off process. Before breakup a microthread of length ℓ_{thres} depending on the hydrodynamics of the thread creates:

$$\ell_{\mathrm{thres}} = 5\ell_{\nu} \left(\frac{\ell_{\mathrm{T}}}{\ell_{\nu}} \right)^{0.401} \qquad \text{where} \qquad \ell_{\mathrm{T}} = \sqrt{\frac{k_{\mathrm{B}}T}{\gamma}} \tag{7.2}$$

ℓ_{T} is the thermal length scale.

7.4 Discussion

Coalescence of neighboring holes depicted in Fig. 1.1 is one source only of droplet production if a thin PS film dewets an AF 1600 substrate. A droplet may also detach from a moving ridge, as for DTS, if the distance D_{m} traveled by the front is large. After pinch-off, the pattern depicted by in Fig. 7.1 shows similarities with DTS, but the mechanism of formation significantly differs. The formation of bulges is initiated by the Rayleigh-Plateau instability independently of the boundary slip conditions, as evidenced in chapter 6. The mechanism of droplet detachment, however, is inherent of the hydrodynamic slip.

Pinch-off based on mass conservation, Reiter and Sharma proposed that the breakup of the rim instability sets in on slippery systems when the rim width reaches a certain threshold value $W_{\mathrm{break-off}}$ which reads

$$W_{\mathrm{break-off}}^2 = \frac{l_{\mathrm{mean}}h_0}{C\theta}, \tag{7.3}$$

where the constant $C = 0.1$ accounts for the asymmetric shape of the rim and l_{mean} is the resulting distance between droplets [105]. The rim width presented in equation 7.3 in fact shows the importance of the contact area at the solid/liquid interface. Authors observed the increase of l_{mean} with film thickness, but did not comment on how to predict the value. At breakup the driving force equilibrates dissipative forces F_{v} and F_{s} respectively due to viscous friction within the liquid and friction of the liquid molecules at the solid/liquid interface, slippage, against the driving force.

Our latest experiments demonstrate a larger distance D_{m} obtained on AF 1600 than on DTS systems independently of the dewetting dynamics. This result first proves that the breakup mechanism takes place on systems which do not necessarily involve slip at the solid/liquid interface since the slip length recorded on AF 1600 is very low and is neglected in the dewetting process [16]. Moreover, equation 7.3 must be completed with a term including the slip length b or the slip length relative to the film thickness b/h_0. Changing the temperature of dewetting showed that D_{m} is purely independent of the dewetting velocity and viscosity on highly slippery systems, but decreases, as does the other transition distance D_{b}, with the increase of viscosity is slippage is neglected. This implies that equation 7.3 requires also a component accounting for viscous dissipation. Measuring the distance of breakup is a good method to determine the area of polymer melt in contact with the substrate which is necessary to determine driving and dissipative forces. A universal equation which predicts D_{m}, however, is difficult to determine and splitting the slip and no-slip situations sounds necessary.

Fingering In opposition to the identical distance D_{m} recorded on DTS at various temperature, the finger length clearly increases with viscosity. The same feature was observed with the increase of molecular weight by Neto et al. on OTS [89] and by Haefner on AF 1600 [53]. Bäumchen et al. evidenced on the latter system a linear growth of the slip length with the molecular weight above a critical molecular weight M_{c}, where entanglement effects cannot be avoided [17], $M_{\mathrm{c}} = 35\,\mathrm{kg.mol}^{-1}$ according to [107]. The fact that the length of the neck remains in the same range below M_{c}, but the finger length abruptly increases with molecular weight above the critical value [53] demonstrates a dependence of the finger length to slippage prevails over viscosity. Fetzer et al. showed a variation of slip length with the inverse of temperature on DTS [41]. Consequently, the long finger we observe in Fig. 7.3 at 110 °C stands for the large slip length to film thickness ratio.

The width of the finger depicted in Fig. 7.3(a) is approximately as large as the width of the rim at valley. The amount of material accumulated in the ridge in the region where fingering builds up is therefore much larger than in the region the furthest away from the finger. The accumulation of material along the straight front, uniform from the homogeneous film prepared, undergoes a flow of material when in contact with the ridge. The gradient of material flow cannot be explained by the impact of the Laplace pressure coming from the curvature of the three phase contact line solely. We explain the transverse flow of polymer by an isotropic slippage. This explanation also helps to understand why the amplitude $A_z(D)$ grows with higher kinetics on slippery substrates in the bulging regime.

After breakup A qualitative analysis of the phenomena appearing after breakup are explained based on the breakup of liquid jets which implies to work under the no-slip boundary conditions. The impact of slippage on the final pattern depends on whether the fingering regime or the bulging regime precedes breakup. The comparison between the diameter of the primary droplet and the secondary droplet indicates the presence of slip or not. Further investigations, however, are necessary to use an optical micrograph of the final pattern as a fingerprint of the slip length found in the system. In order to get a quantitative comparison, further work should be carried on a simpler system such as the impact of slippage on a fiber deposited on a substrate decaying into droplet via the Rayleigh-Plateau instability. First trials are provided in chapter 10.

The appendix of polymer appearing after pinch-off on AF 1600 arises from the competition between the timescale of the relaxation of the three phase contact line after breakup and the timescale of dewetting. Ondarcuhu and Veyssie investigated the case where straight front is immobile [92]. A perturbation of large amplitude initiated along the ridge relaxes exponentially at a rate $\omega \propto (\gamma\theta^3/\eta)q$ with $q = 2\pi/\lambda$. If the three phase contact line was anchored to the surface, we could expect the appendix to rejoin the ridge to lower the energy of the system. Indeed, the Rayleigh condition is not observed anymore after pinch-off due to the sudden decrease of the rim width after droplet detachment which is now small compared to the large wavelength. We are in the large wavenumber condition in which stage Ondarcuhu and Veyssie predicted a decay rate evolving as $\omega \propto q$. The large decay rate suggested, however, do not seem to be fast enough to compete with the dewetting rate. Polymer accumulation involves a predominance of the rim instability over the relaxation of the front.

7.5 Summary

- The final stage of droplet pinch-off observed on DTS at $D \approx 60\,\mu$m contrasts with the scenario observed on AF 1600. The bulge remains directly connected to the ridge even though the distance traveled by the moving front was doubled.

- Normalizing cross sections with the coordinates at maximal height evidence an asymptotic approach of the rim. However, the rim on DTS is asymmetrical before a finger is formed, whereas the shape of a semi-cylinder is almost reached on AF 1600.

- The strong impact of slippage in the DTS case predominates over viscosity on the mechanism of droplet detachment. The same distance D^{m} is obtained changing the temperature of the system. In contrast, length of the finger strongly increases with viscosity. Cohesion forces dominate slippage if the motion of the ridge is limited because the contact angle is observed at either side of the ridge.

- The very sudden droplet detachment observed on AF 1600 is the consequence of forces being equilibrated following the almost ideal semi-cylinder formed on this substrate.

- The diameter of primary droplets is very large on AF 1600 compared to the diameter of the secondary droplet. The ratio of both diameters is much larger in the no-slip case because the AF 1600 system does not go through the fingering regime.

- Satellite drops eventually appear between the primary and a secondary droplet depending whether a thin thread is left over during the pinch-off process.

8 The film thickness, a parameter to determine the extent of the slippage in the flow profile?

Redon et al. interpreted a change on the dewetting dynamics ($D \propto t^\alpha$) for two identical PDMS systems where variation of film thickness ranged around two orders of magnitude as the measurement of slippage at the solid/liquid interface in one case [102]. Similarly, Brochard-Wyart et al. reported the presence various stages in the dewetting dynamics from the first motion of the three phase contact line until the rim height achieved orders of magnitude larger than the initial film thickness [9]. The importance of the dissipation mechanism at the interface seems to vary inversely with the size of the rim. Although normalizing the slip length with the initially prepared film thickness is a good method for universal comparison, comparing the slip length relative to the rim height is as important.

The impact of the rim instability relative to the rim height is tested in this chapter in the strong slip situation with a PS film of various initial film thicknesses. We combine knowledge on the evolution of the rim instability, the rim shape and the dynamics of the growth of the rim height obtained in the previous chapters to explain the impact of slippage on the rim instability and consider dewetting experiment as a tool used quantify to what extend the flow is perturbed by slippage. We extend latest results on the impact of film thickness first on slippage then on the dewetting dynamics to the late stage required to study the rim instability. We explain the results obtained with optical microscopy of dewetting experiments for various film thickness and discuss the use of this technique as a model to compare flow properties in the rim with and without slip.

8.1 Impact of the film thickness on the slip length

Variations of slippage behavior observed for dewetting experiments with thickening of the ridge previously reported occur if the difference between initial and final rim width are huge. With experiments performed with a PS film of thickness ranging from 50 to 230 nm Fetzer et al. found the same slip length using either the hole growth analysis or the rim profile analysis for the strong slip system [41, 38, 39]. The same is true for the no-slip system [13].

The rim profile analysis consists of evaluating the slip length using a fit of the tail of the

Figure 8.1: Optical micrograph of a film of PS(10.3K) retracting from AF 1600 at 140 °C. The thicker rim surrounding the hole (right) is obtained from a doubled film thickness compare to the initial one $H = 115(5)\,$nm (left). The scale bar of $50\,\mu$m evidences a larger wavelength for thicker ridge.
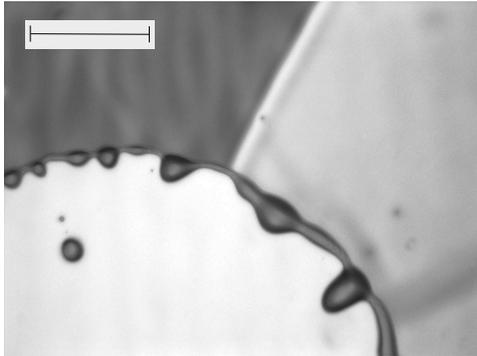
rim plunging into the unperturbed ridge until the rim height reaches approximately 200 nm. Consequently, this method takes into account the first hundreds of nanometers of the rim. Similarly, The hole growth analysis is based on the motion in the vicinity of the contact line. These two methods might not be the best indicator for the impact of slippage over the entire ridge.

8.2 Impact of the film thickness on dewetting dynamics

Fig. 8.1 depicts a bimodal polymer film retracting from a Si wafer covered with AF 1600. The dried zone (white area), imaged for a radius of the hole larger than $50\,\mu$m, is adjacent to a region of the PS film of thickness H of approximately 130 nm (dark grey zone) to another region on the right where the thickness is doubled. This type of system is easily prepared by folding the PS sheet on the already coated film or by picking a second PS film on top of the first one during the floating step. The resulting film formed of twice the initial thickness is considered as homogeneous since we are working below entanglement length, *i.e.* the healing process occurs. We do not consider the region of the film close to the step discussed in [81]. The low molecular weight used for this system allows to neglect the impact of slippage on the dewetting dynamics and to concentrate in the following on the impact of film thickness on the growth of the rim width and the evolution of the dewetting velocity which we analyze in a first part. We then discuss results where slippage predominates over viscous dissipation.

Impact of the film thickness on the rim width

The spatial evolution of the rim width follows equation 8.1 where C_s is a value accounting for the accumulation dynamics of the polymer per unit length which is constant in the studied case and discussed in details in chapter 9. An increase of the film thickness of a factor 2 therefore

involves a growth of the rim width of a factor $\sqrt{2}$ compared to the initial situation.

$$W(D) = C_{\mathrm{s}}\sqrt{H}\sqrt{D} \qquad (8.1)$$

Contrasting the part of the ridge, dark region at the perimeter of the hole in Fig. 8.1, plunging into the film of thickness H with the neighboring part of thickness $2H$, it seems obvious that the rim width thickens with the film thickness. A qualitative agreement is found with the previous chapter.

Impact of the film thickness on the dewetting velocity

Dewetting velocity V is composed from a term v_{v} accounting for the viscous velocity contribution, left part of equation 8.2, and a term v_{s} standing for the slip velocity. Studying both terms separately is rendered possible plotting the velocity V as a function of the inverse of the square root of the dewetted distance, as introduced in section 2.4.2. From the value of the velocity obtained when the dewetted distance becomes infinite, Bäumchen proved that the constant of the viscous part C_{v} is a parameter depending on contact angle and viscosity solely [13]. As a consequence, an increase of the film thickness do not affects the dewetting dynamics when the slip contribution of the velocity is neglected.

$$V = C_{\mathrm{v}}\frac{|S|}{\eta} + \frac{|S|}{3\eta}\frac{b}{W(D)} \qquad (8.2)$$

Fig. 8.1 gives a clear evidence that the previous argument is correct. Disregarding the thicker parts coming from the latter stage of instability, we observe that the contact line grows at the same dewetting velocity despite the variant growth dynamics of the rim induced from the two film thicknesses. With the same driving force and under weak slippage at the solid/liquid interface, the moving velocity of the three phase contact line is independent of the film thickness.

In case the dewetting dynamics depend on the balance of the driving force with dissipation mechanisms based on viscosity dissipation and friction at the solid/liquid interface, we face the faster growth rate of the rim width as a function of the dewetting distance. The slip contribution of the dewetting velocity v_{s} grows theoretically with a factor $\sqrt{2}$ when the film thickness is doubled.

8.3 Impact of the film thickness on the wavelength

The advanced stage of dewetting presented in Fig. 8.1, obtained for a hole of radius larger than $70\,\mu$m, enables a direct estimation of the wavelength via the substantial size of bulges. The distance separating two bulges approximates $10\,\mu$m for the ridge attached to the film of thickness H, whereas this distance is larger than $30\,\mu$m when the film thickness is doubled. This observation is directly correlated to the dependence of the rim width with film thickness discussed below. The wavelength of the rim instability grows proportionally to the rim width. Consequently, the larger rim width found at a given dewetted distance where the film is thicker leads to a longer wavelength of the perturbation in this region.

The transition of the rim instability from the undulation regime (I) to the bulge regime (II) was explained in section 6.3.3 to originate from the sudden sinking of the spatial growth rate of the rim width W' at D^*. The Laplace pressure of the rim instability applied along the ridge becomes higher than the pressure of the flow initiated from the accumulation of polymer from the three phase contact line. The spreading parameter, independent of the film thickness, initiates a driving force at the three phase contact line which is identical whether measured on the usual system or on the same system with twice the film thickness. The fact that the growth rate W' decreases slower for thicker films impacts directly on the balance between the Laplace pressure and the pressure produced by the flow. Thickening of the film might therefore have a direct incidence on the transition time and distance from one regime to another.

8.4 Impact of film thickness on the rim instability

We investigate with optical microscopy the displacement of the liquid front for dewetting experiments taking place on DTS at a film thickness varying in the range 50-230 nm. Experiments run at identical temperature ($T = 120$ °C) were examined using the method presented in part 4.4, which consists of measuring the dewetted distance at thicker regions D_{peak} and the neighboring valley D_{valley}, respectively represented by filled and open symbols in Fig. 8.2.

The pattern obtained for each film thickness is clearly comparable to the pattern described earlier in chapter 4 which implies that the rim instability passes through all three regimes, undulatory, bulging and fingering before a droplet detaches the ridge. The analogy with previous results obtained on DTS suggests that dewetting occurs under slippery conditions since the difference between thicker and thinner regions ($D_{\text{valley}}(t) - D_{\text{peak}}(t)$) is large at late stage of dewetting compared to the value $D_{\text{peak}}(t)$, and the ridge enters the fingering regime before the droplet pinches-off the ridge. We can also assert the presence of slippage by the algebraic power law followed by $D_{\text{peak}} \propto t^\alpha$. The averaged value of the coefficient $\alpha = 0.71(1)$ calculated
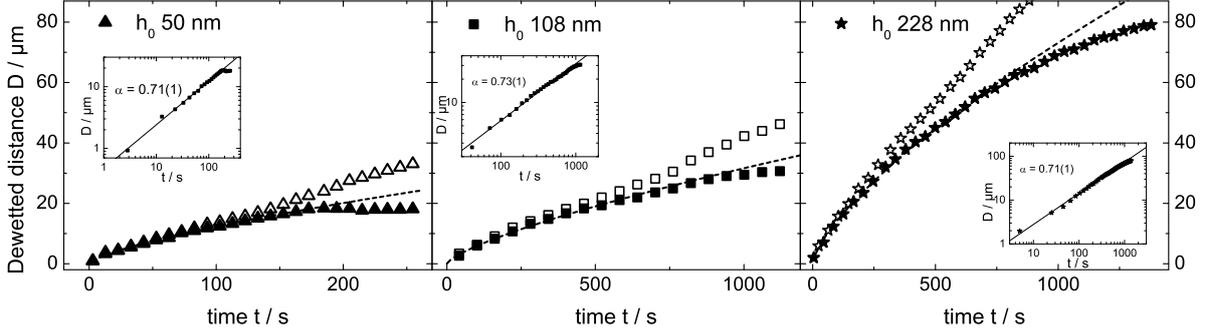
Figure 8.2: Retraction dynamics of a polymer straight front on DTS recorded at peak (filled symbols) and valley (open symbols). The shape of each curve reminds of the dewetting dynamics of the rim instability passing through 4 regimes as in Fig. 4.2. The characteristic distance at droplet detachment grows with the film thickness. Slight changes in viscosity, PS(10.3K) and PS(13.7K) used at 120 °C, do not alter the results for a given film thickness H, as illustrated in Fig. 4.6(a). The solid/liquid boundary condition revealed in the inset the coefficient α corresponds to a strong behavior. The number of point was reduced for clarity.
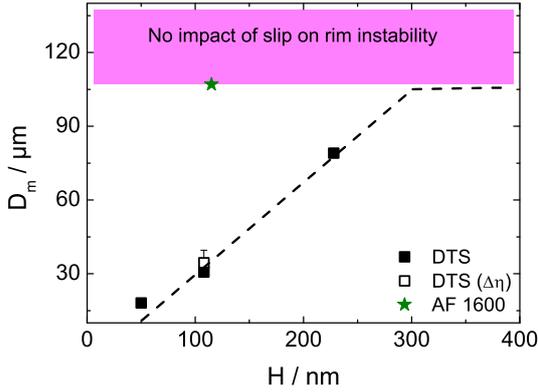
Figure 8.3: The distance of the droplet detachment D_m is displayed as a function of the initial film thickness H of the system for dewetting experiments occurring at 120 °C. The guide to the eye, dashed line, illustrates a growth on DTS with H which reaches a plateau value extrapolated from the D^m obtained on AF 1600. The colored region would suggest an domain where slip does not impact on the rim instability.

over all three systems evidences that slippage impacts under the same qualitative manner on the dynamics in the direction of dewetting.

The range of film thickness and slight changes in viscosity $(2.1 - 2.7.10^{-5}\,\text{Pa.s})$ investigated for the experiments affect the dynamics of the three phase contact line as discussed in the previous part. According to results obtained in section 4.5, the characteristic distance setting the transition between all three regimes and the maximal distance D_m recorded at peak before the droplet pinches-off are not affected by changes in dewetting dynamics. Consequently, various changes in the dewetting velocity induced by the experimental setup are neglected for this study.

Let now concentrate on the distance D_m traveled by the thicker part of the ridge before the droplet is released. We observe that D_m slightly increases from 18 to 30 μm when the initial film thickness H passes from 50 to 108 nm. Further doubling the film thickness to 228 nm

(a) $H = 50\,\text{nm}$, $t = 112\,\text{s}$, $D_\text{p} = 13.3\,\mu\text{m}$, $D_\text{v} = 14.8\,\mu\text{m}$

(b) $H = 108\,\text{nm}$, $t = 480\,\text{s}$, $D_\text{p} = 18.6\,\mu\text{m}$, $D_\text{v} = 21.0\,\mu\text{m}$

(c) $H = 228\,\text{nm}$, $t = 277\,\text{s}$, $D_\text{p} = 29.3\,\mu\text{m}$, $D_\text{v} = 32.7\,\mu\text{m}$

(d) $H = 50\,\text{nm}$, $t = 258\,\text{s}$, $D_\text{p} = 18.1\,\mu\text{m}$, $D_\text{v} = 33.1\,\mu\text{m}$

(e) $H = 108\,\text{nm}$, $t = 1140\,\text{s}$, $D_\text{p} = 30.6\,\mu\text{m}$, $D_\text{v} = 47.1\,\mu\text{m}$

(f) $H = 228\,\text{nm}$, $t = 1380\,\text{s}$, $D_\text{p} = 79.1\,\mu\text{m}$, $D_\text{v} = 119.3\,\mu\text{m}$
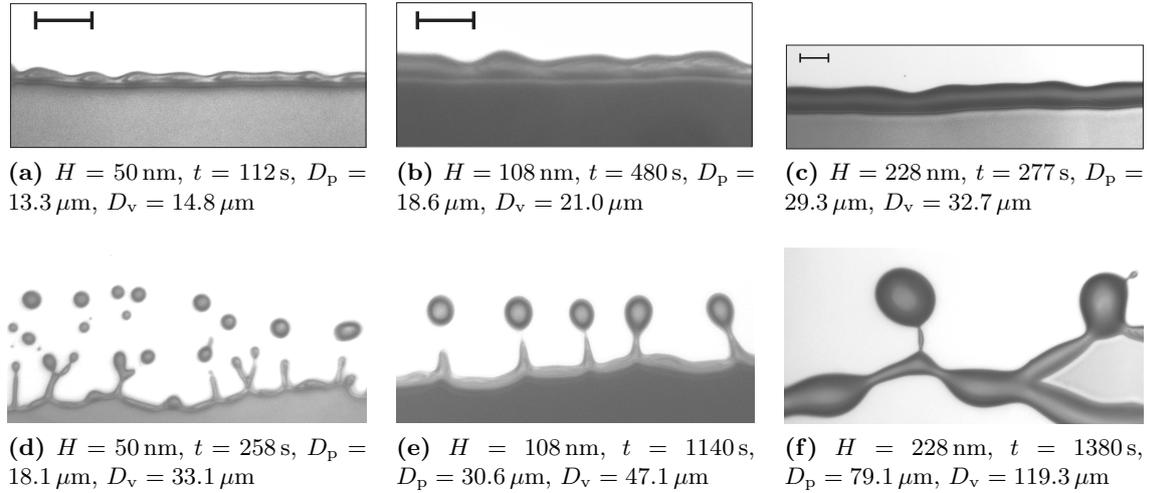
Figure 8.4: Two regimes of the rim instability are pictured from dewetting experiments rising on DTS for various film thicknesses H. The top row illustrates the early stage of dewetting, whereas the bottom row the pinch-off instability.

provides a droplet release at $D_\text{m} \sim 79\,\mu\text{m}$. The increase of D_m with film thickness reported in Fig. 8.3 occurs despite the fact that we are working with a slip length which is the same for all experiments performed on DTS.

The ratio slip length to film thickness remains large for the range of film thicknesses investigated. Dewetting experiments take place in the strong slip regime according to the definition of Münch et al.. However, the thickening of the rim width with the square root of the distance traveled by the liquid front involves a flow profile which is less affected by slippage as dewetting proceeds. The slip length relative to the rim height decreases with D. The ratio $b/H(D)$, where $H_0(D)$ is a theoretical rim height of an unperturbed ridge calculated from the volume of polymer accumulated in the ridge at D, becomes rapidly smaller than unity above D^*. The larger the initial film thickness, the faster the ratio decreases.

The Rayleigh-Plateau type instability developing along the ridge is driven by surface tension. On AF 1600, we have seen in the previous chapter that the process of droplet detachment results from the equalized force applied at both sides of the ridge at late stage due to the symmetrical shape of the rim. The rim instability develops free from slippage, the droplet detaches the ridge at $D_\text{m} = 105\,\mu\text{m}$ under the same experimenting conditions than DTS. The increase of D_m with film thickness on DTS gives evidence that the impact of slippage on the rim instability reduces with the b/H ratio. The extrapolated D_m with film thickness, dashed line in Fig. 8.3(a), suggests that the maximal distance traveled by D_peak reaches the zone where the rim instability develops free from slippage.

The previous statement is confirmed by the morphological aspects of the ridge depicted in Fig. 8.4 presented at early stage (a)-(c) and late stage (d)-(f). A strong asymmetry of the ridge is observed while the instability develops on thinner films (a) coming from the dry side of the ridge which is highly undulated in contrast to the wet side of the ridge which remains fairly flat. This contrast becomes much less pronounced as the film becomes thicker (b). The wet side of the ridge starts to undulate for the largest film thickness (c).

The impact of film thickness on the morphology is also observed on the shape of the final pattern and the distance separating each droplet from its neighbor as depicted in Fig. 8.4(d)-(f). Large fingers of width approximately the same as the diameter of the droplet are created for the 50 nm thick film (d). The aspect ratio droplet diameter to width of the finger increases drastically with the film thickness (e). Parallel to the reduction of the width of the finger, we observe a severe reduction of its length which becomes smaller than the droplet diameter. The rim instability reaches a critical point where the fingering regime is hardly defined. These observations prove that the process of droplet detachment is strongly dependent of the ratio b/H_{v}. A long finger is observed for a ratio closer to unity, whereas the fingering regime is not reached if this ratio is nearing zero.

8.5 Discussion

We investigated in this chapter the impact of slip on the rim instability. With a system displaying strong hydrodynamic slip, a low molecular weight PS film on a DTS substrate, we were able to vary the ratio slip length to rim height at a given distance traveled by the straight front using a wide range of film thickness at preparation. Changes in dewetting dynamics were neglected according to results from section 4.5. We interpret the increase of the distance at which droplet detaches with film thickness resulting from the reduction of the slip length relative the dimension of the rim, commonly represented by the rim height. In other words, slip impacts on the flow of dewetting to lower extents as the rim thickens.

This result is consistent with theoretical expectations made on the transition from a monotonically to an oscillatory decaying rim taking place on DTS described in chapter 5. Münch and Wagner explained that the slip length is non-dimensionalized with the film thickness in numerical simulations. They considered the possibility to pass from a stronger slip regime to lower one as the rim grows [85]. This comment rises the question to what extent slippage impacts the flow behavior normal to the substrate and, more importantly, when can we start to neglect slip.

The setup presented in this chapter provides a new method to quantify how large the hydrodynamic boundary conditions act on the flow profile and on the flow along the ridge . Thanks

Figure 8.5: Sketch of a ridge where the rim instability undergoes. An extrapolation of the velocity profile to the normal of the substrate at $\xi = 0$ defines the slip length b. The flow field is strongly disturbed in the vicinity of the solid/liquid interface for large values of b. Due to the facts that different behavior are observed on DTS and AF 1600 and and the behavior changes on DTS as the film thickness increases, we might wonder to what extent slippage impacts on the flow profile and how the rim instability senses the flow changes via slippage.
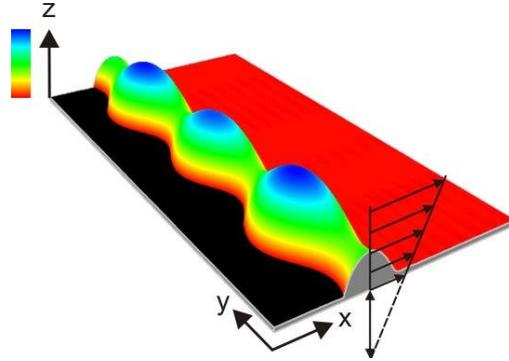
to the knowledge of the rim height reached as a function of D, we know how slip impacts on the droplet detachment. This study helps to draw regions where slip predominates (red zone in Fig. 8.5) and other where viscosity prevails. Further investigations on the distance at which the transition D^* and D_{f} occurs will help to closely quantify slip modified flow normal to the substrate.

8.6 Summary

- Increasing the film thickness involves an increase of the rim height and width for a given dewetted distance. The distance between consecutive droplets also increases.

- The trend of $D(t)$ curves observed at peak and valley on DTS for various film thicknesses is similar, however, characteristic distance measured at each transition increase with the initially prepared film thickness.

- The predominance of the slip length decreases with the increase of the film thickness. Considering a ratio of the slip length to rim height would be preferred to the ratio slip length to film thickness for further theoretical explanations. This would also help in the explanation on the exponential growth of $A_{\mathrm{z}}(t)$ observed on DTS.

9 Impact of the geometry

Up to now, the circular geometry of a dewetting hole was left aside to concentrate on the rectilinear geometry of a straight front, much easier to study the rim instability and draw comparisons with the Rayleigh-Plateau instability well known in the physics of liquid jets. In this purpose, the production of holes in the area of interest was avoided since it might hinder the rim instability. A hole growing in the vicinity of the moving front creates a premature merging of rims forming a semi-cylinder.

The ideal conditions used for the experiments involves a low density of nucleation sites which enables a hole growth unperturbed from any nearby rims. The rim instability is studied for the latter situation in a first part. After a brief description of the dynamics and a qualitative comparison between the rising of the instability on PS rims retracting from DTS and AF 1600, we discuss the evolution of the wavelength for the circular geometry. Now the question rises whether the geometry impacts on the rim instability. In the following part, we concentrate on the direct comparison between the circular and rectilinear geometry focusing comparing first the dewetting dynamics for both geometries before the rim shape is dealt with. We finally end with discussions on the straight front and the impact on numerical simulations.

9.1 Rim instability on the circular geometry

Fig. 9.1 depicts the dewetting scenario of a hole retracting from a Si-wafer hydrophobized with DTS (top row) or AF 1600 (bottom row). The 125(5) nm thick polystyrene film of molecular weight $M_w = 10.3$ kg.mol^{-1} (PS10.3k) is annealed at 120 $°C$ while optical images are recorded *in situ*. Under these circumstances, holes nucleate from the metastable system [15, 111], dry patches represented by the white zone, the polymer melt retracting from the substrate in Fig. 9.1, are initiated around a nucleus and form a disk of growing area with time. The polymer accumulates at the perimeter of the hole into a rim, dark grey zone, of increasing size as the radius of the hole grows as $R(t)$. The film, light grey, remains unperturbed until the wet side of the rim approaches.

Optical micrographs of Fig. 9.1 observed vertically compare the dewetting scenario between DTS and AF 1600 at approximately equivalent area of the 'dry' patches, *i.e.* equivalent dewet-

ted distance. The time given for each picture evidences the faster displacement of the three phase contact line on DTS than AF 1600. Additionally, we observe that the rim turns rapidly into fingers on DTS before the droplet detaches from the rim. Thanks to the similarity of these features with the one reported earlier for the rectilinear geometry reported in section 4.1, we assign the strong asymmetry observed on DTS, evidenced by strong undulations of the three phase contact line (inner perimeter) in the xy-plane compare to the line in contact with the film (outer perimeter) to the four regimes previously described for straight fronts.

At first, we observe a spatial growth of the perimeter of the hole homogeneously distributed around the ridge despite the presence of alternatively thicker and thinner regions growing with $R(t)$. The latter is only hypothesized in this part based on extrapolations of results obtained for straight fronts due to restrictions of the technique used, optical microscopy, for these experiments[1]. As a consequence, it is only possible to give a rough approximation of the transition from the first regime until the protrusion of bulges, which features a deviation of the three phase contact line from peak to valley, evidenced at $t_b < 970\,$s on DTS. The protrusion bulges is correlated to a slowing down of the number of peaks (λ). We can clearly see the onset of fingering occuring around $t_f \sim 1700\,$s and droplet detachment around $t_{\max} \sim 2000\,$s. On AF 1600, t_b is certainly sets above 7000 s.

Similar observations previously made in section 4.4.3 for straight fronts are seen for the circular geometry with a time shift. Referring to Fig. 4.5(b), the sudden increase of the growth dynamics of $W_{\mathrm{peak}}(t)$ for $t > t_b$ for the rectilinear geometry on DTS combined with the decrease of $v_{\mathrm{peak}}(t)$, evidence the production of a finger whose onset is recorded at $t_f \sim 3600$s. The finger grows until the droplet pinches-off at $t_{\max} \sim 4700\,$s.

If we now compare this maximal dewetted distance for straight fronts D_m and holes R_m, we find a larger distance traveled by the three phase contact line for the circular geometry since $D_m \sim 40\,\mu$m and $R_m = 60(4)\,\mu$m [2]. Based on the argument proposed in section 9.3, the rim width for both geometries follows $W_{SF} \sim \sqrt{2}W_{hole}$ at $D = R$. Consequently the same rim width in both situations is obtained for $R \sim 2D$, a trend which is confirmed by experiments.

Disregarding the circular shape of the ridge surrounding the hole, the perturbation developing on AF 1600 at the three phase contact line is found similar at the back of the ridge which suggests that the varicose mode develops on this substrate.

---

[1]In order to provide the necessary resolution normal to the substrate to assert the presence of peaks and valleys around the ridge, a full investigation with Atomic Force Microscopy is required. The latter is, however, difficult to setup because of the constraints of the instrument. Scanning a hole of at least $30\,\mu$m radius would require a scan larger than $80\,\mu$m to provide decent results. This length meets the limits of the instruments and the time required to obtain a good *in-plane* resolution of pictures.

[2]Note that we can neglect slight changes in molecular weight and film thickness when volumes (or distances) are compared.
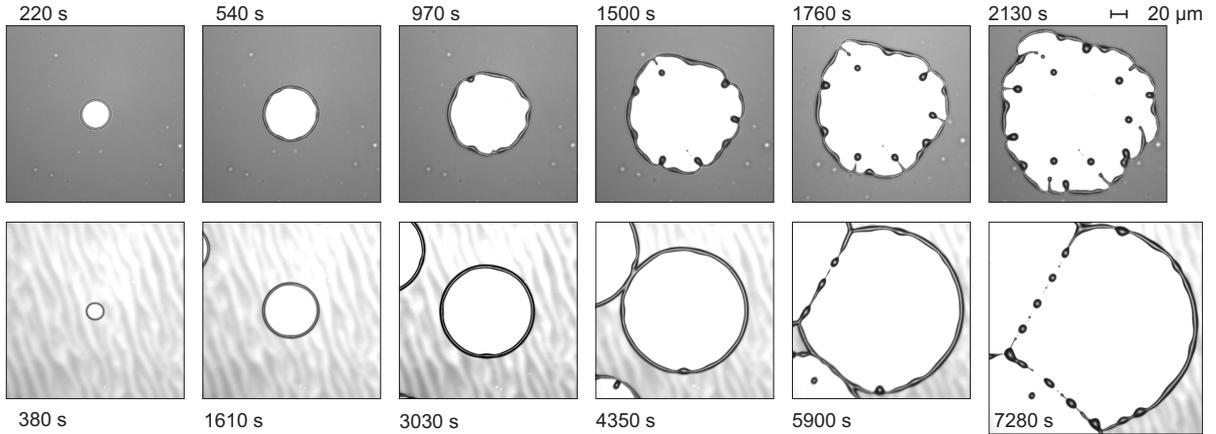
Figure 9.1: Hole growth in a thin PS ($10.3\,\mathrm{kg.mol}^{-1}$, $H = 115(5)\,\mathrm{nm}$) film on DTS (top) and on AF 1600 (bottom) at $120\,^\circ$C. On DTS the rim instability builds up asymmetrically and bulges turn rapidly into fingers before droplets detach from the rim. As for the linear geometry (Figure 1), the fingering regime is not observed on AF1600. The formation of droplets originates from the coalescence of neighboring holes whose rims form straight threads decaying into droplet via a Rayleigh-Plateau instability.

9.2 Coarsening - evolution of the wavelength

The circular geometry complicates the continuous analysis of the evolution of the wavelength due to the large area necessary to scan the hole with atomic force microscopy, the time required for one scan increases significantly with the final size of the image, but also due to the curvature of the tip of the ridge which involves the use of non linear geometry. However, we can estimate the evolution of the wavelength at specific stages of dewetting as depicted in Fig. 9.2.

Depending on the distribution of nucleation sites, proved heterogeneous according to [96, 111], rims may merge with rims of neighboring holes or straight fronts after the three phase contact line retracts from a distance $R(t)$ which depends on the length which separates two nuclei. It seems obvious that the width of the final ridge depends on the length of the radius before the two parts collapse. As a result, the stripe formed from merging holes of smaller $R(t)$ tends to decay into a series of droplets separated from a length λ_1 (Fig. 9.2(a)) smaller than λ_2 found for larger $R(t)$ Fig. 9.2(b). In other words, the number of droplets present for a given length of $100\,\mu$m, scale bar of Fig. 9.2(a-b), is smaller when $R(t)$ is large, $N = 3$-4 in Fig. 9.2(b), compare to the other limit for which we find 6-7 droplets (Fig. 9.2(a)). This reasoning evidences the existing proportionality of the rim instability with the rim width as for the Rayleigh-Plateau instability since the larger the dewetted distance the thicker the thread.

(a)   (b)
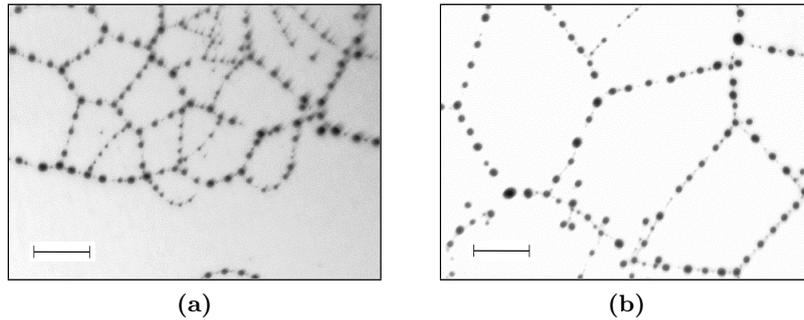
Figure 9.2: Optical micrographs illustrate the result of the Rayleigh-Plateau instability of the ridge formed by two merged rims of neighboring holes. (a) and (b) were recorded at two positions on a 115(5) nm thick PS(10.3K) film retracting from AF 1600 at 140 °C. The random distribution of dewetted areas (white zone) present on micrographs resulting from the varying hole radius before neighboring rims merge lead to ridges of varying rims, smallest on (a). Ridges of larger width (b) provides a spacing between droplets larger than the other case. Scale bars in (a) and (b) are 100 μm.

9.3 Circular versus rectilinear geometry

We now investigate a quantitative comparison of the dewetting dynamics and the impact on the rim instability for both a growing hole and a retracting front.

9.3.1 Dynamics of the three phase contact line

Having both the rectilinear and the circular geometry within one image as presented in Fig. 9.3(a) is the best suitable case to verify the true impact of the geometry over the rim instability. The evolution of the three phase contact line is depicted in Fig. 9.3(b) for the dewetting hole, filled squares $R(t)$, and the straight front, open squares $D(t)$. A shift of t_0 standing for the time required for hole nucleation and the creation of the three phase contact line was applied to the dynamics of hole $R(t)$ in order to obtain $R(t = 0) = D(t = 0) = 0\,\mu$m. Error bars for dewetting holes are defined as the standard deviation from the average between the minimum and maximum hole radius measured. The instrumental error was chosen for straight fronts, much larger than the experimental error calculated from various measurements along the ridge.

Fig. 9.3(b) evidences a faster motion of the three phase contact line for holes than for straight fronts. Although this difference might be interpreted at early stage as part of the error, $R(t)$ clearly deviates from $D(t)$ for $D > 15\,\mu$m. Using the same system for both types of geometry limits the number of parameters varying for the experiments; the viscosity, the surface tension, the film thickness and the rim height are the same for both cases. Since the driving force is

also identical in both cases, it is necessary to find an explanation from dissipation mechanisms and/or the geometry.

(a) (b)
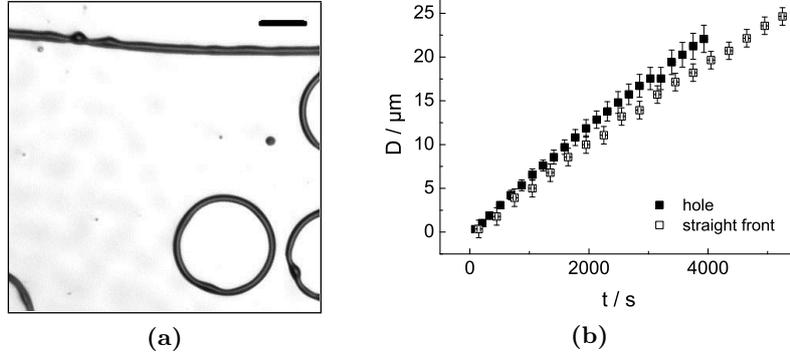
Figure 9.3: Dynamics of the contact line compared between a hole and a straight front, both which are captured in the optical micrograph (a). Measurement was performed for a hole prior to coalescing with neighboring holes. The straight front, dark line, travels from top to bottom. (b) The hole grows faster than the straight front for the 125 nm PS(35K) film retracting from AF 1600 at 130 °C.

9.3.2 Dissipation mechanisms at the solid/liquid interface

Comparing the impact of the viscous dissipation with dissipation due to slippage at the solid/liquid interface is rendered possible using the method developed by Fetzer et al. which consists of plotting the dewetting velocity as a function of $R^{-1/2}$ or $D^{-1/2}$ [42]. As introduced in section 2.4.3, a linear fit of the data provides information on the viscous part via the intercept of the fit with the $y-$axis, denoted v_0, and on the slip contribution via the slope K of the fit. Both results of the fit are displayed in equation 9.1. Since $C_v(\theta)$ is a parameter solely varying with the contact angle θ and S and η are constant, no change is expected for this term for the experiments presented. This trend is confirmed experimentally with the value of $v_0 = 3.6(2)\,\text{nm.s}^{-1}$ obtained for holes and $v_0 = 3.3(4)\,\text{nm.s}^{-1}$ for straight fronts.

$$v_0 = C_{\text{v}}(\theta)\frac{|S|}{\eta} \qquad K = \frac{|S|\,b}{3\,\eta\,C_s\,\sqrt{H}} \tag{9.1}$$

In contrast, the slope (equation 9.1) varies with the geometry studied: $K \simeq 6.7\,\mu\text{m}^{1.5}.\text{s}^{-1}$ for holes and $K \simeq 4.6\,\mu\text{m}^{1.5}.\text{s}^{-1}$ for straight fronts. The slip length calculated for the hole, $b \sim 0.2\,\mu\text{m}$ [19], is the same for both types of geometry, since values obtained for holes in [17] are similar than values obtained for straight-fronts see section 5.2.2. The only parameter which might change is C_{s}, a constant standing for the self affine growth of the rim. The viscosity certainly causes a difference in dynamics.

9.3.3 Flow at the three phase contact line

We can now wonder to what extent the change in geometry affects the dewetting dynamics. Based on the fact that the complete dewetting process occurs via accumulation of polymer in the rim — the film away from the rim remains unperturbed as seen in chapter 5 — and conservation of volume, the volume dewetted per unit length V/L is accumulated in the cross section of the rim with area Q. We obtain in both cases

$$Q_{hole} \approx \frac{h_0 \pi (R+W)^2}{2\pi(R+W/2)} \approx \frac{h_0 R}{2}, \qquad Q_{SF} \approx \frac{h_0 L(D+W)}{L} \approx h_0 D, \tag{9.2}$$

where the rim width has been approximated as the base of the rim for a semi cylinder, *i.e.* the chord of the section of the circle. Fig. 5.1 shows that we can rely on the approximation, as $h_0 << W$. Assuming now that the dewetted distances are large compared to the rim width R or $D >> W$, we obtain a higher area of the sector for a straight front (SF) $Q_{SF}(D_i) \approx 2Q_{hole}(R_i)$ at a given dewetted distance $D_i = R_i$. The last assumption is also reliable as $W/D < 0.25$ even for $D > 20\,\mu$m. Considering the geometry of the section $Q \approx \pi W^2/8$ we can see that at equal dewetted distances, the rim width and height vary as

$$W_{SF}(D) \approx \sqrt{2}W_{hole}(D), \qquad h_{SF}(D) \approx \sqrt{2}h_{hole}(D), \tag{9.3}$$

and that the rim width varies for both geometries as

$$W = C_s\sqrt{H}\sqrt{R}, \tag{9.4}$$

with the proportionality constant affected by the factor $\sqrt{2}$, higher for straight fronts.

9.3.4 Impact on the rim shape

The earlier occurrence of droplet detachment when we concentrate on dewetting of straight fronts compared to dewetting of holes reported in part 9.1 has been explained by the larger uptake of volume per unit length for straight fronts at identical dewetted distance. The self-similar growth of the rim profile allows to compare the actual volume accumulated in the rim for the given dewetted distance. Fig. 9.4 illustrates the rim profiles recorded for the circular and rectilinear geometry for two distances, around $4.5\,\mu$m and $14\,\mu$m, chosen at the early stage of dewetting to avoid strong deviations of rim height due to the rim instability. The red bars drawn at the tip of the rim represent local variations of the rim height with the minimum value standing for the lowest rim height along the ridge and the maximum its highest value. Variations of rim height are therefore within this error bar. Consequently, we see that rims

produced by different geometries do not superimpose at a given dewetted distance $R_i \approx D_i$. The rim profile of the hole is always the smallest.
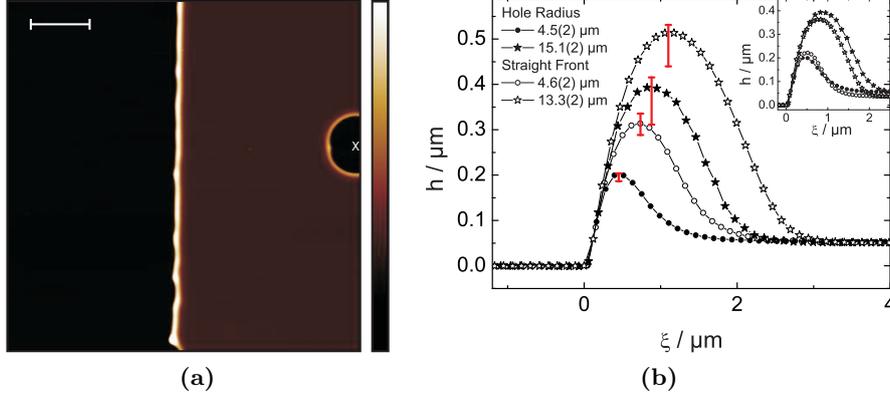
Figure 9.4: Comparison of cross sections of rim analyzed from a hole and a straight front at equivalent dewetted distance. Both types of geometry are captured on the AFM image (a) where the ridge formed (yellow) travels from left to right. The substrate and the film are respectively black and brown. Nucleation of the holes starts from the grey cross. The scale bar is $10 \, \mu m$. (b) For the two distances traveled by the moving front the rim height (h) of the straight front (open symbols) plotted versus the distance ξ from the three phase contact line is larger than the hole (filled symbols). Red bars indicate spatial fluctuations of the height at the tip of the rim, mainly due to the rim instability. The inset illustrate the same rim profiles where a coefficient of $\sqrt{2}$ was applied to the straight front. The density of points was reduced for clarity reason.

The last observation confirms the previous prediction of the existing constant of proportionality existing between the growth of a hole and a straight front. The inset of Fig. 9.3(b) represents the same rim profiles as before where the profile of the straight front was weighted with $\sqrt{2}$. The fact that profiles almost superimpose each other quantitatively confirms the constant of proportionality between straight-fronts and holes.

9.4 Discussions

Diez et al. reported that a simple extrapolation of results obtained from the breakup of liquid rivulets, *i.e.* linear geometry, to a geometry with a radial curvature are not straightforward. For example, a torus converges into one single droplet with a contact angle $\theta < 50°$, whereas decays into droplets via a Rayleigh-Plateau-type instability for larger contact angles [33]. These numerical simulations, however, contrast results from McGraw et al. which observed a toroid decaying into two droplets for a ratio radius to width of the toroid of 3 [81], ratio equivalent for the data presented in [33]. The difference probably comes from the initial radius of the torus

which is several microns large in the work of McGraw et al.. The smaller radius of the torus certainly also explains that no receding of the contact line is observed in the simulations.

In the dynamical situation, a qualitative analysis of the rim instability developing along the ridge of a straight front or a hole leads to the same conclusions, which are, among the most important, the presence of fingering for strong-slip systems, the rise of the instability in varicose mode in the no-slip case, the wavelength is proportional to the ridge. The morphology of a single bulge is also much alike. A quantitative analysis, however, evidence discrepancies mostly concerning a temporal and spatial change of transitions. The most significant being an early distance of droplet detachment for straight fronts compare to holes which is explained by a faster spatial growth rate of the rim width for straight fronts.
The latter observation is important to quantify the rise of the rim instability on either type of system. Comparing experiments with numerical simulations, however, would require a specific constant of proportionality for each system.

9.5 Summary

- A qualitative analysis of the rim instability rising on dewetting holes evidence identical features compared to the straight front geometry, *i.e.* fingering and an asymmetrical growth of the ridge are observed on DTS, the varicose mode type instability is found on AF 1600.

- Comparing quantitatively characteristic distances at transitions from one regime to another between both substrate reveals a transition taking place at lower transitions for straight-fronts.

- The dewetting dynamics is faster for holes than for straight fronts when slippage is involved.

- An impact of the rim geometry on the rim width is observed independently of the slip boundary at the solid/liquid interface. The ratio rim width of the straight front to rim width of the hole at a given dewetted distance approximates $\sqrt{2}$.

10 Instability of a supported liquid thread — the static case of the rim instability

The dynamics of the moving front renders difficult to separate the impact of slippage on the hydrodynamics of dewetting from the hydrodynamics of the rim instability. The asymmetric morphology of the ridge and the fingering regime shows the predominance of dewetting, whereas the fastest rise of the perturbation on DTS, $A_z(D)$, favors the predominance of the instability. This chapter proposes a new approach to focus solely on the impact of slippage on the Rayleigh-Plateau instability. Two methods of preparation of a supported liquid thread of width in the micrometer range are first presented. Advantages and drawbacks are discussed before first results are exposed.

The interconnection between the dynamics of dewetting and the rim instability is obtained if the three phase contact line is kept steady either by a regular pinch of the three phase contact line at a given place, which is extremely difficult to obtain, or by creating a geometry where the driving force counterbalances at either side of the ridge. The latter case is obtained by creating a semi-cylinder on top of the substrate issued from two neighboring holes coalescing or from thread deposited on the surface before annealing. It is also possible to benefit from the nucleation process of holes to produce a thin thread.

10.1 Coalescing neighboring holes

Preparation   Dewetting of the polymer film from heterogeneous nucleation creates a random distribution of holes [112], initiated from stress in the film [96, 106], which enables a variable distance between two neighboring holes before rims from both holes merge. A careful selection of the distance traveled by the moving front enables from one side coalescence of rim prior to fingering or pinch-off, on the other side allows a good control the width of the steady ridge since the volume of polymer collects into the rim due to conservation of volume. The length L of the ridge on which the Rayleigh-Plateau instability undergoes increases with the dynamics depending on the dewetting velocity and the hole radius at merging.
The time scale of the rise of the perturbation is generally slower than the dewetting velocity.

Combining the later with the fact that a bunch of wavelengths competes until the one with the fastest growing rate develops, a thin thread is formed as illustrated in Fig. 10.1(a). The thread grows symmetrically from its center to either side of the ridge if the radius of neighboring holes is approximately the same.

(a)

(b)
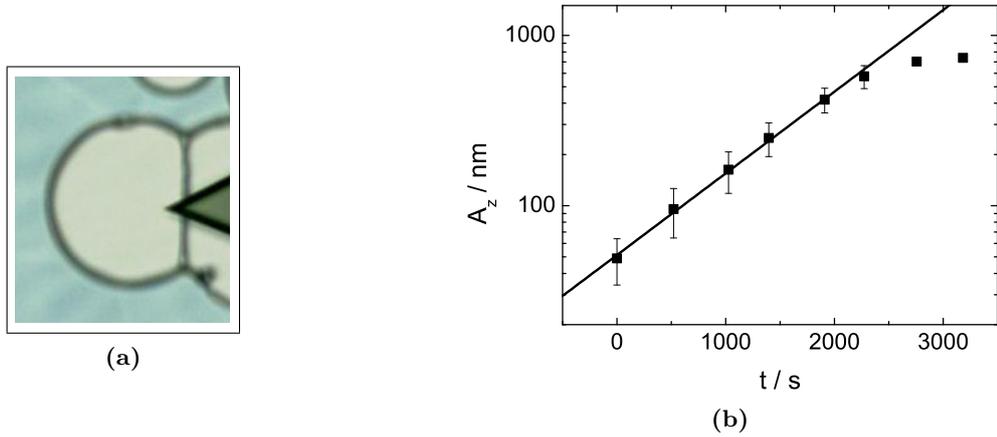
Figure 10.1: Evolution of the Rayleigh-Plateau instability growing on top of a ridge in steady state formed for the merging of two neighboring holes as depicted in (a). The perturbation A_z measured on top of the $1.9(1)\,\mu$m wide and $40\,\mu$m long ridge grows exponentially with time. The system initially prepared was a $115(5)\,$nm thick PS(10.3K) film annealed at $130\,°$C.

Evolution of the thread   In order to confirm that the length of the supported semi-cylinder $L = 40\,\mu$m obtained on DTS is sufficient to avoid superimposition of the dynamics of dewetting with the dynamics of the rise of the perturbation, the temporal evolution of the amplitude A_z of the perturbation recorded along the ridge normal to the substrate was recorded with atomic force microscopy (AFM). The resulting exponential growth of $A_z(t)$ depicted in Fig. 10.1(b) evidences that the perturbation solely develops based on the Rayleigh-Plateau instability. The deviation of data from the straight line in the semi-logarithmic representation above $2000\,$s occurs when the top of the ridge reaches the substrate.

The amount of material accumulated in the ridge depends not only of the hole radius when the two rims come into contact, but also on the initially prepared film thickness. This preparation method gives a large range of rim widths which are possible to experiment with AFM. The limiting parameters are the maximal height of the tip, typically several microns depending on the scan size is maximum $100\,\mu$m. The situation is optimal if dewetting takes place on AF 1600. On DTS, thicker parts deviate rapidly from the axis of thinner parts. The thread formed is therefore strongly undulated if rims merge at large hole radius R or senses the dynamics of dewetting if they merge at small R because of the small size of the ridge achieved. The no-slip

case can be studied with this method, but another preparation technique should be investigated in the strong-slip case.

10.2 Supported fiber

Preparation Fig. 10.2(a) sketches the second method used to create a supported PS semi-cylinder. A small amount of polymer is melted on top of a hydrophobic substrate. A tiny piece of polymer is picked with tweezers in the liquid PS drop and rapidly teared up perpendicular to the droplet's curvature (1). The atmosphere is under normal temperature and pressure conditions, The pulled thread thins while it elongates until the diameter of the solid thread breaks. The thinnest part of the thread, close to the breaking point, is deposited on another hydrophobic substrate (2). Annealed above the glass transition temperature, the thread turns to a semi-cylinder which decays into droplets via the Rayleigh-Plateau instability if conditions are favorable.

(b) PS $5.61\,\mathrm{kg.mol}^{-1}$

(c) PS $51.5\,\mathrm{kg.mol}^{-1}$

(d) PS $186\,\mathrm{kg.mol}^{-1}$

(a) Sketch of preparation of a supported fiber.
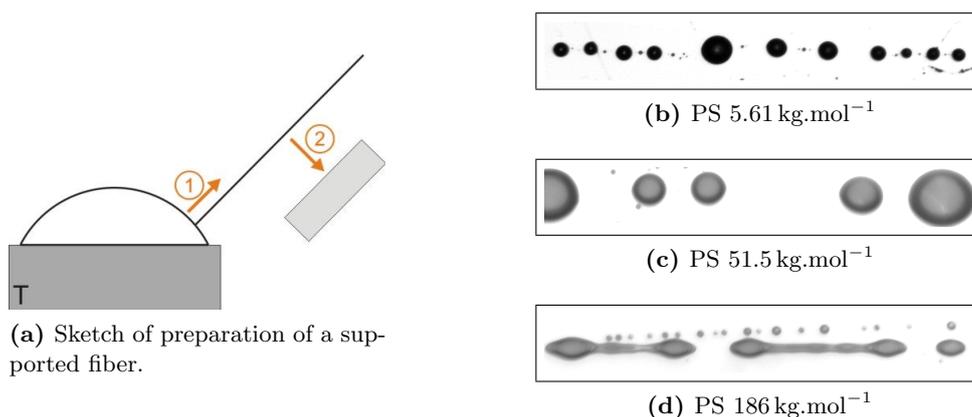
Figure 10.2: (a) Supported fibers are prepared by tearing up a polymer drop, annealed at $T > T_\mathrm{g}$, with tweezers (1) and deposit the fiber obtained a substrate as soon as breakup of the glassy fiber occurs. Preparation of fibers with various M_w is possible (b). A Rayleigh-Plateau-type instability develops on each supported fiber.

The formation of a thread with the tear up process is intrinsically linked to the speed at which the polymer is pulled and the viscosity of the polymer. Working with macromolecules of very high molecular weight allows to work in a wide range of pulling speeds due to larger cohesive force between molecules. In contrast it is necessary to lower the temperature of the stage near T_g and the pulling speed to ease the production of a thread. This process gives a final rim width of semi-cylinders starting from approximately $2\,\mu\mathrm{m}$ with a maximal size chosen below $20\,\mu\mathrm{m}$ to provide the decay into droplets in a reasonable experimenting timescale.

Series of aligned droplets depicted in Fig. 10.2(b)-(d) result from the decaying process of threads prepared with a molecular weights ranging from 5 to $186\,\mathrm{kg.mol^{-1}}$. The Rayleigh-Plateau instability develops whether the polymer chain has a molecular weight below or above the critical entanglement length. Consequently, the later aspect does not impact on the onset of instability, but solely on the rise time of the perturbation. Fig. 10.2(d) confirms the last point with the presence of two threads, a thinner thread (top) whose undulation has already reached the substrate and forms droplet beads. The thicker thread still undergoes the instability (bottom). The distance between droplets appears proportional to the width of the thread at equilibrium.

Advantages and drawbacks of the technique   This technique allows an analysis of the rim instability in the static situation. The dynamics of growth of the perturbation develops unperturbed from the formation of the ridge highlighted with the previous method. The measure of the wavelength takes place on a larger length which enables better statistics since the measurement of the distance separating droplet is evaluated on a longer length with optical microscopy. Due to the fact that the ridge is newly formed, the full dynamics of the rise of the instability can be caught from the earliest stage. However, the fast puling used to produce the liquid thread might engender a large stretching of the polymer which results in a semi-cylinder not being at equilibrium when the perturbation grows.

10.3 Results and discussions

The thicker thread of Fig. 10.2(d) shows an inhomogeneous breakup at $M_\mathrm{w} = 186\,\mathrm{kg.mol^{-1}}$ which is eventually caused by stress initiated during the pulling process. The snapshot evidences a pattern similar to the "end pinching" described in [35] where the polymer of the elongated thread accumulates at each end of the filament. Smaller chain lengths we used to determine the separating distance in this chapter do not show this type of behavior. The wavelength λ plotted in Fig. 10.3 as a function of the initial rim width W follows a linear growth evidenced with the dashed line. The final distance between droplets is neither impacted by the molecular weight nor the type of substrate used for the experiments in the range of rim widths investigated.

The new substrate introduced, studied by [39] for dewetting experiments, was characterized with a slip length b larger than AF 1600 but lower than DTS. Despite the various hydrodynamic slip length recorded for each system, we observe a linear growth of $\lambda(W_0)$, which is in agreement with results obtained for the dynamical case of the rim instability. The value of the ratio λ/W_0 is close to 6 (value of the dashed line) in the steady state, whereas the value is
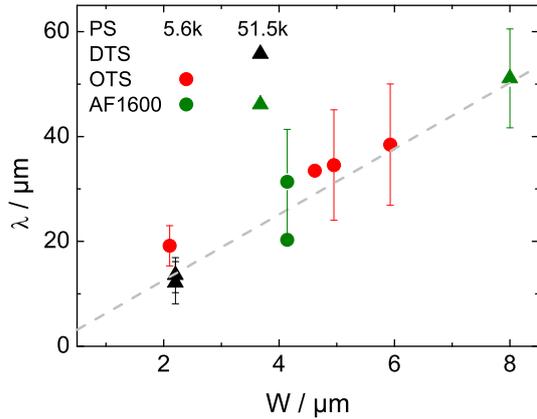
Figure 10.3: Evolution of the lateral distance between two primary droplets λ as a function of the initial rim width W of a liquid thread deposited onto three different substrates via the fiber technique. Polystyrene of molecular weights 5.61 and $51,5\,\mathrm{kg.mol^{-1}}$, respectively denoted PS(5.6k) and PS(51.5k), were used. The dashed line represents a guide to the eyes for a linear growth of $\lambda(W)$.

between both theoretical limits founds by Münch and Wagner and Brochard-Wyart and Redon in the dynamical situation, respectively 2.4 and 4.

The Young contact angle is similar on DTS and OTS, but smaller compared to AF 1600. The same type of evolution of $\lambda(W)$ obtained on Fig. 10.3 on systems with various contact anglea contrasts results obtained by Khare et al., introduced in part 2.5.2, who reported a steeper slope for smaller Young contact angle [65]. Two facts can explain this divergence, on one hand, the wedge geometry used for the experiments involve a strong impact of the contact angle compared to the flat geometry we are using. On the other hand, the width of threads we work with is no smaller than $2\,\mu\mathrm{m}$, much larger than the filling width investigated in [65], lower than $1.5\,\mu\mathrm{m}$. Further investigations of the same system include the impact of slippage at the solid/liquid boundary conditions [66].

Results on the rim instability obtained in chapter 8 for the PS/DTS system for the dynamical case of the rim instability evidence a tremendous decrease of the impact of slippage on the perturbation if the initially prepared film thickness is doubled, $h_0 \sim 230\,\mathrm{nm}$. Compared to experiments performed in the static situation, the lower limit of the width of the ridge, $W_0 \sim 2\,\mu\mathrm{m}$, is consequently too high if we want to bring light on the impact of slippage on the Rayleigh-Plateau instability of a supported ridge. Other techniques should be investigated for the latter purpose.

Methods provided in literature aiming to study the Rayleigh-Plateau instability on polymer melts are based either on the spin-coating technique or on the imprinting process. Spin-coating must be used with a specific substrate, like wedges [65], in order to provide the geometry of threads. Used otherwise the round shape obtained, like toroid [81], requires further investigations on the theoretical aspects to due the circular geometry studied.
Patterning of a polymer film with a mold produced with one-dimensional periodic lines spaced of tens to hundreds of nanometers allows an easier production of threads. Alvine et al. dis-

covered that a residual layer impacts on the perturbation of patterned ridges [1]. Using ridges directly in contact with the substrate, Park et al. noted that the final spacing of droplets is proportional to the initial geometry of the ridge for ridges with a periodicity of lines of the mold spaced in the range 0.8 to 2.5 μm [94]. The Rayleigh-Plateau instability developed in [94] on hydrophilic substrates. Using this method with DTS, OTS and AF 1600 with ridges produced with lines spaced from 0.8 μm, the lower limit might bring light on role played by the hydrodynamic slip boundary conditions.

Narrower ridges haven't been produced yet to the best of our knowledge. The imprinting technique is probably difficult to use because of higher capillary forces than adhesive forces which result in a polymer melt trapped in the mold rather than lying on top of the substrate. An alternative methods is possible by preparing film on the desired substrate, then indent an AFM tip and scratch the surface to reach the bottom of the film over several hundreds of nanometers according to the method described in [53] and repeat this step periodically to create a predefined width of the ridge. It might also be possible to use a modified AFM cantilever with a tube instead of a tip used to pour a tiny amount of polymer solution while the tip is moving in the lateral direction. The use of a good, highly volatile solvent will freeze the polymer into a thin thread which can easily be studied afterwards.

The impact of hydrodynamic slippage on the wavelength of the perturbation obtained at maximal growth rate might be subtle and hard to distinguish. Investing the dynamics of the perturbation with AFM is probably the way to get insight on the maximal growth rate selected by the system and extract the slip length in combination with numerical simulations.

10.4 Summary

- An exponential growth of the perturbation is observed for the static case of the rim instability, such as Rayleigh-Plateau instability, rising on a ridge formed from merging rim of neighbor holes.

- The preparation of supported fibers evidence an instability rising with the wavelength depending of the rim width. The minimal width of each ridge created was 2 μm, too large to observe a slip dependant growth dynamics of the perturbation.

11 Conclusion and outlook

A liquid polystyrene film is metastable when deposited on top of a substrate hydrophobized with DTS or AF 1600. Optical micrographs picturing in Fig. 1.1 the equilibrium stage of identical thin polymer films retracting from the two substrates at the same temperature evidence a strong impact of the solid/liquid interface on the retracting process. Using the same type of experiments Bäumchen et al. demonstrate that nucleated holes grow more rapidly on DTS than AF 1600 despite a stronger driving force on the latter system, which they explain as the presence of strong hydrodynamic slippage on DTS [16]. The origin slip is not completely understood, but methods to quantify the slip length reveal a difference in the absolute value of more than one order of magnitude.

In the course of dewetting, corrugations develop at the liquid/air interface, the rim instability rises. The aim of this work is to understand how slippage acts on the rim instability to give the resulting patterns. We first provide a qualitative analysis of the dewetting scenario before we combine the theory of the dewetting dynamics with the Rayleigh-Plateau instability for a more quantitative comparison.

11.1 Conclusion

Qualitative impact of slippage on the rim instability Analyzing first with optical microscopy the dewetting scenario rising in the plane of dewetting on DTS, we observe that the rim instability passes through three regimes before it reaches the final pinch-off instability: (I) undulations develop along the rim and coarsen while the rim is growing (II) undulations grow into a bulge and (III) bulges protrude from the ridge and emerge into fingers. Each transition from one regime to another is defined via characteristic local changes in a length. (I) Undulations start with the onset of dewetting. This regime is often overseen in literature [105] due to the difficulty of observe it with optical microscopy. Indeed it is necessary to use a higher resolution technique (AFM) to prove the rise of the perturbation A_z as the straight front retracts into the film. (II) The bulging regime is characterized by a rim width which stops growing at D^*. D^* marks the onset of the bilging regime which shall not be confused with the onset of instability starting at $D = 0\,\mu$m. While at $D > 0\,\mu$m the perturbation rises similar to

the Rayleigh-Plateau instability, consequences of the rim being fueled are observed for $D > D^*$. The decrease of the rim height observed with AFM at valley initiates a transverse flow towards peaks above D^* which, added to the flow induced by the Rayleigh-Plateau instability, evidences a growing rim instability at faster rate.

(III) The last stage is characterized by a sudden increase of the rim width at peak on DTS which involves a slowing down of the dewetting velocity. The growth of the bulge into finger is easily observed measuring the deviation of the center of mass of the bulge from the ridge, a bumping length or zigzag length. At equivalent volume the bulge remains well aligned with the ridge on AF 1600. A varicose mode like structure structure develops on this substrate, which contrasts the zigzag mode observed on DTS. These results agree with numerical simulations which predict an asymmetric growth of the ridge for strong slip systems and a symmetrical one for the opposite situation, despite the initial perturbation of the ridge was a zigzag perturbation where both sides of the ridge are perturbed in the same in-plane direction. The working conditions used for the experiments proves a fingering regime developing due to the presence of slippage solely. The newtonian flow used at low Reynolds numbers of the experiments contrasts with experiments from [44] predicting an onset of fingering with a transition from elastic to viscous behavior for viscoelastic systems.

The pinch-off regime evidences another instability which differs with the boundary conditions at the solid/liquid interface. On one hand, the viscosity slows down close to zero while the finger length increases on DTS. At pinch-off a finger is produced with a length increasing with the inverse of viscosity. On the other hand, cross-sections of the rim profile on AF 1600 showed that the droplet detaches while a perfect spherical shape is almost achieved. The distance D_{m} at which pinch-off instability occurs being approximately four times larger on AF 1600 for experiments performed under equivalent dewetting conditions makes the rim instability experiment a relevant method to quickly determine the presence of slippage in the systems, in other words, comparing two optical micrographs at late stage of dewetting allow to see "slippage by eye". Qualitative comparisons are independent of the geometry of the system. Fingering and a small aspect ratio between the diameter of the primary and the secondary drop characterize dewetting taking place with high hydrodynamic slippage. A close loop of the cross-section of rim profiles is another characteristic of such a system since a monotonic and an oscillatory profile can be observed on the same ridge. The local difference of capillary numbers compared at peak and valley initiated by the difference of dewetting velocity enables to be at either side of the transition line of the $Ca(b/H)$ plot.

Dynamics of the rim instability   Slippage impacts on the morphology of the rim instability but also on the dynamics of the three phase contact line. The temporal evolution of the

wavelength and of the amplitude of the instability are driven by the dynamics of the three phase contact line. The fact that the same Rayleigh ratio is found independently of the dewetting velocity suggests that the timescale of the rise of the perturbation matches the timescale of the dewetting experiments. Neglecting the dewetting velocity allows to simplify the system and concentrate on the spatial evolution of the rim instability. Features hidden if the length measured is plotted versus time are revealed when plotted versus the distance. For example, the amplitude of the perturbation $A_z(t)$ shows a good agreement with the theory proposed for the no-slip system combining the dynamics of dewetting $D \propto t^\alpha$ with the dynamics of the rim instability [8]. However, the scale of $D(t)$ (μm.s^{-1}) is much higher than the scale for the amplitude (nm.s^{-1}) involves that the three phase contact line predominates the process; the transition from regime (I) to (II) is overseen. Two growth rates of $A_z(D)$ are however observed before and after D^* which contributes to larger flow rate mentioned in the previous part.

The representation $A_z(D)$ also evidences an increase of D^* with temperature on AF 1600. D^* can first be predicted by a decrease of the spatial growth rate of the rim width as D increases, but also a decrease of the growth rate of the perturbation with the rim width. At first sight, this behavior might be contradictory with the viscous slowing reported for the Rayleigh-Plateau instability, but in this case, the spatial growth is considered.

Besides the impact of viscosity, an impact of the substrate is also observed in $A_z(D)$ with the lower value of D^* obtained on DTS compared to AF 1600. This behavior originates from slippage perceived at the tip of the ridge which can also explain the exponential growth of $A_z(t)$ considering the fact that the perturbation of the flow induced by slip is not homogeneous. The liquid flow is strongly perturbed at the solid/liquid interface compared to away from the interface. As a consequence, corrections from the equation of the growth rate (equation 6.3) should be given to being able to fit $A_z(t)$ also for DTS.

11.2 Outlook

We gave an attempt in this work to explain the origin of the rim instability, concentrating on whether strong hydrodynamic slippage is involved on not. we gave qualitative explanations using basic concepts and theory to explain, for example the transition from regime (I) to regime (II). A strong theoretical input, however, is still required to predict the rise of the rim instability, the impact of viscosity for the no slip case.

For all cases studied, the transition to the bulging regime was observed to take place when an oscillatory decay was observed in the film. It would be interesting to see if the bulging regime is observed for dewetting experiments performed on strong slip systems, *i.e.* exhibiting

a strong monotonic profile, such as AF 1600 with high molecular weight [13] or if the fingering regime is directly obtained.

Along the same line, performing rim instability experiments on AF 1600 for higher molecular weights enables a tune of the slip length over a wider range and therefore allows a better understanding of fingering and the evolution of finger length varying the dewetting viscosity, velocity, chain length.

In order to understand how the ratio slip-length to rim height impacts on the rim instability, variations of the film thickness introduced in chapter 8 appear as an ideal system. Further investigations shall be performed for a larger range of film thicknesses.
A similar information would be also provided with supported fibers as presented in chapter. 10. A new method should investigated, though, to produce supported threads of width smaller than $2\,\mu$m. Producing a liquid thread with a capillary replacing the tip of the AFM could be a good method.
Covering a liquid around a fiber as in [98] is also a good technique to study b/H if the thickness of the liquid can be tailored.

A Calculation of the distance from volume

The following script details the method used to determine the dewetted distance from the volume accumulated in the ridge (see section 3.4.1 for more details).

The preciseness of the measurement performed with AFM gives access to the exact volume of material accumulated in the ridge. Based on the fact that the dewetted film is accumulated at the three phase contact line and homogenously distributed along the ridge, we can extract the dewetted distance from the volume accumulated on top of the ridge V_{acc} above the initial film thickness. We obtain $D_{mean} = \frac{V_{acc}}{LH}$ with H the film thickness and L the length of the ridge measured.

We then used the following method to calculate V_{acc}. ASCII files were exported from AFM data and transferred to Origin. The sample was shifted in height to set the substrate at $H = 0\,\text{nm}$. We suppressed the remaining unperturbed film by setting the absolute difference in height lower than 10 nm to zero. We inserted a threshold to avoid changes at the tip of the ridge. Integrating the matrix obtained gives the total volume of the ridge V, from which we can extract the theoretical unperturbed rim height H_0 and width W_0[1], see part 5.3. We have then subtracted the film thickness H and obtained a new matrix whose integration gives the accumulated volume V_{acc}. A simple program was written in OriginLab to provide a reproducible routine as follows.

---

[1]Note W_0 and H_0 are calculated from the total volume of the ridge $V = V_{acc} + V_{film}$ where V_{film} is the volume of the film sandwiched between the substrate and the substrate and V_{acc}.

```c
#include <Origin.h>
#include <GetNbox.h>
#include <string.h>
#include <wksheet.h>
#include <Page.h>




void AscImpoNoSquare()
{

    PageBase pb;                            // Declare PageBase object
    WorksheetPage wp;                       // Declare WorksheetPage object
    Worksheet wks;                          // Declare Worksheet (Layer) object
    Column col;

    int numrow, i, cc, ll, kk, ratio, orient, orientH, orientV, nratio;
    double ncol, nline,width, height, Xmin, Xmax, Ymin, Ymax, h, thickness, lines, columns;
    double sumleft, sumright, sumbot, sumtop, minsum, minsumH, minsumV;
    double  sum, divider, suml, dividerl, diff, diffmax, corr;
    double volAcc;
    string filename, colname, wksname, details, volAccum, DewetDir, DewetDirH, DewetDirV;


// ----------------------------------------------------------- Browse for filename

 LPCSTR    strGroup = "ascii";
    LPCSTR     strTitle = "Startfile";
    DWORD    dwFlags = 0; //single file
    LPCSTR    strDefaultPath = "D:\Work\PhdThesis_Ludo\01_Diss_ludo\Graphs " ;
    get_open_box_by_file_group(filename, strGroup, strTitle, dwFlags, strDefaultPath);


// -------------------------------------------------------------------Import A
    ASCIMP    ai;

    pb = Project.Pages();
    pb.Destroy();


    if(AscImpReadFileStruct(filename, &ai)==0)
    {

//--------------------------------------------------------------- create and rename Workbook----
        wp.Create();
        wks = wp.Layers();
        wks.AddCol();


//---------------------------------------------------------------Importsettings-------------
        ai.iAutoSubHeaderLines = 0;
        ai.iSubHeaderLines = 1; // 1. LongName 2. Units    3. Expanded Discription(User defined)
        ai.nLongNames = ai.iHeaderLines;
        ai.nUnits = ai.iHeaderLines;
        ai.flags = 4|8;
        ai.iRenameCols = 1;

        wks.ImportASCII(filename, ai); // Import


    }
    else {out_str("failed to read ascii file"); return};

    wks.GetName(wksname);
    wp.Rename(wksname);




    Dataset originaldata(wks,0);
    //i = originaldata.GetSize();
    //lines = sqrt(i);
    //
//---------------------------------------------------------------Open Dialog Box-------------

    GETN_BOX(MatSize);
    GETN_NUM(ncol, "samples per line ", 2560);
    GETN_NUM(nline, "number of lines ", 256);
    GETN_NUM(width, "image width (µm) ", 80);
    GETN_NUM(nratio, "width to height ratio ", 10);
    GETN_NUM(h, "film thickness (nm) ", 118);


    if(GetNBox(MatSize, "Details AFM picture", "Please specify picture dimension value and increment
    {
```

```
            columns = MatSize.ncol.dVal;
            lines = MatSize.nline.dVal;
            Xmax = MatSize.width.dVal;
            ratio = MatSize.nratio.dVal;
            Ymax = round(Xmax/ratio,0);
            thickness = MatSize.h.dVal;
            printf("picture dimension: \n samples per line: %f \n lines: %f \n pic. width: %f µm \n pic.
            Xmin = 0.0;
            Ymin = 0.0;
        }
        else {out_str("failed to read ascii file"); return};



    //-------------------------------------------------------------------Create new columns------------
        //wks.AddCol();
        //wks.AddCol();
        //wks.MoveColumns(0, 1, MOVE_COL_TO_RIGHT);
        //wks.MoveColumns(1, 1, MOVE_COL_TO_RIGHT);
        //wks.SetColDesignations("XYZ");
        //wks.Columns(0).SetLongName("OriginalX");
        //wks.Columns(1).SetLongName("OriginalY");
        //wks.Columns(2).SetLongName("OriginalZ");

        //printf("ähh %d", numcol);

        //out_int(" number of lines:   ", lines);


    //-------------------------------------------------------------------Create matrix--------------
        string matname;

        MatrixPage matpg0;
        matpg0.Create("origin");
        matpg0.SetName("mloriginal");
        MatrixLayer matlay0 = matpg0.Layers(0);
        matlay0.SetName("name");
        matlay0.MatrixObjects(0).SetSize(lines, columns);

        Matrix <double> origmat(matlay0);

        kk=0;

        for(ll=0; ll<lines; ll++)
        {
            for(cc=0; cc<columns; cc++)
            {
                origmat[ll][cc]=originaldata[kk];
                kk++;
            }
        }

        origmat.SetXMin(0);
        origmat.SetXMax(Xmax);
        origmat.SetYMin(0);
        origmat.SetYMax(Ymax);
    //   printf("Size of mloriginal set as %f x %f µm² \n", Xmax, Ymax);


    //---------------------------------------------find orientation picture ---------------
        sumleft=0.0;
        sumright=0.0;
        sumbot=0.0;
        sumtop=0.0;
        for (ll=0; ll<lines; ll++)
        {
            sumleft=sumleft+origmat[ll][0];
            sumright=sumright+origmat[ll][columns-1];
        }
        for (cc=0; cc<columns; cc++)
        {
            sumbot=sumbot+origmat[0][cc];
            sumtop=sumtop+origmat[lines-1][cc];
        }
        sumleft=sumleft/lines;
        sumright=sumright/lines;
        sumbot=sumbot/columns;
        sumtop=sumtop/columns;

        minsum=1E20;
        if (sumleft<sumright)
            {minsumV=sumleft;
            orientV=1; //1 for sumleft
            DewetDirV="from left to right";}
        else
            {minsumV=sumright;
```

```
            orientV=2;//2 for sumright
            DewetDirV="from right to left";}

    if (sumbot<sumtop)
            {minsumH=sumbot;
            orientH = 3;
            DewetDirH="from bottom to top";}
    else
            {minsumH=sumtop;
            orientH=4;
            DewetDirH="from top to bottom";}

    if (ratio != 1)
            {minsum=minsumH;
            orient=orientH;
            DewetDir=DewetDirH;}
    else if (minsumH<minsumV)
            {minsum=minsumH;
            orient=orientH;
            DewetDir=DewetDirH;}
    else
            {minsum=minsumV;
            orient=orientV;
            DewetDir=DewetDirV;}


printf("sumleft(1)= %f \nsumright(2)= %f \nsumbot(3)= %f \nsumtop(4)= %f \nminimum= %f (%d)\n", suml


//-----------------------------------------------find 3 phase contact line & correction factor-----


    diffmax = 0.0;
    sum = 0.0;

    switch (orient)    // integers only
    {
        case 1:         //1_substrate on the left
            for (cc=0; diffmax<30; cc++)
            {
                dividerl = 0.0;
                suml = 0.0;
                for(ll=0; ll<columns; ll++)
                {
                    diff = abs(origmat[ll][cc] - origmat[ll][cc+1]);
                    suml = suml + origmat[ll][cc];
                    dividerl = dividerl + 1;
                    if (diff>diffmax)
                        diffmax = diff;
                }
                sum = sum + suml;
                divider = divider + dividerl;
            }
            sum = sum - suml;
            divider = divider - dividerl;
            corr = sum / divider;
            printf("correction factor of substrate: %f nm \nsubstrate left\n", corr);
            break;

        case 2:   //2_substrate on the right
            for (cc=columns-1; diffmax<30; cc--)
            {
                dividerl = 0.0;
                suml = 0.0;
                for(ll=0; ll<columns; ll++)
                {
                    diff = abs(origmat[ll][cc] - origmat[ll][cc-1]);
                    suml = suml + origmat[ll][cc];
                    dividerl = dividerl + 1;
                    if (diff>diffmax)
                        diffmax = diff;
                }
                sum = sum + suml;
                divider = divider + dividerl;
            }
            sum = sum - suml;
            divider = divider - dividerl;
            corr = sum / divider;
            printf("correction factor of substrate: %f nm \nsubstrate right\n", corr);
            break;

        case 3:   //3_substrate on the bottom (graph)
            for (ll=0; diffmax<30; ll++)
            {
                dividerl = 0.0;
                suml = 0.0;
                for(cc=0; cc<columns; cc++)
                {
```

```
                diff = abs(origmat[ll][cc] - origmat[ll+1][cc]);
                sum1 = sum1 + origmat[ll][cc];
                divider1 = divider1 + 1;
                if (diff>diffmax)
                    diffmax = diff;
            }
            sum = sum + sum1;
            divider = divider + divider1;
        }
        sum = sum - sum1;
        divider = divider - divider1;
        corr = sum / divider;
        printf("correction factor of substrate: %f nm \nsubstrate bottom\n", corr);
        break;

    case 4:    //4_substrate on top (graph)
        for (ll=lines-1; diffmax<30; ll--)
        {
            divider1 = 0.0;
            sum1 = 0.0;
            for(cc=0; cc<columns; cc++)
            {
                diff = abs(origmat[ll][cc] - origmat[ll-1][cc]);
                sum1 = sum1 + origmat[ll][cc];
                divider1 = divider1 + 1;
                if (diff>diffmax)
                    diffmax = diff;
            }
            sum = sum + sum1;
            divider = divider + divider1;
        }
        sum = sum - sum1;
        divider = divider - divider1;
        corr = sum / divider;
        printf("correction factor of substrate: %f nm \nsubstrate top\n", corr);
        break;
    }
//---------------------------------------------------------------------Duplicate matrix-------------

    MatrixPage matpg1;
    matpg1.Create("origin");
    matpg1.SetName("m2ShiftSubstrate");
    MatrixLayer matlay1 = matpg1.Layers(0);
    matlay1.SetName("PlaneFit");
    matlay1.MatrixObjects(0).SetSize(lines, columns);

//---------------------------------------------------------------------Set Matrix Value & Dimension--
    Matrix <double> origshift(matlay1);
    origshift = origmat - corr;

    origshift.SetXMin(0);
    origshift.SetXMax(Xmax);
    origshift.SetYMin(0);
    origshift.SetYMax(Ymax);

//---------------------------------------------------------------------Duplicate matrix-------------

    MatrixPage matpg2;
    matpg2.Create("origin");
    matpg2.SetName("m3Ridge");
    MatrixLayer matlay2 = matpg2.Layers(0);
    matlay2.SetName("Ridge");
    matlay2.MatrixObjects(0).SetSize(lines, columns);

    Matrix <double> matridge(matlay2);
    matridge = origshift;

//---------------------------------------------------------------------set coordinates to  matrix----

    matridge.SetXMin(0);
    matridge.SetXMax(Xmax);
    matridge.SetYMin(0);
    matridge.SetYMax(Ymax);
//  printf("Size of matridge set as %f x %f µm² \n", Xmax, Ymax);
//---------------------------------------------------------------------Recalculate matrix ridge------

    for(ll = 0; ll < lines-1 ; ll++)
    {
        for(cc = 0; cc < columns ; cc++)
        {
            if (matridge[ll][cc]<200 )
            {
                if( abs(matridge[ll][cc] -    matridge[ll+1][cc]) < 20)
                {
                    matridge[ll][cc]=0;
                }
            }
        }
```

```
            }
        //matridge[lines-1][cc] = 0;
        }

//-----------------------------------------------------------------Duplicate matrix-------------

    MatrixPage matpg3;
    matpg3.Create("origin");
    matpg3.SetName("m4Accumulated");
    MatrixLayer matlay3 = matpg3.Layers(0);
    matlay3.SetName("VolAccum.");
    matlay3.MatrixObjects(0).SetSize(lines, columns);

    Matrix <double> matcumul(matlay3);


//---------------------------------------------------------------set coordinates to  matrix----

    matcumul.SetXMin(0);
    matcumul.SetXMax(Xmax);
    matcumul.SetYMin(0);
    matcumul.SetYMax(Ymax);
    printf("Size of m4accumulated set as %f x %f µm² \n", Xmax, Ymax);


//-----------------------------------------------------------------Recalculate matrix ridge------

    matcumul = matridge - thickness;

    for(ll = 0; ll < lines ; ll++)
    {
        for(cc = 0; cc < columns - 1 ; cc++)
        {
            if (matcumul[ll][cc]<0)
                {
                    matcumul[ll][cc] = 0;
                }
        }
        //matcumul[ll][columns - 1] = 0;
    }

//-------------------------------------------------------------------integrate matrix---------

    volAcc = ocmath_2d_integrate(lines, columns, Xmin, Ymin, Xmax, Ymax, matcumul);
    printf("volume %f .10^(-3) µm3 ", volAcc);

//-----------------------------------------------------------------write results in note----

    Note note;

    details = "samples per line: " + columns + "\nlines: " + lines + "\npic. width: " + Xmax + " µm
    note.Create();              // Create a new empty Notes window
    note.SetName("PicDetails");
    if( note.IsValid() )
        {
        note.Text = details;
        }

    volAccum = "film dewets " +DewetDir+ " (see graph) \ncorrection factor (z_substrate = 0): " +cor
    note.Create();              // Create a new empty Notes window
    note.SetName("Results");
    if( note.IsValid() )
        {
        note.Text = volAccum;
        }

}
```

Bibliography

[1] K. J. Alvine, Y. F. Ding, J. F. Douglas, H. W. Ro, B. C. Okerberg, A. Karim, and C. L. Soles. Capillary instability in nanoimprinted polymer films. *Soft Matter*, 5(15):2913–2918, 2009.

[2] D. Andelman, J. F. Joanny, and M. Robbins. Complete wetting on rough surfaces: statics. *Europhys. Lett.*, 7(8):731–736, 1988.

[3] D. L. Angst and G. W. Simmons. Moisture absorption characteristics of organosiloxane self-assembled monolayers. *Langmuir*, 7(10):2236–2242, 1991.

[4] R. M. A. Azzam and N. M. Bashara. *Ellipsometry and polarized light*. Noth Holland, Amsterdam, 1977.

[5] L. Bocquet and J. L. Barrat. Flow boundary conditions from nano- to micro-scales. *Soft Matter*, 3(6):685–693, 2007.

[6] J. Brandrup, E. H. Immergut, and E. A. Grulke. *Polymer Handbook, 4th ed.* John Wiley & Sons Inc.: New York, 1999.

[7] M. P. Brenner and D. Gueyffier. On the bursting of viscous films. *Phys. Fluids*, 11(3):737, 1999.

[8] F. Brochard-Wyart and C. Redon. Dynamics of liquid rim instabilities. *Langmuir*, 8(9):2324–2329, 1992.

[9] F. Brochard-Wyart, P.-G. de Gennes, H. Hervert, and C. Redon. Wetting and slippage of polymer melts on semi-ideal surfaces. *Langmuir*, 10(5):1566–1572, 1994.

[10] F. Brochard-Wyart, G. Debregeas, R. Fondecave, and P. Martin. Dewetting of supported viscoelastic polymer films: Birth of rims. *Macromolecules*, 30(4):1211–1213, 1997.

[11] H. R. Brown and T. P. Russell. Entanglements at polymer surfaces and interfaces. *Macromolecules*, 29(2):798–800, 1996.

[12] J. B. Brzoska, I. Ben Azouz, and F. Rondelez. Silanization of solid substrates - a step toward reproducibility. *Langmuir*, 10(11):4367–4373, 1994.

[13] O. Bäumchen. *Fluidics of Thin Polymer Films - Boundary Conditions and Interfacial Phenomena*. Thesis, Universität des Saarlandes, 2010.

[14] O. Bäumchen and K. Jacobs. Slip effects in polymer thin films. *J. Phys.: Condens. Matter*, 22 (3):033102, 2010.

[15] O. Bäumchen and K. Jacobs. Can liquids slide? linking stability and dynamics of thin liquid films to microscopic material properties. *Soft Matter*, 2010.

[16] O. Bäumchen, R. Fetzer, and K. Jacobs. Probing slippage and flow dynamics of thin dewetting polymer films. *Proc. Eur. Conf. on Microfluidics*, 2008.

[17] O. Bäumchen, R. Fetzer, and K. Jacobs. Reduced interfacial entanglement density affects the boundary conditions of polymer flow. *Phys. Rev. Lett.*, 103(24):247801–4, 2009.

[18] O. Bäumchen, R. Fetzer, A. Münch, B. Wagner, and K. Jacobs. Comprehensive analysis of dewetting profiles to quantify hydrodynamic slip. *IUTAM Bookseries*, 15:51–65, 2009.

[19] O. Bäumchen, R. Fetzer, M. Klos, M. Lessel, L. Marquant, H. Hähl, and K. Jacobs. Slippage and nanorheology of thin liquid polymer films. *Journal of Physics: Condensed Matter*, 24(32):325102, 2012.

[20] H J Butt and M Jaschke. Calculation of thermal noise in atomic force microscopy. *Nanotechnology*, 6(1):1, 1995.

[21] G. A. Carson and S. Granick. Self-assembly of octadecyltrichlorosilane monolayers on mica. *Journal of Materials Research*, 5(08):1745–1751, 1990.

[22] A. M. Cazabat, F. Heslot, S. M. Troian, and P. Carles. Fingering instability of thin spreading films driven by temperature-gradients. *Nature*, 346(6287):824–826, 1990.

[23] S. Chandrasekhar. *Hydrodynamic and Hydromagnetic Stabilityra.* Dover Publications, 1961.

[24] F. Charru and P. de Forcrand-Millard. *Hydrodynamic instabilities.* Cambridge University Press, 2011.

[25] S. H. Davis. Moving contact lines and rivulet instabilities. part 1. the static rivulet. *Journal of Fluid Mechanics*, 98(02):225–242, 1980.

[26] P.-G. de Gennes. *Scaling concepts in polymer physics.* Cornell University Press, 1979.

[27] P. G. de Gennes. Wetting: statics and dynamics. *Rev. Mod. Phys.*, 57(3):827–, July 1985.

[28] P.-G. de Gennes, F. Brochard-Wyart, and D. Quéré. *Capillarity and Wetting Phenomena: Drops, Bubbles, Pearls, Waves.* Springer, 2004.

[29] P.G. de Gennes. *Séances Acad. Sci., Ser. B*, 288:210, 1979.

[30] G. Debregeas, P. Martin, and F. Brochard-Wyart. Viscous bursting of suspended films. *Physical Review Letters*, 75(21):3886–3889, 1995.

[31] M. Delmas, M. Monthioux, and T. Ondarćuhu. Contact angle hysteresis at the nanometer scale. *Phys. Rev. Lett.*, 106(13):136102, 2011.

[32] J. A. Diez and L. Kondic. Contact line instabilities of thin liquid films. *Physical Review Letters*, 86(4):632–635, 2001.

[33] J. A. Diez, A. G. Gonzalez, and L. Kondic. On the breakup of fluid rivulets. *Phys. Fluids*, 21(8): 082105, 2009.

[34] P. G. Drazin and W. H. Reid. *Hydrodynamic Stability.* Cambridge University Press, Cambridge, UK, 1981.

[35] Jens Eggers. Nonlinear dynamics and breakup of free-surface flows. *Rev. Mod. Phys.*, 69(3):865–, 1997.

[36] Jens Eggers and Emmanuel Villermaux. Physics of liquid jets. *Rep. Prog. Phys.*, 71:036601, 2008.

[37] C. J. Ellison and J. M. Torkelson. The distribution of glass-transition temperatures in nanoscopically confined glass formers. *Nat. Mater.*, 2(10):695–700, 2003.

[38] R. Fetzer. *Einfluss von Grenzflächen auf die Fluidik dünner Polymerfilme.* Thesis, Universität des Saarlandes, 2006.

[39] R. Fetzer and K. Jacobs. Slippage of newtonian liquids: Influence on the dynamics of dewetting thin films. *Langmuir*, 23(23):11617–11622, 2007.

[40] R. Fetzer, K. Jacobs, A. Münch, B. Wagner, and T. P. Witelski. New slip regimes and the shape of dewetting thin liquid films. *Phys. Rev. Lett.*, 95(12):127801–, 2005.

[41] R. Fetzer, M. Rauscher, A. Munch, B. A. Wagner, and K. Jacobs. Slip-controlled thin-film dynamics. *Europhys. Lett.*, 75(4):638–644, 2006.

[42] R. Fetzer, A. Munch, B. Wagner, M. Rauscher, and K. Jacobs. Quantifying hydrodynamic slip: A comprehensive analysis of dewetting profiles. *Langmuir*, 23(21):10559–10566, 2007.

[43] S. Gabriele, S. Coppée, G. Reiter, and P. Damman. On the mechanics of rim instabilities in viscoelastic polymer thin films. *Eur. Phys. J. Special Topics*, 166(1):55–61, 2009.

[44] Sylvain Gabriele, Severine Sclavons, Gunter Reiter, and Pascal Damman. Disentanglement time of polymers determines the onset of rim instabilities in dewetting. *Phys. Rev. Lett.*, 96(15):156105–4, 2006.

[45] Y. Gan. Atomic and subnanometer resolution in ambient conditions by atomic force microscopy. *Surface Science Reports*, 64(3):99–121, 2009.

[46] L. A. Girifalco and R. J. Good. *Journal of Physical Chemistry*, 61:904, 1957.

[47] R. J. Good and L. A. Girifalco. A theory for estimation of surface and interfacial energies .3. estimation of surface energies of solids from contact angle data. *Journal Of Physical Chemistry*, 64(5):561–565, 1960.

[48] R. J. Good, L. A. Girifalco, and G. Kraus. *Journal of Physical Chemistry*, 62:1418, 1958.

[49] J. Gun and J. Sagiv. On the formation and structure of self-assembling monolayers: Iii time of formation, solvent retention, and release. *Journal of Colloid and Interface Science*, 112(2): 457–472, 1986.

[50] J. Gun, R. Iscovici, and J. Sagiv. On the formation and structure of self-assembling monolayers: Ii a comparative study of langmuir–blodgett and adsorbed films using ellipsometry and ir reflection–absorption spectroscopy. *Journal of Colloid and Interface Science*, 101(1):201–213, September 1984.

[51] P. Gutfreund, O. Bäumchen, D. van der Grinten, R. Fetzer, M. Maccarini, K. Jacobs, H. Zabel, and M. Wolff. Surface correlation affects liquid order and slip in a newtonian liquid. *http://arxiv.org/abs/1104.0868v1*, 2011.

[52] P. Gutfreund, O. Bäumchen, R. Fetzer, D. van der Grinten, M. Maccarini, K. Jacobs, H. Zabel, and M. Wolff. Solid surface structure affects liquid order at the polystyrene – self-assembled-monolayer interface. *Phys. Rev. E*, 87(1):012306, 2013.

[53] S. Haefner. Fliessverhalten komplexer flüssigkeiten: Einfluss des rutschens auf die entnetzungsmorphologie gerader polymerfronten. Master's thesis, Universität des Saarlandes, 2012.

[54] A. Haenlein. über den zerfall eines flüssigkeitsstrahles. *Forsch. Gebiete Ing.*, 2:139–149, 1931.

[55] S. Herminghaus, K. Jacobs, and R. Seemann. Viscoelastic dynamics of polymer thin films and surfaces. *Eur. Phys. J. E*, 12(1):101–110, 2003.

[56] J. Israelachvili. *Intermolecular and Surface Forces*. Academic Press, New York, 2 edition, 1992.

[57] K. Jacobs. *Stabilität und dynmamik flussiger Polymerfilme*. Phdthesis, Universität Konstanz, 1997.

[58] K. Jacobs, R. Seemann, G. Schatz, and S. Herminghaus. Growth of holes in liquid films with partial slippage. *Langmuir*, 14(18):4961–4963, 1998.

[59] K. Jacobs, R. Seemann, and S. Herminghaus. *Stability and dewetting of thin liquid films Polymer Thin Films*. Singapore: World Scientific, 2008.

[60] Karin Jacobs, Stephan Herminghaus, and Klaus R. Mecke. Thin liquid polymer films rupture via defects. *Langmuir*, 14(4):965–969, 1998.

[61] J. F. Joanny and P. G. de Gennes. A model for contact angle hysteresis. *J. Chem. Phys.*, 81(1): 552–562, 1984.

[62] K. Kargupta, A. Sharma, and R. Khanna. Instability, dynamics, and morphology of thin slipping films. *Langmuir*, 20(1):244–253, 2004.

[63] D. E. Kataoka and S. M. Troian. Patterning liquid flow on the microscopic scale. *Nature*, 402 (6763):794–797, 1999.

[64] J. L. Keddie, R. A. L. Jones, and R. A. Cory. Size-dependent depression of the glass-transition temperature in polymer-films. *Europhysics Letters*, 27(1):59–64, July 1994.

[65] K. Khare, M. Brinkmann, B. M. Law, E. L. Gurevich, S. Herminghaus, and R. Seemann. Dewetting of liquid filaments in wedge-shaped grooves. *Langmuir*, 23(24):12138–12141, 2007. ISSN 0743-7463.

[66] Krishnacharya Khare. Impact of slippage on the dewetting of liquid filaments in wedge-shaped grooves. Private communication.

[67] J. King, A. Münch, and B. Wagner. Linear stability analysis of a sharp-interface model for dewetting thin films. *J. Eng. Math.*, 63(2):177–195, 2009.

[68] G. Kitavtsev and B. Wagner. Coarsening dynamics of slipping droplets. *J. Eng. Math.*, 66(1-3): 271–292, 2010.

[69] M. Klos. Entnetzung von polymerfilmen auf hydrophobisierten oberflächen - einfluss von oberflächencharakteristika auf die entnetzungsdynamik. Master's thesis, Universität des Saarlandes, 2010.

[70] K. Kostourou, D. Peschka, A. Münch, B. Wagner, S. Herminghaus, and R Seemann. Interface morphologies in liquid/liquid dewetting. *Chemical Engineering and Processing: Process Intensification*, 50(5):531–536, 2011.

[71] P. Lafrance. Nonlinear breakup of a laminar liquid jet. *Phys. Fluids*, 18(4):428–432, 1975.

[72] E Lauga, M P Brenner, and H A Stone. *Microfluidics: the no-slip boundary condition — Springer Handbook of Experimental Fluid Mechanics*. Berlin: Springer, 2007.

[73] S. H. Lee, P. J. Yoo, S. J. Kwon, and H. H. Lee. Solvent-driven dewetting and rim instability. *J. Chem. Phys.*, 121(9):4346–4351, 2004.

[74] P. M. Loskill. Einfluss langreichweitiger van der waals-wechselwirkungen auf die adh¨asion von bakterien - eine afm studie. Thesis, Universität des Saarlandes, 2009.

[75] G. Magnus. Hydraulische undersuchungen. *Ann. Phys. Chem.*, 95:1, 1855.

[76] S. N. Magonov and D. H. Reneker. Characterization of polymer surfaces with atomic force microscopy. *Annu. Rev. Mater. Sci.*, 27(1):175–222, 1997.

[77] J. Mainka. Instabilitäten in flüssigen filmen: Strukturbildung beim entnetzen. Thesis, Universität des Saarlandes, 2007.

[78] R. Maoz and J. Sagiv. On the formation and structure of self-assembling monolayers. i. a comparative atr-wettability study of langmuir–blodgett and adsorbed films on flat substrates and glass microbeads. *Journal of Colloid and Interface Science*, 100(2):465–496, 1984.

[79] J.-L. Masson and P. F. Green. Hole formation in thin polymer films: A two-stage process. *Phys. Rev. Lett.*, 88(20):205504, 2002.

[80] J.-L. Masson, O. Olufokunbi, and P.F. Green. Flow instabilities in entangled polymer thin films. *Macromolecules*, 35(18):6992–6996, 2002.

[81] J. D. McGraw, J. Li, D. L. Tran, A.-C. Shi, and K. Dalnoki-Veress. Plateau-rayleigh instability in a torus: formation and breakup of a polymer ring. *Soft Matter*, 6(6):1258–1262, 2010.

[82] F. Melo, J. F. Joanny, and S. Fauve. Fingering instability of spinning drops. *Phys. Rev. Lett.*, 63 (18):1958–1961, 1989.

[83] A Münch. Dewetting rates of thin liquid films. *J. Phys.: Condens. Matter*, 17(9):S309, 2005.

[84] A. Münch and B. Wagner. Contact-line instability of dewetting thin films. *Physica D*, 209(1-4):178–190, 2005.

[85] A. Münch and B. Wagner. Impact of slippage on the morphology and stability of a dewetting rim. *Journal of Physics: Condensed Matter*, 23(18):184101, 2011.

[86] A. Münch, B. Wagner, and T. Witelski. Lubrication models with small to large slip lengths. *J. Eng. Math.*, 53(3):359–383, 2005.

[87] A. Münch, C. P. Please, and B. Wagner. Spin coating of an evaporating polymer solution. *Phys. Fluids*, 23(10):102101–12, 2011.

[88] C.-L. Navier. Mémoire sur les lois du mouvement des fluids. *Mem. Acad. Sci. Inst. Fr.*, 6:389–440, 1823.

[89] C. Neto, A. Münch, R. Seemann, and K. Jacobs. Fingering instability in dewetting films induced by slippage. 2004.

[90] C. Neto, D. R Evans, E. Bonaccurso, H.-J. Butt, and V. S J Craig. Boundary slip in newtonian liquids: a review of experimental studies. *Reports on Progress in Physics*, 68(12):2859, 2005.

[91] J. A. Nollet. Recherches sur les causes particuli'eres des phénom'enes électriques. *Chez les fr'eres Guérin, Paris, France*, 36:0–444, 1749.

[92] T. Ondarcuhu and M. Veyssie. Relaxation modes of the contact line of a liquid spreading on a surface. *Nature*, 352(6334):418–420, August 1991.

[93] A. Oron, S. H. Davis, and S. G. Bankoff. Long-scale evolution of thin liquid films. *Rev. Mod. Phys.*, 69(3):931, 1997.

[94] J.-Y. Park, K. Y. Suh, and H. H. Seo, S.and Lee. Anisotropic rupture of polymer strips driven by rayleigh instability. *J. Chem. Phys.*, 124(21):214710–5, 2006.

[95] J Plateau. *Experimental and theoretical statics of liquids subject to forces only.* Paris: Gauthier-Villars, 1873. French title: Statique expérimental et théorique des lliquides soumis aus seules forces moléculaires.

[96] D. Podzimek, A. Saier, R. Seemann, K. Jacobs, and S. Herminghaus. A universal nucleation mechanism for solvent cast polymer film rupture. *arXiv*, 2001. arXiv:cond-mat/0105065v1 [cond-mat.soft].

[97] D. Quere. Fluid coating on a fiber. *Annual Review of Fluid Mechanics*, 31:347–384, 1999.

[98] D. Quere, J.-M. di Meglio, and F. Brochard-Wyart. Spreading of liquids on highly curved surfaces. *Science*, 249(4974):1256–1260, September 1990.

[99] Rayleigh. On the instability of a cylinder of viscous liquid under capillary force. *Philosophical Magazine*, 34(207):145–154, 1892.

[100] F.R.S. Rayleigh. On the instability of jets. *Proc. London Math. Soc.*, 1(4):1–10, 1878.

[101] C. Redon, F. Brochard-Wyart, and F. Rondelez. Dynamics of dewetting. *Phys. Rev. Lett.*, 66(6):715–, February 1991.

[102] C. Redon, J. B. Brzoska, and F. Brochard-Wyart. Dewetting and slippage of microscopic polymer films. *Macromolecules*, 27(2):468–471, January 1994.

[103] G. Reiter. Evolution of rim instabilities in the dewetting of slipping thin polymer films. *The Journal of Adhesion*, 81(3):381–395, 2005.

[104] G. Reiter and R. Khanna. Real-time determination of the slippage length in autophobic polymer dewetting. *Phys. Rev. Lett.*, 85(13):2753–2756, September 2000.

[105] G. Reiter and A. Sharma. Auto-optimization of dewetting rates by rim instabilities in slipping polymer films. *Phys. Rev. Lett.*, 87(16):166103, October 2001.

[106] G. Reiter, M. Hamieh, P. Damman, S. Sclavons, S. Gabriele, T. Vilmin, and E. Raphael. Residual stresses in thin polymer films cause rupture and dominate early stages of dewetting. *Nat. Mater.*, 4(10):754–758, October 2005.

[107] M. Rubinstein and R. H. Colby. *Polymer Physics.* New York: Oxford University Press, 2003.

[108] F.a Savart. *Annales de chimie*, 53:337, 1833.

[109] F. Schreiber. Structure and growth of self-assembling monolayers. *Progress in Surface Science*, 65(5–8):151–257, November 2000.

[110] R. Seemann, S. Herminghaus, and K. Jacobs. Shape of a liquid front upon dewetting. *Phys. Rev. Lett.*, 87(19):196101–, October 2001.

[111] R. Seemann, S. Herminghaus, and K. Jacobs. Gaining control of pattern formation of dewetting liquid films. *Journal of Physics-condensed Matter*, 13(21):4925–4938, May 2001.

[112] R. Seemann, S. Herminghaus, and K. Jacobs. Dewetting patterns and molecular forces: A reconciliation. *Physical Review Letters*, 86(24):5534–5537, June 2001.

[113] K. Sekimoto, R. Oguma, and K. Kawasaki. Morphological stability analysis of partial wetting. *Annals Of Physics*, 176(2):359–392, June 1987.

[114] Y. Seo and W. Jhe. Atomic force microscopy and spectroscopy. *Reports on Progress in Physics*, 71(1):016101, 2008.

[115] R. Sherman, J. Grob, and W. Whitlock. Dry surface cleaning using carbon dioxide snow. *J. Vac. Sci. Technol. B*, 9(4):1970–1977, July 1991.

[116] H. A. Stone and M. P. Brenner. Note on the capillary thread instability for fluids of equal viscosities. *Journal of Fluid Mechanics*, 318:373–374, 1996.

[117] H. G. Tompkins and W. A. McGahan. *Spectroscopic ellipsometry and relflectometry: a user's guide.* John Wiley & Sons, New York, 1999.

[118] C. P. Tripp and M. L. Hair. Reaction of alkylchlorosilanes with silica at the solid/gas and solid/liquid interface. *Langmuir*, 8(8):1961–1967, August 1992.

[119] S. M. Troian, E. Herbolzheimer, S. A. Safran, and J. F. Joanny. Fingering instabilities of driven spreading films. *Europhysics Letters*, 10(1):25–30, 1989.

[120] A. Ulman. Formation and structure of self-assembled monolayers. *Chemical Reviews*, 96(4): 1533–1554, January 1996.

[121] S. R. Wasserman, Y. T. Tao, and G. M. Whitesides. Structure and reactivity of alkylsiloxane monolayers formed by reaction of alkyltrichlorosilanes on silicon substrates. *Langmuir*, 5(4): 1074–1087, 1989. ISSN 0743-7463.

[122] R. C. Weast. *Handbook of Chemistry and Physics.* CRC Press, 1978.

[123] R. H. Weiland and S. H. Davis. Moving contact lines and rivulet instabilities. part 2. long waves on flat rivulets. *Journal of Fluid Mechanics*, 107:261–280, 1981.

[124] C. Williams. Ink-jet technology moves beyond paper. *Phys. World*, 19:24, 2006.

[125] L. Xu, T. Shi, P. K. Dutta, and L. An. Rim instability by solvent-induced dewetting. *J. Chem. Phys.*, 127(14):144704–7, October 2007.

[126] T. Young. *Trans. Roy. Soc*, 95:65, 1805.

Publication

Thin dewetting polymer films

- O. Bäumchen, R. Fetzer, M. Klos, M. Lessel, L. Marquant, H. Hähl and K. Jacobs, "Slippage and nanorheology of thin liquid polymer films", *J. of Phys. Cond. Mat.*, **24**, 325102 (2009).

- O. Bäumchen*, L. Marquant*, K. Jacobs, R. Blossey, A. Münch, B. Wagner, "Slip controls the Rayleigh-Plateau rim instability in dewetting polymer films". *Phys. Rev. Let.*, **113** 014501 (2014)
  * same authors contribution

Conductive polymer films

- C. Badre, L. Marquant, A. Alsayed, and L. Hough, "Highly conductive poly(3,4-ethylene-dioxythiophene): poly(styrenesulfonate) films using ionic liquid as dopant", *Adv. Funct. Mater.*, **12**, 13, 2723 (2012)

Conference contributions

Scientific Talks

- "Stability and dynamics of thin polymer films",
  PolyFUM, POLYFILM workshop, Saclay (F) (01/2006).

- "Stability and dynamics of thin polymer films",
  POLYFILM, Lyon (F) (04/2006).

- "Thin liquid polymer films: Preparation parameters impact fluid dynamics",
  mid-term review POLYFILM meeting, Mulhouse (F) (09/2006).

- "Thin liquid polymer films: Preparation parameters impact fluid dynamics",
  Winterschool 2006, Feldberg (D) (12/2006).

- "Thin liquid polymer films: Preparation parameters impact fluid dynamics",
  PhD Students' Day 2007, Saarbrücken (D) (03/2007).

- "Thin liquid polymer films: Preparation parameters impact fluid dynamics",
  POLYFILM meeting, Sheffield (UK) (09/2007).

- "Fingering instabilities in thin polymer films",
  Feldberg's Winterschool, Feldberg (D) (12/2007).

- "Fingering instabilities in thin polymer films",
  PhD Students' Day 2008, Saarbrücken (D) (04/2008).

- "Dewetting of thin polymer films: old and new phenomena",
  POLYFILM meeting, Leuven (B) (04/2008).

- "Fingering instabilities in dewetting of thin polymer films",
  Feldberg's Winterschool, Feldberg (D) (12/2008).

- "Fingering instabilities in dewetting of thin polymer films",
  PhD Students' Day 2009, Saarbrücken (D) (02/2009).

- "Roughness affects slippage and slippage affects hydrodynamic instabilities",
  DPG-Frühjahrstagung, Saarbrücken (D) (02/2009).

- "Fingering instabilities in dewetting of thin polymer films",
  Summer-Workshop 2009 SPP 1164, Bad Honnef (D) (07/2009).

- "Fingering instabilities in dewetting of thin polymer films",
  Feldberg's Winterschool, Feldberg (D) (12/2009).

Poster presentations

- "Stability and dynamics of polystyrene films",
  Workshop on dynamics under confinement, Grenoble (F) (03/2006).

- "Thin liquid polymer films: Preparation parameters impact fluid dynamics",
  DPG-Frühjahrstagung 2007, Regensburg (D) (03/2007).

- "Fingering instabilities in thin polymer films",
  DPG-Frühjahrstagung, Berlin (D) (02/2008).

- "Thin dewetting polymer films: Fingering and the effect of interfaces",
  Schwerpunktprogramm Mikro- und Nanofluidik, Bad Honnef (D) (07/2008).

- "Roughness affects slippage and slippage affects hydrodynamic instabilities",
  DPG-Frühjahrstagung, Dresden (D) (03/2009).

Acknowledgement

Eidesstattliche Erklärung

Hiermit versichere ich an Eides statt, dass ich die vorliegende Arbeit selbständig und ohne Benutzung anderer als der angegebenen Hilfsmittel angefertigt habe. Die aus anderen Quellen oder indirekt übernommenen Daten und Konzepte sind unter Angabe der Quelle gekennzeichnet.

Die Arbeit wurde bisher weder im In- noch im Ausland in gleicher oder ähnlicher Form in einem Verfahren zur Erlangung eines akademischen Grades vorgelegt.

Saarbrücken, den 30. Juli 2013

(Ludovic Marquant)